Development and Understanding of Novel Compounds Designed as Potential MRI Contrast Agents

THÈSE N^{O} 5095 (2011)

PRÉSENTÉE LE 19 JUILLET 2011

À LA FACULTÉ SCIENCES DE BASE
LABORATOIRE DE CHIMIE INORGANIQUE ET BIOINORGANIQUE
PROGRAMME DOCTORAL EN CHIMIE ET GÉNIE CHIMIQUE

ÉCOLE POLYTECHNIQUE FÉDÉRALE DE LAUSANNE

POUR L'OBTENTION DU GRADE DE DOCTEUR ÈS SCIENCES

PAR

Hugues JACCARD

acceptée sur proposition du jury:

Prof. G. Laurenczy, président du jury
Prof. L. Helm, directeur de thèse
Prof. C. Geraldes, rapporteur
Dr E. Jakab Tóth, rapporteur
Prof. K. Severin, rapporteur

ÉCOLE POLYTECHNIQUE
FÉDÉRALE DE LAUSANNE

Suisse
2011

Table of Contents

Abstract **1**
Résumé **3**

Chapter I: Introduction

I.1 Nuclear Magnetic Resonance **7**
I.1.1. Zeeman effect 7
I.1.2. Excitation process 8
I.1.3. Macroscopic magnetization 9
I.1.4. Rotating frame 10
I.1.5. Free Induction Decay 11
I.1.6. Chemical shift 12
I.1.7. Diamagnetism and paramagnetism 12
I.2 Relaxation **14**
I.2.1. Autocorrelation and spectral density functions 15
I.2.2. Longitudinal relaxation 16
I.2.3. Transverse relaxation 18
I.2.4. Bloch equations 20
I.3 Relaxation mechanisms **21**
I.3.1. Dipolar interaction 21
I.3.2. Scalar relaxation 22
I.3.3. Quadrupolar relaxation 23
I.3.4. Chemical shift anisotropy 24
I.3.5. Curie relaxation 25
I.3.6. Spin-Rotation Relaxation 25
I.4 Paramagnetic Relaxation Enhancement **26**
I.4.1. Relaxivity 26
I.4.2. Paramagnetic metal complex 26
I.4.3. Inner-sphere proton relaxivity 27
I.4.4. Solomon-Bloembergen-Morgan theory 28
I.4.5. Lipari-Szabo approach for internal rotation 32
I.4.6. Outer-sphere contribution 32
I.4.7. NMRD profile 33
I.4.8. ^{17}O NMR measurements 35
I.4.9. Rast-Fries-Belorizky approach 37
I.4.10. Modified Florence approach 38
I.5 Magnetic Resonance Imaging **39**
I.5.1 MRI principle 39
I.5.2 MRI Contrast Agents 41
I.6 Scope of this work **45**
I.7 References **48**

Chapter II : Synthesis, complexation and NMR relaxation properties of Gd^{3+} complexes of $Mes(DO3A)_3$

II.1. Introduction 55
II.2. Experimental Section 57
II.2.1. Ligand synthesis and characterization 57
II.2.2. Sample preparation 59
II.2.3. Transmetallation 61
II.2.4. ^{1}H relaxometry 61
II.2.5. ^{17}O NMR spectroscopy 61
II.2.6. Data treatment 61
II.2.7. Molecular mechanics 62
II.3. Results and discussion 63
II.3.1. Ligand synthesis 63
II.3.2. Complexation 63
II.3.3. Structural transition induced by pH 65
II.3.4. ^{1}H NMRD profiles 66
II.3.5. ^{17}O NMR spectroscopy 67
II.3.6. Molecular modeling 71
II.4. Conclusion 73
II.5. Acknowledgements 75
II.6. References 76

Chapter III : Dynamic aggregation of the mid-size gadolinium complex $\{Ph_4[Gd(DTTA)(H_2O)_2]^-_3\}$

III.1 Introduction 81
III.2 Experimental Section 84
III.2.1 Ligand synthesis and characterization 84
III.2.2 Sample preparation 86
III.2.3 ^{1}H relaxivities 87
III.2.4 ^{17}O NMR spectroscopy 87
III.2.5 Data treatment 88
III.2.6 Molecular modeling 88
III.3 Results and discussion 89
III.3.1. Ligand synthesis 89
III.3.2. Concentration effect 90
III.3.3. ^{1}H NMRD profiles 92
III.3.4. ^{17}O NMR spectroscopy 92
III.3.5. ^{17}O and ^{1}H NMR data fittings with SB-LS-RFB 94
III.3.6. ^{1}H NMRD data fittings with the modified Florence approach 98
III.3.7. Aggregate size estimation 101
III.3.8. ^{1}H relaxivity as a function of pH 103
III.3.9. ^{1}H relaxivity in presence of phosphate buffer 103
III.3.10. ^{1}H relaxivity in presence of human serum 104
III.4 Conclusion 106
III.5 Acknowledgements 108
III.6 References 109

Chapter IV : Characterization and relaxivities of the complex $[Gd(DTTA)(H_2O)_2]^-$ conjugated to the polysaccharide chitosan

IV.1. Introduction 115
IV.2. Experimental Section 118
IV.2.1. Ligand synthesis and characterization 118
IV.2.2. Structural characterization of the modified chitosan 121
IV.2.3. Ng{Chi[Gd(DTTA-N'but)$(H_2O)_2]^-$} characterization 122
IV.2.4. Bulk Magnetic Susceptibility 122
IV.2.5. ^{1}H relaxivities 122
IV.2.6. Data treatment 123
IV.3. Results and discussion 124
IV.3.1 Ligand synthesis 124
IV.3.2 Structural characterization of the chitosan chain 126
IV.3.3 ^{1}H relaxivities of $[Gd(DTTA\text{-}N'but)(H_2O)_2]^{2-}$ 128
IV.3.4 ^{1}H relaxivities of {Chi[Gd(DTTA-*N*'but)$(H_2O)_2]^-$} 130
IV.3.5 Effect of concentration on the relaxivity 132
IV.3.6 Time stability of the relaxivity 133
IV.3.7 Formation of the nanogels Ng{Chi[Gd(DTTA-*N*'but)$(H_2O)_2]^-$} 133
IV.3.8 Ng{Chi[Gd(DTTA-*N*'but)$(H_2O)_2]^-$} characterization 134
IV.3.9 ^{1}H relaxivities of Ng{Chi[Gd(DTTA-*N*'but)$(H_2O)_2]^-$} 137
IV.4. Conclusion 139
IV.5. Acknowledgements 141
IV.6. References 142

Chapter V : Monomeric and dimeric bombesin Gd-DOTA complexes : potential MRI contrast agents for tumor targeting

V.1. Introduction 149
V.2. Experimental Section 151
V.2.1. Synthesis and characterization 151
V.2.2. Sample preparation 156
V.2.3. ^{1}H relaxivities 156
V.2.4. Data treatment 157
V.3. Results and discussion 158
V.3.1 Ligands and conjugates synthesis 158
V.3.2 ^{1}H relaxivities of the four Gd-DOTA-bombesin conjugates 158
V.4. Conclusion 163
V.5. Acknowledgements 164
V.6. References 165

Chapter VI : General conclusions

VI.7. Conclusions and perspectives 169
VI.8. General acknowledgements 173
VI.9. References 175

Chapter VII : Appendix

VII.1 General appendix 179
VII.1.1. Symbols 179
VII.1.2. Abbreviations 181
VII.1.3. Constants and numbers 182
VII.2 Appendix to Chapter II 183
VII.2.1 Transmetallation 183
VII.2.2 Normalized peak areas as a function of pH 184
VII.2.3 ^{17}O NMR data of $\{Mes(H_2DO3A)[Gd(DO3A)(H_2O)]_2\}^-$ 184
VII.2.4 ^{17}O NMR data of $\{Mes[Gd(DO3A)(H_2O)_2]_3\}$ 185
VII.2.5 ^{1}H NMRD data of bis-Gd and tris-Gd complexes 186
VII.3 Appendix to Chapter III 187
VII.3.1 Relaxivity of $\{Ph_4[Gd(DTTA)(H_2O)_2]^-_3\}$ as a function of $[Gd^{3+}]$ 187
VII.3.2 ^{1}H NMRD data of $\{Ph_4[Gd(DTTA)(H_2O)_2]^-_3\}$ 188
VII.3.3 ^{17}O NMR data of $\{Ph_4[Gd(DTTA)(H_2O)_2]^-_3\}$ 189
VII.3.4. Relaxivities of $\{Ph_4[Gd(DTTA)(H_2O)_2]^-_3\}$ as a function of pH 189
VII.3.4 Relaxivities time evolution of $\{Ph_4[Gd(DTTA)(H_2O)_2]^-_3\}$ vs. $[PO_4^{3-}]$ 190
VII.3.5 Relaxivities time evolution of $\{Ph_4[Gd(DTTA)(H_2O)_2]^-_3\}$ in human serum 190
VII.4 Appendix to Chapter IV 191
VII.4.1. ICP-MS instrumentation parameters and performance report 191
VII.4.2. ICP-MS experimental data 191
VII.4.3. ^{1}H NMRD data of $[Gd(DTTA\text{-}N'but)(H_2O)_2]^{2-}$ and $[Gd(DTTA\text{-}Me)(H_2O)_2]^-$ 193
VII.4.4. ^{1}H NMRD data of $\{Chi[Gd(DTTA\text{-}N'but)(H_2O)_2]^-\}$ and $Ng\{Chi[Gd(DTTA\text{-}N'but)(H_2O)_2]^-\}$ 194
VII.4.5. Relaxivities of $\{Chi[Gd(DTTA\text{-}N'but)(H_2O)_2]^{2-}\}$ as a function of $[Gd^{3+}]$ 195
VII.4.6. Relaxivities time evolution of $\{Chi[Gd(DTTA\text{-}N'but)(H_2O)_2]^{2-}\}$ 195
VII.4.7. ZetaSizer Nano-ZS parameters of the Standard Operating ..... Procedures (SOP) 195
VII.4.8. DLS size distribution of $Ng\{Chi[Gd(DTTA\text{-}N'but)(H_2O)_2]^-\}$ 196
VII.5 Appendix to Chapter V 197
VII.5.1. ^{1}H NMRD data of monovalent peptide conjugates 197
VII.5.2. ^{1}H NMRD data of divalent peptide conjugates 198

Curriculum Vitae 199
Publications 200
Poster Presentations 200

Abstract

The two last decades have witnessed the appearance and the successful development of magnetic resonance imaging (MRI) contrast agents (CAs). Though MRI, which has become an essential medical diagnostic tool, can be performed without contrast agents, its rather low sensitivity implies long and tedious examination times. This time can be considerably reduced by the use of CAs. Paramagnetic ion complexes, and particularly gadolinium (III) complexes, can thus significantly accelerate the longitudinal relaxation rate $1/T_1$ of the water proton, one of the most common parameters measured in MRI experiments. The relaxivity, the property describing the paramagnetic relaxation enhancement, or PRE, is mainly affected by four parameters : the number of water molecules in the inner coordination sphere of the complex, the proton exchange rate in this inner sphere, the rotational correlation times, related to the size of the molecule, and the electron spin relaxation rates.

This work deals with the development of four new types of compounds designed as potential MRI T_1 contrast agents. The four compounds have different properties and were therefore developed to observe different effect on the relaxivity. High-field CAs, medium-field CA aggregates, linear polymeric and nanoparticular CAs, and targeted CAs are the four different specificities studied in this work.

The first compound, presented in Chapter II, is the tricephalous complex {Mes[Gd(DO3A)(H_2O)$_2$]}. This mid-size molecule was designed as a potential high-field CA. The standard complexation method does not lead to the complete complexation, most probably due to an intramolecular folding of the compound. The complexation is therefore performed in two steps : a complete pre-complexation with magnesium (II) followed by a transmetallation to replace Mg^{2+} by Gd^{3+} in the three complexation sites. This newly developed complexation method can be really useful to achieve complete complexation of mid-size molecules, where complexation shared by two neighboring chelating units can occur.

Chapter III deals with another mid-size trimeric complex, the {Ph_4[Gd(DTTA)(H_2O)$_2$]$^-_3$}. The central core of this compound, composed of four phenyl rings, was designed to favor

aggregation. The relaxivities of the big entities formed is expected to increase significantly in the medium resonance frequency range, *i.e.* between 10 and 200 MHz. The dynamic aggregation is observed by the concentration dependence of the relaxivity. The parameters obtained by fitting the experimental data allow the estimation of the number of molecule in the entities, ranging from the monomer in diluted solution to a few units for more concentrated solutions.

Chapter IV presents Gd3+ chelate complexes conjugated to the linear polysaccharide chitosan. The coupling reaction, performed directly with the Gd^{3+} complex, is achieved through the condensation of a carboxylate uncomplexing arm on the chelating unit with the free amine of the chitosan. The ratio of modified chitosan units in the compound {Chi[Gd(DTTA-*N*'but)$(H_2O)_2$]$^-$} is determined by ICP-MS and elemental analysis. Porous hydrogels nanoparticles, or nanogels, are subsequently formed from the modified linear chitosan by the ionic gelation method. As the material becomes bigger and more rigid, the relaxivities of the formed nanogels were expected to become higher than that of the linear chain. This does unfortunately not occur, most probably because of a partial complexation of the anion triphosphate, used for the formation of the particles, or by limited water diffusion inside the nanogels.

The final chapter of results, Chapter V, presents a family of four compounds designed as target CAs for a specific kind of malignant tumor, such as prostate, breast or some lung cancer cells, which overexpress bombesin receptors. The four studied compounds are therefore composed by the peptide bombesin conjugated to a Gd^{3+} chelate complexe. In order to optimize the peptide-receptor interaction, two bombesin analogues, the Lys^3-bombesin and the Ahx-bombesin(4-14), are used for the synthesis of the monovalent and the divalent peptide conjugates. The relaxometric properties of the four compounds are measured and compared.

Key words : aggregation, bombesin, chitosan, complexation, contrast agent, gadolinium (III), high-field, longitudinal relaxation, magnetic resonance imaging, nanogels, relaxivity, targeted, transmetallation.

Résumé

Les deux dernières décennies ont vu l'apparition et le développement efficace d'agents de contraste pour l'imagerie par résonance magnétiques (IRM). Bien que cette technique, devenue un outil incontournable pour le diagnostique médical, puisse être exécutées sans agent de contraste, sa relativement basse sensibilité implique des temps d'examen longs et fastidieux. Ces temps peuvent être considérablement réduits par l'utilisation d'agent de contraste. Les complexes d'ions paramagnétiques, et particulièrement ceux du gadolinium (III), accélèrent ainsi significativement la vitesse de relaxation longitudinale $1/T_1$ du proton de l'eau, l'un des paramètres les plus mesurés lors d'examens IRM. La relaxivité, propriété décrivant l'augmentation de la relaxation paramagnétique, est modulée principalement par quatre paramètres : le nombre de molécules d'eau dans la première sphère de coordination du complexe, la vitesse d'échange du proton dans cette première sphère de coordination, le temps de corrélation rotationnel et les vitesses de relaxation du spin électronique.

Ce travail traite du développement de quatre nouveaux types de composés, conçus comme de potentiels agents de contraste T_1 pour l'IRM. Ces quatre composés, présentant des propriétés différentes, ont été développés pour observer différents effets sur la relaxivité. Les agents de contraste pour hauts champs, des agrégats pour champs moyens, des agents de contraste nanoparticulaires, ainsi que des agents de contraste ciblés sont les quatre spécificités étudiées dans ce travail.

Le premier composé, présenté dans le Chapitre II, est le complexe tricéphalique {Mes[Gd(DO3A)(H_2O)$_2$]}. Cette molécule de taille moyenne a été développée comme un agent de contraste potentiel pour haut champs magnétiques. La méthode de complexation standard ne permet pas la complexation totale, probablement à cause d'un repliement intramoléculaire du composé. La complexation doit alors être effectuée en deux temps : une pré-complexation totale avec du magnésium (II) suivit d'une transmetallation pour remplacer Mg^{2+} par Gd^{3+} dans les trois sites de complexation. Cette nouvelle méthode de complexation peut être réellement utile pour obtenir une complexation totale de molécules de taille moyenne, où la coordination partagée par deux unités de chélation voisines peut se produire.

Le Chapitre III traite également d'une molécule de taille moyenne portant trois complexes, le $\{Ph_4[Gd(DTTA)(H_2O)_2]^-_3\}$. Le centre de ce composé, formé de quatre cycles phényles, a été conçu pour favoriser l'agrégation de molécules. On attend de la relaxivité de ces grandes entités formées une augmentation importante dans la région des moyennes fréquences de résonance, c'est-à-dire entre 10 et 200 MHz. L'agrégation dynamique est observée par la dépendance de la relaxivité à la concentration. Les paramètres obtenus par le fit des données expérimentales permettent l'estimation du nombre de molécule dans les agrégats, allant du seul monomère dans les solutions diluées à quelques unités pour les solutions plus concentrées.

La Chapitre IV présente le polysaccharide linéaire chitosan sur lequel sont conjugués des complexes de Gd^{3+}. La réaction de couplage, accomplie directement avec le complexe de Gd^{3+}, est réalisée par la condensation d'un carboxylate non complexant de l'unité de chélation avec l'amine libre du chitosan. Le taux de modification des unités du chitosan modifié $\{Chi[Gd(DTTA\text{-}\textit{N}\text{'but})(H_2O)_2]^-\}$ est déterminé par ICP-MS et analyse élémentaire. Des nanoparticules poreuses d'hydrogel, ou nanogels, sont ensuite formées avec le chitosan linéaire modifié par la méthode de gélation ionique. Comme le composé devient plus grand et plus rigide, on s'attend à ce que les relaxivités des nanogels formés soient plus élevées que celles de la chaîne linéaire. Cela n'est malheureusement pas observé, probablement à cause d'une complexation partielle de Gd^{3+} par l'anion triphosphate, utilisé pour la formation des particules, ou d'une diffusion limitée de l'eau à l'intérieur des nanogels.

Le dernier chapitre de résultats, le Chapitre V, présente une famille de quatre composés conçus pour cibler un type spécifique de cellules tumorales malignes, telle que celles des cancers de la prostate, du sein ou des poumons, qui surexpriment des récepteurs de bombésine. Les quatre composés étudiés sont donc composés du peptide bombésine conjugué à des chélates de Gd^{3+}. Dans le but d'optimiser l'interaction peptide-récepteur de peptide, deux analogues de la bombésine, le Lys^3-bombésine et le Ahx-bombésine(4-14), sont utilisés pour synthétiser les conjugués monovalents et divalents. Les propriétés relaxométriques des quatre composés sont mesurées et comparées.

Mots clés : agent de contraste, agrégation, bombésine, chitosan, ciblé, complexation, gadolinium (III), haut-champ, imagerie par résonance magnétique, nanogels, relaxation longitudinale, relaxivité, transmétallation.

Chapter I:

Introduction

I.1 Nuclear Magnetic Resonance 7
I.1.1. Zeeman effect 7
I.1.2. Excitation process 8
I.1.3. Macroscopic magnetization 9
I.1.4. Rotating frame 10
I.1.5. Free Induction Decay 11
I.1.6. Chemical shift 12
I.1.7. Diamagnetism and paramagnetism 12
I.2 Relaxation 14
I.2.1. Autocorrelation and spectral density functions 15
I.2.2. Longitudinal relaxation 16
I.2.3. Transverse relaxation 18
I.2.4. Bloch equations 20
I.3 Relaxation mechanisms 21
I.3.1. Dipolar interaction 21
I.3.2. Scalar relaxation 22
I.3.3. Quadrupolar relaxation 23
I.3.4. Chemical shift anisotropy 24
I.3.5. Curie relaxation 25
I.3.6. Spin-Rotation Relaxation 25
I.4 Paramagnetic Relaxation Enhancement 26
I.4.1. Relaxivity 26
I.4.2. Paramagnetic metal complex 26
I.4.3. Inner-sphere proton relaxivity 27
I.4.4. Solomon-Bloembergen-Morgan theory 28
I.4.5. Lipari-Szabo approach for internal rotation 32
I.4.6. Outer-sphere contribution 32
I.4.7. NMRD profile 33
I.4.8. ^{17}O NMR measurements 35
I.4.9. Rast-Fries-Belorizky approach 37
I.4.10. Modified Florence approach 38
I.5 Magnetic Resonance Imaging 39
I.5.1 MRI principle 39
I.5.2 MRI Contrast Agents 41
I.6 Scope of this work 45
I.7 References 48

I.1 Nuclear Magnetic Resonance

The theoretical introduction of this work will frequently refer to many Nuclear Magnetic Resonance (NMR) concepts. This phenomenon is therefore briefly introduced to define properly the introduced notions.[1-4]

I.1.1. Zeeman effect

The principle of the nuclear magnetic resonance is based on the interactions between nuclei and a magnetic field. Numerous elements, or more precisely isotopes, have an intrinsic nuclear spin angular momentum. Though it is a purely quantum mechanical concept, the spin of a particle can be represented in a classical model as an angular momentum due to its rotation around an axis. The spin angular momentum $\boldsymbol{I}$ is a vector quantity, whose magnitude is given by the equation I.1. The spin quantum number I of the nucleus, a positive multiple of 1/2, is an intrinsic property of a given nuclei. The components of this angular momentum vector are also quantized and there are $2I+1$ possible values for a spin-I nucleus with respect to a given direction. The projection of this vector I_z on an arbitrary chosen z-axis is given by equation I.2.

$$|\boldsymbol{I}| = \hbar\sqrt{I(I+1)} \qquad \text{I.1}$$

$$I_z = m\hbar \qquad \text{I.2}$$

The magnetic quantum number m has $2I+1$ values in integral steps from $-I$ to I ($-I$, $-I+1$, …, I). This means that the spin-1/2 particles, such as the most commonly studied nuclei in NMR ^{1}H, ^{13}C, ^{19}F or ^{31}P, have two permitted orientations ($m = \pm 1/2$). Nuclei with $I = 1$, like ^{14}N, have three possible directions, while nuclei with $I = 0$, like ^{12}C or ^{16}O, have no angular momentum and can consequently not be observed by NMR. From this angular momentum results a magnetic moment $\boldsymbol{\mu}$ directly proportional to $\boldsymbol{I}$ by a factor γ, a constant characteristic for each magnetic isotope and known as the gyromagnetic ratio (equation I.3).

$$\boldsymbol{\mu} = \gamma\, \boldsymbol{I} \qquad \text{I.3}$$

Unsurprisingly this magnetic moment interacts with magnetic fields. The 2*I*+1 orientations of a *I*-spin nuclei, degenerated in the absence of a magnetic field, split into different energy levels when a magnetic field $\boldsymbol{B}_0$ is applied. This phenomenon is called the *Zeeman effect*, and the energy gap is given by equation I.4. By defining the *z*-axis along the magnetic field, this leads to equation I.5, using I.2 and I.3, with B_0 the magnitude of the magnetic field $\boldsymbol{B}_0$.

$$E = -\boldsymbol{\mu} \cdot \boldsymbol{B}_0 \qquad \text{I.4}$$

$$E = -\mu_z B_0 = -m\hbar\gamma B_0 \qquad \text{I.5}$$

The energy levels of the 2*I*+1 states are equally spaced and the gaps are equal to $\hbar\gamma B_0$. The frequency for electromagnetic radiation ν_0 corresponding to these energy gaps can be expressed by equation I.6.

$$\Delta E = h\nu_0 = \hbar\gamma B_0 \;\Rightarrow\; \nu_0 = \frac{\gamma B_0}{2\pi} \text{ or } \omega_0 = \gamma B_0 \qquad \text{I.6}$$

I.1.2. Excitation process

With magnetic fields used in NMR, the frequency corresponding to the energy difference between the nuclear spin states corresponds to the radiofrequency (RF) region of the electromagnetic spectrum. The principle of NMR is based on the energy absorption of a provided radiofrequency wave with a very precise energy. For a typical magnetic field of 9.4 T used in NMR, this gives a frequency of 400 MHz for protons (with the ^{1}H gyromagnetic ratio $\gamma_H = 2.675 \cdot 10^8$ $T^{-1}s^{-1}$), 100.6 MHz for ^{13}C (with $\gamma_C = 6.73 \cdot 10^7$ $T^{-1}s^{-1}$) or 54.3 MHz for ^{17}O (with $\gamma_O = -3.63 \cdot 10^7$ $T^{-1}s^{-1}$).

As the angular momentum $\boldsymbol{I}$ forms an angle with $\boldsymbol{B}_0$ different from 0°, the magnetic moment $\boldsymbol{\mu}$ experience a torque $\boldsymbol{F}$ trying to align it along $\boldsymbol{B}_0$ (equation I.7). By definition, this torque is the time derivative of $\boldsymbol{I}$ (equation I.8).

$$\boldsymbol{F} = \boldsymbol{\mu} \times \boldsymbol{B_0} \qquad \text{I.7}$$

$$\frac{d\boldsymbol{I}}{dt} = \boldsymbol{F} \qquad \text{I.8}$$

The equation I.3, I.7 and I.8 are combined to describe the motion of the magnetic moment $\boldsymbol{\mu}$ (equation I.9). This motion is a revolution, or precession, around $\boldsymbol{B}_0$ and perpendicular to both $\boldsymbol{\mu}$ and $\boldsymbol{B}_0$. The angular frequency $\boldsymbol{\omega}_0$ of the precession is given by equation I.10.

$$\frac{d\boldsymbol{\mu}}{dt} = \gamma\boldsymbol{\mu} \times \boldsymbol{B}_0 \qquad \text{I.9}$$

$$\boldsymbol{\omega}_0 = -\gamma \boldsymbol{B}_0 \qquad \text{I.10}$$

I.1.3. Macroscopic magnetization

The probability of inducing a transition from the lower to the upper energy level is nearly equal to the probability of inducing the reverse transition. The net energy absorption, meaning the intensity of the NMR signal, can be observed thanks to the small population difference of the different energy states. The spin populations of the different energy states follow a Boltzmann distribution (equation I.11).

$$N_m = N_0 \frac{e^{\frac{-E_m}{k_B T}}}{\sum_{n=-I}^{n=I} e^{\frac{-E_n}{k_B T}}} \qquad \text{I.11}$$

Where N_m is the population in the state m, E_m is the energy of the state m, N_0 is the total number of spins, T the absolute temperature and k_B the Boltzmann constant. For a spin-1/2 nucleus such as ^{1}H, the population ratio of two energy states, called spin *up* and spin *down* for the low and high energy states respectively, is given by equation I.12. The difference of population depends on the strength of the applied magnetic field and the temperature. For the proton at 9.4T and 25°C, this ratio is equal to 1.000065, indicating that only one nucleus in about 15000 can be observed.

$$\frac{N_{up}}{N_{down}} = e^{\frac{\Delta E}{k_B T}} = e^{\frac{\gamma \hbar B_0}{k_B T}} \qquad \text{I.12}$$

The macroscopic magnetization $\boldsymbol{M}$ is defined as the vector sum of all individual microscopic moments $\boldsymbol{\mu}$ of all nuclei in the magnetic field. The spins are randomly distributed around the *z*-axis and precess around it in an incoherent way, which averages to zero the magnetization in the *xy*-plane. However, the small population difference between the unlike energy level

induces a non-zero magnetization component along the *z*-axis. This magnetization M_z can be calculated from equations I.5 and I.11, using the approximation $e^x \approx 1+x$ (for x << 1). The resulting relation between the magnetization and the magnetic field strength is known as the Curie's law (equation I.13).

$$M_z = \frac{N_0 \gamma^2 \hbar^2 I(I+1)}{3k_B T} B_0 \qquad \text{I.13}$$

I.1.4. Rotating frame

The motion of the magnetization $\boldsymbol{M}$ in a magnetic field $\boldsymbol{B}$ is a precession around it with an angular frequency $\omega = \gamma B$ (equation I.10). In an NMR experiment, the field $\boldsymbol{B}_{eff}$ is actually composed of two magnetic fields, the strong static field $\boldsymbol{B}_0$ and a weak field $\boldsymbol{B}_1(t)$ produced by the radiofrequency field applied along the *x*-axis and oscillating along it with the angular frequency $\boldsymbol{\Omega}$. This linear oscillation can be considered as the sum of two rotating vectors $\boldsymbol{B}_{1cw}$ and $\boldsymbol{B}_{1ccw}$, rotating in opposite directions with frequencies $-\boldsymbol{\Omega}$ and $\boldsymbol{\Omega}$ (equation I.14).

$$\boldsymbol{B}_1 = \boldsymbol{B}_{1cw} + \boldsymbol{B}_{1ccw} = \begin{bmatrix} B_1\cos(-\Omega t) \\ B_1\sin(-\Omega t) \\ 0 \end{bmatrix} + \begin{bmatrix} B_1\cos(\Omega t) \\ B_1\sin(\Omega t) \\ 0 \end{bmatrix} = \begin{bmatrix} 2B_1\cos(\Omega t) \\ 0 \\ 0 \end{bmatrix} \qquad \text{I.14}$$

The complex motion of the magnetization in an oscillating field can be simplified by considering a new Cartesian coordinates system (*x'*, *y'*, *z'*) rotating around the *z*-axis in phase with the rotating vector $\boldsymbol{B}_{1cw}$ with the angular frequency $-\boldsymbol{\Omega}$. In this new frame, called the *rotating frame*, $\boldsymbol{B}_{1cw}$ will appear static, while $\boldsymbol{B}_{1ccw}$ will seem to rotate with an angular frequency of $2\boldsymbol{\Omega}$. The time derivative of the magnetization in both the laboratory frame ($d\boldsymbol{M}/dt$) and the rotating frame ($\partial\boldsymbol{M}/\partial t$) are related by equation I.15.

$$\frac{d\boldsymbol{M}}{dt} = \frac{\partial \boldsymbol{M}}{\partial t} + (\boldsymbol{\Omega} \times \boldsymbol{M}) \qquad \text{with } \boldsymbol{\Omega} = \begin{bmatrix} 0 \\ 0 \\ -\Omega \end{bmatrix} \qquad \text{I.15}$$

The dynamics of the magnetization $\boldsymbol{M}$, described by the equation I.16 in the laboratory frame (from equation I.9), becomes therefore equation I.17, where $\boldsymbol{B}_{eff}$ is defined as the effective field, *i.e.* the sum of $\boldsymbol{B}_0$, $\boldsymbol{B}_1$ and $\boldsymbol{\Omega}/\gamma$ (Figure I.1).

$$\frac{d\boldsymbol{M}}{dt} = \gamma \boldsymbol{M} \times (\boldsymbol{B}_0 + \boldsymbol{B}_1) \qquad \text{I.16}$$

$$\frac{\partial \boldsymbol{M}}{\partial t} = \frac{d\boldsymbol{M}}{dt} - (\boldsymbol{\Omega} \times \boldsymbol{M}) = \gamma \boldsymbol{M} \times (\boldsymbol{B}_0 + \boldsymbol{B}_1) + (\boldsymbol{M} \times \boldsymbol{\Omega}) = \gamma \boldsymbol{M} \times \left(\boldsymbol{B}_0 + \boldsymbol{B}_1 + \frac{\boldsymbol{\Omega}}{\gamma} \right) \qquad \text{I.17}$$
$$= \gamma \boldsymbol{M} \times \boldsymbol{B}_{eff}$$

The two fields $\boldsymbol{\Omega}$ and $\boldsymbol{B}_0$, in opposite directions, compensate if $\Omega = \gamma B_0$. The resulting $\boldsymbol{B}_{eff}$ becomes equal to $\boldsymbol{B}_1$, composed by the static $\boldsymbol{B}_{1cw}$–field and the rotating $\boldsymbol{B}_{1ccw}$–field. The latter rotates with the fast angular frequency of $2\boldsymbol{\Omega}$ and will have no effect when averaged in time. An applied radiofrequency field will therefore result in a precession of the magnetization around the $\boldsymbol{B}_{1cw}$-component with the angular velocity $\boldsymbol{\omega}_1 = -\gamma \boldsymbol{B}_1$. The so-called *flip angle* $\beta_1 = \omega_1 t$ corresponds to the angle of rotation of the magnetization $\boldsymbol{M}$ around the *x*-axis resulting from a $\boldsymbol{B}_1$ application during a time *t*.

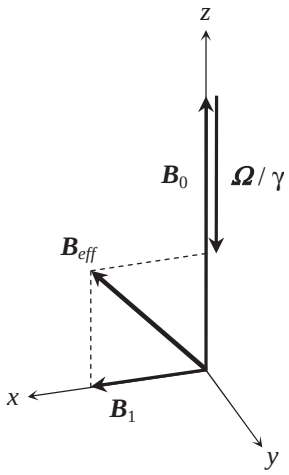

Figure I.1 – The effective magnetic $\boldsymbol{B}_{eff}$ in the rotating frame resulting from the static $\boldsymbol{B}_0$ and the RF fields components $\boldsymbol{B}_1$ and $\boldsymbol{\Omega} / \gamma$.

I.1.5. Free Induction Decay

After $\boldsymbol{B}_1$ is turned off, the magnetization $\boldsymbol{M}$ will have a component in the *xy*-plane, $\boldsymbol{M}_{xy}$, and will continue to rotate around $\boldsymbol{B}_0$ (equation I.16). This rotating magnetization in the *xy*-plane can be observed thanks to the induced current in a detector coil. This signal, known as the FID for Free Induction Decay, allows the determination of the resonance frequency, or Larmor frequency (Figure I.2). The Larmor frequencies of distinctive nuclei and their respective contribution are obtained by Fourier transform of this signal. The intensity of the signal decreases due to relaxation as will be explained in Chapter I.2.

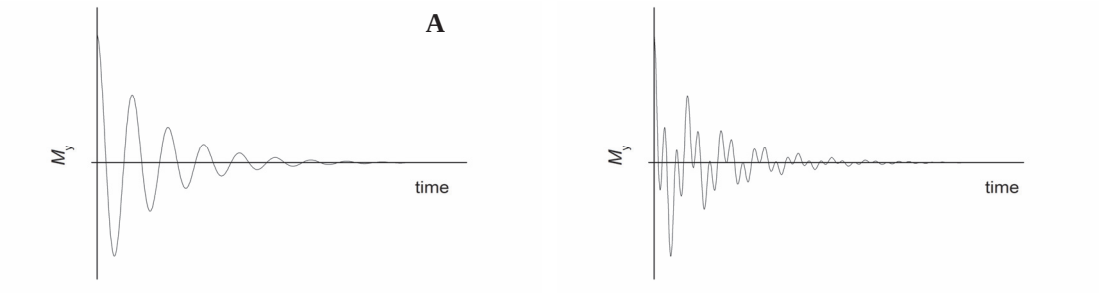

Figure I.2 **–** FID generated by a single Larmor frequency (A) and by two Larmor frequencies of equal intensities (B).

I.1.6. Chemical shift

In a molecule, all the nuclei of a magnetic isotope do not have exactly the same resonance frequency. This phenomenon arises from the magnetic field $\boldsymbol{B}$ actually experienced by a nucleus, that differs slightly from the applied field $\boldsymbol{B}_0$. The experienced magnetic field depends on the environment of the nucleus, determined by the local electronic distribution on the atom. The motion of electrons within their molecular orbitals generates a small magnetic field that affects the local magnetic field. This effect, known as the *chemical shift*, allows discriminating the different types of an isotope and is used to characterize molecules.

The chemical shift δ is always defined by the frequency difference of the signal with respect to the frequency of a reference nucleus (equation I.18). The order of magnitude of this frequency difference is about one million times smaller than the reference frequency ν_{ref} and is therefore expressed in part per million (*ppm*). The non-dependence of the chemical shift to the applied magnetic field is an appreciable advantage of this notion.

$$\delta = 10^6 \frac{(\nu - \nu_{ref})}{\nu_{ref}} \qquad \text{I.18}$$

I.1.7. Diamagnetism and paramagnetism

When placed in a magnetic field, any substance induces a magnetic moment. This phenomenon is known as the *magnetic induction*. This magnetization $\boldsymbol{M}_0$ is related to the applied field $\boldsymbol{B}_0$ through a proportional constant χ_v, called the *volume magnetic susceptibility*, representing the magnetization capability of the compound (equation I.19). The specific molar

magnetic susceptibility χ_M is obtained by multiplying the volume magnetic susceptibility χ_v by the molar mass *M*, divided by the density d (equation I.20).

$$\boldsymbol{M}_0 = \chi_v \boldsymbol{B}_0 \qquad \text{I.19}$$

$$\chi_M = \frac{M}{\mathrm{d}} \chi_v \qquad \text{I.20}$$

Diamagnetism is characterized by a negative volume magnetic susceptibility $\chi_v < 0$, indicating an induced magnetization opposed to the external field. This effect arises from the interactions between the magnetic field and the movement of the electrons in their orbitals. It is systematic and present in any compound.

Paramagnetic compounds are characterized by a positive magnetic susceptibility ($\chi_v > 0$). The induced magnetic moment is now parallel to the field and reinforces it. This effect is generated by one or more unpaired electrons and is therefore present either in free organic radicals or in metal complexes. The interaction of the unpaired electron spins with nuclear spins is strong, and it influences the nuclear magnetic resonance in two ways. First it changes the resonance frequency of the nucleus, *i.e.* its chemical shift. Secondly, it reduces tremendously the time for the system to recover the equilibrium, known as the relaxation time (see Chapter I.2). The latter point will be discussed in more details in Chapter I.4. Unless specified, the paramagnetic species described in this work will always refer to paramagnetic metal complexes.

It is relevant to point out that the magnetic susceptibility of compounds characterized by the conservation of the magnetization without external field, such as ferromagnetic or antiferromagnetic compounds, is also positive, while a null susceptibility corresponds to vacuum.

I.2 Relaxation

After the excitation by an RF pulse, the magnetization will not precess perpetually around the $\boldsymbol{B}_0$-field but will return to its equilibrium position along the *z*-axis. This phenomenon is known as *relaxation*. The motion of the magnetization during the relaxation (Figure I.3 A) can be described in three processes:

- The precession of ***M*** around the z-axis
- The evolution of the M_z component toward the thermal equilibrium position along z, known as longitudinal relaxation (Figure I.3 B)
- The evolution of the M_{xy} component toward zero, defined as the transverse relaxation (Figure I.3 C).

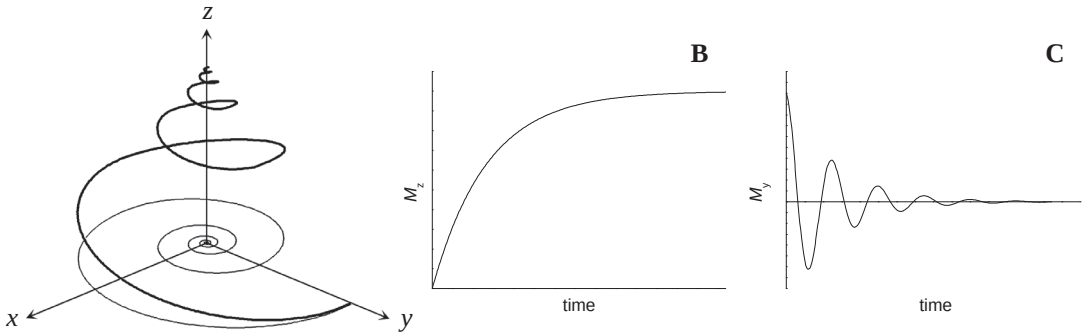

Figure I.3 – The evolution of the magnetization ***M*** towards the equilibrium along the *z*-axis after a 90° RF pulse combining the three processes (A), the recovery of total M_z component (B) and the loss of signal in the *xy*-plane, seen from the *y*-axis (C).[2]

The longitudinal relaxation represents the return of the populations toward the Boltzmann equilibrium, while the transverse relaxation corresponds to the loss of the spin coherence. The relaxation processes are described by the relaxation times T_1 and T_2 and the relaxation rates $R_1 = 1 / T_1$ and $R_2 = 1 / T_2$ respectively.

I.2.1. Autocorrelation and spectral density functions

In order to describe the evolution of the magnetization and the causes of the relaxation, mathematics tools have to be introduced. The correlation function of a stochastic signal given by the time function *f(t)* is used to describe its time dependence. The most simple autocorrelation function $G(\tau)$ is defined by the mean value of the variable at time *t* multiplied by the variable at a time $t + \tau$ (equation I.21).

$$G(\tau) = \langle f(t) f(t+\tau) \rangle \qquad \text{I.21}$$

Where the average is written with brackets $\langle\ \rangle$. For $\tau = 0$, the function *f(t)* is multiplied by itself, resulting in the initial mean square value $\langle f(t)^2 \rangle$, while a long τ will make $G(\tau)$ average to zero. $G(\tau)$ describes the correlation of the function *f(t)*, that is the rate of fluctuation of the stochastic variable. Fast fluctuating *f(t)* is characterized by a correlation function dropping rapidly to zero (Figure I.4 A) and slow fluctuations will lead to slowly decreasing $G(\tau)$ (Figure I.4 B).

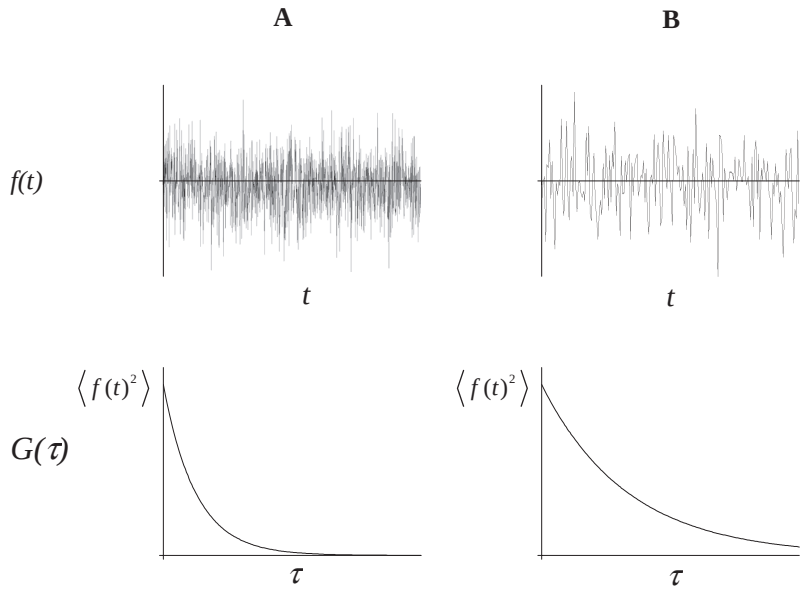

Figure I.4 – The autocorrelation function $G(\tau)$ corresponding to the stochastic time function *f(t)* for fast (A) and slow (B) fluctuations.

$G(\tau)$ is in general approximated by a simple negative exponential with the initial value $\left\langle f(t)^2 \right\rangle$. The decay rate is characterized by the so-called correlation time τ_c, describing the "loss of memory" of the stochastic time function (equation I.22).

$$G(\tau) = \left\langle f(t)^2 \right\rangle \exp\left(-\frac{|\tau|}{\tau_c} \right) \qquad \text{I.22}$$

The Fourier Transform of this correlation function, leading to a Lorentzian function, allows the determination of the characteristic frequencies of the fluctuations described by the correlation function $G(\tau)$. The obtained function $J(\omega)$ is called the spectral density function, given by equation I.23 under its normalized form and illustrated by Figure I.5.

$$J(\omega) = 2\left\langle f(t)^2 \right\rangle^{-1} \int_0^{+\infty} G(\tau) \exp(-i\omega\tau)\, d\tau = 2\frac{\tau_c}{1+\omega^2\tau_c^2} \qquad \text{I.23}$$

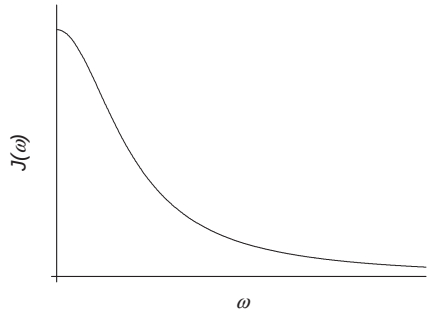

Figure I.5 **–** Positive part of the spectral density function $J(\omega)$

Applied to NMR, the stochastic variable is simply the intensity of the fluctuating magnetic field. The mean square value of the stochastic function $\left\langle f(t)^2 \right\rangle$ is therefore written $\left\langle B^2 \right\rangle$.

I.2.2. Longitudinal relaxation

The recovery of the magnetization along the *z*-axis represents the return of the spin populations to the Boltzmann equilibrium. This implies a transition from the high-energy state to the low-energy state, achieved either by spontaneous or stimulated emission. The probability of spontaneous emission, whose rate depends on the third power of the transition frequency, is however negligible at NMR frequencies.

The magnetic noise, *i.e.* the magnetic field fluctuations, is the source of the stimulations needed for these stimulated emissions. The fluctuations are created by the random motions of the molecules and can arise from several mechanisms generating time-dependent magnetic interactions, such as dipolar coupling, scalar coupling and electric quadrupole interaction to name a few (Chapter I.3). All these mechanisms contribute to the observable relaxation rate. The efficiency of the relaxation depends on the probability of finding an oscillation at the appropriate frequency. The relaxation rate for the ideal random field mechanism is described by equation I.24.[4] $\langle B^2 \rangle$ represents the mean square value of the local fluctuating field.

$$\frac{1}{T_1} = \gamma^2 \langle B^2 \rangle J(\omega_0) = \gamma^2 \langle B^2 \rangle \frac{\tau_c}{1+(\omega_0 \tau_c)^2} \qquad \text{I.24}$$

The NMR pulse sequence used to measure the longitudinal relaxation time T_1 is called *inversion recovery* (IR). This sequence inverts the equilibrium magnetization along the *z*-axis M_0 by a 180° pulse. The magnetization undergoes a longitudinal relaxation during a variable time τ, leading to the magnetization $M_z(\tau)$. Finally, $M_z(\tau)$ is laid down in the *xy*-plane by a 90° pulse in order to detect the free induction decay.

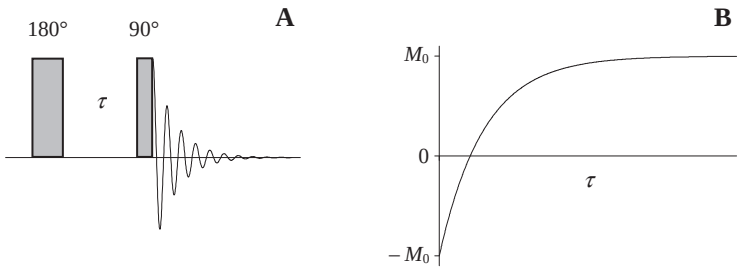

Figure I.6 **–** The inversion recovery pulse sequence (A) and the evolution of the magnetization $M_z(\tau)$ with the variable delay τ (B).

The exponential evolution of the magnetization with respect to the variable delays τ allows the calculation of the longitudinal relaxation time T_1, according to equation I.25.

$$M_z(\tau) = M_0 \left[1 - 2\exp\left(\frac{-\tau}{T_1} \right) \right] \qquad \text{I.25}$$

I.2.3. Transverse relaxation

After a RF pulse, all the individual spins magnetic moments precess coherently around the *z*-axis, creating a magnetization component in the *xy*-plane. The process called the transverse relaxation corresponds to the disappearance of this magnetization in the *xy*-plane and is characterized by the transverse relaxation time T_2. This decay is due on one hand to the return of the magnetization along the *z*-axis, seen in case of the longitudinal relaxation, and on the other hand to the loss of coherence of the individual spin magnetic moments with each other. This spin phase dispersion, or spin *dephasing*, arises from the fluctuating magnetic field cause by molecular motions and $\boldsymbol{B}_0$-field inhomogeneities.

As the magnetization recovery along the *z*-axis will inescapably lead to the decay of the M_{xy}-component, the T_2-relaxation can never be slower than the T_1-relaxation. It can however be much faster. The transverse relaxation rate for the ideal random field mechanism is described by equation I.26.[4]

$$\frac{1}{T_2} = \frac{1}{2}\gamma^2 \left\langle B^2 \right\rangle J(\omega_0) + \frac{1}{2}\gamma^2 \left\langle B^2 \right\rangle J(0) = \frac{1}{2}\gamma^2 \left\langle B^2 \right\rangle \frac{\tau_c}{1+\omega^2\tau_c^2} + \gamma^2 \left\langle B^2 \right\rangle \frac{1}{2}\tau_c \qquad \text{I.26}$$

The first term of this expression represents the T_2-relaxation due to the longitudinal relaxation and is negligible in the slow motion limit ($\omega_0\tau_c >> 1$). In the extreme narrowing limit ($\omega_0\tau_c << 1$), the two parts of this expression become equal ($J(\omega_0) \approx J(0)$), implying that the transverse relaxation rate is equal to the longitudinal relaxation rate. Figure I.7 presents the evolution of both relaxation times T_1 and T_2 with variable correlation time.

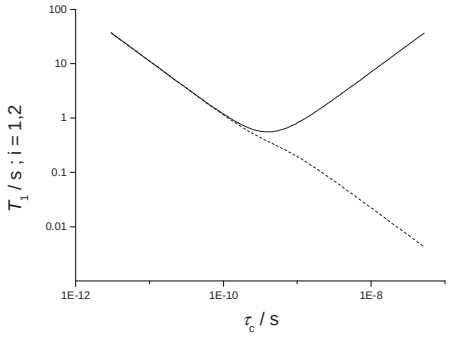

Figure I.7 – Evolution of the longitudinal relaxation time T_1 (solid) and the transverse relaxation time T_2 (dash) with the correlation time τ_c, using $\gamma^2 \left\langle B^2 \right\rangle$ = 4.5 · 10^9 s^{-2} and $\omega_0/2\pi$ = 400 MHz.

Corresponding to the loss of the magnetization in the *xy*-plane, the FID decay represents in principle the transverse relaxation time T_2. However, because of the inhomogeneities of the static field, it does not reflect the real T_2, but the observed relaxation time T_2^* (equation I.27).

$$\frac{1}{T_2^*} = \frac{1}{T_2} + \frac{1}{T_2(\Delta B_0)} \qquad \text{I.27}$$

To sidestep this difficulty, the chosen method to measure T_2 consists in a series of spin echoes to refocus the spins and observe the real decay of the signal in the *xy*-plane. The so-called *Carr-Purcell-Meiboom-Gill (CPMG) sequence* is composed of one 90° pulse along the *x*-axis to lay down the magnetization in the *xy*-plane followed by a series of 180° pulses along the *y*-axis that refocus the signal by spin echoes (Figure I.8 A). The exponential decrease of the echo amplitude is due to the effective T_2 and is related to variable delay τ (equation I.28). The plot of the echo amplitude $A(\tau)$ against τ (Figure I.8 B), obtained by repeated experiments with variable τ, allows the determination of T_2.

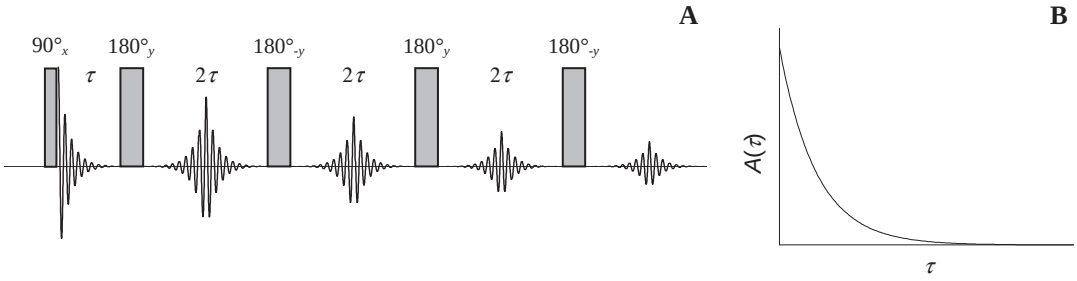

Figure I.8 **–** The CPMG pulse sequence (A) and the echo intensity as a function as the variable delay τ (B) used to determined the transverse relaxation time T_2.

$$A(\tau) = A(0)\exp\left(-\frac{\tau}{T_2}\right) \qquad \text{I.28}$$

I.2.4. Bloch equations

The rate of change of the global magnetization ***M*** due to the relaxation is expressed by three differential equations, proposed in 1946 by Felix Bloch and hence known as the Bloch equations (equations I.29) (with M_0 the equilibrium magnetization along the *z*-axis).

$$\left.\begin{aligned} \frac{dM_x}{dt} &= -\frac{M_x}{T_2} \\ \frac{dM_y}{dt} &= -\frac{M_y}{T_2} \\ \frac{dM_z}{dt} &= -\frac{M_z - M_0}{T_1} \end{aligned}\right\} \qquad \text{I.29}$$

The superposition of the relaxation processes with the precession motion describes the total rate of change of ***M***. This is expressed by equation I.30, that combines the Bloch equations under their matrix notation with the precession equation I.17.

$$\frac{d\boldsymbol{M}}{dt} = \gamma \boldsymbol{M} \times \boldsymbol{B}_{eff} - \boldsymbol{R}\left(\boldsymbol{M} - \boldsymbol{M}_0\right) \qquad \text{I.30}$$

with $\boldsymbol{R} = \begin{pmatrix} \frac{1}{T_2} & 0 & 0 \\ 0 & \frac{1}{T_2} & 0 \\ 0 & 0 & \frac{1}{T_1} \end{pmatrix}$ and $\boldsymbol{M}_0 = \begin{pmatrix} 0 \\ 0 \\ M_0 \end{pmatrix}$

I.3 Relaxation mechanisms

This chapter presents the different mechanisms that can result in magnetic field fluctuations responsible for the relaxation. The contribution of each mechanism has to be taken into account to describe a global, or observed, relaxation. Because the relaxation rates constants, *i.e.* the reciprocal of the relaxation times, are additive magnitudes, the global relaxation rate is equal to the sum of the relaxation rates of each contribution (equation I.31, where $1/T_i^m$ is the relaxation time of the mechanism *m*). The contribution of the various mechanisms differs drastically depending on the type of the nucleus, the chemical environment or the magnetic field strength. Though different mechanisms can interfere and induce a so-called cross-correlation mechanism, the mechanisms will be considered as independent and no cross-correlation will be treated.[5-7]

$$\frac{1}{T_{\mathrm{i}}} = \sum_m \frac{1}{T_{\mathrm{i}}^m} \qquad \text{I.31}$$

I.3.1. Dipolar interaction

Field fluctuations can arise from the interaction between two magnetic dipoles, known as the dipole-dipole or dipolar coupling. Due to the perpetual alignment of the spins along the magnetic field, the local dipolar field of a neighboring spin experienced by a nucleus depends on the orientation of the molecule (Figure I.9). This interaction can be *heteronuclear* or *homonuclear,* depending if the nuclei are different or the same sort respectively, and *intra-* or *intermolecular*. Moreover, in the case of a paramagnetic system, this interaction occurs with unpaired electrons (Chapter I.4). In 1/2 spin systems, the dipolar mechanism is the main contribution to the relaxation. This process is still important for higher spin systems.

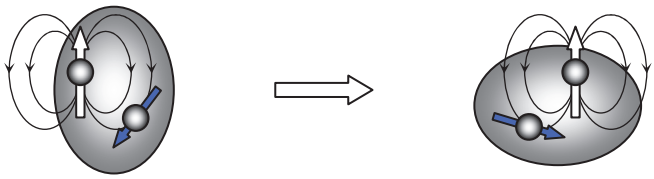

Figure I.9 **–** Intramolecular orientation-dependent dipolar field experienced by a neighboring spin

The relaxation rate constants of spin *I* due to the dipolar interaction with spin *S* have been described by Solomon in 1955 (equations I.32 and I.33).[8]

$$\frac{1}{T_1^{DD}} = \frac{2}{15} S(S+1) C_{DD}^2 \left[J(\omega_S - \omega_I, \tau_d) + 3J(\omega_I, \tau_d) + 6J(\omega_S + \omega_I, \tau_d) \right] \qquad \text{I.32}$$

$$\frac{1}{T_2^{DD}} = \frac{1}{15} S(S+1) C_{DD}^2 \left[4J(0, \tau_d) + J(\omega_S - \omega_I, \tau_d) + 3J(\omega_I, \tau_d) + 6J(\omega_S, \tau_d) + 6J(\omega_S + \omega_I, \tau_d) \right] \qquad \text{I.33}$$

With $$C_{DD} = \frac{\gamma_I \gamma_S \hbar}{r_{IS}^3} \frac{\mu_0}{4\pi} \qquad \text{I.34}$$

Where γ_I and γ_S are the gyromagnetic ratios of spins *I* and *S* respectively, μ_0 is the permeability of vacuum and r_{IS} the inter-spin distance, C_{DD} (I.34) is the dipolar coupling constant and $J(\omega, \tau_d)$ the spectral density (equation I.23) with τ_d the specific correlation time.

I.3.2. Scalar relaxation

In addition to the strong dipole-dipole interaction between the nucleus and an electron, paramagnetic systems offer a new pathway for nuclear relaxation by considering as non-zero the probability of finding an electron at the nucleus. This interaction, known as the *Fermi contact interaction*, or *scalar interaction*, occurs when the nucleus-electron distance is about the nuclear radius (~ 10 fm) and where the particles can not be considered as point dipoles.

The so-called delocalization contribution considers the probability of finding the unpaired electron on an interacting nucleus. This contribution is however not always important or even possible. Only nuclei bound directly to paramagnetic specie can undergo a scalar interaction. Moreover, the magnitude of this interaction depends on the shape of the *Singly Occupied Molecular Orbital* (SOMO). For instance, the accessible SOMOs of the transition metal induce an important effect, while the lanthanides, where the SOMOs are hidden, will not interact. As well as this spin delocalization contribution, such systems provide a spin polarization effect. In this contribution, the unpaired electrons draw the neighbor electrons of the same spin, which polarizes the orbital and changes their shapes. The probability of finding an electron on its own nucleus becomes then non-zero.[9,10] The equation I.35 and I.36 describes the relaxation rates of the scalar contribution.

$$\frac{1}{T_1^{SC}} = \frac{2}{3} S(S+1) \left(\frac{A}{\hbar} \right)^2 J(\omega_S - \omega_I, \tau_{sc2}) \qquad \text{I.35}$$

$$\frac{1}{T_2^{SC}} = \frac{1}{3} S(S+1) \left(\frac{A}{\hbar} \right)^2 \left[J(0, \tau_{sc1}) + J(\omega_S - \omega_I, \tau_{sc2}) \right] \qquad \text{I.36}$$

Where $A/\hbar$ is the scalar coupling constant, S the spin of the nucleus S and τ_{sc1} and τ_{sc2} the effective correlation times related to the electronic relaxation rates $1/T_{1e}$ and $1/T_{2e}$.

I.3.3. Quadrupolar relaxation

Besides their magnetic dipole moments, nuclei with spin quantum number I larger than 1/2 possess an *electric quadrupolar moment*. The charge distribution in the nucleus, which can be visualized as elliptic with positive charge excess at the poles and charge depletion at the equator, induces a nuclear quadrupole moment Q.

Quadrupoles, unlike dipoles, do not interact with uniform electric fields, but only with *electric field gradients*. In high symmetry systems (cubic, spherical, octahedral, tetrahedral), the electric field generated by surrounding charges cancel out, resulting in no quadrupolar interaction. In lower symmetry environments however, the nuclei experience an anisotropic electric field gradient, depending on the orientation of the molecule in the magnetic field. Due to this anisotropy, the random rotational reorientation of the molecule makes the local magnetic field fluctuate and induces consequently relaxation. Equation I.37 describes the longitudinal relaxation time due to the quadrupolar contribution. This mechanism prevails for diamagnetic $I > ½$ spin systems.

$$\frac{1}{T_1^Q} = \frac{3\pi^2}{50} \frac{2I+3}{I^2(2I-1)} \chi^2 \left(1 + \frac{\eta^2}{3} \right) \left[J(\omega_I, \tau_c) + 4J(2\omega_I, \tau_c) \right] \qquad \text{I.37}$$

With $$\chi = \left(\frac{e^2 q_{zz} Q}{h} \right) \qquad \text{I.38}$$

$$eq_{zz} = \frac{\partial^2 V}{\partial z^2} \qquad \text{I.39}$$

$$\eta = \frac{\left| eq_{xx} - eq_{yy} \right|}{eq_{zz}} \qquad \text{I.40}$$

Where $\chi^2\left(1+\eta^2/3\right)$ is the quadrupolar coupling constant (equation I.38) with eq_{zz} the electric field gradient along the arbitrary z axis (equation I.39), η the asymmetry parameter of the electric field gradient (equation I.40), and I is the nuclear spin.

I.3.4. Chemical shift anisotropy

Due to the interactions with the neighboring groups or magnetic moments induced by the external field, the chemical shift can be dependent on the orientation of the molecule in the field. Though it averages to zero in solution, this *chemical shift anisotropy* (CSA) can nevertheless provide a relaxation mechanism by modulating the magnetic field experienced by a nucleus. The CSA of an aromatic ring due to the magnetic field induced by the diamagnetic current is presented in Figure I.10.

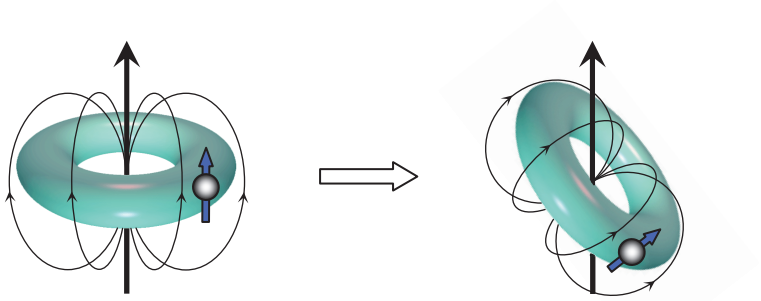

Figure I.10 – Field fluctuations induced by the chemical shift anisotropy of an aromatic ring.

The chemical shift anisotropy $\Delta\sigma$ is presented in equation I.41 while the CSA longitudinal and transversal relaxation rates are given in equations I.42 and I.43 respectively.

$$\Delta\sigma = \frac{\left[2\sigma_{zz} - \left(\sigma_{xx} + \sigma_{yy}\right)\right]}{3} \qquad \text{I.41}$$

$$\frac{1}{T_1^{CSA}} = \frac{\gamma_I^{\,2} B_0^{\,2} \left(\Delta\sigma\right)^2}{15} J(\omega_I, \tau_c) \qquad \text{I.42}$$

$$\frac{1}{T_2^{CSA}} = \frac{\gamma_I^{\,2} B_0^{\,2} \left(\Delta\sigma\right)^2}{90} \left[4J(0, \tau_c) + 3J(\omega_I, \tau_c)\right] \qquad \text{I.43}$$

Where σ_{xx}, σ_{yy} and σ_{zz} are the components of the CSA tensor, γ_I is the gyromagnetic ratio of nuclei I. The relaxation rates are field dependent, and are proportional to $B_0^{\,2}$ under conditions of fast molecular motion ($\omega_I^{\,2}\tau_c^{\,2} << 1$).

I.3.5. Curie relaxation

In paramagnetic systems, the differences in populations of the electron spins energy levels due to the Boltzmann distribution induce a magnetic moment. The relaxation arising from this perturbation is known as the Curie relaxation. The Curie relaxation rates and the induced magnetization $\langle S_z \rangle$ are given by equations I.44, I.45 and I.46 respectively, with C_{DD} the dipolar coupling constant (equation I.34).

$$\frac{1}{T_1^C} = \frac{2}{5} C_{DD}^2 \langle S_z \rangle^2 \left[3J(\omega_I, \tau_c) \right] \qquad \text{I.44}$$

$$\frac{1}{T_2^C} = \frac{1}{5} C_{DD}^2 \langle S_z \rangle^2 \left[4J(0, \tau_c) + 3J(\omega_I, \tau_c) \right] \qquad \text{I.45}$$

$$\langle S_z \rangle = \frac{\gamma_S \hbar S(S+1) B_0}{3k_B T} = \frac{\hbar S(S+1)\omega_S}{3k_B T} \qquad \text{I.46}$$

I.3.6. Spin-Rotation Relaxation

This field fluctuation arises from magnetic moments created by the movement of the electrons in the molecule. The Spin-Rotation relaxation is particularly important for small molecules undergoing fast rotations in a non-viscous lattice. The longitudinal relaxation rate is given by equation I.47.

$$\frac{1}{T_1^{SR}} = \frac{I_r{}^2 C_{SR}^2}{9\hbar^2 \tau_c} \qquad \text{I.47}$$

Where I_r is the molecular inertia moment and C_{SR} is the spin-rotation constant, in Hz. This relationship is valid only for spherical molecules.

I.4 Paramagnetic Relaxation Enhancement

As mentioned in previous chapters, the rates of both longitudinal and transverse nuclear relaxation are increased by the presence of paramagnetic species in solution, which offers new relaxation pathways. This phenomenon, known as the *Paramagnetic Relaxation Enhancement* (PRE), arises from the interaction of the nucleus with the magnetic moment of electron spins, called the hyperfine interaction. Because the gyromagnetic ratio of the electron is about 658 times that of the proton, the hyperfine interaction is much stronger than the nucleus-nucleus interaction.[5-7]

I.4.1. Relaxivity

The observed relaxation rates $1/T_i^{obs}$ are the sums of the diamagnetic and paramagnetic contributions, $1/T_i^d$ and $1/T_i^p$ respectively (equation I.48). While the nucleus-nucleus dipole-dipole, the quadrupolar, the CSA and the spin rotation mechanisms represent the diamagnetic contribution, the paramagnetic relaxation is caused by the nucleus-electron dipole-dipole, the scalar and the Curie interactions.

$$\frac{1}{T_i^{obs}} = \frac{1}{T_i^d} + \frac{1}{T_i^p} \quad ; \; i = 1,2 \qquad \text{I.48}$$

The paramagnetic relaxation rate is directly proportional to the concentration of the paramagnetic species. To refer their efficiency to enhance the relaxation rate, the notion of relaxivity r_i, in units of $mM^{-1}\,s^{-1}$, has been introduced. The observed relaxation rate in terms of relaxivity and concentration of the paramagnetic species [M] is given by equation I.49.

$$\frac{1}{T_i^{obs}} = \frac{1}{T_i^d} + r_i\left[\mathrm{M}\right] \quad ; \; i = 1,2 \qquad \text{I.49}$$

I.4.2. Paramagnetic metal complex

Because of the rapid vanishing of the magnetic field with distance, a nucleus has to be in the immediate vicinity of the paramagnetic center in order to experience the PRE. The binding of

water molecules to a paramagnetic metal ion is a possible chemical interaction that allows this proximity. The inner coordination sphere water molecules and their protons exchange with bulk water molecules and protons, which propagates the paramagnetic effect to the bulk. The solvent molecules of the bulk however also experience the paramagnetic influence when diffusing nearby the metal ion. This contribution is defined as the outer sphere relaxation. The total paramagnetic relaxation rate enhancement $1/T_i^p$ is therefore constituted by the inner-sphere (IS) and the outer-sphere (OS) contributions (equations I.50 and I.51), that can contribute about the same extent.

$$\frac{1}{T_i^p} = \left(\frac{1}{T_i^p}\right)^{\mathrm{IS}} + \left(\frac{1}{T_i^p}\right)^{\mathrm{OS}} \qquad \text{I.50}$$

$$r_i = r_i^{\mathrm{IS}} + r_i^{\mathrm{OS}} \qquad \text{I.51}$$

I.4.3. Inner-sphere proton relaxivity

The inner-sphere contribution arises from the chemical exchange of the coordinated water proton with the bulk. Equations I.52 and I.53 present the longitudinal and transverse inner-sphere relaxation rates.[11-13]

$$\left(\frac{1}{T_1^p}\right)^{\mathrm{IS}} = \frac{q[\mathrm{M}]}{[\mathrm{H_2O}]}\left(\frac{1}{T_{1M}+\tau_M}\right) = P_M \frac{1}{T_{1M}+\tau_M} \qquad \text{I.52}$$

$$\left(\frac{1}{T_2^p}\right)^{\mathrm{IS}} = \frac{P_M}{\tau_M}\left[\frac{T_{2M}^{-2} + \tau_M^{-1}T_{2M}^{-1} + \Delta\omega_M^2}{\left(\tau_M^{-1}+T_{2M}^{-1}\right)^2 + \Delta\omega_M^2}\right] \qquad \text{I.53}$$

Where [M] is the molality of the paramagnetic species M, q is the number of bound water molecules per paramagnetic center (hydration number), P_M is the mole fraction of the bound water molecules, τ_M is the lifetime of a water proton in the inner sphere of the complex (the reciprocal of the water exchange rate k_{ex}), T_{iM} is the nuclear relaxation time in the paramagnetic environment and $\Delta\omega_M$ the chemical shift difference between the bound and the bulk water.

I.4.4. Solomon-Bloembergen-Morgan theory

The contribution of the Curie mechanism to the paramagnetic relaxation enhancement is often very small, particularly for the longitudinal relaxation, and will therefore be neglected. The relaxation rate enhanced by the presence of a paramagnetic species is therefore assumed to be induced only by the dipole-dipole (DD) and scalar (SC) mechanisms contributions (equation I.32 to I.36). Considering the interaction between a proton and an electron, these equations can be simplified with the very good approximation that the Larmor frequency of the electron is much higher than that of the nuclei $\omega_S >> \omega_I$ (equation I.6 : $\omega = \gamma B$, with $\gamma_e \approx 658\ \gamma_H$), and therefore $\omega_S \pm \omega_I \approx \omega_S$. The resulting equations are known as the modified Solomon-Bloembergen equations (I.54 to I.59).

$$\frac{1}{T_i} = \frac{1}{T_i^{DD}} + \frac{1}{T_i^{SC}} \; ; i = 1,2 \qquad \text{I.54}$$

$$\frac{1}{T_1^{DD}} = \frac{2}{15} S(S+1) C_{DD}^2 \left[7J(\omega_S, \tau_{d2}) + 3J(\omega_I, \tau_{d1}) \right] \qquad \text{I.55}$$

$$\frac{1}{T_1^{SC}} = \frac{2}{3} S(S+1) \left(\frac{A}{\hbar} \right)^2 J(\omega_S, \tau_{sc2}) \qquad \text{I.56}$$

$$\frac{1}{T_2^{DD}} = \frac{1}{15} S(S+1) C_{DD}^2 \left[4J(0, \tau_{d1}) + 13J(\omega_S, \tau_{d2}) + 3J(\omega_I, \tau_{d1}) \right] \qquad \text{I.57}$$

$$\frac{1}{T_2^{SC}} = \frac{1}{3} S(S+1) \left(\frac{A}{\hbar} \right)^2 \left[J(0, \tau_{sc1}) + J(\omega_S, \tau_{sc2}) \right] \qquad \text{I.58}$$

With $$C_{DD} = \frac{\gamma_I \gamma_S \hbar}{r_{IS}^3} \frac{\mu_0}{4\pi} = \frac{\gamma_I g_e \mu_B}{r_{IS}^3} \frac{\mu_0}{4\pi} \qquad \text{I.59}$$

As discussed in Chapter I.3.1 and Figure I.9, the nucleus-electron dipolar interaction depends on the reorientation of the molecule. Moreover, this interaction is obviously affected by the orientation of the electron spin and the water proton exchange. The characteristic correlation time of the dipolar process τ_{di} depends therefore on the rotational correlation time τ_R, the electronic relaxation time T_{ie} (i = 1,2) and the lifetime of the nucleus in the inner sphere τ_M (equation I.60).

$$\frac{1}{\tau_{di}} = \frac{1}{\tau_R} + \frac{1}{T_{ie}} + \frac{1}{\tau_M} \; ; \; i = 1,2 \qquad \text{I.60}$$

The scalar interaction is also dependent on the electron spin relaxation and the water proton exchange, but remains unsurprisingly unaffected by the orientation of the molecule. The effective correlation time of the scalar interaction is therefore given by the equation I.61.

$$\frac{1}{\tau_{sci}} = \frac{1}{T_{ie}} + \frac{1}{\tau_M} \; ; \; i = 1,2 \qquad \text{I.61}$$

A model of the electron spin relaxation rates was described by Bloembergen and Morgan (equations I.62 to I.64),[14] based on the work of McLachlan[15] and the Redfield theory.[16,17] For systems with $S > 1/2$, the electron spin relaxations are interpreted in terms of a zero-field-splitting (ZFS) interaction. The ZFS, *i.e.* the non-degeneration of the electron spin levels in the absence of the magnetic field, arises principally from the interaction of two neighboring electron spins and from the spin-orbit coupling combined with a ligand field. This model assumes the spherical symmetry of the complex and therefore no static ZFS. It considers however a transient ZFS, induced by the distortion of this symmetry.

$$\left(\frac{1}{T_{1e}}\right)^{ZFS} = \frac{2}{50}\left[4S(S+1)-3\right]\Delta^2\tau_v\left[J(\omega_S,\tau_v)+4J(2\omega_S,\tau_v)\right] \qquad \text{I.62}$$

$$\left(\frac{1}{T_{2e}}\right)^{ZFS} = \frac{1}{50}\left[4S(S+1)-3\right]\Delta^2\tau_v\left[3J(0,\tau_v)+5J(\omega_S,\tau_v)+2J(2\omega_S,\tau_v)\right] \qquad \text{I.63}$$

With $$\Delta^2 = \frac{5}{\left[4S(S+1)-3\right]\tau_v\tau_{S0}} \qquad \text{I.64}$$

Where τ_v is the correlation time for the modulation of the ZFS interaction, Δ is the amplitude of the transient ZFS and τ_{S0} the electron spin relaxation time at zero field. Let's note that the equations I.62 to I.64 are correct for the case $S = 1$ (exponential relaxation) but becomes an approximation for higher spin systems ($S = 3/2$ and $S = 2$ are biexponential, while $S = 5/2$ is characterized by three time constants).[16]

The combination of equations I.54 to I.64 constitutes a complete theory describing the observed PRE. This model is referred as the Solomon-Bloembergen-Morgan (SBM) theory. The whole system is however rather complex and necessitates as previously mentioned several approximations and assumptions, which are listed below :[16]

- The Redfield limit[18] is applied for the electron spin relaxation, *i.e.* the motion in the lattice occurs on a much faster time scale than the motions in the spin system.
- The electron spin relaxation is uncorrelated with molecular reorientation.
- The electron spin system is dominated by the electronic Zeeman interaction (single electron spin relaxation rate).
- The electron spin is considered as a point-dipole centered at the metal ion.
- The electron Landé g-tensor g_e is assumed to be isotropic ($g_e = \gamma_e \hbar / \mu_B$)
- The reorientation of the electron spin is isotropic and characterized by a single correlation time.
- The chemical exchange is not correlated with the motions of the lattice.

The equations I.52 to I.64 introduce numerous parameters that influence the protons relaxivity. The metal-proton distance has a sixth-power dependence and influence significantly the dipolar relaxation rate (equations I.55, I.57 and I.59) (in particular, the Gd^{3+}-coordinated water proton distance has been determined precisely by Astashkin *et al.*[19] at 3.1 ± 0.1 Å and turned out to be rather constant in all complexes studied). The hydration number *q*, having a proportional effect (equation I.52), and the parameters determining the effective correlation time (i.e. the rotational correlation time, the electronic relaxation time and the proton exchange rate) are usually considered as the four parameters affecting the paramagnetic relaxation (Figure I.11).

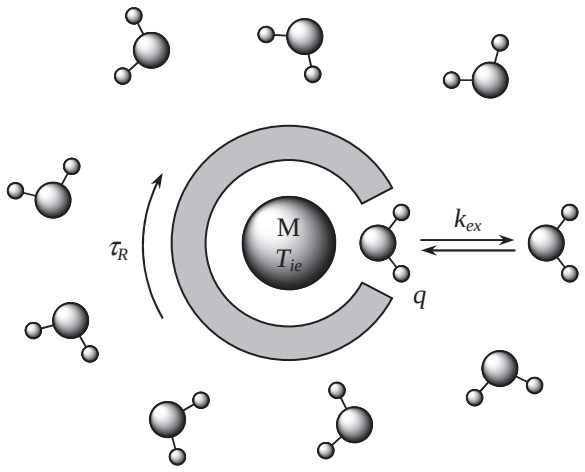

Figure I.11 **–** Schematic representation of a paramagnetic chelate complex in water and the structural parameters affecting the proton relaxivity.

Two reactions are involved in the exchange of coordinated water protons : the exchange of the entire water molecule in the inner sphere of the complex and the exchange of the proton on the complexing water molecule. The latter case is accelerated by acid- and base-catalyzed processes (equation I.65). Between about pH 2 and pH 8 however, the proton exchange on a water molecule can be neglected, and the proton exchange rate equals the water exchange rate.

$$k_{ex} = k_{ex}^{H_2O} + k_{ex}^{H}\left[H^+\right] + k_{ex}^{OH}\left[OH^-\right] \qquad \text{I.65}$$

If the water exchange is the limiting contribution for the relaxivity ($T_{1M} << \tau_M$), the latter would be determined only by this exchange rate (equation I.52). On the contrary, if the exchange is fast ($T_{1M} >> \tau_M$), the observed relaxivity will be given by the relaxation rate of the coordinated proton T_{1m}, which depends on the proton exchange rate, the rotational correlation time and the electronic relaxation rate. The three parameters τ_R, k_{ex} and T_{ie} have therefore to be optimized at the same time to attain a maximum relaxivity.

The water exchange rate constant k_{ex} is temperature-dependent, and is assumed to follow the Eyring equation (I.66), where $\Delta S^{\ddagger}$ and $\Delta H^{\ddagger}$ are the entropy and enthalpy of activation for the exchange process and k_{ex}^{298} is the exchange rate constant at 25°C.

$$k_{ex} = \frac{1}{\tau_M} = \frac{k_B T}{h}\exp\left(\frac{\Delta S^{\ddagger}}{R} - \frac{\Delta H^{\ddagger}}{RT}\right) = \frac{k_{ex}^{298} T}{298.15}\exp\left[\frac{\Delta H^{\ddagger}}{R}\left(\frac{1}{298.15} - \frac{1}{T}\right)\right] \qquad \text{I.66}$$

All other correlation times τ_c are also temperature-dependent. The related activation energy E_a described by the Arrhenius equation is often preferred to describe the system (equation I.67).

$$\tau_c = \tau_c^{298}\exp\left[\frac{E_a}{R}\left(\frac{1}{T} - \frac{1}{298.15}\right)\right] \qquad \text{I.67}$$

The activation enthalpies and energies are interchangeable quantities to describe an activation barrier. They can be related to each other by the equation I.68.

$$E_a = \Delta H^{\ddagger} + RT \qquad \text{I.68}$$

I.4.5. Lipari-Szabo approach for internal rotation

The global isotropic rotational correlation time describes perfectly the tumbling of small sphere-like chelate complexes in solution. It fails however in the case of larger molecules bearing several metal complexes, in which the motion of the chelate complex could be described by an overall rotation of the whole molecule and a local rotation around the arm connecting the chelate to the central core (anisotropic motion). The "model-free" Lipari-Szabo approach introduces therefore two motions and hence two rotational correlation times to describe the spectral density function (equation I.69).[20-22]

$$J(\omega) = \left(\frac{S^2 \tau_g}{1+\omega^2 \tau_g^2} + \frac{\left(1-S^2\right)\tau}{1+\omega^2 \tau^2} \right) \qquad \text{I.69}$$

With $\tau^{-1} = \tau_g^{-1} + \tau_l^{-1}$

The generalized order parameter S^2 is a model-independent measure of the degree of spatial restriction of the local motion. The value of S^2 is included between 0 and 1, indicating respectively a completely independent or a completely restricted local motion. In the latter case, the second part of the equation I.69 is equal to zero, reducing this expression to its original simple form (equation I.23). This parameter gives therefore indications on the rigidity of the molecule.

I.4.6. Outer-sphere contribution

The water molecules outside of the first coordination shell of the metal complex are actually constituted by two distinct types of molecules : the second-sphere water molecules, which remain in the proximity of the complex by interacting with the hydrophilic groups, and the bulk water molecules, whose random motions can bring them to the vicinity of the paramagnetic species. Though theoretical models considering a separate treatment for this two kinds of water exist,[23,24] they will here be treated without distinction and referred as outer-sphere water molecules.

The interaction between the paramagnetic electron spin *S* and the water proton nuclear spin *I* is described by the only *intermolecular dipolar interaction*. The field fluctuations arise

exclusively from the random translational motion of the molecules and no interaction between the molecules is assumed. The resulting relaxation rate is given by equation I.70.[25,26]

$$\frac{1}{T_1^{OS}} = \frac{32\pi}{405} S(S+1)\left(\frac{\mu_0}{4\pi}\right)^2 \gamma_I^2 \gamma_S^2 \hbar^2 \frac{N_A[\mathrm{M}]}{dD}\left[7J_2^{OS}(\omega_S) + 3J_1^{OS}(\omega_I)\right] \qquad \text{I.70}$$

With $$J_k^{OS}(\omega) = \mathrm{Re}\left\{\frac{1+\frac{z}{4}}{1+z+\frac{4z^2}{9}+\frac{z^3}{9}}\right\}$$

$$z = \sqrt{i\omega\tau + \frac{\tau}{T_{ke}}} \;\; ; \;\; \tau = \frac{d^2}{D} \;\; ; \;\; k = 1,2$$

Where N_A is the Avogadro number, d is the closest distance of approach of spins I and S, D is the relative diffusion coefficient ($D = D_I + D_S$), [M] is the millimolar concentration of the paramagnetic metal and S is the electron spin. The spectral densities $J^{OS}(\omega)$ depend on the conditional probability for the relative diffusion of spins I and S.

I.4.7. NMRD profile

As seen throughout the Chapter I.4, the PRE depends significantly on the magnetic field. The measurement of the relaxivities (equation I.49) over a wide range of magnetic field is called relaxometry and the plot presenting the relaxivities as a function of the Larmor frequency is called Nuclear Magnetic Relaxation Dispersion (NMRD) profiles. Because the different contributions to the relaxation will manifest themselves differently, the NMRD profiles can vary drastically depending on the metal center and the type of molecules and can therefore be used to characterize paramagnetic systems.

The Figure I.12 shows the NMRD profiles of a Gd^{3+} complex, which presents different zones. In the low field region (from 0.01 MHz to about 1 MHz), the relaxation is governed by the electron spin relaxation rate, which is field independent and presents therefore a plateau. The relaxivity drop, or dispersion, from 1 MHz to 10 MHz is due to the dipolar contribution. The relaxivity in the high field region, *i.e.* from 20 to 200 MHz, is governed by the rotational correlation time. This region is probably the most interesting part of an NMRD profile, as it can change radically depending on the size of the molecule. It can be seen from equation I.52

that the contribution of the water exchange rate and the number of molecule in the inner sphere is present throughout the frequency range.

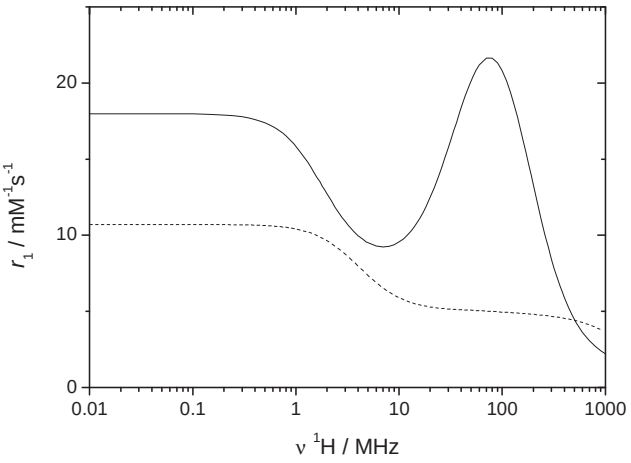

Figure I.12 **–** Typical shape of NMRD profiles of a Gd^{3+} complex simulated for slowly rotating (τ_R = 1 ns) (solid) and fast rotating (τ_R = 0.1 ns) (dash) molecules. Other used parameters : τ_M = 100 ns; τ_v = 10 ps; $\Delta^2 = 0.5 \cdot 10^{20}$ s^{-2}; q = 1.

The equations presented in this chapter (equations I.48 to I.70) represent a whole system describing the relaxation rates. They can therefore be used to fit the NMRD profiles, *i.e.* the relaxivity as a function of the Larmor frequency, and determine numerous parameters characterizing the paramagnetic entity. This is performed by computer methods minimizing errors on a fitted functions, such as the Levenberg-Marquardt algorithm.[27,28] Though some common values can be used for similar systems, such as the distances, the diffusion coefficient or the quadropolar coupling constant for instance, this method does not allow the exact determination of all relaxation influencing parameters. The solution to this problem is to fit simultaneously the NMRD with completing data sharing some parameters with the water proton relaxation rates. The two techniques Electron Paramagnetic Relaxation (EPR) and ^{17}O NMR have proved to be especially useful to complete the protons relaxivity experimental data. The linewidth of EPR spectra gives direct access to transverse electron spin relaxation rates, while ^{17}O NMR relaxation rates and chemical shifts at variable temperature, pressure or magnetic field gives information on the water exchange rate, the number of water molecules in the inner sphere, the rotational correlation time or the longitudinal electronic relaxation rates.

I.4.8. ^{17}O NMR measurements

Because the water oxygen is bound to the metal center, variable temperature ^{17}O NMR measurements allow the direct determination of the water exchange rate, through the reduced relaxation times T_{ir} (equation I.71) and the reduced chemical shifts $\Delta\omega_r$ (I.72).

$$\frac{1}{T_{ir}} = \frac{1}{P_M}\left(\frac{1}{T_i} - \frac{1}{T_i^{ref}}\right) \;;\; i = 1,2 \qquad \text{I.71}$$

$$\Delta\omega_r = \frac{1}{P_m}\left(\omega - \omega^{ref}\right) \qquad \text{I.72}$$

With $P_M = \dfrac{q[\mathrm{M}]}{55.56}$

The external reference used to obtain the reduced values can be the diamagnetic analogue of the paramagnetic compound (Y(III) instead of Gd(III) for instance) but acid water (pH 3.5 perchloric acid solution), that ensure a fast proton exchange regime, is often preferred for practical reasons.

The transverse relaxation rate is related to the water molecule lifetime in the inner sphere of the complex τ_M through equation I.73. If we neglect the outer-sphere contribution to the ^{17}O relaxation[29] and the chemical shift of the bound oxygen ($\Delta\omega_M << 1/T_{2M}$; $1/\tau_M$), this equation simplifies to lead to the second part of equation I.73. Because the oxygen is directly bound to the metal center, the scalar mechanism is the most important contribution to the relaxation rate (equation I.74).[11,12,30]

$$\frac{1}{T_{2r}} = \frac{1}{\tau_M}\frac{T_{2M}^{-2} + \tau_M^{-1}T_{2M}^{-1} + \Delta\omega_M^2}{\tau_M\left(\tau_M^{-1} + T_{2M}^{-1}\right) + \Delta\omega_M^2} + \frac{1}{T_{2OS}} \approx \frac{1}{T_{2M} + \tau_M} \qquad \text{I.73}$$

$$\frac{1}{T_{2M}} \cong \frac{1}{T_2^{SC}} = \frac{S(S+1)}{3}\left(\frac{A}{\hbar}\right)^2 \tau_{sc1} \qquad \text{I.74}$$

With $\dfrac{1}{\tau_{sc1}} = \dfrac{1}{\tau_M} + \dfrac{1}{T_{1e}}$

The scalar coupling constant $A/\hbar$ determines the chemical shift of the coordinated water oxygen $\Delta\omega_M$ (equation I.76), related to the reduced chemical shift $\Delta\omega_r$ (equation I.75). The

measurement of $\Delta\omega_r$ allows therefore the determination of $A/\hbar$, used to determine the water exchange rate. The outer-sphere contribution to the ^{17}O chemical shift $\Delta\omega_{OS}$ is assumed to be proportional to $\Delta\omega_M$ though the empirical proportionality constant C_{OS} (equation I.77).[29-31]

$$\Delta\omega_r = \frac{\Delta\omega_M}{\left(1+\tau_M T_{2M}^{-1}\right)^2 + \tau_M^2 \Delta\omega_M^2} + \Delta\omega_{OS} \qquad \text{I.75}$$

With $$\Delta\omega_M = \frac{g_e \mu_B S(S+1) B}{3k_B T} \frac{A}{\hbar} \qquad \text{I.76}$$

$$\Delta\omega_{OS} = C_{OS} \Delta\omega_M \qquad \text{I.77}$$

Where g_e is the isotropic Landé g-factor of the electron, m_B is the Bohr magneton, S is the electron spin and B is the magnetic field.

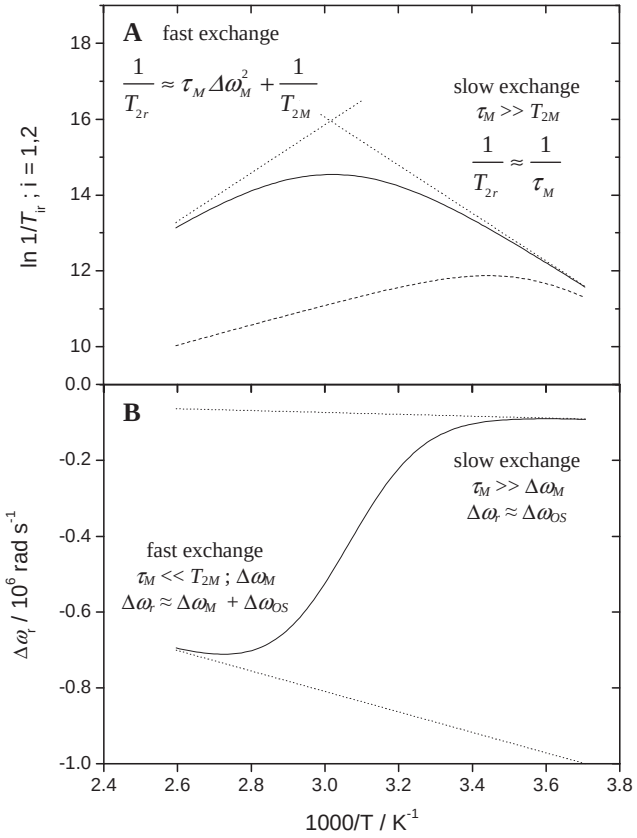

Figure I.13 – Variable temperature ^{17}O $\ln(1/T_{2r})$ (solid), $\ln(1/T_{1r})$ (dash) (A) and $\Delta\omega_r$ (straight) (B) and limiting cases (dot) for fast and slow exchange regions. Calculated with the following parameters : $\Delta H^{\ddagger}$ = 50 kJ/mol; k_{ex}^{298} = 10^6 s^{-1}; τ_R = 500 ps; τ_v = 6 ps; $A/\hbar$ = -$3.7\cdot10^6$ rad s^{-1}; $\Delta^2 = 0.5\cdot10^{20}$ s^{-2}; C_{OS} = 0.1 and B = 9.4 T.

I.4.9. Rast-Fries-Belorizky approach

As mentioned in Chapter I.4.4, the SBM theory, and particularly its electronic relaxation treatment, is based on many assumptions and is therefore valid under very precise circumstances. Considering only a transient ZFS due to the distortion of the octahedral symmetry, this theory fails for systems with large static ZFS such as Ni^{2+}, Fe^{2+}, Co^{2+} and for systems whose electronic relaxation is not dominated by the ZFS, such as the lanthanides other than Gd^{3+}. The electronic relaxation of the latter is however described by only one relaxation time, instead of the four required for a 7/2 electron-spin such as Gd^{3+} ($m_S = \pm 7/2 \leftrightarrow \pm 5/2$, $m_S = \pm 5/2 \leftrightarrow \pm 3/2$, $m_S = \pm 3/2 \leftrightarrow \pm 1/2$ and $m_S = +1/2 \leftrightarrow -1/2$). The resulting effect is a poor description of the relaxation rate, especially at low field where the relaxivity is governed by the electronic relaxation.

Several theories have been developed in order to describe in a better way the electronic relaxation.[32] Among them, the so-called Rast-Fries-Belorizky (RFB) or Grenoble approach, introduces a static ZFS and separates the electronic relaxation rate into a static and a transient ZFS contributions (equation I.78).[33-35] The static ZFS is modulated by the rotational motion of the molecule, implying a τ_R-dependence of the electron spin relaxation rate. The theoretical description is elaborated up to the six order for the static ZFS part and to the second order for the transient part, leading to the introduction of up to four parameters describing the ZFS : a_2, a_4, a_6 and a_{2T} (equations I.79 and I.80).[36]

$$\frac{1}{T_{1e}} = \frac{1}{T_1^{static}} + \frac{1}{T_1^{transient}} \qquad \text{I.78}$$

$$\frac{1}{T_{1e}^{static}} = \sum_{k=2}^{K} \frac{6}{(2S+1)S(S+1)} \frac{1}{(2k+1)^2} \times \frac{(k!)^2(2S+k+1)!}{2^k(2k)!(2S-k)!} a_k^2 \tau_R^{(k)} \sum_{n=1}^{k} \frac{n^2}{1+(n\omega_S \tau_R^{(k)})^2} \qquad \text{I.79}$$

$$\frac{1}{T_{1e}^{transient}} = \frac{4S(S+1)-3}{25} a_{2T}^2 \tau' \sum_{n=1}^{2} \frac{n^2}{1+(n\omega_S \tau')^2} \qquad \text{I.80}$$

With $\frac{1}{\tau'} = \frac{1}{\tau_v} + \frac{1}{\tau_R^{(2)}}$ and $K = 4$ for d electrons and 6 for f electrons

Though the RFB approach ameliorates considerably the description of the electronic relaxation rate, compared to the SBM theory, this model is not suitable to fit the relaxation of slowly tumbling molecules at low magnetic field.

I.4.10. Modified Florence approach

The so-called modified Florence approach, based on a Liouville superoperator formalism, was developed to describe PRE for big and slowly rotating molecules.[37-39] This model assumes a slow reorientation of the metal complex, which modulates both the hyperfine dipolar interaction and the static ZFS, and considers no correlation between molecular reorientation and the electronic relaxation.[39] The latter assumption is known as the decomposition approximation and is valid only for slowly rotating systems.[40] The electronic relaxation treatment assumes modulations of a transient ZFS, arising from the distortion due to the collisions with surrounding solvent molecules. These modulations are described by a pseudorotation model, which assumes a constant magnitude and a directional change following a rotational diffusion equation.[31,41,36] The electronic relaxation treatment is described by a static and a transient ZFS, with amplitudes D and Δ, respectively, and the correlation time τ_v for the transient ZFS modulation.

I.5 Magnetic Resonance Imaging

The Magnetic Resonance Imaging (MRI) is a widespread clinical technique for medical diagnostic. This not invasive and seemingly harmless method is based on the Nuclear Magnetic Resonance, and more exactly on the relaxation phenomenon.

In 1971, the American scientist Raymond Vahan Damadian glimpsed a medical application to NMR and presented a method allowing tumor detection by NMR.[42] Benefiting from the progress in the field of medical imaging by tomography, the American chemist Paul Lauterbur and the British physicist Sir Peter Mansfield developed in 1973 simultaneously but independently a NMR imaging based on the magnetic field gradient allowing the obtaining of a 2D section.[43,44] They shared the Nobel Prize in Physiology or Medicine in 2003 "for their discoveries concerning magnetic resonance imaging".[45]

Thanks to the advances in the domains of informatics and electronics, the technique evolved rapidly. Richard Ernst used the Fourier transform to analyze the coding in frequency and phase of the NMR signal in 1975.[46] The same year, Mansfield achieved the first imaging of human tissue and the imaging of a whole living human body is performed by Damadian in 1977.

This method is nowadays essential in the medical diagnostic and is in perpetual progress thanks to the development of new sequences and techniques, allowing for instance functional MRI (fMRI)[47,48] or angiography.[49]

I.5.1 MRI principle

The opportunity of measuring spatial NMR experiment is possible through the method of *pulsed field gradient*s, *i.e.* spatially inhomogeneous magnetic fields. The technique leads to position-dependent resonance frequencies and allows therefore the spatially selective excitation, and thus observation, by tuning the frequency of the RF pulse.

Equation I.10, presenting the relation between the magnetic field and the Larmor frequency, can be reformulated by equation I.81 in the case an inhomogeneous field. The field gradient $\boldsymbol{G}$ and the magnetic field at position $\boldsymbol{r}$ are therefore given by equations I.82 and I.83, respectively.

$$\boldsymbol{\omega}(\boldsymbol{r},t) = -\gamma \boldsymbol{B}(\boldsymbol{r},t),\ \boldsymbol{r} = \begin{bmatrix} x \\ y \\ z \end{bmatrix} \qquad \text{I.81}$$

$$\boldsymbol{G}(t) = \frac{\partial B_z(\boldsymbol{r},t)}{\partial \boldsymbol{r}} = \begin{bmatrix} \frac{\partial B_z(\boldsymbol{r},t)}{\partial x} \\ \frac{\partial B_z(\boldsymbol{r},t)}{\partial y} \\ \frac{\partial B_z(\boldsymbol{r},t)}{\partial z} \end{bmatrix} \qquad \text{I.82}$$

$$B_z(\boldsymbol{r},t) = B_0 + \boldsymbol{G}_r(t) \cdot \boldsymbol{r} \qquad \text{I.83}$$

As seen in Chapter I.1.4, an applied RF pulse generates a magnetic field $\boldsymbol{B}_1$ along the x' axis of the rotating frame. Considering a time constant gradient along the z-axis with strength G_z, the effective magnetic field $\boldsymbol{B}_{eff}$ experienced at position Δz is given by the equation I.84 (from equation I.17).

$$\boldsymbol{B}_{eff} = \boldsymbol{B}_0 + \boldsymbol{B}_1 + \frac{\boldsymbol{\Omega}}{\gamma} + \boldsymbol{G} \cdot \boldsymbol{r} = \begin{bmatrix} B_1 \\ 0 \\ B_0 + G_z \Delta z - \Omega / \gamma \end{bmatrix} \qquad \text{I.84}$$

If the RF frequency Ω is tuned in order to be equal to $\gamma(B_0 + G_z\Delta z)$, the z-component of the effective magnetic field would be zero and $\boldsymbol{B}_{eff}$ would result in $\boldsymbol{B}_1$ along x'. The magnetization $\boldsymbol{M'}$ rotating around $\boldsymbol{B}_{eff}$ would therefore rotate around the x'-axis. On the contrary, if the z-component of $\boldsymbol{B}_{eff}$ is large compared to $\boldsymbol{B}_1$, $\boldsymbol{M'}$ would be nearly unaffected by the RF pulse. This allows consequently the selective excitation of any slice along the z'-axis by adjusting the frequency Ω of the RF pulse. The thickness of the slice is controlled with the strength of either the $\boldsymbol{B}_1$ field or the gradient $\boldsymbol{G}$. If applied to the three dimensions, the selective spatial element corresponds to a cube, known as the voxel $\Delta V(\boldsymbol{r})$, which represents the volume element of the NMR experiments.

Because this method does not apply to a specific pulse sequence, many different NMR experiments can be performed to obtain a specific spatial result and can be adapted to parameter of interest. Angiography for instance can be obtained by measuring the anisotropic diffusion of blood in veins through DOSY experiments,[49] but the most common methods for body MR imaging are based on three parameters : the spin density ρ and the longitudinal and transverse relaxation times T_1 and T_2 of the water proton. The resulting images are classified according to the sensitivity of the principal parameters measured by the specific sequence. They are called proton-density-weighted (ρ-weighted), T_1-weighted and T_2-weighted images (Figure I.14).

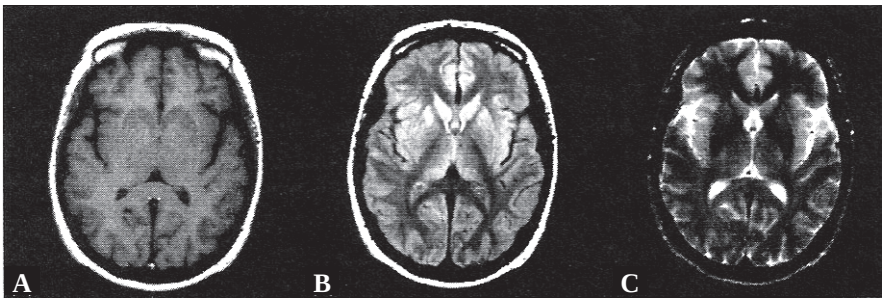

Figure I.14 – Brain MRI measured by the most common methods for soft tissues imaging : (a) T_1-weighted image, (b) ρ-weighted image and (c) T_2-wighted images.[1]

I.5.2 MRI Contrast Agents

Because it has a natural isotopic abundance of 99.99%, a very high gyromagnetic ratio and is a constituent of the water that represents about 70% w/w of a living body, the water proton is the perfect nucleus for such experiments. The MRI acquisition is however very long, typically a few tens of minutes, because of the main drawback of MRI, and that of NMR in general : its low sensitivity. This long examination, during which the patient cannot move, is tiresome and unprofitable. This acquisition time can be considerably reduced through the use of contrast agents (CAs). The contrast enhancement is obtained through the acceleration of relaxation via the use of paramagnetic or superparamagnetic substances, which can moreover permit the visualization of not very discernible tissues, such as brain lesions, in specific occasion (Figure I.15). The so-called T_1 CAs decrease principally the longitudinal relaxation times and lead to a positive contrast, while the T_2 CAs increase the transverse relaxation rate and are characterized by a negative contrast. Though T_2 CAs are commonly used, principally under

the form of nanoparticular superparamagnetic iron oxides (SPIO), this work will only refer to T_1 contrast agents.

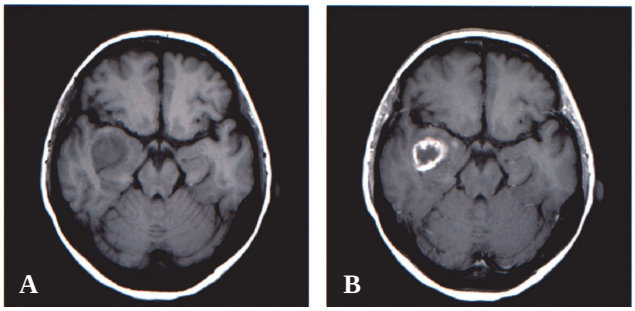

Figure I.15 – MRI T_1-weighted image of a brain lesion before (A) and after (B) contrast agent uptake.[1]

The most widely spread contrast agents for clinical use are gadolinium (III) complexes using cyclic or acyclic poly(aminocarboxylate) ligands. With its seven unpaired electrons and its slow electronic relaxation, the Gd^{3+} is the paramagnetic metal that provides the most effective PRE (Chapter I.4) and is therefore the best candidate for CAs. The free metal ion is however highly toxic and can not be injected in living bodies. Free Gd^{3+} ions are rapidly sequestered within the bone and the liver, with biologic half-time of several weeks. This long-term retention of Gd^{3+} ions within the body favors interactions with physiologic systems and the inhibition of the activity of numerous endogenous enzymes, mainly through Ca^{2+} replacement. The calcium channel inhibition has severe consequences on processes that depend upon the Ca^{2+} influx, such as neural transmission and blood coagulation. Furthermore, the formation of insoluble complexes with phosphates or hydroxides at pH higher than 6.2, which can disrupt the immune system, and the crossing of the blood-brain-barrier figure also amongst the hazards of free Gd^{3+} ions. Finally, it has been proved that free gadolinium was closely related to the development of the serious syndrome nephrogenic systemic fibrosis (NSF).[50,51]

The gadolinium has therefore to be injected under the stable form of chelate complexes. These inert forms prevent the metal ion to interact with endogenous compounds and ensure a rapid renal excretion.[52] Chelate complexes including more than two water molecules in the inner sphere are not stable enough to permit any *in vivo* injection, but most of the commercial CAs encompass only one water molecules. Some example of the most widely used commercial Gd-based contrast agents are presented in Figure I.16.

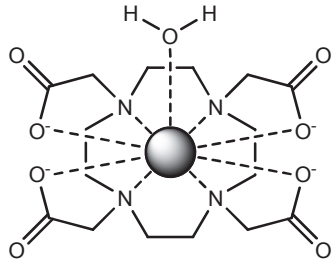

[Gd(DOTA)(H_2O)]$^-$
Dotarem®

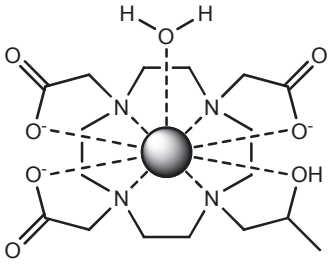

[Gd(HP-DO3A)(H_2O)]
ProHance®

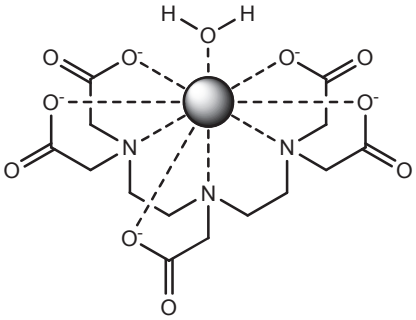

[Gd(DTPA)(H_2O)]$^{2-}$
Magnevist®

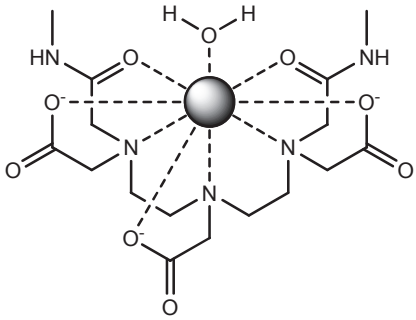

[Gd(DTPA-BMA)(H_2O)]
Omniscan®

Figure I.16 **–** Structures, common names and commercial names of some gadolinium complexes commercially used as MRI contrast agents.

For research, *in vitro* and animal experiment, the linear DTTA (H_5DTTA = diethylenetriaminetetraacetic acid = 2,2',2'',2'''-[iminobis(ethane-2,1-diylnitrilo)]tetraacetic acid) and the cyclic DO3A (H_4DO3A = 1,4,7,10-tetraazacyclododecane-*N*,*N'*,*N''*-triacetate) (Figure I.17), leading respectively to negative and neutral Gd^{3+} complexes, are widely employed chelating units. These two heptadentate chelators form stable complexes with Gd^{3+} including theoretically two water molecules in the inner sphere. The presence of the secondary amine, that can easily be functionalized to conjugate the complexes to other compounds, is moreover a very interesting property.

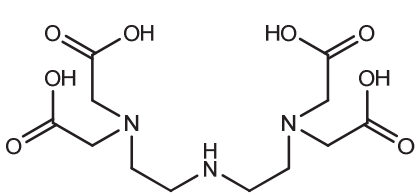

H_5DTTA

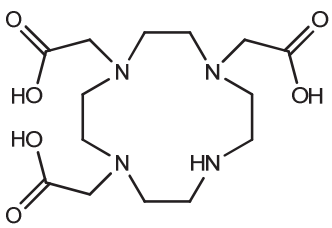

H_4DO3A

Figure I.17 **–** Structure of the common chelating units DTTA and DO3A.

Many studies using Gd^{3+} complexes have been achieved to graft several chelate complexes on a central structure aiming to increase the molecular relaxation enhancement, *i.e.* the relaxivity multiplied by the number of chelate complexes per particle. Macromolecular compounds have been particularly investigated to increase the relaxivity between 10 and 200 MHz. This had been performed with various materials such as linear polymers,[22,53-56] dendrimers,[57-61] micelles[62-66], proteins[67-70], carbon nanotubes[71,72] or gold nanoparticles[73,74]. The optimization of the relaxivity at frequencies higher than 200 MHz has also been investigated. These so-called high field contrast agent should have rotational correlation times between 0.5 and 1 ns[75] and are formed with a few complexes around a small central core.[76-79]

Conjugated Gd^{3+} complexes are also used for the development of smart, or responsive, contrast agents, which generate a signal depending on some variable in their immediate environment,[80] such as temperature,[81] pH,[82,83] oxygen pressure[84] or metal ion concentration[85,86]. Finally, the so-called targeted contrast agents are also developed from gadolinium complexes. This CA class aims to target specifically organs and tissues presenting particular properties through interaction with cell surface,[87] antibodies[88-90] or peptide receptors,[91,92] to name a few.

I.6 Scope of this work

This thesis deals with the development of new potential MRI contrast agents. These new compounds present different properties and were designed to induce different effects on the relaxivity. The synthesis, the analytical characterizations, the relaxivity measurements and the theoretical treatments of each compound will be presented in the upcoming chapters.

Chapter II presents the tricephalous complex $\{Mes[Gd(DO3A)(H_2O)_2]^{-}{}_3\}$ (Figure I.18), composed by three Gd-DO3A complexes bound to a central benzene ring, and designed as a potential high field CAs. The difficulty to insert three Gd^{3+} ions has constrained us to develop an alternative complexation method, based on a Mg^{2+} complexation and transmetallation.

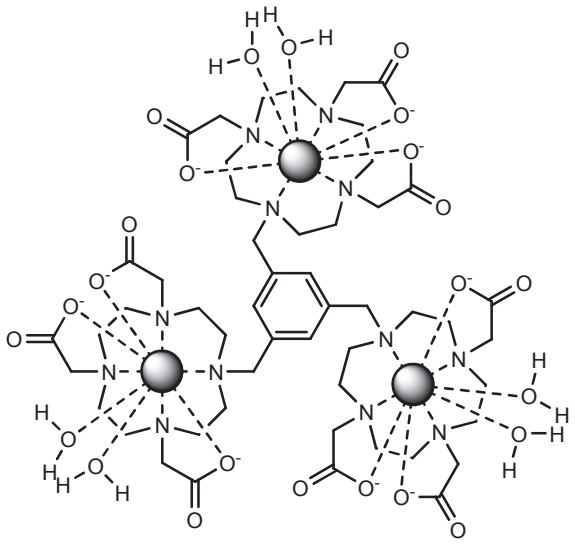

Figure I.18 **–** The trinuclear complex $\{Mes[Gd(DO3A)(H_2O)_2]^{-}{}_3\}$ (Chapter II).

Chapter III presents another trinuclear complex around an aromatic central core, the $\{Ph_4[Gd(DTTA)(H_2O)_2]^{-}{}_3\}$ (Figure I.19). The central core of this compound is constituted by a system of four benzene rings and was designed to form aggregates. As expected, this compound presents exceptionally high relaxivities for such a mid-size compound. The dynamic aggregation is investigated and characterized.

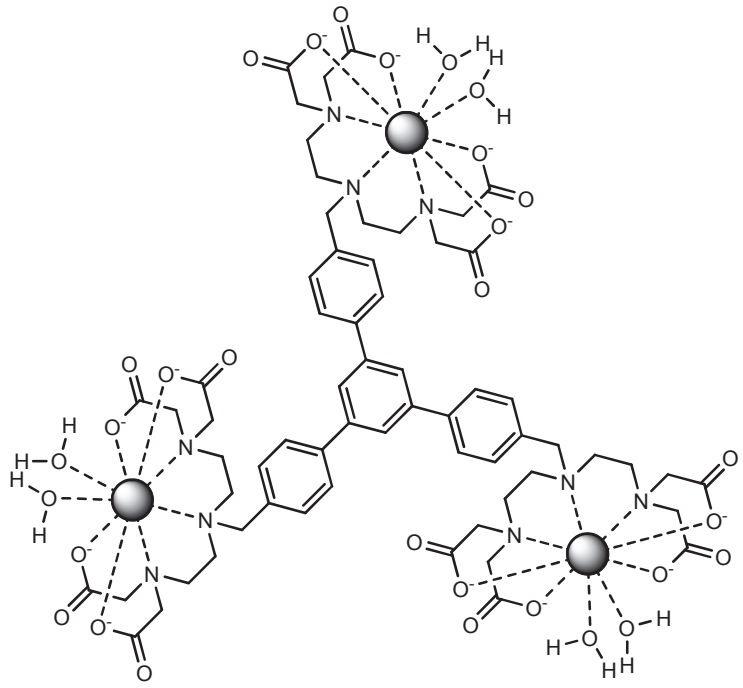

Figure I.19 **–** The trinuclear complex $\{Ph_4[Gd(DTTA)(H_2O)_2]^-_3\}$ (Chapter III).

Chapter IV deals with the controlled coupling of the complex $[Gd(DTTA\text{-}N'but)(H_2O)_2]^-$ on the linear polysaccharide chitosan (Figure I.20). This compound, obtained from chitin, has remarkable chemical and biomedical properties. A particular kind of nanoparticles, called nanogels, is produced from the linear chain. The structural and relaxometric characterization of the linear polysaccharide and the nanogels will be presented and discussed.

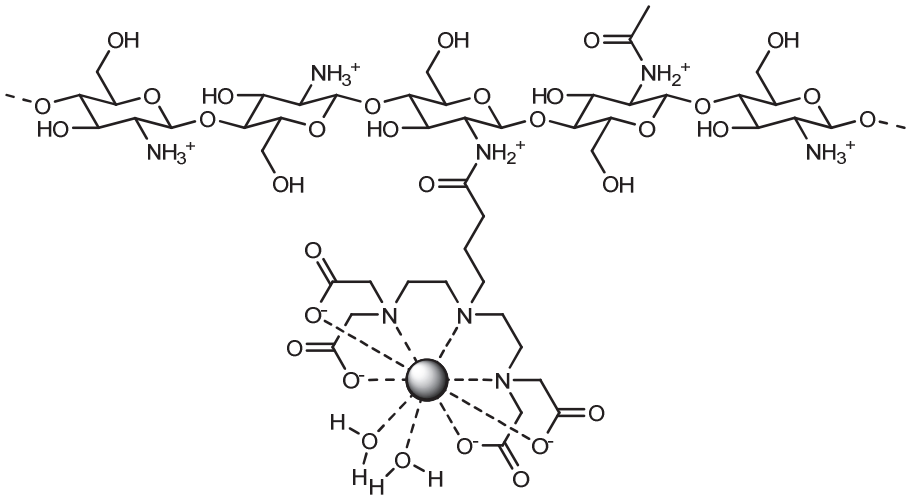

Figure I.20 **–** Structure of the modified chitosan linear chain $\{Chi[Gd(DTTA)(H_2O)_2]^-\}$ (Chapter IV).

Chapter V presents a family of potential targeting CAs composed by a Gd-DOTA complex on which the peptide bombesin is conjugated. The latter is a peptide neurotransmitter, whose receptors are overexpressed by numerous malignant tumor cells, including prostate, breast and small cell lung cancers. The particular affinity of the peptide towards these cells is a promising route to develop specific MRI CAs. To optimize this affinity, these compounds have been synthesized with two bombesin analogues : the Lys^3-bombesin and the Ahx-bombesin(4-14). The relaxivities of compounds presenting one and two bombesin peptide grafted on the chelating units DOTA (Figure I.19) are measured and characterized.

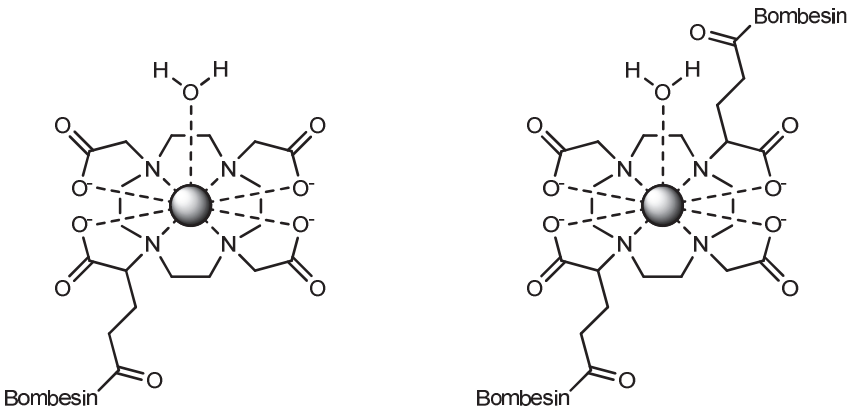

Figure I.21 **–** The potential specific CAs {BN[Gd(DOTA)(H_2O)]$^-$} and {BN_2[Gd(DOTA)(H_2O)]$^-$} (Chapter V).

I.7 References

1. Mansson, S.; Bjornerud, A. In *The Chemistry of Contrast Agents in Medical Magnetic Resonance Imaging;* Merbach, A. E.; Tóth, É. Eds.; John Wiley & Sons, Ltd: Chichester, 2001; pp. 1-43.
2. Hore, P. J. *Nuclear Magnetic Resonance*; Oxford Univ. Press: New York, 1995.
3. Piguet, C. *Cours de magnetisme moleculaire - Structure Electronique et Magnetisme des complexes minéraux et de coordination*; Université de Genève, 2001.
4. Slichter, C. P. *Principles of magnetic resonance*, 3rd ed.; Springer-Verlag: Berlin, 1986.
5. Tóth, É.; Helm, L.; Merbach, A. E. In *The Chemistry of Contrast Agents in Medical Magnetic Resonance Imaging;* Merbach, A. E.; Tóth, É. Eds.; John Wiley & Sons, Ltd: Chichester, 2001; pp. 45-119.
6. Bakhmutov, V. I. *Practical NMR Relaxation for Chemists*; John Wiley & Sons, Ltd: Chichester, 2004.
7. Banci, L.; Bertini, I.; Luchinat, C. *Nuclear and Electron Relaxation*; VCH Verlagsgesellschaft mbH.: Weinheim, 1991.
8. Solomon, I. *Physical Review* **1955,** *99*, 559-565.
9. Yazyev, O. V.; Helm, L. *European Journal of Inorganic Chemistry* **2008**, 201-211.
10. Yazyev, O. V.; Helm, L.; Malkin, V. G.; Malkina, O. L. *Journal of Physical Chemistry A* **2005,** *109*, 10997-11005.
11. Swift, T. J.; Connick, R. E. *The Journal of Chemical Physics* **1962,** *37*, 307-320.
12. Swift, T. J.; Connick, R. E. *The Journal of Chemical Physics* **1964,** *41*, 2553-2554.
13. Luz, Z.; Meiboom, S. *The Journal of Chemical Physics* **1964,** *40*, 2686-2692.
14. Bloembergen, N.; Morgan, L. O. *The Journal of Chemical Physics* **1961,** *34*, 842-850.
15. McLachlan, A. D. *Proceedings of the Royal Society of London, Series A* **1964,** *280*, 271-88.
16. Kowalewski, J.; Nordenskiold, L.; Benetis, N.; Westlund, P. O. *Progress in Nuclear Magnetic Resonance Spectroscopy* **1985,** *17*, 141-185.
17. Powell, D. H.; Merbach, A. E.; Gonzalez, G.; Brücher, E.; Micskei, K.; Ottaviani, M. F.; Kohler, K.; Vonzelewsky, A.; Grinberg, O. Y.; Lebedev, Y. S. *Helvetica Chimica Acta* **1993,** *76*, 2129-2146.
18. Redfield, A. G. *Ibm Journal of Research and Development* **1957,** *1*, 19-31.

19. Astashkin, A. V.; Raitsimring, A. M.; Caravan, P. *Journal of Physical Chemistry A* **2004,** *108*, 1990-2001.
20. Lipari, G.; Szabo, A. *Journal of the American Chemical Society* **1982,** *104*, 4546-4559.
21. Lipari, G.; Szabo, A. *Journal of the American Chemical Society* **1982,** *104*, 4559-4570.
22. Tóth, É.; Helm, L.; Kellar, K. E.; Merbach, A. E. *Chemistry-a European Journal* **1999,** *5*, 1202-1211.
23. Aime, S.; Botta, M.; Crich, S. G.; Giovenzana, G. B.; Pagliarin, R.; Piccinini, M.; Sisti, M.; Terreno, E. *Journal of Biological Inorganic Chemistry* **1997,** *2*, 470-479.
24. Botta, M. *European Journal of Inorganic Chemistry* **2000**, 399-407.
25. Fries, P.; Belorizky, E. *Journal De Physique* **1978,** *39*, 1263-1282.
26. Albrand, J. P.; Taieb, M. C.; Fries, P. H.; Belorizky, E. *Journal of Chemical Physics* **1983,** *78*, 5809-5815.
27. Levenberg, K. *Quarterly of Applied Mathematics* **1944,** *2*, 164-168.
28. Marquardt, D. W. *SIAM Journal on Applied Mathematics* **1963,** *11*, 431-441.
29. Micskei, K.; Helm, L.; Brücher, E.; Merbach, A. E. *Inorganic Chemistry* **1993,** *32*, 3844-3850.
30. Helm, L.; Nicolle, G. M.; Merbach, A. E. In *Advances in Inorganic Chemistry;* van Eldik, R.; Bertini, I. Eds.: San Diego, 2005; pp. 327-379.
31. Gonzalez, G.; Powell, D. H.; Tissieres, V.; Merbach, A. E. *Journal of Physical Chemistry* **1994,** *98*, 53-59.
32. Belorizky, E.; Fries, P. H.; Helm, L.; Kowalewski, J.; Kruk, D.; Sharp, R. R.; Westlund, P. O. *Journal of Chemical Physics* **2008,** *128*.
33. Rast, S.; Fries, P. H.; Belorizky, E. *Journal of Chemical Physics* **2000,** *113*, 8724-8735.
34. Rast, S.; Borel, A.; Helm, L.; Belorizky, E.; Fries, P. H.; Merbach, A. E. *Journal of the American Chemical Society* **2001,** *123*, 2637-2644.
35. Rast, S.; Fries, P. H.; Belorizky, E.; Borel, A.; Helm, L.; Merbach, A. E. *Journal of Chemical Physics* **2001,** *115*, 7554-7563.
36. Helm, L. *Progress in Nuclear Magnetic Resonance Spectroscopy* **2006,** *49*, 45-64.
37. Bertini, I.; Galas, O.; Luchinat, C.; Parigi, G. *Journal of Magnetic Resonance Series A* **1995,** *113*, 151-158.
38. Bertini, I.; Kowalewski, J.; Luchinat, C.; Nilsson, T.; Parigi, G. *Journal of Chemical Physics* **1999,** *111*, 5795-5807.
39. Kruk, D.; Nilsson, T.; Kowalewski, J. *Physical Chemistry Chemical Physics* **2001,** *3*, 4907-4917.

40. Kowalewski, J.; Kruk, D.; Parigi, G. In *Advances in Inorganic Chemistry*; Academic Press, 2005; pp. 41-104.
41. Rubinstein, M.; Baram, A.; Luz, Z. *Molecular Physics* **1971,** *20*, 67-80.
42. Damadian, R. *Science* **1971,** *171*, 1151-1153.
43. Lauterbur, P. C. *Nature* **1973,** *242*, 190-191.
44. Mansfield, P.; Grannell, P. K. *Journal of Physics C: Solid State Physics* **1973,** *6*.
45. *http://nobelprize.org/nobel_prizes/medicine/laureates/2003/index.html*.
46. Kumar, A.; Welti, D.; Ernst, R. R. *Naturwissenschaften* **1975,** *62*, 34.
47. Kwong, K. K.; Belliveau, J. W.; Chesler, D. A.; Goldberg, I. E.; Weisskoff, R. M.; Poncelet, B. P.; Kennedy, D. N.; Hoppel, B. E.; Cohen, M. S.; Turner, R.; Cheng, H. M.; Brady, T. J.; Rosen, B. R. *Proceedings of the National Academy of Sciences of the United States of America* **1992,** *89*, 5675-5679.
48. Ogawa, S.; Tank, D. W.; Menon, R.; Ellermann, J. M.; Kim, S. G.; Merkle, H.; Ugurbil, K. *Proceedings of the National Academy of Sciences of the United States of America* **1992,** *89*, 5951-5955.
49. Johnson Jr., C. S. *Progress in Nuclear Magnetic Resonance Spectroscopy* **1999,** *34*, 203-256.
50. Ersoy, H.; Rybicki, F. J. *Journal of Magnetic Resonance Imaging* **2007,** *26*, 1190-1197.
51. Grobner, T. *Nephrology Dialysis Transplantation* **2006,** *21*, 1104-1108.
52. Oksendal, A. N.; Hals, P. A. *Journal of Magnetic Resonance Imaging* **1993,** *3*, 157-165.
53. Tóth, É.; van Uffelen, I.; Helm, L.; Merbach, A. E.; Ladd, D.; Briley-Sæbø, K.; Kellar, K. E. *Magnetic Resonance in Chemistry* **1998,** *36*, S125-S134.
54. Dunand, F. A.; Tóth, É.; Hollister, R.; Merbach, A. E. *Journal of Biological Inorganic Chemistry* **2001,** *6*, 247-255.
55. Yan, G. P.; Zhuo, R. X.; Xu, M. Y.; Zhang, X.; Li, L. Y. *Polymer International* **2002,** *51*, 892-898.
56. Duarte, M. G.; Gil, M. H.; Peters, J. A.; Colet, J. M.; Vander Elst, L.; Muller, R. N.; Geraldes, C. F. G. C. *Bioconjugate Chemistry* **2001,** *12*, 170-177.
57. Tóth, É.; Pubanz, D.; Vauthey, S.; Helm, L.; Merbach, A. E. *Chemistry-a European Journal* **1996,** *2*, 1607-1615.
58. Wiener, E. C.; Brechbiel, M. W.; Brothers, H.; Magin, R. L.; Gansow, O. A.; Tomalia, D. A.; Lauterbur, P. C. *Magnetic Resonance in Medicine* **1994,** *31*, 1-8.
59. Margerum, L. D.; Campion, B. K.; Koo, M.; Shargill, N.; Lai, J. J.; Marumoto, A.; Sontum, P. C. *Journal of Alloys and Compounds* **1997,** *249*, 185-190.

60. Bryant, L. H.; Brechbiel, M. W.; Wu, C. C.; Bulte, J. W. M.; Herynek, V.; Frank, J. A. *Journal of Magnetic Resonance Imaging* **1999,** *9*, 348-352.
61. Nicolle, G. M.; Tóth, É.; Schmitt-Willich, H.; Radüchel, B.; Merbach, A. E. *Chemistry-a European Journal* **2002,** *8*, 1040-1048.
62. André, J. P.; Tóth, É.; Fischer, H.; Seelig, A.; Mäcke, H. R.; Merbach, A. E. *Chemistry-a European Journal* **1999,** *5*, 2977-2983.
63. Nicolle, G. M.; Tóth, É.; Eisenwiener, K. P.; Macke, H. R.; Merbach, A. E. *Journal of Biological Inorganic Chemistry* **2002,** *7*, 757-769.
64. Hovland, R.; Aasen, A. J.; Klaveness, J. *Organic & Biomolecular Chemistry* **2003,** *1*, 1707-1710.
65. Accardo, A.; Tesauro, D.; Roscigno, P.; Gianolio, E.; Paduano, L.; D'Errico, G.; Pedone, C.; Morelli, G. *Journal of the American Chemical Society* **2004,** *126*, 3097-3107.
66. Kimpe, K.; Parac-Vogt, T. N.; Laurent, S.; Pierart, C.; Vander Elst, L.; Muller, R. N.; Binnemans, K. *European Journal of Inorganic Chemistry* **2003**, 3021-3027.
67. Aime, S.; Fasano, M.; Terreno, E.; Botta, M. In *The Chemistry of Contrast Agents in Medical Magnetic Resonance Imaging;* Merbach, A. E.; Tóth, É. Eds.; John Wiley & Sons Ltd.: Chichester, 2001; pp. 193-241.
68. Aime, S.; Botta, M.; Fasano, M.; Crich, S. G.; Terreno, E. *Journal of Biological Inorganic Chemistry* **1996,** *1*, 312-319.
69. Caravan, P.; Cloutier, N. J.; Greenfield, M. T.; McDermid, S. A.; Dunham, S. U.; Bulte, J. W. M.; Amedio, J. C.; Looby, R. J.; Supkowski, R. M.; Horrocks, W. D.; McMurry, T. J.; Lauffer, R. B. *Journal of the American Chemical Society* **2002,** *124*, 3152-3162.
70. Lauffer, R. B.; Parmelee, D. J.; Dunham, S. U.; Ouellet, H. S.; Dolan, R. P.; Witte, S.; McMurry, T. J.; Walovitch, R. C. *Radiology* **1998,** *207*, 529-538.
71. Hartman, K. B.; Laus, S.; Bolskar, R. D.; Muthupillai, R.; Helm, L.; Tóth, É.; Merbach, A. E.; Wilson, L. J. *Nano Letters* **2008,** *8*, 415-419.
72. Tran, L. A.; Krishnamurthy, R.; Muthupillai, R.; da Graça Cabreira-Hansen, M.; Willerson, J. T.; Perin, E. C.; Wilson, L. J. *Biomaterials* **2010,** *31*, 9482-9491.
73. Moriggi, L.; Cannizzo, C.; Dumas, E.; Mayer, C. R.; Ulianov, A.; Helm, L. *Journal of the American Chemical Society* **2009,** *131*, 10828-10829.
74. Park, J.-A.; Kim, H.-K.; Kim, J.-H.; Jeong, S.-W.; Jung, J.-C.; Lee, G.-H.; Lee, J.; Chang, Y.; Kim, T.-J. *Bioorganic & Medicinal Chemistry Letters* **2010,** *20*, 2287-2291.
75. Helm, L. *Future Medicinal Chemistry* **2010,** *2*, 385-396.

76. Costa, J.; Ruloff, R.; Burai, L.; Helm, L.; Merbach, A. E. *Journal of the American Chemical Society* **2005,** *127*, 5147-5157.
77. Costa, J.; Tóth, É.; Helm, L.; Merbach, A. E. *Inorganic Chemistry* **2005,** *44*, 4747-4755.
78. Lee, T. M.; Cheng, T. H.; Ou, M. H.; Chang, C. A.; Liu, G. C.; Wang, Y. M. *Magnetic Resonance in Chemistry* **2004,** *42*, 329-336.
79. Livramento, J. B.; Helm, L.; Sour, A.; O'Neil, C.; Merbach, A. E.; Tóth, É. *Dalton Transactions* **2008**, 1195-1202.
80. Jacques, V.; Desreux, J. In *Contrast Agents I;* Krause, W. Ed.; Springer Berlin / Heidelberg, 2002; pp. 123-164.
81. Fossheim, S. L.; Il'yasov, K. A.; Hennig, J.; Bjornerud, A. *Academic Radiology* **2000,** *7*, 1107-1115.
82. Zhang, S. R.; Wu, K. C.; Sherry, A. D. *Angewandte Chemie-International Edition* **1999,** *38*, 3192-3194.
83. Aime, S.; Barge, A.; Botta, M.; Howard, J. A. K.; Kataky, R.; Lowe, M. P.; Moloney, J. M.; Parker, D.; de Sousa, A. S. *Chemical Communications* **1999**, 1047-1048.
84. Aime, S.; Ascenzi, P.; Comoglio, E.; Fasano, M.; Paoletti, S. *Journal of the American Chemical Society* **1995,** *117*, 9365-9366.
85. Li, W. H.; Fraser, S. E.; Meade, T. J. *Journal of the American Chemical Society* **1999,** *121*, 1413-1414.
86. Hanaoka, K.; Kikuchi, K.; Urano, Y.; Nagano, T. *Journal of the Chemical Society-Perkin Transactions 2* **2001**, 1840-1843.
87. Aime, S.; Botta, M.; Garino, E.; Crich, S. G.; Giovenzana, G.; Pagliarin, R.; Palmisano, G.; Sisti, M. *Chemistry-a European Journal* **2000,** *6*, 2609-2617.
88. Unger, E. C.; Totty, W. G.; Neufeld, D. M.; Otsuka, F. L.; Murphy, W. A.; Welch, M. S.; Connett, J. M.; Philpott, G. W. *Investigative Radiology* **1985,** *20*, 693-700.
89. Sipkins, D. A.; Cheresh, D. A.; Kazemi, M. R.; Nevin, L. M.; Bednarski, M. D.; Li, K. C. P. *Nature Medicine* **1998,** *4*, 623-626.
90. Anderson, S. A.; Rader, R. K.; Westlin, W. F.; Null, C.; Jackson, D.; Lanza, C. M.; Wickline, S. A.; Kotyk, J. J. *Magnetic Resonance in Medicine* **2000,** *44*, 433-439.
91. Abiraj, K.; Jaccard, H.; Kretzschmar, M.; Helm, L.; Maecke, H. R. *Chemical Communications* **2008**, 3248-3250.
92. Sturzu, A.; Kalbacher, H.; Echner, H.; Klose, U.; Gharabaghi, A.; Heckl, S. *Amino Acids* **2010,** *38*, 1415-1421.

Chapter II :

Synthesis, complexation and NMR relaxation properties of Gd^{3+} complexes of $Mes(DO3A)_3$

II.1. Introduction 55
II.2. Experimental Section 57
II.2.1. Ligand synthesis and characterization 57
II.2.2. Sample preparation 59
II.2.3. Transmetallation 61
II.2.4. ^{1}H relaxometry 61
II.2.5. ^{17}O NMR spectroscopy 61
II.2.6. Data treatment 61
II.2.7. Molecular mechanics 62
II.3. Results and discussion 63
II.3.1. Ligand synthesis 63
II.3.2. Complexation 63
II.3.3. Structural transition induced by pH 65
II.3.4. ^{1}H NMRD profiles 66
II.3.5. ^{17}O NMR spectroscopy 67
II.3.6. Molecular modeling 71
II.4. Conclusion 73
II.5. Acknowledgements 75
II.6. References 76

II.1. Introduction

Currently all approved gadolinium based contrast agents (CA) for magnetic resonance Imaging (MRI) are based on complexes with chelating poly(amino carboxylate) ligands.[1] These octa-dentate ligands, which are either acyclic like DTPA or DTPA-BMA or macrocyclic like DOTA or HP-DO3A (see chapter I.5.2), form extremely stable complexes with lanthanides offering space for the coordination of one water molecule.[2] Tremendous efforts have been spent in the last decade to develop new compounds with increased efficiency required for targeted CA and molecular imaging. The enhancement of longitudinal nuclear spin relaxation, commonly expressed as relaxivity (r_1) if normalized to 1 mM solution of gadolinium ions, could be increased by more than an order of magnitude, mainly by slowing down the rotational diffusion of the molecules.[3] This increase in relaxivity has been achieved at magnetic fields common to MRI instruments actually used in clinical application.

However, most highly efficient CA lose nearly all of the gain in relaxivity at high magnetic fields above 3 T. MRI instruments working at 7 T or even above are now successively installed in research institutions, creating a need for contrast agents designed for application at these conditions.[4] Theoretical calculations using the simple Solomon-Bloembergen-Morgan approach[5-8] show that the relaxivity which can be reached at magnetic fields above 3 T is well below the performance which can be achieved between 1 and 1.5 T.[8,9] Staying with chelate complexes of gadolinium, the only way to boost the efficiency of CA is to increase the number (q) of water molecules directly bound to Gd^{3+} and the assembly of many chelating units in larger molecules. The theoretical calculations have also shown that the compounds should have a reasonable size leading to rotational correlation times between 0.5 and 1 ns.

Several mid-size molecules assembled around a benzene ring have been synthesized and tested for their relaxation enhancement capabilities (Figure II.1).[10-12] The chelating groups used are either the acyclic DTTA (H_4DTTA = diethylenetriaminetetraacetic acid = 2,2',2'',2'''-[iminobis(ethane-2,1-dinitrilo)tetraacetic acid) or the macrocyclic DO3A (1,4,7,10-tetraazacyclododecane-*N*,*N'*,*N''*-triacetate). Both can form Gd^{3+} complexes with two water molecules (q = 2) in the first coordination sphere. Surprisingly it had been found that the compounds with DO3A[11] had q = 1 and formed aggregates in aqueous solution.

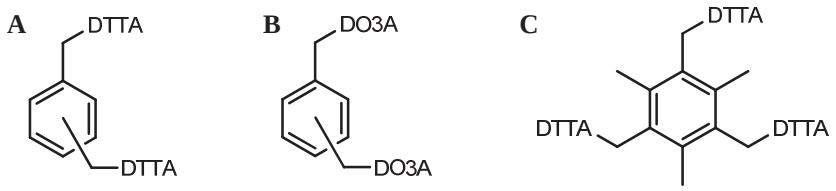

Figure II.1 – Structures of benzene based mid-size molecules which can complex 2 Gd^{3+} ions (pX(DTTA)$_2$, mX(DTTA)$_2$ (A),[10] pX(DO3A)$_2$ (L^1) and mX(DO3A)$_2$ (L^2) (B)[11]) or three Gd^{3+} ions (L) (C)[12].

To further investigate the behavior of gadolinium-DO3A complexes bound to a benzene ring we decided to synthesize and to determine the relaxivity of {Mes[Gd(DO3A)$(H_2O)_2]_3$}, a tris-gadolinium complex formed by mesitylene substituted with three DO3A units on the three methyl positions (Figure II.2). It would be interesting to see if these compounds form aggregates in aqueous solution. The aromatic part sits in the center of the molecule and aggregation by π-stacking of the benzene rings would be strongly disfavored. A second question we intended to answer concerns the number of inner sphere water molecules. Will we also find q = 1 as for the xylene-cored dinuclear Gd chelates[11] and for other DO3A based dimeric Gd complexes[13,14] or will we find $q \cong 2$ as for the DO3A monomer[15] ?

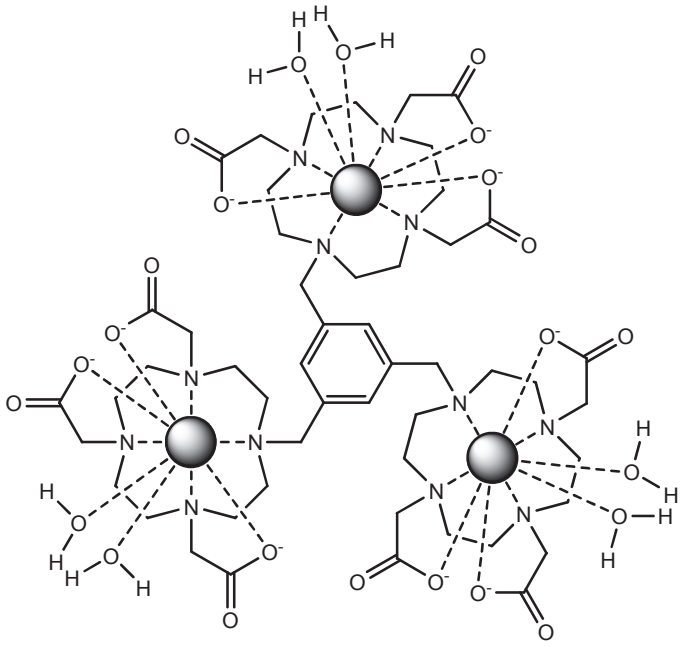

Figure II.2 – The trinuclear complex {Mes[Gd(DO3A)$(H_2O)_2]_3$}

II.2. Experimental Section

II.2.1. Ligand synthesis and characterization

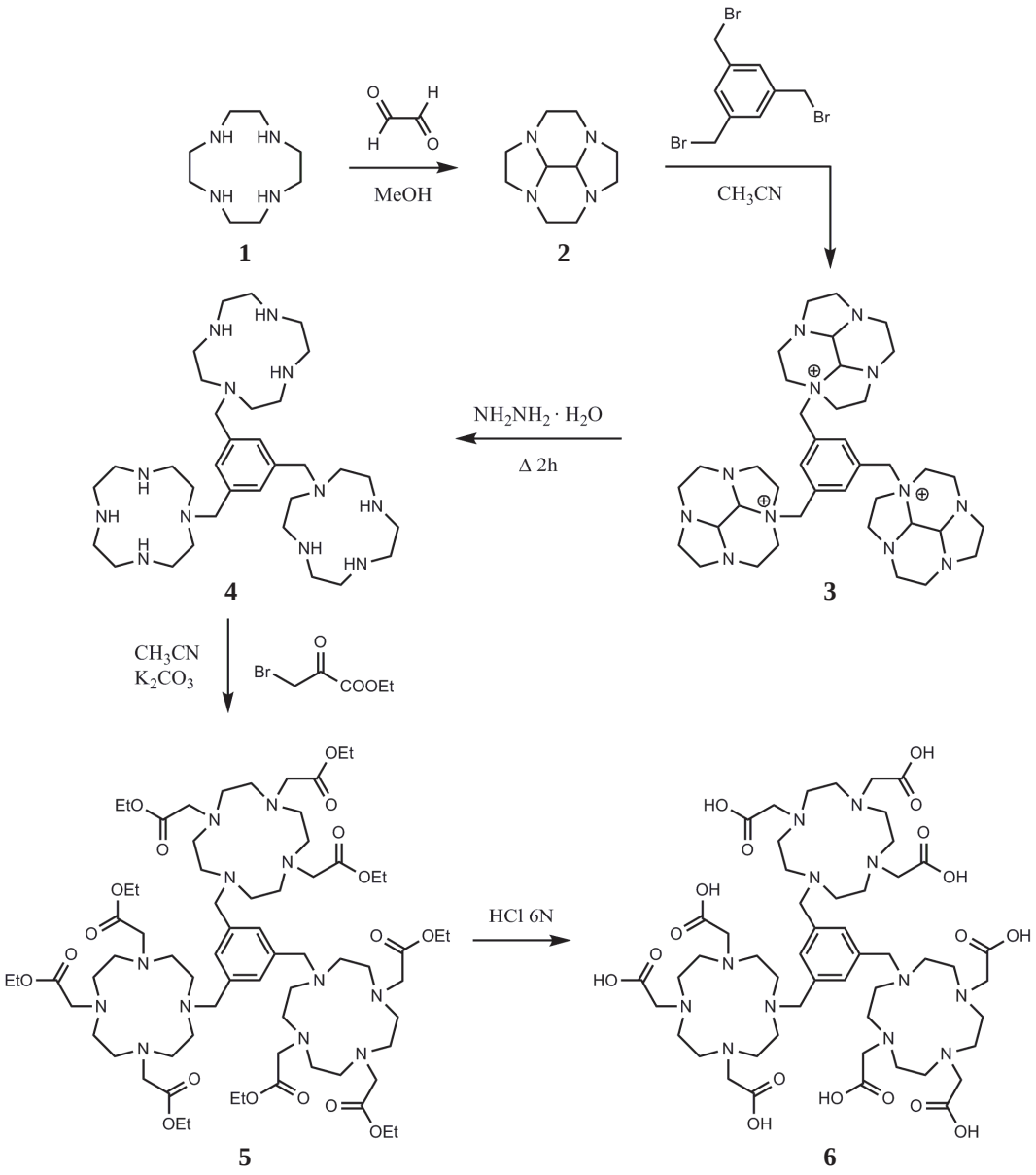

Figure II.3 **–** $Mes(DO3A)_3$ synthesis scheme

This synthesis was performed by Felipe Reviriego and Raphaël Tripier, from UMR CNRS 6521, Université de Bretagne Occidentale in Brest, France.

Reagents were purchased from ACROS Organics and from ALDRICH Chemical Co. NMR and mass spectrometry were investigated at the "services communs" of the University of Brest. Elemental analyses were performed at the Service de Microanalyse, CNRS, Gif sur Yvette, France.

Synthesis of decahydro-2a,4a,6a,8a-tetraazacyclopenta[*fg*]acenaphthylene (2)

This compound, referred as cyclen-glyoxal, was synthesized by direct condensation of glyoxal with cyclen **1** as previously reported.[16-19]

Synthesis of 2a,2a',2a''-(benzene-1,3,5-triyltrimethanediyl)tris(decahydro-4a,6a,8a-triaza-2a-azoniacyclopenta[*fg*]acenaphthylene (3)

To a solution of cyclen-glyoxal (**2**) (0.97 g, 5 mmol, 3.3 eq.) in anhydrous acetonitrile (5 mL) vigorously stirred at room temperature was slowly added 1,3,5-tris(bromomethyl)benzene (0.54 g, 1.5 mmol) in anhydrous acetonitrile (10 mL). When the addition was complete the reaction was allowed to proceed for 2 weeks. The solid was filtered off and dried in vacuum to give compound **3** (90 %). ^{13}C NMR (100 MHz, D_2O, 298 K): δ = 141.23 (CAr), 133.13 (CHAr), 86.38 (CH), 74.32 (CHaminal), 64.39 (αCH_2-Ar), 62.87, 60.02, 54.12, 51.03, 50.87, 50.33 (2), 46.35 (αCH_2) ppm. Anal. calcd. for $C_{39}H_{63}Br_3N_{12}$ (939.72): C 49.85, H 6.76, N 17.89; found: C 49.72, H 6.51, N 17.33.

Synthesis of 1,1',1''-(benzene-1,3,5-triyltrimethanediyl)tris(1,4,7,10-tetraazacyclodidecane) (4)

Compound **3** was refluxed in 10 mL of hydrazine hydrate for 2 hours. After cooling, the solvent was removed to dryness to yield **4** (quantitative yield).^{13}C NMR (100 MHz, $CDCl_3$, 298 K): δ = 138.9 (CAr), 129.4 (CHAr), 59.0 (αCH_2Ar), 51.0, 47.2, 46.6, 45.1(αCH2). Anal. calcd. for $C_{33}H_{66}N_{12}$ (630.97): C 62.82, H 10.54, N 26.64; found: C 62.71, H 10.66, N 26.32. MS (FAB) : *m/z* (%) 631.1 (100) $[M+H]^+$.

Synthesis of 1,1',1''-(benzene-1,3,5-triyltrimethanediyl)tris[triethyl 2,2',2''-(1,4,7,10-tetraazacyclododecane-1,4,7-triyl)triacetate] (5)

1.57 g (9.3 eq) of ethyl bromoacetate in acetonitrile (mL) was slowly added to a solution of compound **4** (0.63 g, 1 mol) with K_2CO_3 in acetonitrile. The reaction was allowed to proceed

to reflux for 24 hours and the solution was filtered. After solvent evaporation, the residue was dissolved in water (20 mL) and extracted with chloroform (3 x 20 mL). The organic phase was dried with $MgSO_4$ and evaporated to dryness to yield **5** as a solid (93%). ^{13}C NMR (100 MHz, $CDCl_3$, 298 K): δ = 171.40 (CO), 138.71 (br s, CAr), 128.25 (br s, CHAr), 61.32 (CH_2CAr), 60.09 (CH_2CH_3), 55.24, 51.74, 51.59 (αCH_2), 14.03 (CH_3) ppm. Anal. calcd. for $C_{69}H_{120}N_{12}O_{18}$ (1405.78): C 58.95, H 8.60, N 11.96; found: C 59.01, H 8.72, N 11.59. MS (FAB) : *m/z* (%) 1406.1 (100) $[M+H]^+$.

Synthesis of 2,2',2'',2''',2'''',2''''',2'''''',2''''''',2'''''''',2'''''''''-[benzene-1,3,5-triyltris(methanediyl-1,4,7,10-tetraazacyclododecane-10,1,4,7-tetrayl)]nonacetic acid (6)

This compound will be referred as $Mes(DO3A)_3$. Compound **5** was dissolved in a hydrochloric acid solution (6N) and stirred at 80 ºC during 12 h. After evaporation to dryness the compound was dissolved in water and evaporated (3 times). The product was dissolved in a small amount of water (5 mL) and eluted first through a column packed with a Dowex 50WX8 (H^+ form) cation exchange resin with ammonium hydroxide and after eluted through a column with a Dowex 1X2-200 (OH^- form) anion exchange resin with hydrochloric acid. The compound was obtained in 93% of yield like a maroon solid as an adduct with hydrochloric acid. ^{13}C NMR (100 MHz, D_2O, 298 K): δ = 176.54, 170.84 (vbr s, CO), 138.03 (vbr s, CAr-CH_2), 132.10 (vbr s, CAr), 58.93 (br s, CH_2-CAr), 55.83, 54.52, 51.53 (vbr s, CH_2) ppm. Anal. calcd. for $C_{51}H_{84}N_{12}O_{18} \cdot 12\ HCl \cdot 2.5\ H_2O$ (1635.86) : C 37.45, H 6.22, N 10.27, Cl 26.01; found: C 37.20, H 6.52, N 10.00 Cl 25.98. MS (ESI) : *m/z* (%) : 577.79 (50) $[M+2H]^{2+}$, 385.36 (100) $[M+3H]^{3+}$.

II.2.2. Sample preparation

The purity of the ligand molecule was checked with gas chromatography (HP 6890 with a 20m FFAP column specific for carboxylic acids). One single and pure compound was detected at 10.55 min.

A 29.5 mM Gd^{3+} solution in water was prepared from $GdCl_3$ (79.0 mg of $GdCl_3$ (0.3 mmol) in 10.0 mL H_2O). The exact concentration of the metal ion was measured by complexometric titration with Na_2H_2EDTA 5 mM in urotropine/HCl buffer and xylenol orange as metal indicator. 97.3 mg of the solid ligand **6** ($C_{51}H_{84}N_{12}O_{18} \cdot 12\ HCl \cdot 2.5\ H_2O$, *M* = 1635.86 g mol^{-1}, 59.48 μmol) were dissolved in 1.00 mL of water in order to obtain a theoretical 59.5

mM solution. The exact concentration of **6**, determined by complexometric back titration of a Gd^{3+} excess with Na_2H_2EDTA 5 mM in urotropine buffer and xylenol orange as metal indicator, was determined at 58.8 mM based on the formation of the complex $\{Mes(H_2DO3A)[Gd(DO3A)(H_2O)]_2\}^-$.

All attempts to prepare the tris-Gd complex by mixing a ligand solution with an adequate amount of Gd^{3+} solution failed. In all cases the bis-Gd complex $\{Mes(H_2DO3A)[Gd(DO3A)(H_2O)]_2\}^-$ with an excess of free Gd^{3+} was obtained. Finally solutions $\{Mes(H_2DO3A)[Gd(DO3A)(H_2O)]_2\}^-$ without free gadolinium ions were prepared by mixing a ligand solution with a $GdCl_3$ stock solution in a 1:2 stoichiometric ratio. The pH, which drops spontaneously after mixing to 1.2, was corrected to 5.8 by adding NaOH (0.01 M) (measured with combined glass electrode on a Metrohm 713 pH Meter, calibrated with Metrohm buffers). The solution was stirred overnight and finally heated to 60°C under argon bubbling in order to remove carbon dioxide. The absence of free Gd^{3+} was verified with the xylenol orange test.

The tris-Gd complex $\{Mes[Gd(DO3A)(H_2O)_2]_3\}$ was prepared by complexing **6** in a first step with Mg^{2+} followed by transmetallation with Gd^{3+}. 11.8 mg of $MgCl_2 \cdot 2H_2O$ (58 µmol, 3 eq.) in 100 µL H_2O were added to the ligand solution (31.5 mg, 19.3 µmol, 1 eq.). The pH was set to 8.9 with NaOH (2 M) and the solution was stirred overnight. The following day, the pH was adjusted to 5.8 with HCl and the solution was added to 3 mL of a 29.50 mM Gd^{3+} (88.5 µmol, 4.59 eq.) solution, previously adjusted to pH 5.9 with NaOH (0.1 M) and degassed with argon for 15 min. The transmetallation reaction was followed by relaxometry. The excess of Gd^{3+} and the released Mg^{2+} were removed by size exclusion chromatography (Sephadex G-25 resin, eluted with water). The fractions containing the complex were identified by its yellow color and confirmed by UV (254 nm) on a TLC silica plate. The xylenol orange test was performed to indicate the absence of free ions. The collected fractions were dried and the solid complex was recovered.

Gadolinium and carbon mass contents were measured by ICP-MS (Perkin-Elmer) and by elemental analysis, respectively. Gd/ligand ratios were calculated from Gd/C ratios assuming that carbons are only from the ligand (51 C atoms per ligand). The exact concentrations of the paramagnetic Gd^{3+} were determined by bulk magnetic susceptibility (BMS)[20] at 25°C on a Bruker DRX-400 NMR spectrometer.

II.2.3. Transmetallation

The transmetallation from Mg^{2+} to Gd^{3+} was followed by NMR relaxometry at 25 °C and 30 MHz using a Bruker Minispec mq40. In a first step the longitudinal relaxation rate of the $GdCl_3$ solution has been measured. In a second step the $GdCl_3$ and $\{Mes[Mg(DO3A)(H_2O)_x]_3\}^{3-}$ solutions were mixed (8% excess of Gd^{3+} with respect to the DO3A binding sites) at 25 °C and the solution degassed for 5 min with argon. The relaxation rates were measured at 10 minutes intervals during 800 minutes after mixing.

II.2.4. ^1H relaxometry

Longitudinal relaxation times T_1 for a full NMRD profile were measured at ^1H Larmor frequencies from 0.01 to 400 MHz using the following equipment: Stellar Spinmaster FFC relaxometer (0.01 to 20 MHz),[21] Bruker Minispec mq40 (30 and 40 MHz) and mq60 (60 MHz), and Bruker NMR spectrometers working at 100, 200 and 400 MHz. The measurements were made at 25.0 °C and 37.0 °C using Gd^{3+} concentrations of 5.53 and 20.15 mM for $\{Mes(H_2DO3A)[Gd(DO3A)(H_2O)]_2\}^-$ and 12.79 mM for $\{Mes[Gd(DO3A)(H_2O)_2]_3\}$.

II.2.5. ^{17}O NMR spectroscopy

Two ^{17}O enriched solutions (2% in ^{17}O obtained by diluting 20% ^{17}O enriched normalized water, Isotec) were prepared with final concentrations of Gd^{3+} 20.15 mM $\{Mes(H_2DO3A)[Gd(DO3A)(H_2O)]_2\}^-$ and 20.61 mM $\{Mes[Gd(DO3A)(H_2O)_2]_3\}$. Relaxation measurements ($R_1 = 1/T_1$ by the inversion-recovery method[22,23] and $R_2 = 1/T_2$ by the Carr-Purcell-Meiboom-Gill method[23,24]) and chemical shifts (using spherical samples to avoid susceptibility corrections[25]) were performed on a Bruker ARX-400 spectrometer (9.4 T, 54.2 MHz). Acidified water ($HClO_4$, pH = 3.0) was used as external reference. In all measurements, the temperature was maintained by a Bruker B-VT 3000 temperature control unit, and was measured by a substitution technique.[26]

II.2.6. Data treatment

Solomon-Bloembergen-Morgan (SBM) theory[6,7] has been used for data analysis (for equations see ref. 7). ^1H NMRD profiles, ^{17}O relaxation and chemical shifts were fitted in a

simultaneous fit using the Visualiseur/Optimiseur 3.5.0 program[27,28] running on a Matlab® 6.5 platform.

II.2.7. Molecular mechanics

All calculations were performed using Scigress Explorer Ultra Version 7.70.47 (Fujitsu Ltd) and the classical MM3 force field. Gd^{3+} ions have been replaced by Y^{3+} having the same ionic radius. The $[Mes\{DO3A\}\{Y(DO3A)(H_2O)\}_2]^{3-}$ complex was embedded into a drop of water consisting of 393 H_2O molecules. Convergence was supposed to be attaint for an energy gradient < 10-5 kcal/mol.

II.3. Results and discussion

II.3.1. Ligand synthesis

Poly-tetraazacycloalkane ligands are very attractive compounds for coordination chemistry since they are now easily obtained by selective *N*-alkylation of the starting macrocycle.[16-19] As shown in Figure II.3, the studied ligand **6** consists in three DO3A moieties linked with a mesitylenyl center and is obtained following an easy route involving the bisaminal methodology of tetraazacycloalkanes.[29-32] In a first step, the macrocyclic bis-aminal **2** has been obtained by condensation of glyoxal with cyclen **1** as previously described.[33] Reaction of one equivalent of the tris-electrophile 1,3,5-tris(bromomethyl)benzene with **2** leads to the tris-salt **3**, easily deprotected by hydrazine monohydrate to obtain the tris-cyclen **4** in quantitative yield. This step is followed by the alkylation of the three secondary amine functions of each cyclen moities with ethyl bromoacetate. Finally, the nine-fold ester derivative is hydrolyzed in HCl (6N) with 78 % overall yield.

II.3.2. Complexation

The classical complexation method consists in mixing a ligand solution with stoichiometric quantities of Gd^{3+} calculated for $\{Mes[Gd(DO3A)(H_2O)_2]_3\}$ (see Experimental Section, chapter II.2.2.). In the case of our ligand **6** this leads to a surprising result. From the back titration of free Gd^{3+} is has been found that only 1.98 Gd^{3+} are bound to the ligand instead of the 3 expected. The calculation of this Gd/L ratio has been based on the molar mass established from the elementary analysis ($C_{51}H_{84}N_{12}O_{18} \cdot 12HCl \cdot 2.5H_2O$). This surprising result is confirmed by the Gd/L ratio of 2.17 which is obtained from gadolinium to carbon mass ratios determined by ICP-MS and elementary analysis for Gd and C, respectively.

The observed difficulties to complex a third Gd^{3+} ion by the ligand **6** could arise subsequently from the important pH drop during the complexation reaction (pH ~ 1.2 after mixing). This pH drop implies a protonation of the amines of the third DO3A ring, which prevents the chelation of the third Gd^{3+}. After restoring the pH to 5.8, the two acetates of the uncomplexed DO3A, instead of staying deprotonated and free, are suspected to bind immediately to the two chelated Gd^{3+} ions by replacing one water molecule from the first coordination sphere of each

of the two paramagnetic centers (Figure II.4).[34,35] We therefore conclude that we synthesized the compound $\{Mes(H_2DO3A)[Gd(DO3A)(H_2O)]_2\}^-$, which we named bis-Gd (Figure II.4 B) as opposed to $\{Mes[Gd(DO3A)(H_2O)_2]_3\}$ which we named tris-Gd (Figure II.4 A).

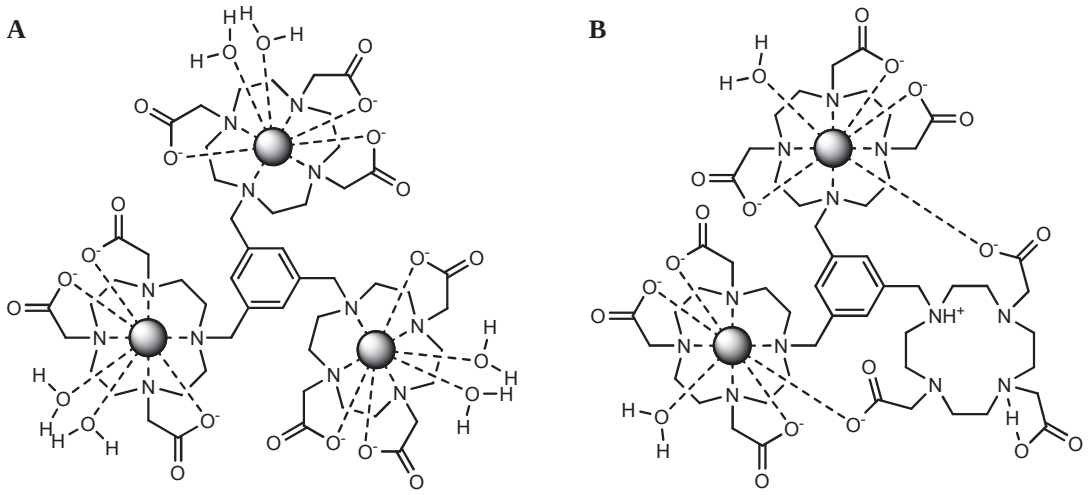

Figure II.4 – Proposed structures of the tris-Gd complex $\{Mes[Gd(DO3A)(H_2O)_2]_3\}$ (A) and the bis-Gd complex $\{Mes(H_2DO3A)[Gd(DO3A)(H_2O)]_2\}^-$ (B).

A preparation of the tris-Gd complex by starting the reaction at much higher pH is not possible due to the formation of gadolinium hydroxide at pH > 5.9. We therefore decided to prepare $\{Mes[Gd(DO3A)(H_2O)_2]_3\}$ in two steps. In a first step we complex the ligand $Mes(DO3A)_3$ with a metal ion forming much weaker complexes than Gd^{3+}. A condition is that this metal should not form precipitating hydroxides at a pH at which only one or two amines of the DO3A are protonated (pH ~ 9).[35,36] In a second step this first complex is transformed to the final gadolinium compound by transmetallation at pH 5.8. We have chosen the Mg^{2+} ion to perform the first complexation step of **6**. Besides the much lower stability of DO3A complexes with 2+ ions[36] we selected the smallest alkali earth ion to disfavor binding of acetate groups from another DO3A chelate of **6** due to steric crowding around the cation. After adjusting the pH of the solution to 5.8 by adding NaOH a solution containing an excess of $GdCl_3$ was added. The advancement of the reaction has been followed by measuring the water proton relaxation rate $R_1 = 1/T_1$ at 30 MHz (Figure II.5). The relaxation rate drops after mixing and reaches a stable value after ~800 min. The pH of the mixture did not change during the transmetallation reaction. After eliminating the excess of Gd^{3+} and free Mg^{2+} ions by size exclusion chromatography a Gd^{3+}/ligand ratio of 2.96 has been determined by ICP-MS / elemental analysis.

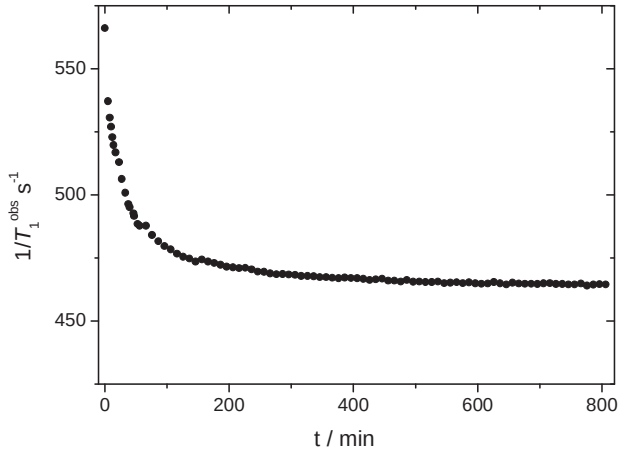

Figure II.5 – Transmetallation reaction from $\{Mes[Mg(DO3A)(H_2O)_x]_3\}^{3-}$ to $\{Mes[Gd(DO3A)(H_2O)_2]_3\}$ followed by ^1H NMR relaxation of water at 30 MHz and 25.0°C.

II.3.3. Structural transition induced by pH

In a simple experiment we tried to confirm the binding of two acetate groups of the uncomplexed DO3A to the two Gd^{3+} ions bound to the other two chelating groups. By replacing the paramagnetic lanthanide Gd^{3+} by the diamagnetic Y^{3+}, which has the same charge and a very similar ionic radius, we are able to measure the ^1H NMR spectrum of the bis-Y complex in D_2O solution. The ^1H NMR spectra are rather complex due to the presence of different geometrical isomers in slow exchange. At about neutral pH there are two relatively broad signals in the aromatic region at 7.09 ppm and 7.52 ppm corresponding to two main isomers of the bis-Gd complex, called isomer A and isomer B. Varying the pH of the solution by adding 2 M NaOD in D_2O shows an isomer transition, occurring between pH 3 and 5.6 and shifting the equilibrium from isomer B to A (Figure II.6). We attribute the isomer A to the closed, or capped, form of the bis-Y complex, *i.e.* with acetate groups bound to the Y^{3+}-ions as presented in Figure II.4 (B). Isomer B would correspond to the open form of the bis-Y complex with protonated and unbound acetate groups. The isomer transition would prove the formation of a closed conformation, unable to bind a third metal center at working pH. (4 to 5.8).

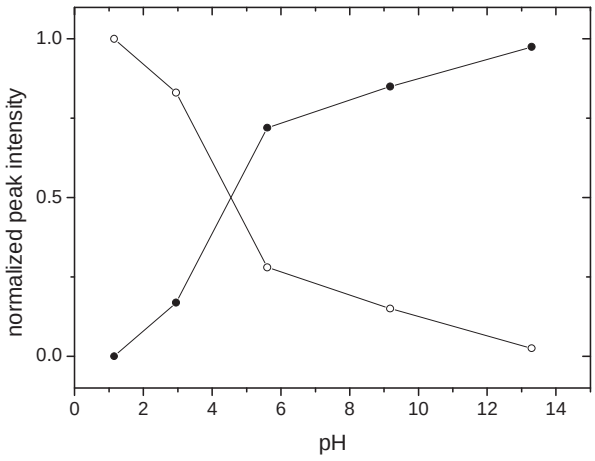

Figure II.6 – Normalized peak area of the aromatic ^{1}H NMR signals at 7.09 ppm (isomer A, ●) and 7.52 ppm (isomer B, ○) vs. pH for $\{Mes(H_2DO3A)[Y(DO3A)(H_2O)]_2\}^-$.

II.3.4. ^{1}H NMRD profiles

To characterize the relaxivity of the bis-Gd and tris-Gd complexes nuclear magnetic relaxation dispersion (NMRD) profiles of water protons have been measured at 25.0 °C and 37.0 °C (Figure II.7). Comparison of the relaxation enhancement at low Larmor frequencies (ν < 1 MHz) induced by 1 mM Gd^{3+} (relaxivity, r_1) shows that the relaxivity of the bis-Gd compound (Figure II.7 empty symbols) is about half of that of the tris-Gd compound (Figure II.7 filled symbols). Assuming similar relaxation rates of the Gd^{3+} electron spin for both compounds the only explanation for this difference in relaxivity is a change in the number q of coordinated water molecules.

It has been shown that $[Gd(DO3A)(H_2O)_q]$ shows an equilibrium between 8 and 9 coordination and q = 1.8 and 1.9 has been determined by UV-Vis spectroscopy and luminescence lifetime of $[Eu(DO3A)(H_2O)_q]$[15] and $[Tb(DO3A)(H_2O)_q]$[37], respectively. We can therefore conclude that in the tris-Gd complex two water molecules are directly bound to the cation (q = 2). For the bis-Gd complex two structures with two first coordinations sphere water molecules per compound are conceivable: the first one having one Gd^{3+} with q = 2 and one with q = 0 and the second one having two Gd^{3+} ions with q = 1. For the first compound the coordination sphere of the Gd^{3+} with q = 0 is completed by two acetate groups from the metal free DO3A. For the second compound each Gd^{3+} ion binds one acetate group of the free DO3A (Figure II.4 (B)). Molecular mechanics calculations (Chapter II.3.6) show that the first structure leads to high intramolecular strain if compared to the second structure. This

reinforces our assumption of the structure proposed in Figure II.4 (B) with coordination of acetate groups of the uncomplexed DO3A to each of the two gadolinium ions in $\{Mes(H_2DO3A)[Gd(DO3A)(H_2O)]_2\}^-$.

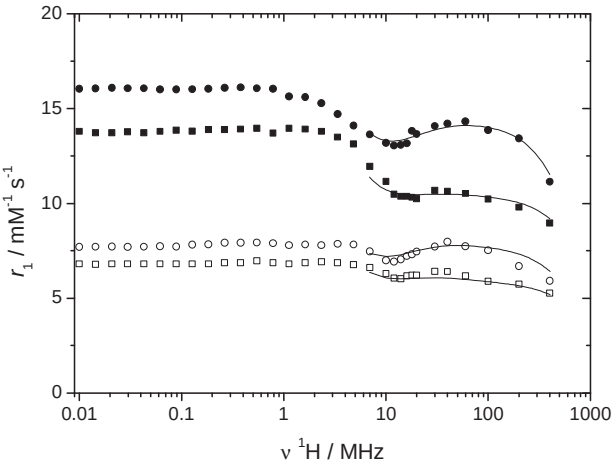

Figure II.7 – NMRD Profiles of the tris-Gd complex (filled symbols) and of the bis-Gd complex (empty symbols) at 25 ° C (○,●) and at 37°C (□,■). Lines calculated from a simultaneous fit of ^{1}H NMRD and ^{17}O NMR data using the parameters presented in Table II.1.

II.3.5. ^{17}O NMR spectroscopy

The longitudinal and transverse ^{17}O NMR relaxation enhancements as well as the ^{17}O NMR chemical shift differences, all with respect to acidified water, have been measured as a function of temperature. The reduced relaxation rates $1/T_{1r}$, $1/T_{2r}$, and the reduced chemical shift differences, $\Delta\omega_r$, are calculated by equations I.71 and I.72 and the results shown in Figure II.8. The mole fraction of bound water, P_M, has been calculated for the bis-Gd and the tris-Gd complexes using $q = 1$ and $q = 2$, respectively.

The ^{17}O paramagnetic chemical shift experienced by water molecules directly bound to gadolinium ions is governed by the scalar or Fermi contact term.[38] At high temperatures (T > 322 K, 1000/T < 3.1 K^{-1}) in the fast exchange regime the reduced chemical shift $\Delta\omega_r$ is directly given by the chemical shift of the bound water molecules, $\Delta\omega_M$.[2] Because $\Delta\omega_M$, which is proportional to the scalar coupling constant $A/\hbar$, is very similar for complexes with the same chelating unit,[11,15] it can be used to estimate the number of coordinated water molecules. From the chemical shift results in Figure II.8 it can be seen that the reduced shifts for bis-Gd and tris-Gd complexes are essentially the same. Because their values have been calculated

using q = 1 for bis-Gd and q = 2 for tris-Gd this confirms that the number of water molecules bound to the Gd^{3+} ions is different for the bis-Gd and tris-Gd complexes.

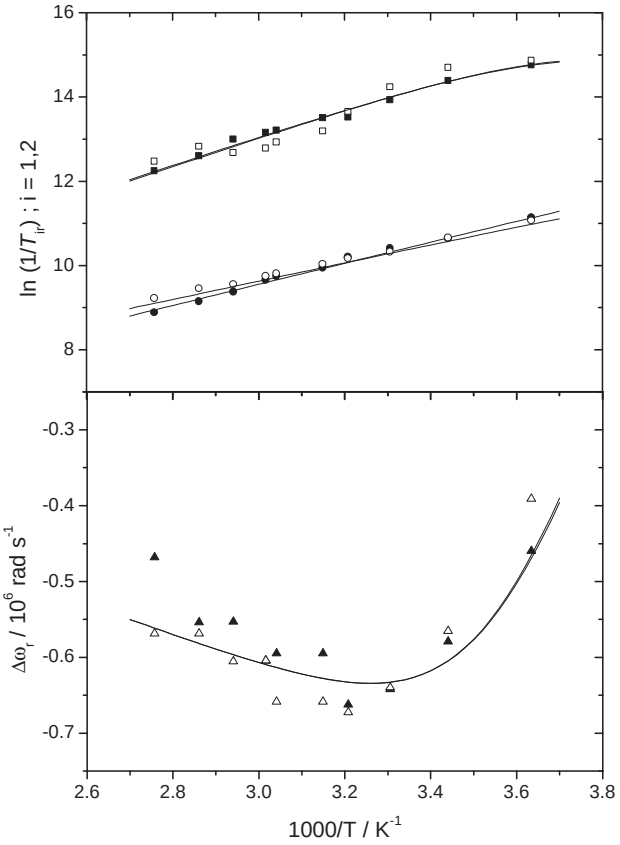

Figure II.8 – Reduced ^{17}O NMR relaxation rates $1/T_{2r}$ (■,□) and $1/T_{1r}$ (●, ○) and reduced chemical shifts, $\Delta\omega_r$ (▲,△), for the tris-Gd (filled symbols) and for the bis-Gd complex (open symbols). Lines calculated from the fitted parameters presented in Table II.1.

Like the chemical shift differences, the reduced enhancement of transverse ($1/T_{2r}$) and longitudinal ($1/T_{1r}$) relaxation are very similar for bis-Gd and tris-Gd (Figure II.8). The continuous decrease of $1/T_{2r}$ with increasing temperature is a clear indication that the water exchange is in the fast exchange regime.[39] The reduced ^{17}O NMR transverse relaxation rates, $1/T_{2r}$, are determined by the water exchange rate constant k_{ex}, the scalar relaxation of bound oxygen atoms and the chemical shift difference $\Delta\omega_M$.[39] Because the $1/T_{2r}$ values of bis-Gd and tris-Gd complexes are so similar we can conclude that the water exchange rates are the same over the temperature range of the study.

The quantitative analysis of the NMR data has been performed in two steps using the standard Solomon-Bloembergen-Morgan approach.[6] If we are not interested in detailed information

about the electron spin relaxation and if we restrict the data analysis to medium to high magnetic fields the SBM approach gives reliable information on dynamic processes like water exchange rate constants and rotational correlation times for small to mid-size complexes.[40] In a first step we fitted the ^{17}O relaxation rates and chemical shift data of both compounds together. We fixed the distance between Gd^{3+} and the water oxygen, r_{GdO}, to 2.5 Å. The nuclear quadrupole coupling constant, $\chi(1+\eta^2/3)^{1/2}$, has been fixed to the value of neat water, 7.58 MHz. From the fit we obtained for the exchange rate constant $k_{ex}^{298} = 3.2\times10^7$ s^{-1} and $\Delta H^{\ddagger} = 25.8$ kJ mol^{-1}. A mean rotational correlation time $\tau_R^{298} = 212$ ps ($E_R = 19.7$ kJ mol^{-1}) has been calculated from the longitudinal ^{17}O spin relaxation.

In a second step we fitted the ^{17}O NMR data together with the high frequency ^1H relaxivity ($\nu(^1H) > 6$ MHz) in separate fits for bis-Gd and tris-Gd. In these separate fits we fixed the exchange rate constant and activation enthalpy to the values obtained from the ^{17}O NMR data analysis. The water proton-Gd distance, r_{GdH}, and parameters defining the outer sphere contribution to the ^1H relaxivity have been fixed to common values (Table II.1). Rotational correlation times and parameters defining the electron spin relaxation (Δ^2, the amplitude of the transient zero-field splitting, and τ_v, the correlation time for the transient zero-field splitting) are obtained from the two fits (Table II.1). The reasonable quality of the fits (calculated curves in Figure II.7 and Figure II.8) confirms once again the difference in water coordination numbers q of the two compounds.

The water exchange rate constant is surprising in two aspects. First of all it is unexpected that the water exchange rates in the bis-Gd and the tris-Gd compounds are so similar. If we accept the coordination of one of the acetate to the Gd^{3+} ion as proposed above the coordination number of gadolinium is nine at all coordination sites in the two compounds. The local electric charge is however different since an acetate oxygen is more negatively charged than a water oxygen. This should lead to a marked difference.[2,41,42] As a general trend it has been found that a higher negative overall charge favors the departure of the water molecule in a dissociative process.[42] We expected therefore a faster exchange on the negatively charged $\{Mes(H_2DO3A)[Gd(DO3A)(H_2O)]_2\}^-$ with respect to the neutral $\{Mes[Gd(DO3A)(H_2O)_2]_3\}$. This is clearly not observed. The second unexpected result is the fast water exchange due to the low activation enthalpy ($\Delta H^{\ddagger} = 25.8$ kJ mol^{-1}). The water exchange rate constant on $[Gd(DO3A)(H_2O)_2]$ has been measured to 11×10^6 s^{-1} which is about three times slower.[15]

Terreno *et al*[43] concluded from two DO3A derivatives that the water exchange rate is modulated by the basicity of the macrocylic nitrogen atom bearing the pendant group: a lower basicity results in a slower water exchange rate. The fastest exchange rate constant measured (k_{ex}^{298} = 17.6×10^6 s^{-1} on [Gd(NH$_2$PhDO3A)(H$_2$O)$_2$]) is about 1.8 times slower than our exchange rate. Botta et al[44] measured a 1.7 times faster water exchange on a substituted DO3A complex (Figure II.4 (B)) which has also q = 2. The activation entropy is negative ($\Delta S^{\ddagger}$ = -14.7 J K^{-1} mol^{-1}) suggesting a change in mechanism from dissociative activation to associative activation. This would mean that for both compounds an incoming water molecule helps the bound water molecule to leave the first coordination sphere.

Parameters / complex	bis-Gd	tris-Gd
q	**1**	**2**
E_R / kJ mol^{-1}	18 ± 1	20.9 ± 0.5
τ_R^{298} / ps	193 ± 4	201 ± 2
τ_v^{298} / ps	18.5 ± 4	10.9 ± 1
Δ^2 / 10^{20} s^{-2}	0.38 ± 0.04	0.19 ± 0.01
k_{ex}^{298} / 10^6 s^{-1}	<u>32 ± 3</u>	
$\Delta H^{\ddagger}$ / kJ mol^{-1}	<u>25.8 ± 1.2</u>	
$\Delta S^{\ddagger}$ / kJ mol^{-1}	<u>-14.7 ± 4</u>	
$A/\hbar$ / 10^6 rad^{-1}	<u>-3.1 ± 0.2</u>	
r_{GdO} / Å	**2.5**	
r_{GdH} / Å	**3.1**	
$\chi(1+\eta^2/3)^{1/2}$ / MHz	**7.58**	
d_{GdH} / Å	**3.6**	
D_{GdH}^{298} / 10^{-5} cm^2 s^{-1}	**2.5**	
E_{GdH} / kJ mol^{-1}	**20**	
E_v / kJ mol^{-1}	**1**	

Table II.1 – Parameters obtained from the simultaneous fits of the ^{17}O NMR and the ^{1}H NMRD data, using the Solomon-Bloembergen-Morgan approach. Underlined values obtained from the preliminary ^{17}O NMR fit. Bold values fixed.

II.3.6. Molecular modeling

Simple molecular mechanics studies have been performed to evaluate different theoretical structures for $[Mes\{H_2DO3A\}\{Gd(DO3A)(H_2O)\}_2]^-$. The first structure minimized is shown in Figure II.9 (A). The structure corresponds to that proposed in Figure II.4 (B) : two carboxylates from the uncomplexed DO3A-unit bind to two different Y^{3+} ions on the two other DO3A. Each Y^{3+} ion has one water molecule in the first coordination sphere. This structure corresponds to the lowest energy of all minimized structures (-2363 kcal / mol).

The second structure (Figure II.9 (B)) was obtained by starting with a configuration with two carboxylates bound to the same Y^{3+}. The second Y^{3+} has two water molecules in the first coordination sphere. This structure could only be minimized by introducing a hydrogen bond between the ion and a carboxylate oxygen. The energy of this conformation is 481 kcal / mol higher than that of Figure II.9 (A).

The conformation shown in Figure II.9 (C) is obtained by deleting the weak Y^{3+}-O bond introduced in Figure II.9 (B) followed by energy minimization. One of the two acetates leaves the first coordination sphere of the Y^{3+}. The energy of conformation (C) is 288 kcal / mol higher than that of conformation (A). If the second weak bond is also deleted the carboxylate stays in the first coordination sphere but the energy decreases again and the difference to (A) is now +98 kcal / mol.

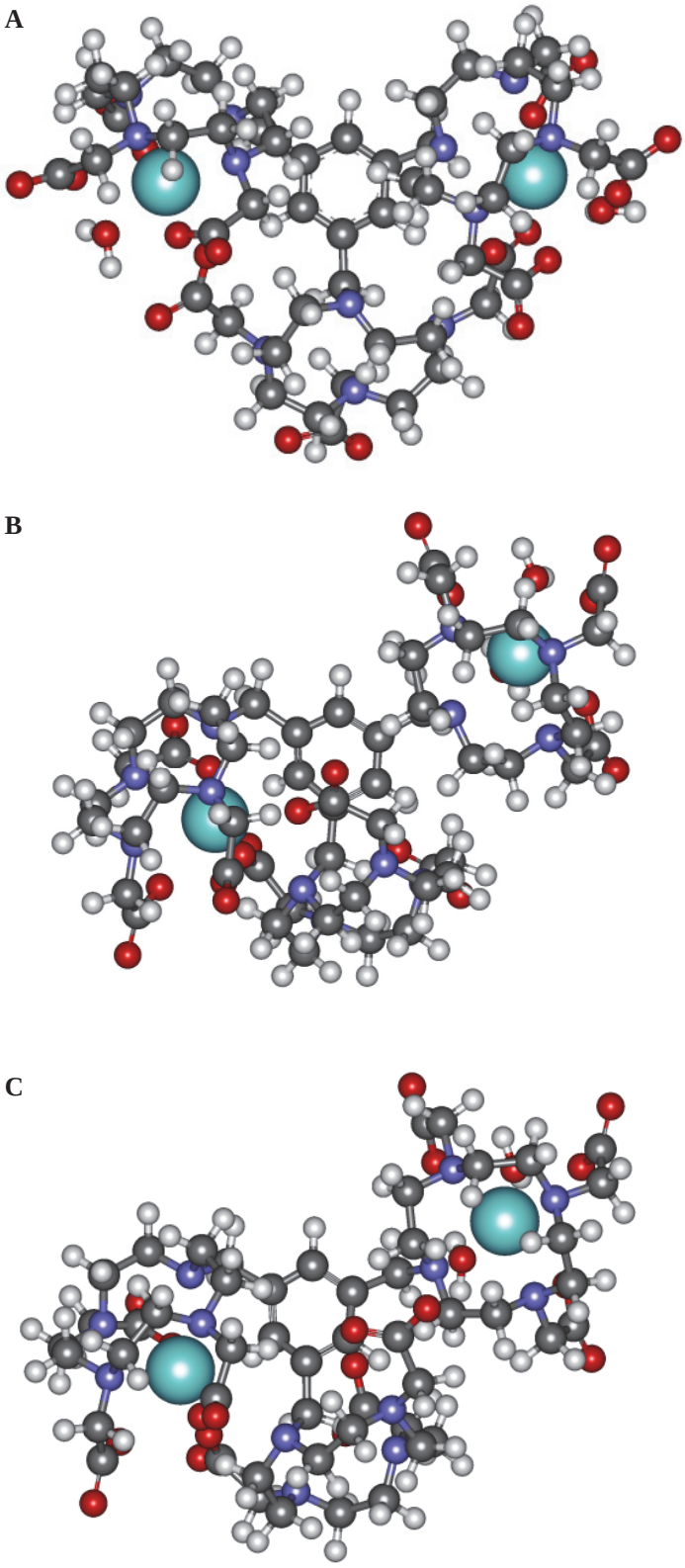

Figure II.9 – Structures of $\{Mes(H_2DO3A)[Gd(DO3A)(H_2O)]_2\}^-$ from molecular mechanics using MM3 force field. All structures have been minimized in a drop of 393 water molecules.

II.4. Conclusion

In order to develop new high field MRI contrast agents based on small molecules bearing multiple Gd^{3+} complexes, we synthesized the novel ligand $Mes(DO3A)_3$. Its trinuclear complex with Gd^{3+} was characterized and a relaxivity of 10.2 mM^{-1} s^{-1} (13.7 mM^{-1} s^{-1}) has been determined at 20 MHz and 37°C (25°C). This relaxivity is slightly higher than that measured for similar trimeric compounds (see, for example, Table 21 in Caravan *et al.*[41]). The complexation of the ligand was however not straightforward since the classical method lead to the undesired binuclear chelate complex $\{Mes(H_2DO3A)[Gd(DO3A)(H_2O)]_2\}^-$. This has been seen through the ^1H NMR relaxivities r_1 and the reduced ^{17}O NMR chemical shifts $\Delta\omega_r$. Surprisingly, water exchange rate on both complexes, the negatively charged $\{Mes(H_2DO3A)[Gd(DO3A)(H_2O)]_2\}^-$ with $q = 1$ and the neutral $\{Mes[Gd(DO3A)(H_2O)_2]_3\}$ with $q = 2$, is very similar. The measured rate constant is among the highest found so far on DO3A-type Gd-complexes (Table II.2).

To achieve the complete complexation, we had to develop a new alternative method, using pre-complexation with Mg^{2+} and transmetallation. This complexation method turned out to be very efficient to sidestep the coordination of neighboring chelating units preventing the complete complexation. The vicinity of the chelators in this mide-size molecule and the use of cyclic chelating unit, whose complexation kinetics are slow, have probably favored the coordination of neighboring carboxylate groups.

Compound	q	k_{ex}^{298} 10^6 s^{-1}	$\Delta H^{\ddagger}$ kJ mol^{-1}	$\Delta S^{\ddagger}$ kJ mol^{-1}	Ref
Mononuclear					
$[Gd(DO3A)(H_2O)_q]$	1.9	11	33.6	+2	[15]
$[Gd(NO_2PhDO3A)(H_2O)_q]$	1	7.4	33.8	(0) [a]	[43]
$[Gd(NH_2PhDO3A)(H_2O)_q]$	1	17.6	36.2	(+15.2) [a]	[43]
$[Gd(B\text{-}DO3A)(H_2O)_q]$ [b]	2	55	40.8	(+40.1) [a]	[44]
Dinuclear					
$\{pip[Gd(DO3A)(H_2O)_q]_2\}$	2	1.5	34.2	-12	[14]
$\{bisoxa[Gd(DO3A)(H_2O)_q]_2\}$	2	1.4	38.5	+2	[14]
$\{pX[Gd(DO3A)(H_2O)_q]_2\}$	1	7.5	45.9	+41	[11]
$\{mX[Gd(DO3A)\ (H_2O)_q]_2\}$	1	11	41.0	+28	[11]
$\{mX(COOH)[Gd(DO3A)(H_2O)_q]_2\}$	1	12	32.7	+0.3	[11]
$\{Mes(H_2DO3A)[Gd(DO3A)(H_2O)]_2\}^-$	1	32	25.8	-14.7	
Trinuclear					
$\{Mes[Gd(DO3A)(H_2O)_q]_3\}$	2	32	25.8	-14.7	

[a] Calculated from k_{ex}^{298} and $\Delta H^{\ddagger}$. [b] Ligand 5 in ref. [44].

Table II.2 – Hydration numbers *q*, water exchange rates k_{ex}^{298}, activation enthalpies $\Delta H^{\ddagger}$ and activation entropies $\Delta S^{\ddagger}$ for a selection of DO3A-type Gd chelates.

II.5. Acknowledgements

I warmly thank the following persons for their essential contributions to this work :

Pascal Miéville for his excellent work in our laboratory. His ability, ideas and experience have been really precious and greatly appreciated.

Dr. Raphaël Tripier and Dr. Felipe Reviriego for the synthesis of the ligand $Mes(DO3A)_3$.

Prof. Lothar Helm for the molecular modeling calculations.

II.6. References

1. Laurent, S.; Elst, L. V.; Muller, R. N. *Contrast Media & Molecular Imaging* **2006,** *1*, 128-137.
2. Toth, E.; Helm, L.; Merbach, A. E. In *The Chemistry of Contrast Agents in Medical Magnetic Resonance Imaging;* Merbach, A. E.; Toth, E. Eds.; John Wiley & Sons, Ltd: Chichester, 2001; pp. 45-119.
3. Caravan, P. *Chem. Soc. Rev* **2006,** *35*, 512-523.
4. Trattnig, S.; Pinker, K.; Ba-Ssalamah, A.; Nobauer-Huhmann, I. M. *European Radiology* **2006,** *16*, 1280-1287.
5. Toth, E.; Helm, L.; Merbach, A. E. In *Top. Curr. Chem.;* Krause, W. Ed.; Springer-Verlag: Heidelberg, 2002; pp. 61-101.
6. Kowalewski, J.; Kruk, D.; Parigi, G. In *Advances in Inorganic Chemistry;* van Eldik, R.; Bertini, I. Eds.: San Diego, 2005; pp. 41-104.
7. Helm, L. *Progress in Nuclear Magnetic Resonance Spectroscopy* **2006,** *49*, 45-64.
8. Helm, L. *Future Medicinal Chemistry* **2010,** *2*, 385-396.
9. Caravan, P.; Farrar, C. T.; Frullano, L.; Uppal, R. *Contrast Media & Molecular Imaging* **2009,** *4*, 89-100.
10. Costa, J.; Toth, E.; Helm, L.; Merbach, A. E. *Inorganic Chemistry* **2005,** *44*, 4747-4755.
11. Costa, J.; Balogh, E.; Turcry, V.; Tripier, R.; Le Baccon, M.; Chuburu, F.; Handel, H.; Helm, L.; Toth, E.; Merbach, A. E. *Chemistry-a European Journal* **2006,** *12*, 6841-6851.
12. Livramento, J. B.; Helm, L.; Sour, A.; O'Neil, C.; Merbach, A. E.; Tóth, É. *Dalton Transactions* **2008**, 1195-1202.
13. Toth, E.; Vauthey, S.; Pubanz, D.; Merbach, A. E. *Inorganic Chemistry* **1996,** *35*, 3375-3379.
14. Powell, D. H.; Ni Dhubhghaill, O. M.; Pubanz, D.; Helm, L.; Lebedev, Y. S.; Schlaepfer, W.; Merbach, A. E. *Journal of the American Chemical Society* **1996,** *118*, 9333-9346.
15. Toth, E.; Ni Dhubhghaill, O. M.; Besson, G.; Helm, L.; Merbach, A. E. *Magnetic Resonance in Chemistry* **1999,** *37*, 701-708.

16. Develay, S.; Tripier, R.; Le Baccon, M.; Patinec, V.; Serratrice, G.; Handel, H. *Dalton Transactions* **2006**, 3418-3426.
17. Bernier, N.; Allali, M.; Tripier, R.; Conan, F.; Patinec, V.; Develay, S.; Le Baccon, M.; Handel, H. *New Journal of Chemistry* **2006,** *30*, 435-441.
18. Develay, S.; Tripier, R.; Bernier, N.; Le Baccon, M.; Patinec, V.; Serratrice, G.; Handel, H. *Dalton Transactions* **2007**, 1038-1046.
19. Delepine, A. S.; Tripier, R.; Handel, H. *Organic & Biomolecular Chemistry* **2008,** *6*, 1743-1750.
20. Corsi, D. M.; Platas-Iglesias, C.; Bekkum, H. v.; Peters, J. A. *Magnetic Resonance in Chemistry* **2001,** *39*, 723-726.
21. Ferrante, G.; Sykora, S. In *Advances in Inorganic Chemistry;* van Eldik, R.; Bertini, I. Eds.: San Diego, 2005; pp. 405-470.
22. Vold, R. L.; Waugh, J. S.; Klein, M. P.; Phelps, D. E. *Journal of Chemical Physics* **1968,** *48*, 3831-&.
23. Farrar, T. C.; Becker, E. D. *Pulse and Fourier Transform NMR. Introduction to Theory and Methods*; Academic, 1971.
24. Meiboom, S.; Gill, D. *Review of Scientific Instruments* **1958,** *29*, 688-691.
25. Hugi, A. D.; Helm, L.; Merbach, A. E. *Helvetica Chimica Acta* **1985,** *68*, 508-521.
26. Ammann, C.; Meier, P.; Merbach, A. E. *Journal of Magnetic Resonance* **1982,** *46*, 319-321.
27. Yerly, F. *OPTIMISEUR 3.0.0* **2002,** *EPFL*.
28. Yerly, F. *VISUALISEUR 2.3.6* **2004,** *EPFL*.
29. Kotek, J.; Hermann, P.; Vojtisek, P.; Rohovec, J.; Lukes, I. *Collection of Czechoslovak Chemical Communications* **2000,** *65*, 243-266.
30. Le Baccon, M.; Chuburu, F.; Toupet, L.; Handel, H.; Soibinet, M.; Dechamps-Olivier, I.; Barbiere, J. P.; Aplincourt, M. *New Journal of Chemistry* **2001,** *25*, 1168-1174.
31. Develay, S. P.; Tripier, R.; Chuburu, F.; Le Baccon, M.; Handel, H. *European Journal of Organic Chemistry* **2003**, 3047-3050.
32. Chuburu, F.; Tripier, R.; Le Baccon, M.; Handel, H. *European Journal of Organic Chemistry* **2003**, 1050-1055.
33. Weisman, G. R.; Rogers, M. E.; Wong, E. H.; Jasinski, J. P.; Paight, E. S. *Journal of the American Chemical Society* **1990,** *112*, 8604-8605.
34. Desreux, J. F.; Merciny, E.; Loncin, M. F. *Inorganic Chemistry* **1981,** *20*, 987-991.

35. Kumar, K.; Chang, C. A.; Francesconi, L. C.; Dischino, D. D.; Malley, M. F.; Gougoutas, J. Z.; Tweedle, M. F. *Inorganic Chemistry* **1994,** *33*, 3567-3575.
36. Kumar, K.; Tweedle, M. F.; Malley, M. F.; Gougoutas, J. Z. *Inorganic Chemistry* **1995,** *34*, 6472-6480.
37. Zhang, X.; Chang, C. A.; Brittain, H. G.; Garrison, J. M.; Telser, J.; Tweedle, M. F. *Inorganic Chemistry* **1992,** *31*, 5597-5600.
38. Yazyev, O. V.; Helm, L. *Journal of Chemical Physics* **2007,** *127*, 084506/1-8.
39. Helm, L.; Nicolle, G. M.; Merbach, A. E. In *Advances in Inorganic Chemistry;* van Eldik, R.; Bertini, I. Eds.: San Diego, 2005; pp. 327-379.
40. Fries, P. H.; Belorizky, E. *Journal of Chemical Physics* **2005,** *123*.
41. Caravan, P.; Ellison, J. J.; McMurry, T. J.; Lauffer, R. B. *Chemical Reviews* **1999,** *99*, 2293-2352.
42. Hermann, P.; Kotek, J.; Kubicek, V.; Lukes, I. *Dalton Transactions* **2008**, 3027-3047.
43. Terreno, E.; Boniforte, P.; Botta, M.; Fedeli, F.; Milone, L.; Mortillaro, A.; Aime, S. *European Journal of Inorganic Chemistry* **2003**, 3530-3533.
44. Botta, M.; Quici, S.; Pozzi, G.; Marzanni, G.; Pagliarin, R.; Barra, S.; Crich, S. G. *Organic & Biomolecular Chemistry* **2004,** *2*, 570-577.

Chapter III :

Dynamic aggregation of the mid-size gadolinium complex $\{Ph_4[Gd(DTTA)(H_2O)_2]^-_3\}$

III.1 Introduction 81
III.2 Experimental Section 84
III.2.1 Ligand synthesis and characterization 84
III.2.2 Sample preparation 86
III.2.3 ^{1}H relaxivities 87
III.2.4 ^{17}O NMR spectroscopy 87
III.2.5 Data treatment 88
III.2.6 Molecular modeling 88
III.3 Results and discussion 89
III.3.1. Ligand synthesis 89
III.3.2. Concentration effect 90
III.3.3. ^{1}H NMRD profiles 92
III.3.4. ^{17}O NMR spectroscopy 92
III.3.5. ^{17}O and ^{1}H NMR data fittings with SB-LS-RFB 94
III.3.6. ^{1}H NMRD data fittings with the modified Florence approach 98
III.3.7. Aggregate size estimation 101
III.3.8. ^{1}H relaxivity as a function of pH 103
III.3.9. ^{1}H relaxivity in presence of phosphate buffer 103
III.3.10. ^{1}H relaxivity in presence of human serum 104
III.4 Conclusion 106
III.5 Acknowledgements 108
III.6 References 109

III.1 Introduction

The two last decades have witnessed tremendous effort and successful progress in the optimization of the efficiency of magnetic resonance imaging (MRI) T_1 contrast agents (CA). The latter are constituted by paramagnetic metal chelate complexes, mainly gadolinium (III) chelated with cyclic or acyclic poly(amino caboxylate) ligands, that increase the relaxation rate of the water protons. The efficiency of a contrast agent, called the relaxivity r_1, depends on the electronic relaxation of the metal center, on the number of water molecules in the inner sphere of the complex and their exchange rate, and finally on the rotational correlation time τ_R, linked to the size of the molecule.

The rotational correlation time is the predominant parameter of the relaxivity from about 10 to 200 MHz, as illustrated in Figure III.1. This range, typically 64 MHz (1.5 T), corresponded until a few years ago to the working frequencies of most medical MRI magnets.[1] The optimization of the efficiency of MRI CA had then to go through big and slowly tumbling molecules and many developments had been achieved with the intention of augmenting the molecular size.

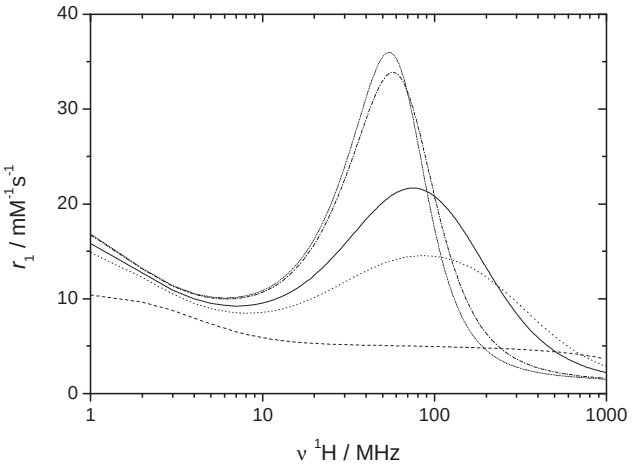

Figure III.1 – Simulated effect of the rotational correlation time on the relaxivity as a function of the Larmor frequency, calculated by SBM for τ_R = 0.1 ns (dash), 0.5 ns (dot), 1 ns (straight), 5 ns (dash dot) and 10 ns (short dot). Other parameters : τ_M = 100 ns; τ_v = 10 ps; $\Delta^2 = 0.5 \cdot 10^{20}$ s^{-2}; q = 1.

With the technological progress of the magnets however, developed to counteract the relative low sensitivity of NMR and MRI, these big CA became less and less effective with the increasing of the MRI magnetic field (Figure III.1). MRI high-field magnets (3T, 127 MHz) for human medical use became commercially available since approximately 1998,[1,2] the first results performed on human using a 9.4 T magnet (400 MHz) were published in 2006,[3] and the upcoming French brain imaging center NeuroSpin announce a 17 T (724 MHz) research murine magnet and a 11.7 T (500 MHz) human medical magnet.[4] In order to optimize their efficiency towards current technological march, contrast agents whose rotational correlation times ranges from 0.5 to 1 ns are nowadays developed (Figure III.1).

Though the efficiency of CA is characterized by the relaxivity, defined as the relaxation rate enhancement induced by 1 mM of the paramagnetic species, the density of metal complexes plays also an important role on the effect on the relaxation time. The term "density of relaxivity" is used to describe the efficiency of CA per unit of mass. From this perspective, many studies have been carried out on the purpose to develop mid-size compounds bearing several coordination sites, with central benzene[5-8] or metal[9-12] core.

Within this framework, Costa *et al.* described unusual systems, constituted by two $DO3A^{3-}$ chelating units linked in *meta* and *para* to a central xylene core, presenting exceptionally high relaxivities for mid-size molecules (Figure III.2) ($DO3A^{3-}$ = 1,4,7,10-tetraazacyclododecane-1,4,7-triacetate).[6] Self-aggregations, constituted of about ten "monomers", were proved to be accountable for these unexpected relaxivities. As such aggregates have not been observed in non-aromatic dimeric Gd^{3+} complexes,[13,14] the intermolecular interactions result most probably from π-stacking of the aromatic core, though other hydrophobic interactions or hydrogen bonding can not be excluded.

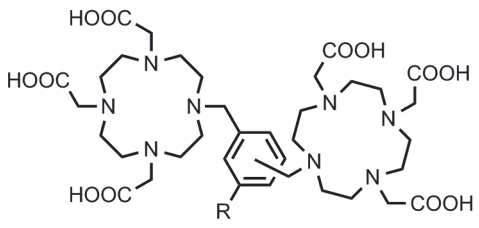

Figure III.2 **–** Costa *et al.* aggregating systems, with R = H (DO3A in meta and para positions) and R = COOH (DO3A in 3,5-meta position)

In line with this project, this chapter presents the molecule Ph_4DTTA_3 (1,3,5-tris-{4-[(bis{2-[bis(carboxymethyl)amino]ethyl}amino)methyl]phenyl}benzene), composed by three heptadentate DTTA chelating moieties around a central core constituted by four benzene rings. The aromatic central core has been designed specially to favor formation of aggregates, thought to be induced by strong π-stacking intermolecular interactions. We report here the synthesis of the ligand and the relaxometric characterization of its Gd^{3+} complexes of this compound designed as a potential MRI contrast agent (Figure III.3).

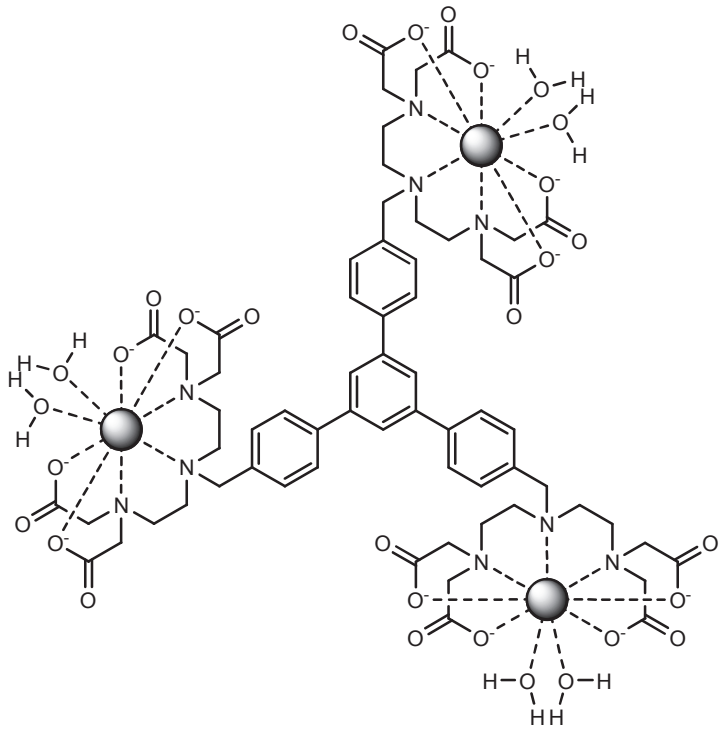

Figure III.3 **–** The gadolinium (III) complex {$Ph_4[Gd(DTTA)(H_2O)_2]^-_3$}

III.2 Experimental Section

III.2.1 Ligand synthesis and characterization

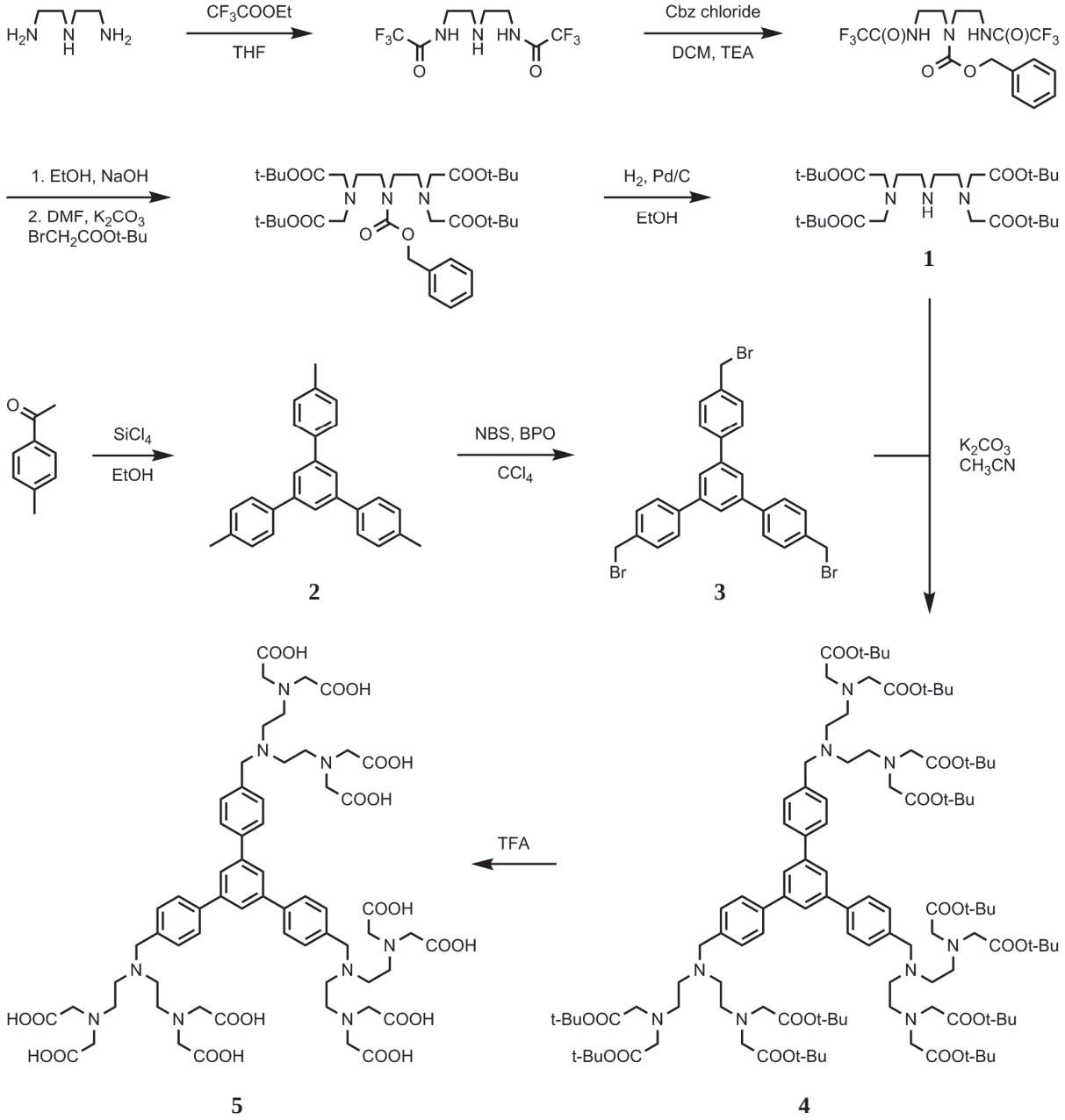

Figure III.4 **–** Ph_4DTTA_3 synthesis scheme

All chemicals were purchased from high quality grade chemical sources (Sigma-Adrich, Acros) and were used as received without purification.

All ^1H and ^{13}C NMR spectra were recorded on a Bruker DRX-400 spectrometer (9.4 T). Mass Spectrometry analyses were performed on a Thermo Fischer TSQ7000 spectrometer using ESI ion source. HPLC purifications were performed on a Dionex system made up of a UVD 170U detector and a P580 Pump, using a Sunfire™ Prep C_{18} OBD™ 5 μm column (19 x 150 mM). Elemental analysis was performed by Dr. Euro Solari at the Elemental Analysis Service at ISIC, EPFL.

Synthesis of *tert*-butyl 2,2',2'',2'''-[iminobis(ethane-2,1-diylnitrilo)]tetraacetate (1)

This compound, referred as or DTTA+, was synthesized according to literature.[15,7]

Synthesis of 1,3,5-tris-(4-methylphenyl)benzene (2) and 1,3,5-tris-(4-bromomethylphenyl)benzene (3)

These compounds, referred as Ph_4Me_3 and Ph_4Br_3 respectively, were synthesized according to literature.[16-19]

Synthesis of 1,3,5-tris-{4-[(bis{2-[bis(*tert*-butyl acetate)amino]ethyl}amino)methyl] phenyl}benzene (4)

This compound will be referred as Ph_4DTTA+_3. 1.83 g (3.27 mmol) of DTTA+ (**1**) was dissolved in 90 ml of dry DMF. 608.7 mg (1.040 mmol) of 1,3,5-tris-(4-bromomethylphenyl)benzene (**3**), dissolved in 10 mL of dry DMF, were added dropwise under argon atmosphere. The reaction mixture was stirred overnight at 55°C and evaporated to dryness. The residue was dissolved in 200 ml of DCM and washed three times with 100 ml of water. The organic phase was dried over sodium sulfate and evaporated to dryness. The crude product was purified by silica gel chromatography (DCM/MeOH 95:5) (R_f = 0.19). 212 mg (yield 10%) of pure compound (**4**) were obtained. ^1H-NMR ($CDCl_3$, 400 MHz) δ in ppm : 1.43 (s, 108 H), 2.67 (t, J undetermined, 12 H), 2.87 (t, J undetermined, 12 H), 3.43 (s, 24 H), 3.70 (s, 6H), 7.41 (d, J = 7.0 Hz, 6 H), 7.61 (d, J = 7.0 Hz, 6 H), 7.74 (s, 3 H). MS (ESI) m/z (%) : 675.1 (100) $[M+3H]^{3+}$, 1011.3 (5) $[M+2H]^{2+}$.

Synthesis of 1,3,5-tris-{4-[(bis{2-[bis(carboxymethyl)amino]ethyl}amino)methyl] phenyl}benzene (5)

This compound will be referred as Ph_4DTTA_3. 200 mg (99 μmol) of Ph_4DTTA+_3 (**4**) were dissolved in 5 ml of a 5% water in TFA solution and stirred for 3 h. The solvents were

removed by evaporation and the residue was washed with 10 ml of water and evaporated to dryness five times. The resulting solid was dissolved in 12 ml of a 0.1 M triethylammonium acetate buffer and purified on a C18 preparative HPLC column, using 0.1 M triethylammonium acetate buffer and a 0 to 60% in 30 minutes acetonitrile gradient as elution system. The pure fractions, eluted after 15.0 minutes, were collected, evaporated and washed until no triethylammonium acetate remained. 52 mg (39 μmol) of the pure product (**5**) were obtained (yield 39%). ^{1}H-NMR (D_2O, 400 MHz) δ in ppm : 2.99 (t, J undetermined, 12 H), 3.51 (t, J undetermined, 12 H), 3.69 (s, 24 H), 3.82 (s, 6 H), 7.54 (d, J = 6.7 Hz, 6 H), 7.80 (d, J = 6.4 Hz, 6H), 7.96 (s, 3 H). ^{13}C-NMR (D_2O, 54.3 MHz) δ in ppm : 47.38 (CH_2-N), 52.12 (CH_2-N), 56.73 (CH_2-CO), 57.64 (Ar-CH_2-N), 124.89 (CHAr), 127.69 (CH-CHAr), 130.51 (CH-CHAr), 135.91 (CAr), 139.96 (CAr), 141.55 (CAr), 170.34 (CO). MS (ESI) m/z (%) : 675.3 (100) $[M+2H]^{2+}$, 1349.5 (96) $[M+H]^{+}$. Elemental analysis calculated (%) for $[H_{15}Ph_4DTTA_3]^{3+}[Cl]^{-}_3$ ($C_{63}H_{84}Cl_3N_9O_{24}$) + 0.67 $[HNEt_3^{+}Cl^{-}]$ ($C_6H_{15}ClN$; integration of ^{1}H NMR peak) ($C_{67.03}H_{94.09}Cl_{3.67}N_{9.67}O_{24}$; 1549.64 g mol^{-1}) : C 51.96, H 6.12, N 8.74 ; found : C 52.15, H 6.05, N 8.64.

III.2.2 Sample preparation

The solid salt $GdCl_3 \cdot x\ H_2O$ ($x \approx 6.7$) was dissolved in H_2O to prepare the Gd^{3+} stock solution. The exact ion concentration was measured by complexometric titration using Na_2H_2EDTA 5 mM. Ph_4DTTA_3 solution was prepared in H_2O and the chelator concentration was determined by back titration of a Gd^{3+} excess with Na_2H_2EDTA 5 mM. The titrations were performed on a Metrohm 665 Dosimat, using xylenol orange as complexometric indicator and buffered at pH 5.8 with a 5% (w/v) urotropine solution in water. The complex $\{Ph_4[Gd(DTTA)(H_2O)_2]^{-}_3\}$ was prepared by adding a slight deficit of Gd^{3+} (2%) to the ligand solution. The pH was brought back to 5.8 with 0.1 M NaOH and the absence of free gadolinium was checked by the xylenol orange test. Finally, the exact final Gd^{3+} concentration was measured by bulk magnetic susceptibility (BMS)[20] at 23.3°C on a Bruker DRX-400 (9.4 T, 400 MHz) spectrometer. This was performed by measuring the shift of the *tert*-butanol alkyl protons in the paramagnetic environment compared to the diamagnetic reference contained in a coaxial NMR tube.

III.2.3 ^{1}H relaxivities

T_1 were determined by the inversion-recovery method[21] using the following equipment : Stelar Spinmaster Fast Field Cycling (FFC) NMR relaxometer[22] ($2.35 \cdot 10^{-4}$ to 0.47 T; ^{1}H Larmor frequencies : 0.01 to 20 MHz) equipped with a VTC90 temperature control unit, Bruker Minispec mq20 0.47 T (20 MHz), mq40 0.70 T (30 MHz), mq40 0.94 T (40 MHz) and mq60 1.41 T (60 MHz), Bruker Avance-200 console connected to a 2.35 T (100 MHz) and a 4.7 T (200 MHz) cryomagnets, Bruker Avance-II 9.4 T (400 MHz) and Bruker Avance-II 18.8 T (800 MHz). The spectrometers were equipped with Bruker BVT3000 temperature control units and Bruker BCU05 cooling units. All temperatures were measured by substitution techniques.[23] The relaxation rates $1/T_1$ were corrected by diamagnetic contributions of 0.366 s^{-1} and 0.326 s^{-1} for 25°C and 37°C respectively.

The $1/T_1$ NMRD profiles of {$Ph_4[Gd(DTTA)(H_2O)_2]^-_3$} were measured at 25.0°C (Gd^{3+} concentrations of 18.18 mM, 1.838 mM and 0.1010 mM) and 37.0°C (Gd^{3+} concentrations of 18.18 mM and 1.838 mM). Samples in 7.5 mm tubes were used on Bruker mq40s and mq60 while samples sealed in glass spheres adapted for 10 mm NMR tubes were used for all other instruments.

Relaxivities of {$Ph_4[Gd(DTTA)(H_2O)_2]^-_3$} ~ 0.77 mM solutions at six different pH between 4 and 7 were measured at 25°C and 30 MHz.

Relaxivities of {$Ph_4[Gd(DTTA)(H_2O)_2]^-_3$} ~ 2.25 mM solutions containing 0, 11, 21, 51, 116, 222 and 507 mM of phosphate buffer were measured at 25°C and 30 MHz 10 minutes after phosphate addition and then every 24h. The phosphate buffer was prepared from mono and dibasic sodium phosphate in order to obtain a final pH 5.8 solution. At the same time, the relaxivity of the 2.25 mM complex in human serum (32% w/w) (Human serum from human male AB plasma, Sigma-Aldrich) was measured in the same conditions.

III.2.4 ^{17}O NMR spectroscopy

Variable temperature ^{17}O NMR measurements were performed on a Bruker Avance-II 9.4 T (54.3 MHz) spectrometer, equipped with a Bruker BVT3000 temperature control unit and a Bruker BCU05 cooling unit. 10.5% ^{17}O-enriched water (Irakli Gverdtsiteli Research and

Technology Center on High Technologies and Super Pure Material LTD) was added to the sample to obtain a final 2% ^{17}O enrichment and a 15.37 mM Gd^{3+} concentration. The sample was sealed in a glass sphere adapted for 10 mm NMR tubes to avoid susceptibility corrections to the chemical shifts. Transverse and longitudinal relaxation rates, using the inversion-recovery[21] and the Carr-Purcell-Meiboom-Gill[24] pulse sequences respectively, and the chemical shift differences in comparison to the pH 3.5 water reference (1% ^{17}O enrichment) were measured at 11 different temperatures spread from -2°C to 89.9°C.

III.2.5 Data treatment

Simultaneous fit on the ^{1}H NMRD and ^{17}O NMR data using a Solomon-Bloembergen based theory[25-27] supplemented with the Lipari-Szabo free-model approach for the internal rotation[28,29] and the Rast-Fries-Belorizky model for electronic spin relaxation,[30] were performed on Visualiseur/Optimiseur[31,32] running on a MATLAB© 7.3.0 (R2006b) platform. This approach will be referred as SB-LS-RFB.

The fittings of the NMRD profiles using the "modified Florence approach"[33-35] calculations were performed with the "modified Florence program"[36] adapted to run on a MATLAB© 7.3.0 (R2006b) platform.

III.2.6 Molecular modeling

The molecular simulation was performed by molecular mechanics using the MM3 force field[37-39] with Scigress Explorer ™ Ultra 7.7.0.47.

III.3 Results and discussion

III.3.1. Ligand synthesis

The use of the chelator DTTA presents many advantages. First, this acyclic poly(amino carboxylate) is heptadentate, which allows two water molecules in the inner sphere of the Gd^{3+} complex (Figure III.5), and hence doubles its relaxivity. Then, the two water molecules in the complex are not adjacent which prevents complexation with bidentate salts, such as carbonate typically, and allows skipping of degassing steps. Finally, its synthesis using a succession of protection and deprotection is straightforward (four steps, Figure III.4), inexpensive, and leads to acceptable global yield (40%).[7] Though its stability would not allow human applications, this chelating unit is stable enough for *in vitro* or *in vivo* animal studies.[40]

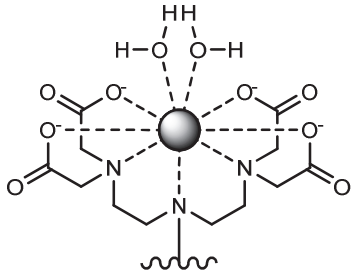

Figure III.5 **–** The Gd^{3+} chelating complex $[Gd(DTTA)(H_2O)_2]^-$

The overall synthesis route of the ligand Ph_4DTTA_3, presented on Figure III.4, consists in three major steps : the synthesis of the chelating unit DTTA (**1**), the synthesis of the central core Ph_4Br_3 (**3**) and their conjugation.

1,3,5-tris-(4-methylphenyl)benzene (**2**) is formed with good yield through the triple condensation of the 1-(4-methylphenyl)ethanone. The next step, the bromination of the methyl groups, using *N*-bromosuccinimide (NBS) and benzoyl peroxide (BPO) is more delicate. The exact quantity of NBS has to be added dropwise in order to brominate every methyl position and to avoid the massive formation of dibrominated methyl. The presence of side products, consisting of the compound **3** with unsubstituted, disubstituted or hydrolized (-

OH instead of -Br) methyl makes the separation arduous throughout the synthesis until the preparative HPLC purification.

The next step consists in the conjugation of the protected chelating moieties DTTA+ on the three alkyl halides of the core Ph_4Br_3 (**3**) in the presence of K_2CO_3. It gives the desired compound Ph_4DTTA+_3 (**4**), but its purification by chromatography, using a dichloromethane / methanol system and turned out to be laborious due to the presence of side products in the majority of the fractions. These impurities were essentially the compound **4** with one unsubsituted methyl, arising from its unbromination, or with hydroxymethyl, coming from hydrolyzation of unreacted bromide. This difficult separation, besides the three S_N2 reactions on the same molecule, explains the unexpected low yield (10%).

Finally, the *tert*-butyl protecting groups were removed by TFA to obtain the free acid Ph_4DTTA_3 (**5**). Due to the behavior of this compound, which precipitates in aqueous solutions with pH lower than 3, the purification of this step was here again fastidious. The cationic exchange resin, commonly used to purify poly(amino carboxylates), was not possible, while the anionic exchange resin as well as the size exclusion resin Sephadex^{TM} LH-20 turned out to be inefficient. The purification has finally been possible by preparative HPLC, using water with 0.1 M triethylammonium acetate as buffer and ion pairing agent in a water/acetonitrile system. ESI-MS analyses were performed with pure methanol without formic acid to prevent any precipitation in the capillary. Eventually, ligand **5** was isolated in 8 steps with an overall yield of 2 %.

III.3.2. Concentration effect

Early relaxivity measurements revealed exceptionally high values for a mid-size molecule. Moreover, the relaxivity turned out to be dependent on the concentration. As the electronic relaxation rate, the water exchange rate and the number of molecules in the inner sphere of the complex are supposed to be unaffected by the concentration, this concentration dependence has to be induced by the rotational correlation time τ_R, directly related to the size. The formation of dynamic intermolecular structures, such as aggregation by π-stacking, is probably the only way to explain the high relaxivities and their concentration dependence by increasing the rotational correlation time.

Figure III.6 shows the reproducible concentration-dependent relaxivities of two $\{Ph_4[Gd(DTTA)(H_2O)_2]^-_3\}$ systems issued from two different synthesis and complexations. To get a better idea of this effect, the results are presented in both linear and log scales. The evolution of the relaxivities with the Gd^{3+} concentration presents a sigmoid shape that can be described in three phases :

- A relaxivity stationary plateau around r_1 = 27 $mM^{-1}s^{-1}$ for Gd^{3+} concentrations up to 0.1 mM. This plateau indicates that the size of the entities does not significantly change for this concentration range. This could correspond to the monomeric species.
- A marked increase for Gd^{3+} concentrations between 0.1 and 1 mM. The formation of aggregates is favored in this concentration rate, and their size increase with the concentration.
- A flattening of the relaxivity enhancement for concentrations higher than 1 mM. The formation of bigger aggregates still occurs but their size increase less when augmenting the concentration.

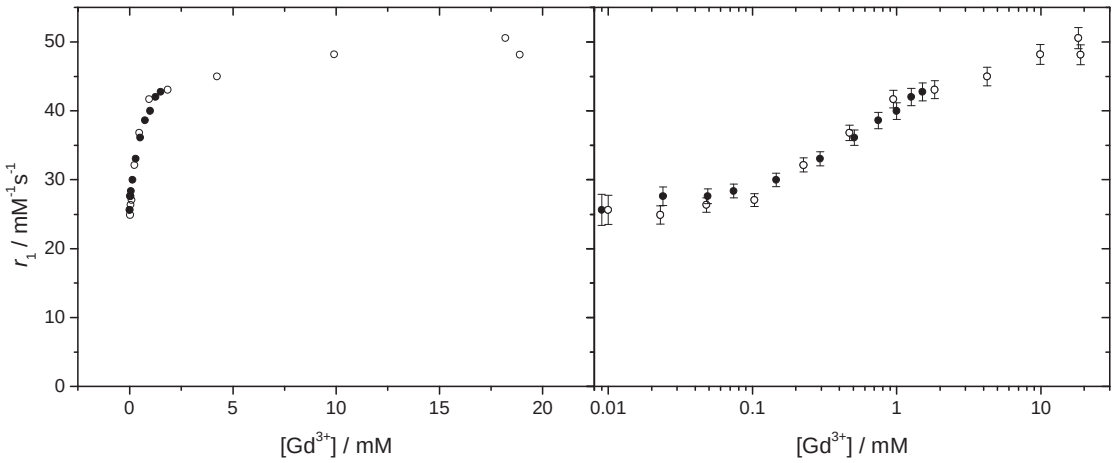

Figure III.6 – Concentration-dependent relaxivities r_1, in linear and log scales, of two different $\{Ph_4[Gd(DTTA)(H_2O)_2]^-_3\}$ systems (●) and (○) at 30 MHz, 25.0°C.

Calculations of the propagation of uncertainty (only shown on the log scale of Figure III.6) has been performed by considering a relative error of 3% on both the observed and the diamagnetic reference relaxation times and by assuming the Gd^{3+} concentration as being exact. The equation III.1 has been used to determine the relative error on the relaxivity r_1.

$$\frac{\Delta r_1}{r_1} = \frac{\Delta\left(\frac{1}{T_1^{obs}} - \frac{1}{T_1^{dia}}\right)}{\frac{1}{T_1^{obs}} - \frac{1}{T_1^{dia}}} = \frac{\sqrt{\left(\Delta\left(\frac{1}{T_1^{obs}}\right)\right)^2 + \left(\Delta\left(\frac{1}{T_1^{dia}}\right)\right)^2}}{\frac{1}{T_1^{obs}} - \frac{1}{T_1^{dia}}} = \frac{\sqrt{\left(\frac{\Delta T_1^{obs}}{\left(T_1^{obs}\right)^2}\right)^2 + \left(\frac{\Delta T_1^{dia}}{\left(T_1^{dia}\right)^2}\right)^2}}{\frac{1}{T_1^{obs}} - \frac{1}{T_1^{dia}}} \qquad \text{(III.1)}$$

III.3.3. ^{1}H NMRD profiles

The concentration dependence of the size of the entities, and hence their relaxivities, leads to typical NMRD profiles for each concentration. This is exemplified by Figure III.7 showing the NMRD profiles at 25°C of the system for Gd^{3+} concentrations of 0.101 mM, 1.84 mM and 18.2 mM. The shape of the profiles, particularly the relaxivity humps between 10 and 100 MHz, flat for the diluted and steep for the concentrated samples, the increasing hump amplitude with the concentration and the shift of the hump maximum are strong evidences for a change of the size of the particles with the concentration (see Figure III.1). The complete NMRD profiles at 25°C and 37°C are independently presented in Figure III.8. Due to the very short relaxation times (about 1 ms), T_1 measurements on the 18.2 mM sample were not achievable on the FFC relaxometer, *i.e.* from 0.01 to 16 MHz. The NMRD profiles of this sample were therefore measured only from 20 to 800 MHz.

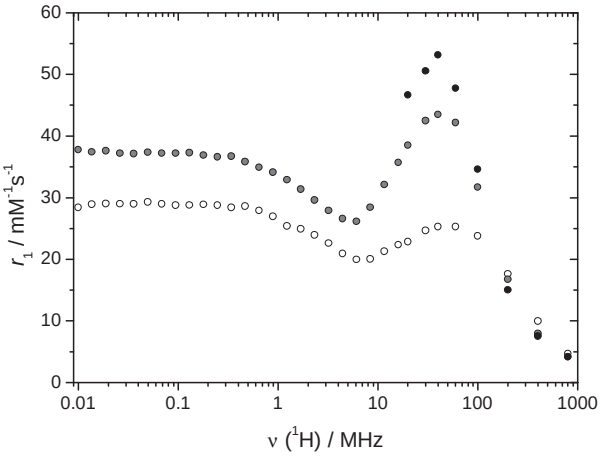

Figure III.7 **–** NMRD profiles of $\{Ph_4[Gd(DTTA)(H_2O)_2]^-_3\}$ at 25°C for 0.101 mM (○), 1.84 mM (◉) and 18.2 mM (●) samples.

III.3.4. ^{17}O NMR spectroscopy

This experiment was achieved to allow a simultaneous fit of ^{17}O NMR data with ^{1}H NMRD data of the concentrated samples. This allows the determination of several parameters common to all systems, whatever the concentration. The variable temperature ^{17}O NMR

measurements, performed on a 15.4 mM sample, are presented on Figure III.9. The reduced relaxation rates T_{1r} and T_{2r} and the reduced chemical shift differences $\Delta\omega_r$ are calculated using equations I.71 and I.72. All values were calculated with respect to acidic water, interpolated reference chemical shifts were used for the calculation of $\Delta\omega_r$. The number of water molecules in the inner sphere of the complex q was fixed to 2.

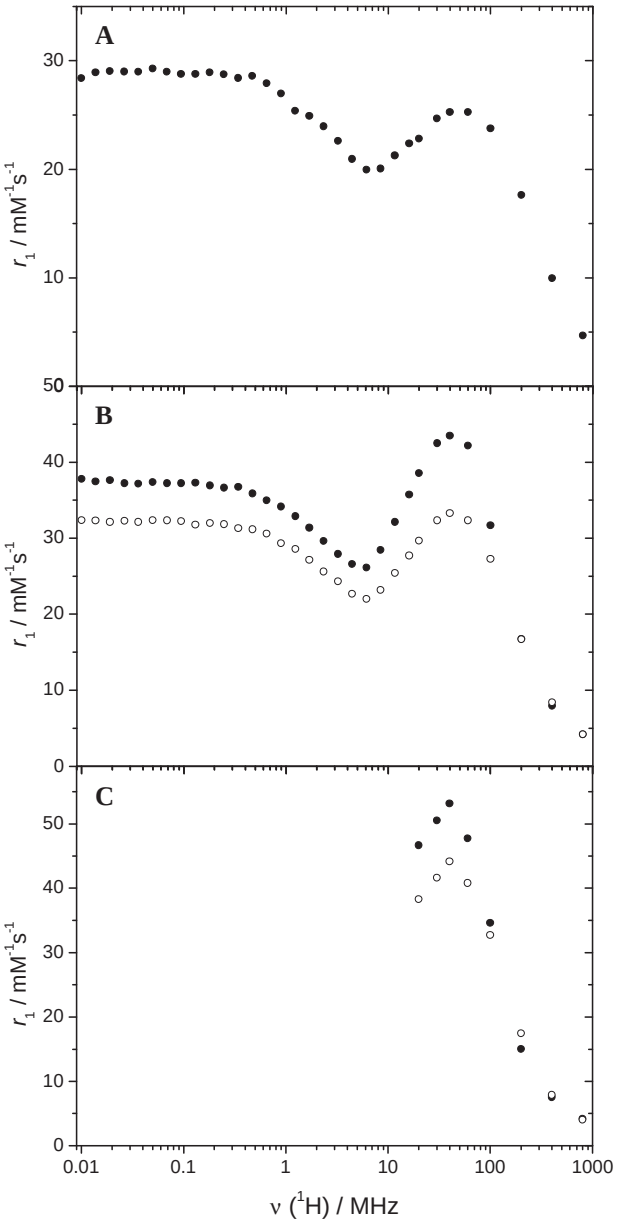

Figure III.8 – NMRD profiles of $\{Ph_4[Gd(DTTA)(H_2O)_2]^-_3\}$ at (A) 0.101 mM 25°C (●), (B) 1.84 mM 25°C and 37°C (○) (●) and (C) 18.2 mM 25°C (●) and 37°C (○).

III.3.5. ^{17}O and ^{1}H NMR data fittings with SB-LS-RFB

The simultaneous fit (Figure III.9) and ^{17}O NMR and NMRD data allows most of the parameters common to each samples to be determined.

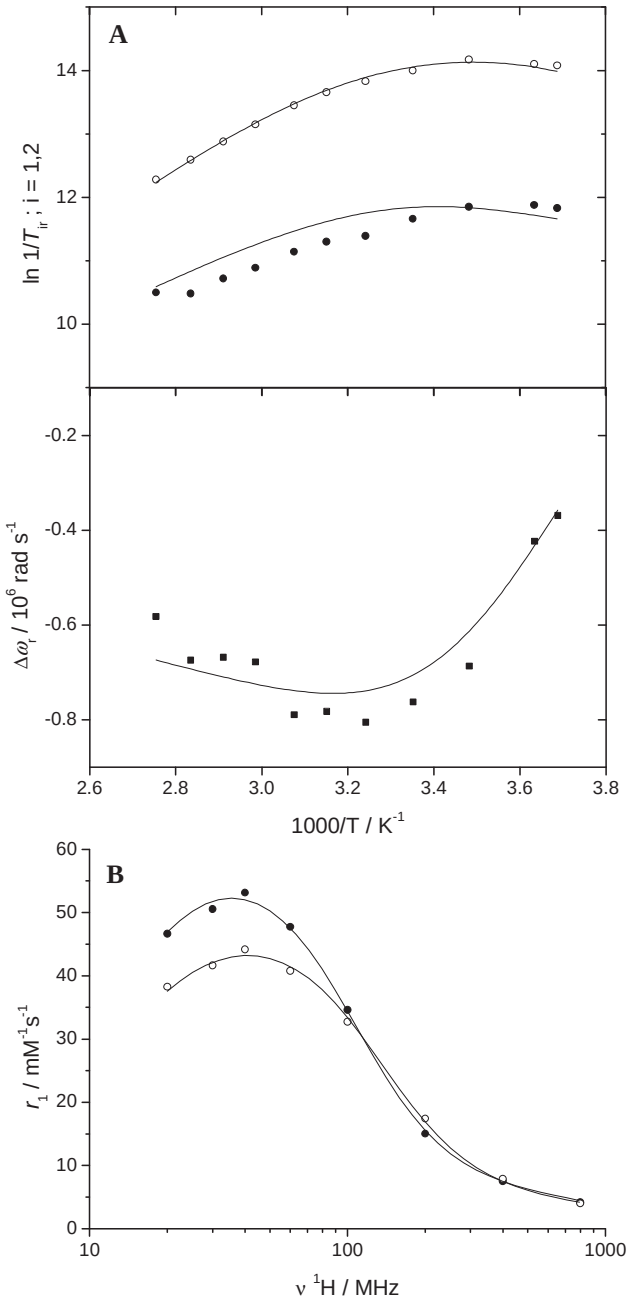

Figure III.9 – SB-LS-RFB simultaneous best fittings of (A) the ^{17}O NMR data (ln $1/T_{1r}$ (●), ln $1/T_{2r}$ (○) and $\Delta\omega_r$ (■)) and (B) the NMRD profile of high concentrated $\{Ph_4[Gd(DTTA)(H_2O)_2]^-_3\}$ samples at 25°C (●) and 37°C (○).

As the concentration dependence of the relaxivity is supposed to arise exclusively from the size of the aggregates, only global rotational correlation time τ_R and possibly the rigidity of the particle, characterized by the Lipari-Szabo factor S^2, should be affected by the concentration. All other fitted parameters, including the water exchange rate constant k_{ex}^{298}, the scalar coupling constant $A/\hbar$ or the electronic relaxation parameters for instance, are expected to remain unchanged whatever the size of the agglomerates.

The approach of the calculation is to fit simultaneously the ^{1}H NMRD and the ^{17}O NMR measurements of high concentration samples. All parameters, except the global rotational correlation time τ_R and the Lipari-Szabo factor S^2, will then be fixed and used as it is to fit the NMRD profiles of the samples at 0.1 and 1.8 mM. Though the sample concentration of the ^{1}H NMRD and the ^{17}O measurements are slightly different ($[Gd^{3+}]$ = 18.2 mM and 15.4 mM for the ^{1}H NMRD and the ^{17}O measurements respectively), they are assumed to be compatible (Figure III.6). By considering potentially too high ^{1}H relaxivities, the only affected parameter would be the τ_R^{HW}/τ_R^{OW} ratio, caused by the internal rotation of the water molecule in the inner sphere, which will appear slightly higher. With a fitted value for τ_R^{HW}/τ_R^{OW} of 0.88 instead of the theoretical 0.7 or 0.8, this artifact is actually observed. The simultaneous fit of the highly concentrated sample experimental points (^{17}O $1/T_{1r}$, $1/T_{2r}$, $\Delta\omega_r$ and high field ^{1}H NMRD) are shown on Figure III.9 and the best fitted parameters are reported on Table III.1.

The fit on experimental data of the concentrated samples was first performed by fitting the ^{17}O NMR data, leading to a fit very close to experimental points. The high field ^{1}H NMRD profiles data has been incorporated subsequently to the fitted data. Very few parameters, including the various constants and distances, are kept fixed in the final fit. A possible outersphere contribution to the chemical shifts has been neglected and the higher order static ZFS terms a_4 and a_6, very close to zero when fitted, are decided to be fixed to zero.

Let's note that the temperature of the sample probably affects also the size of the aggregates, generating smaller particles at higher temperature. As a wide temperature range is used, this can have an influence on the ^{17}O NMR experimental points, particularly on the values of T_1, dependent to the rotational correlation time τ_R^{298}.[41] This phenomenon can also have a slight effect on the NMRD profiles, where the entities are supposed to be bigger at 25°C than at 37°C. The relaxivities of the latter case will be a bit lower than expected in the hump region

(20 to 100 MHz, corresponding to the fitted region), leading to a bigger gap between the two temperature profiles at this frequencies. The expected effect on the fitted parameters would result in unusually high rotation activation energy E_R, which is exactly what has been observed (26.8 kJ mol^{-1}) (Table III.1).

Parameters / [Gd^{3+}]	18 mM	1.8 mM	0.10 mM
$\Delta H^{\ddagger}$ / kJ mol^{-1}	39.9 ± 7.9	39.9	39.9
k_{ex}^{298} / 10^6 s^{-1}	17.0 ± 5.1	17.0	17.0
E_R / kJ mol^{-1}	26.8 ± 5.7	26.8	26.8
τ_R^{298} / ps	2770 ± 628	1987 ± 99	817 ± 100
E_l / kJ mol^{-1}	18.0 ± 4.9	18.0	18.0
τ_l^{298} / ps	197 ± 331	197	197
E_v / kJ mol^{-1}	1	1	1
τ_v^{298} / ps	0.756 ± 0.191	0.756	0.756
$A/\hbar$ / 10^6 rad s^{-1}	3.70 ± 0.68	-3.70	-3.70
C_{os}	0	0	0
g	2	2	2
D_{GdH}^{298} / 10^{-10} m^2 s^{-1}	25	25	25
E_{DGdH} / kJ mol^{-1}	22	22	22
r_{GdO} / Å	2.5	2.5	2.5
τ_R^{HW} / τ_R^{OW}	0.88 ± 1.43	0.88	0.88
a_2 / 10^{10} s^{-1}	0.88 ± 0.71	0.88	0.88
a_4 / 10^{10} s^{-1}	0	0	0
a_6 / 10^{10} s^{-1}	0	0	0
a_{2T} / 10^{10} s^{-1}	0.52 ± 0.16	0.52	0.52
S^2	0.61 ± 0.02	0.54 ± 0.02	0.47 ± 0.05
$\chi\left(1+\eta^2/3\right)$ / MHz	7.58	7.58	7.58
q_{WAT}	2	2	2
$r_{GdH\ 1^{st}}$ / Å	3.1	3.1	3.1
$r_{GdH\ 2^{nd}}$ / Å	3.2	3.5	3.5

Table III.1 – Best fitted parameters by SB-LS-RFB theory of ^{17}O NMR and ^{1}H NMRD data for $\{Ph_4[Gd(DTTA)(H_2O)_2]^-_3\}$ at various concentrations. Fixed values underlined.

Most of the fitted parameters obtained for the highly concentrated samples are then used to fit the ^{1}H NMRD profiles of the lower concentration samples (Figure III.10). Only the rotational correlation time τ_R^{298} and the Lipari-Szabo factor S^2 are released for the fittings. The best fitted parameters are also presented on Table III.1.

The approach SB-LS-RFB however is not suitable for slow tumbling molecules at low magnetic fields.[42] A fitting performed on the whole profile would inexorably induce erroneous τ_R^{298}. For this reasons, the NMRD profiles of the compound at 1.8 mM and 0.1 mM are fitted only from 16 MHz to 800 MHz.

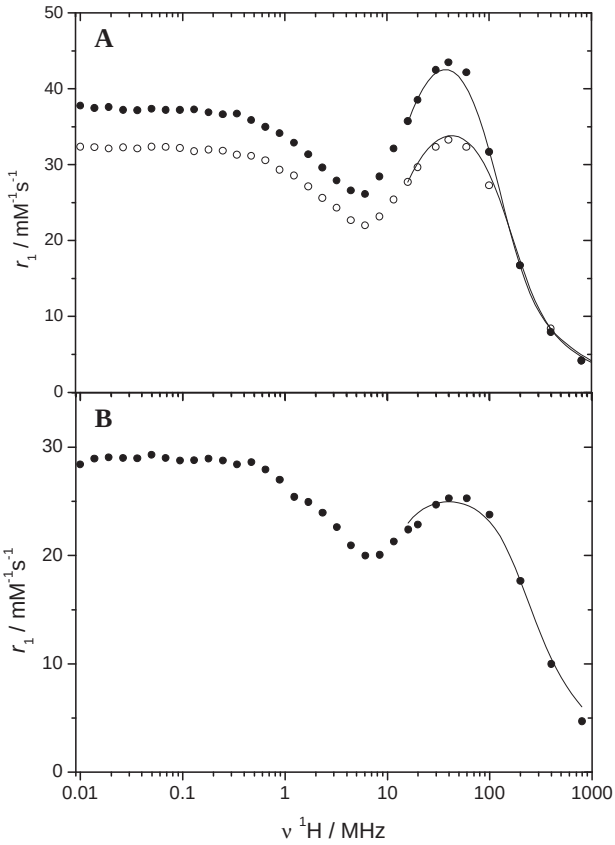

Figure III.10– NMRD profile of $\{Ph_4[Gd(DTTA)(H_2O)_2]^-_3\}$ at (A) 1.8 mM at 25°C (●) and 37°C (○) and (B) 0.10 mM at 25°C (●), fitted with SB-LS-RFB.

When comparing the fitted parameters for the three different concentrations, we see that the rotational correlation time changes significantly with the concentration, reinforcing the hypothesis that the size of the molecule is dependent on the concentration.

It can be noticed that the Lipari-Szabo factor S^2 is notably lower in the case of the diluted sample, indicating a more flexible structure. The chelating units of molecules wedged in an aggregate are supposed to have less degree of freedom for internal rotation than the monomers or molecules on the edge. With more "stacked" molecules, the bigger aggregates induce therefore more rigid structures, and hence bigger S^2.

Furthermore, it cannot be excluded that aggregation influences the relaxivity contribution of the outer sphere. The water environment of "stacked" and "edge" complexes may be different. Though outer sphere does nearly not affect the relaxation of oxygen relaxation, it has a non-negligible effect on the proton T_1 and therefore on the NMRD profile and the fitting.

III.3.6. ^{1}H NMRD data fittings with the modified Florence approach

As mentioned, the SB-LS-RFB model is not valid for slowly rotating compounds. The fitting of the whole NMRD profiles has to be performed with a method appropriated for slowly rotating molecules, as the modified Florence approach. This model considers also a static and a transient ZFS, but assumes slow reorientation of the complex and no correlation between the rotation and translation of the complex and the electronic spin dynamics.[34,43]

The approach we have chosen in our calculation is to use a few fixed parameters calculated with the SB-LS-RFB model (see chapter III.3.5) to implement it in the "modified Florence program". The water exchange parameters k_{ex} (= $1/\tau_M$) and $\Delta H^{\ddagger}$, fitted from experimental ^{17}O NMR data, as well as the internal rotation parameters τ_{l}, E_{l} and S^2 obtained by SB-LS-RFB are kept unchanged.

At first, the 1.8 mM NMRD profiles, because full NMRD profiles at two temperatures were available (Figure III.11), were fitted with free electronic relaxation parameters E_{v}, τ_{v}, Δ and D, and global rotation parameters E_{R} and τ_{R}.

The obtained electronic relaxation parameters were then fixed and used to fit the NMRD profiles of the 18.2 and 0.10 mM samples, considering the only parameters E_{R} and τ_{R} as variable. The best fitting parameters and the fitted NMRD profiles at other concentrations are presented on Table III.2 and Figure III.12, respectively.

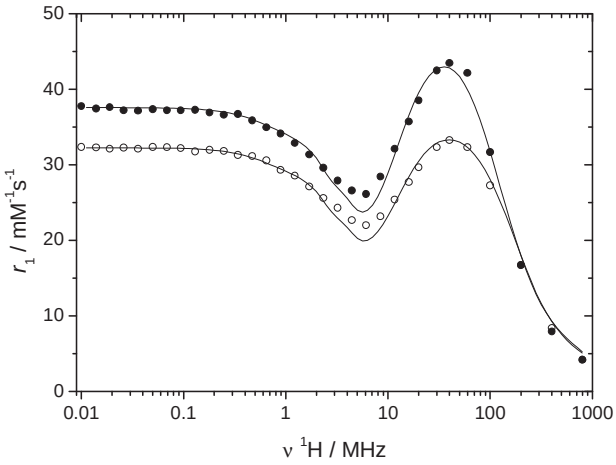

Figure III.11 – NMRD profile of $\{Ph_4[Gd(DTTA)(H_2O)_2]^-_3\}$ at 1.8 mM at 25°C (●) and 37°C (○) fitted with the Florence approach.

Parameters / [Gd^{3+}]	18 mM	1.8 mM	0.10 mM
E_R / kJ mol^{-1}	14.71	22.29	-
τ_R^{298} / ps	1586	1344	612.7
E_v / kJ mol^{-1}	12.53	12.53	-
τ_v^{298} / ps	51.73	51.73	51.73
Δ / cm^{-1}	0.02224	0.02224	0.02224
D / cm^{-1}	0.04234	0.04234	0.04234
S^2	0.61	0.544	0.47
E_l / kJ mol^{-1}	18.0	18.0	18.0
τ_l^{298} / ps	197	197	197
E_M / kJ mol^{-1}	39.9	39.9	-
τ_M / 10^{-6} s	0.05882	0.05882	0.05882
E_{DGdH} / kJ mol^{-1}	22	22	-
D_{GdH}^{298} / 10^{-5} cm^2 s^{-1}	2.5	2.5	2.5
q_{WAT}	2	2	2
$r_{GdH\ 1^{st}}$ / Å	3.1	3.1	3.1
$r_{GdH\ 2^{nd}}$ / Å	3.5	3.5	3.5

Table III.2 – Best fitted parameters using the Florence approach and ^{1}H NMRD data for $\{Ph_4[Gd(DTTA)(H_2O)_2]^-_3\}$ 18.2 mM, 1.84 mM and 0.101 mM. Fixed values underlined.

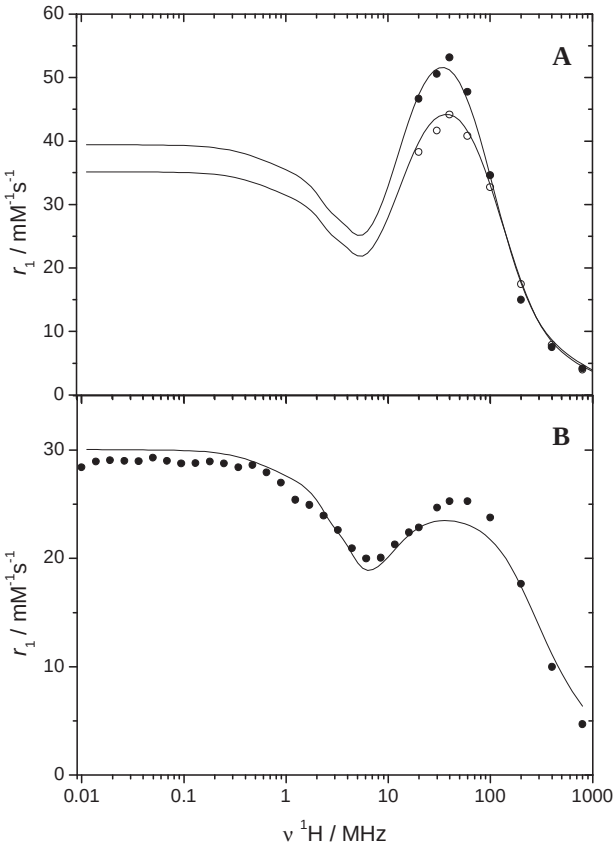

Figure III.12 – NMRD profile of $\{Ph_4[Gd(DTTA)(H_2O)_2]^-_3\}$ at (A) 18.2 mM at 25°C (●) and 37°C (○) and (B) 0.10 mM at 25°C (●) fitted with the Florence approach using the parameters of the 1.8 mM sample.

As the NMRD profile of the 0.1 mM sample was measured only at 25°C, the activation energies can not be calculated, and hence do not appear in the table. The unit conversion to compare with the SB-LS-RFB fitted values of the transient ZFS term Δ (using equation III.2, with c the speed of light = $3 \cdot 10^{10}$ cm s^{-1}), corresponding to a_{2T}, and the static ZFS term *D*, equivalent to a_2, led to the consistent values of $0.419 \cdot 10^{10}$ s^{-1} and $0.798 \cdot 10^{10}$ s^{-1} respectively.

$$\Delta^2[s^{-2}] = \left(\Delta[cm^{-1}] \cdot 2\pi c\right)^2 \qquad \text{(III.2)}$$

Though the rotational correlation times τ_R calculated with the two fitting methods do not correspond perfectly, they indicate in both cases a clear dependence on the concentration. Moreover, the modification of this only parameter and the LS factor S^2 allows remarkably good fitting of the profiles for the different concentrations. Finally, the three profiles have been fitted particularly well with the Florence approach by keeping the water exchange

parameters and the local rotation parameters obtained by the SB-LS-RFB theory, which points out the coherence of the fitted values for the system.

III.3.7. Aggregate size estimation

The equation of Stokes-Einstein-Debye (SED), using l = 2 spherical harmonics,[44] (equation III.3) allows the mean radii of the aggregates to be estimated from the rotational correlation time. The calculated radii for the two fitting methods are presented in the Table III.3.

$$\tau_R = \frac{4\pi r^3 \eta}{3k_B T} \qquad \text{(III.3)}$$

Where τ_R is the correlation time, r the radius of the corresponding sphere, η the viscosity coefficient (η = 0.891 cP at 25°C)[45], k_B the Boltzmann constant and T the temperature.

Fitting method / $[Gd^{3+}]$		18 mM	1.8 mM	0.10 mM
r / nm	SB-LS-RFB	1.5	1.3	1.0
	Florence	1.2	1.1	0.9

Table III.3 – Estimated mean radii (in nm) of the $\{Ph_4[Gd(DTTA)(H_2O)_2]^-_3\}$ agglomerates at various concentration and 25°C, using the SED equation.

To compare, a simple molecular modeling (Figure III.13) was performed to determine the radius and the thickness of the monomer, estimated at 1.3 nm and 0.8 nm respectively. The calculated dimension of the most diluted sample is astonishingly close to the ones determined by molecular modeling. Moreover, the relaxivities do not decrease with decreasing concentration below 0.1 mM (Figure III.6). Those two elements let us presume that no aggregations are formed at Gd^{3+} concentrations smaller than 0.1 mM (corresponding to $\{Ph_4[Gd(DTTA)(H_2O)_2]^-_3\}$ concentration of 33 µM).

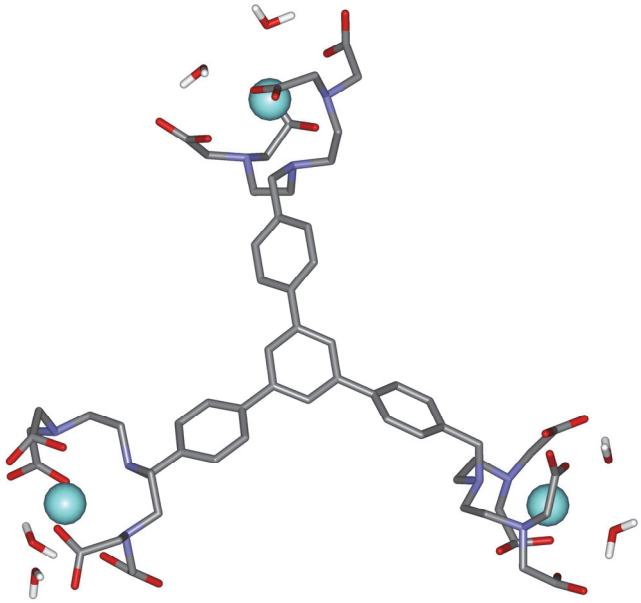

Figure III.13 – Molecular modeling of the $\{Ph_4[Gd(DTTA)(H_2O)_2]^-_3\}$ complex.

Another evidence is observed when comparing the NMRD profiles and the fitted rotational correlations times of $\{Ph_4[Gd(DTTA)(H_2O)_2]^-_3\}$ 0.1 mM to other DTTA systems with comparable size (Figure III.14 and Table III.4).

	τ_R^{298} / ps		
Compound / Fit method	SB-LS-RFB	SBM	Florence
$\{Ph_4[Gd(DTTA)(H_2O)_2]^-_3\}$ 0.1 mM	817 ± 100	-	613
$[Gd_3L(H_2O)_6]^{3-}$ [7]	-	540 ± 100	-
$[Fe(tpy\text{-}DTTA)_2Gd_2(H_2O)_4]$ [9]	-	410 ± 10	-
$\{Ru[Gd_2bpy\text{-}DTTA_2(H_2O)_4]_3\}^{4-}$ [12]	-	1120	833

Table III.4 – Obtained fitted τ_R^{298} of systems comparable to $\{Ph_4[Gd(DTTA)(H_2O)_2]^-_3\}$ 0.1 mM.

The $\{Ph_4[Gd(DTTA)(H_2O)_2]^-_3\}$ monomeric system is expected to be a bit bigger than the xylene core trinuclear complex described by Livramento *et al.*[7] and the iron terpyridine dimeric complex,[9] while it is significantly smaller than the ruthenium-based metallostar described by Moriggi *et al.*[12] The observed relaxivities correspond fully to these expectations, reinforcing the idea of the presence of the only monomeric specie at Gd^{3+} concentrations lower than 0.1 mM.

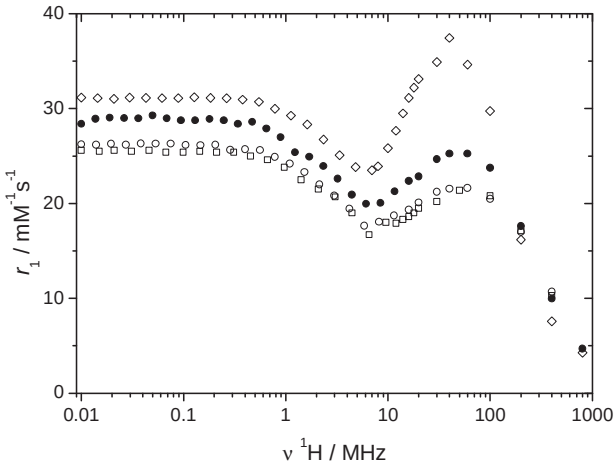

Figure III.14 – NMRD profiles at 25°C of $\{Ph_4[Gd(DTTA)(H_2O)_2]^-_3\}$ 0.1 mM (●), $[Gd_3L(H_2O)_6]^{3-}$ (○)[7] , $[Fe(tpy\text{-}DTTA)_2Gd_2(H_2O)_4]$ (□)[9] and $\{Ru[Gd_2bpy\text{-}DTTA_2(H_2O)_4]_3\}^{4-}$ (◊)[12]

III.3.8. ^{1}H relaxivity as a function of pH

The relaxivity was proved to be unaffected by the pH throughout the working pH range (Figure III.15).

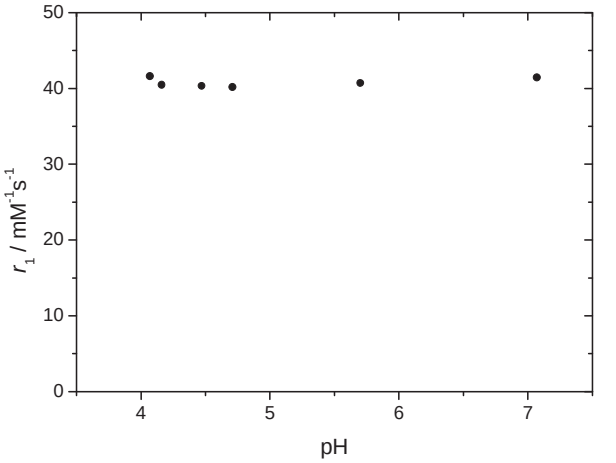

Figure III.15 – Relaxivity of $\{Ph_4[Gd(DTTA)(H_2O)_2]^-_3\}$ 0.8 mM as a function of pH

III.3.9. ^{1}H relaxivity in presence of phosphate buffer

This experiment was designed to break the aggregates, ideally until the total disaggregation of the system to leave the only monomer in solution. That was tried by adding from 5 to 250 equivalents of phosphate buffer, which proved to be an efficient disaggregating agent for π-

stacking systems,[46,47] to a 2.25 mM solution of $\{Ph_4[Gd(DTTA)(H_2O)_2]^-_3\}$. This relative high concentration was necessary in order to induce aggregates. The evolution of the relaxivities with time for the different phosphate concentrations is presented on Figure III.16.

Though a clear relaxivity drop is observed, this experiment turned out to be not quantitative, as the phosphate makes the compound precipitate, even in the most phosphate diluted sample. The relaxivity decrease is therefore not only due to a disaggregation.

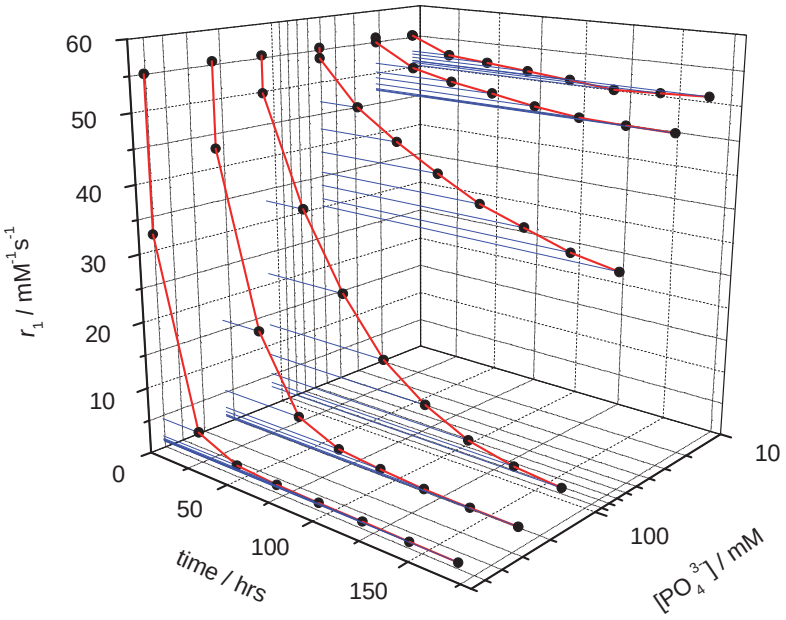

Figure III.16 – Relaxivity evolution in time of 2.3 mM samples containing various concentrations of phosphate buffer

III.3.10. ^{1}H relaxivity in presence of human serum

An experiment to test if the aggregates can exist in human serum was also performed. A slight relaxivity decrease is observed (Figure III.17). Because of the turbidity of the serum however, precipitation of the compound is not clearly distinguishable but cannot be excluded. The inorganic phosphate concentration in adult serum ranges to 0.8 to 1.45 mM,[48] which implies a concentration between 0.26 and 0.46 mM with the dilution. In addition to phosphate ions that precipitate the molecule, the concentrations of other salts in the serum have to be taken into account to explain the minor relaxivity drop. The sodium chloride can indeed play a role in disaggregation,[46] while lactates and carbonates can complex, monodentately in the case of the DTTA for the two free positions are not adjacent, the gadolinium. The higher initial

relaxivities in serum compared to water are certainly due to the higher viscosity of the solution.

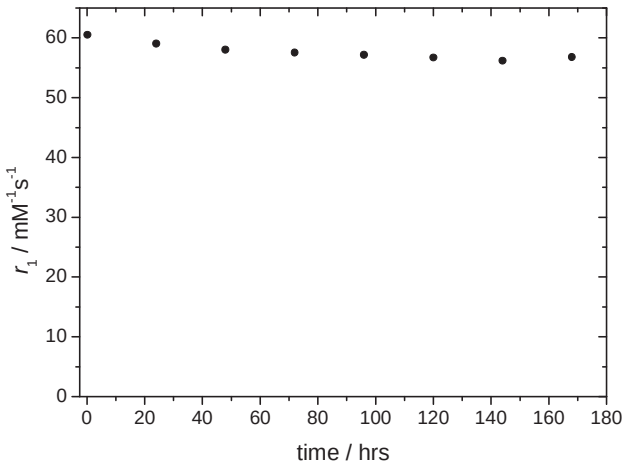

Figure III.17 – Relaxivity evolution in time of a 2.3 mM sample in human serum

III.4 Conclusion

In the framework of the development of potential MRI CAs, composed by several Gd^{3+} chelate complexes around a small or mid-size central core, we describe the synthesis of the compound 1,3,5-tris-{4-[(bis{2-[bis(*tert*-butyl acetate)amino]ethyl}amino)methyl] phenyl}benzene, referred as Ph_4DTTA_3.

This synthesis was carried out through the coupling of the central core Ph_4Br_3 with the protected chelating agent DTTA+. Though the purification of the protected compound Ph_4DTTA+_3 was not trivial, mainly due to the presence of disubstituted compound, this synthesis has been achieved with no major difficulty. After the deprotection however, the purification and the characterization of the compound Ph_4DTTA_3 turned out to be fussy, for this molecule precipitates at pH lower than 3. The purification has finally been possible by preparative HPLC using the volatile buffer triethylammonium acetate (Et_3NH^+ COO^-) as ion pairing agent.

After the complexation with Gd^{3+} and the first relaxivities measurements, the exceptionally high relaxivities for such a mid-size molecule and the difficulties to obtain reproducible values indicated an unusual system. This was confirmed with the concentration-dependence of the relaxivities of the complex $\{Ph_4[Gd(DTTA)(H_2O)_2]^-_3\}$. The size is the only parameter that acts on the relaxivities and that can change by the only dilution. A dynamic aggregation of the molecules was therefore the only possible reason for this atypical behavior.

The size variation has been proved by the measurements of the NMRD profiles at three different concentrations and the ^{17}O NMR measurements of the more concentrated sample. Simultaneous fits using the Solomon-Bloembergen theory together with the Lipari-Szabo free-model approach for the internal rotation and an electronic treatment according to Rast-Fries-Belorizky allowed the setting of all the parameters of this system, excepted the rotational correlation time τ_R and the Lipari-Szabo rigidity factor S^2 which remain the only parameters specific for each concentration. Furthermore, the entire NMRD profiles have been precisely fitted with the modified Florence approach, suitable for big slowly rotating molecules, using the internal rotation and the water exchange parameters fitted with SB-LS-

RFB. With this method also it was possible to fit the different concentration NMRD by varying S^2 and releasing τ_R.

The fitted rotational correlations times were used to estimate the number of molecules in the aggregates. It turned out that only the monomer might exist at Gd^{3+} concentration lower than 0.1 mM (compound concentration of 33 μM). The mean number of molecules in aggregates at higher concentrations was estimated to a few units. Compared to other described aggregating systems, the number of aggregating molecules is relatively low for a compound specially designed to induce aggregation. This is probably due to the steric hindrance of the three massive chelating units. A system composed by the same aromatic core with only two chelating units (Figure III.18), or a system composed by a mix of *bis* and *tris* substituted aromatic core might significantly increase the relaxivity, thought it would decrease the density of relaxivity.

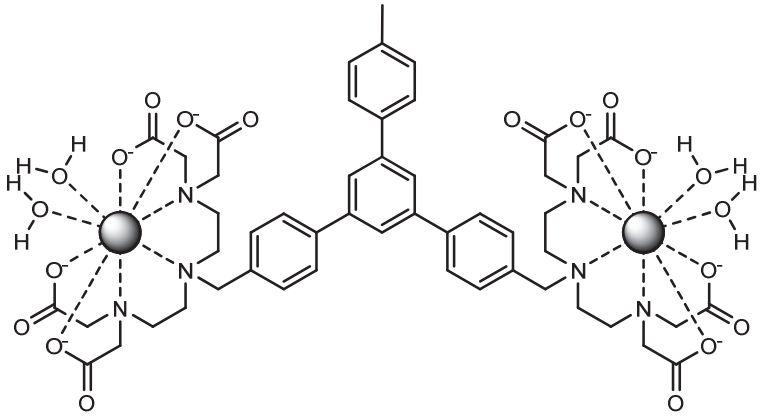

Figure III.18 – The complex $\{Ph_4[Gd(DTTA)(H_2O)_2]^-_2\}$ potentially interesting to form bigger aggregates.

Though the size of the aggregates has been characterized by fittings methods of the relaxometric data, many questions remain on this system. Direct size measurement methods such as MALDI-TOF mass spectrometry or Dynamic Light Scattering (DLS) turned out to be unsuccessful. Other size characterization methods such as Analytical Ultracentrifugation (AUC) might be successful. Furthermore, the type of interaction inducing aggregations has not been proved yet, though the π-stacking seems to be the most probable option.

III.5 Acknowledgements

I warmly thank the following persons for their precious contributions to this work :

Dr. Cédric R. Mayer from the Institut Lavoisier in Versailles for the synthesis route of the compound Ph_4Br_3 and the primary synthesis of this molecule.

Dr. Caroline Cannizzo from EPFL and the Laboratoire de Physico-chimie des Polymères et des Milieux Dispersés in Paris for the first synthesis of the compound Ph_4DTTA_3.

Dr. Luc Reymond in the group of the Prof. Kai Johnsson at EFPL for the provision of the analytical and preparative HPLC and his numerous advice and ideas. Dr. Laure Menin from the ISIC's MS service at EPFL for the measurements and purification by LC-MS. Dr. Christophe Roussel and Stéphane Thonney from EPFL for their help on the measurements by analytical HPLC.

Kim Von Allmen for the fastidious purifications of $Ph_4DTTA^+_3$ by silica gel chromatography and the various assists.

Dr. Joël Teuscher and Catherine Schütz from EPFL for the time they devoted on the trials of Dynamic Light Scattering.

Prof. Lothar Helm for the molecular modeling.

III.6 References

1. Trattnig, S.; Pinker, K.; Ba-Ssalamah, A.; Nobauer-Huhmann, I. M. *European Radiology* **2006,** *16*, 1280-1287.
2. Helm, L. *Future* Medicinal *Chemistry* **2010,** *2*, 385-396.
3. Vaughan, T.; DelaBarre, L.; Snyder, C.; Tian, J.; Akgun, C.; Shrivastava, D.; Liu, W.; Olson, C.; Adriany, G.; Strupp, J.; Andersen, P.; Gopinath, A.; Van De Moortele, P. F.; Garwood, M.; Ugurbil, K. *Magnetic Resonance in Medicine* **2006,** *56*, 1274-1282.
4. *http://www.meteoreservice.com/neurospin/*.
5. Costa, J.; Tóth, É.; Helm, L.; Merbach, A. E. *Inorganic Chemistry* **2005,** *44*, 4747-4755.
6. Costa, J.; Balogh, E.; Turcry, V.; Tripier, R.; Le Baccon, M.; Chuburu, F.; Handel, H.; Helm, L.; Tóth, É.; Merbach, A. E. *Chemistry-a European Journal* **2006,** *12*, 6841-6851.
7. Livramento, J. B.; Helm, L.; Sour, A.; O'Neil, C.; Merbach, A. E.; Tóth, É. *Dalton Transactions* **2008**, 1195-1202.
8. Miéville, P.; Jaccard, H.; Reviriego, F.; Tripier, R.; Helm, L. *Dalton Transactions* **2011,** *40*, 4260-4267.
9. Costa, J.; Ruloff, R.; Burai, L.; Helm, L.; Merbach, A. E. *Journal of the American Chemical Society* **2005,** *127*, 5147-5157.
10. Livramento, J. B.; Sour, A.; Borel, A.; Merbach, A. E.; Tóth, É. *Chemistry-a European Journal* **2006,** *12*, 989-1003.
11. Livramento, J. B.; Tóth, É.; Sour, A.; Borel, A.; Merbach, A. E.; Ruloff, R. *Angewandte Chemie-International Edition* **2005,** *44*, 1480-1484.
12. Moriggi, L.; Aebischer, A.; Cannizzo, C.; Sour, A.; Borel, A.; Bunzli, J.-C. G.; Helm, L. *Dalton Transactions* **2009**, -.
13. Tóth, É.; Vauthey, S.; Pubanz, D.; Merbach, A. E. *Inorganic Chemistry* **1996,** *35*, 3375-3379.
14. Lee, T. M.; Cheng, T. H.; Ou, M. H.; Chang, C. A.; Liu, G. C.; Wang, Y. M. *Magnetic Resonance in Chemistry* **2004,** *42*, 329-336.
15. Platzek, J.; Niedballa, U.; Radüchel, B. **1996,** *DE* 19508058, 13.
16. Elmorsy, S. S.; Pelter, A.; Smith, K. Tetrahedron *Letters* **1991,** *32*, 4175-4176.
17. Plater, M. J. *Synlett* 1993, 405-406.

18. Cherioux, F.; Guyard, L. *Advanced Functional Materials* **2001,** *11*, 305-309.
19. Xia, H.; He, J.; Peng, P.; Zhou, Y.; Li, Y.; Tian, W. *Tetrahedron Letters* **2007,** *48*, 5877-5881.
20. Corsi, D. M.; Platas-Iglesias, C.; Bekkum, H. v.; Peters, J. A. *Magnetic Resonance in Chemistry* **2001,** *39*, 723-726.
21. Vold, R. L.; Waugh, J. S.; Klein, M. P.; Phelps, D. E. *Journal of Chemical Physics* **1968,** *48*, 3831-&.
22. Ferrante, G.; Sykora, S. In Advances *in Inorganic Chemistry;* van Eldik, R.; Bertini, I. Eds.: San Diego, 2005; pp. 405-470.
23. Ammann, C.; Meier, P.; Merbach, A. E. *Journal of Magnetic Resonance* **1982,** *46*, 319-321.
24. Meiboom, S.; Gill, D. *Review of Scientific Instruments* **1958,** *29*, 688-691.
25. Solomon, I.; Bloembergen, N. Journal *of Chemical Physics* **1956,** *25*, 261-266.
26. Bloembergen, N. *Journal of Chemical* Physics **1957,** *27*, 572-573.
27. Bloembergen, N. *The Journal of Chemical* Physics **1957,** *27*, 595-596.
28. Lipari, G.; Szabo, A. *Journal of the* American *Chemical Society* **1982,** *104*, 4546-4559.
29. Lipari, G.; Szabo, A. *Journal of the American Chemical Society* **1982,** *104*, 4559-4570.
30. Rast, S.; Borel, A.; Helm, L.; Belorizky, E.; Fries, P. H.; Merbach, A. E. *Journal of the American Chemical Society* **2001,** *123*, 2637-2644.
31. Yerly, F. *VISUALISEUR 2.3.6* **2004,** *EPFL*.
32. Yerly, F. *OPTIMISEUR 3.0.0* **2002,** *EPFL*.
33. Bertini, I.; Kowalewski, J.; Luchinat, C.; Nilsson, T.; Parigi, G. *Journal of Chemical Physics* **1999,** *111*, 5795-5807.
34. Kruk, D.; Nilsson, T.; Kowalewski, J. *Physical Chemistry Chemical Physics* **2001,** *3*, 4907-4917.
35. Kowalewski, J.; Kruk, D.; Parigi, G. In *Advances in Inorganic Chemistry;* van Eldik, R.; Bertini, I. Eds.: San Diego, 2005; pp. 41-104.
36. Bertini, I.; Galas, O.; Luchinat, C.; Parigi, G. *Journal of Magnetic Resonance Series A* **1995,** *113*, 151-158.
37. Allinger, N. L.; Yuh, Y. H.; Lii, J. H. *Journal of the American Chemical Society* **1989,** *111*, 8551-8566.
38. Lii, J. H.; Allinger, N. L. Journal *of the American Chemical Society* **1989,** *111*, 8566-8575.

39. Lii, J. H.; Allinger, N. L. *Journal of the American Chemical Society* **1989,** *111*, 8576-8582.
40. Moriggi, L.; Cannizzo, C.; Prestinari, C.; Berriere, F.; Helm, L. *Inorganic Chemistry* **2008,** *47*, 8357-8366.
41. Powell, D. H.; Ni Dhubhghaill, O. M.; Pubanz, D.; Helm, L.; Lebedev, Y. S.; Schlaepfer, W.; Merbach, A. E. *Journal of the American Chemical Society* **1996,** *118*, 9333-9346.
42. Helm, L. Progress in Nuclear Magnetic Resonance Spectroscopy **2006,** 49, 45-64.
43. Moriggi, L., Ecole Polytechnique Fédérale de Lausanne, 2008.
44. Kowalewski, J.; Maeler, L. Nuclear spin relaxation in liquids: Theory, experiments, and applications; CRC Press, 2006.
45. Bruker. Almanac Ed., 2010.
46. Laus, S.; Sitharaman, B.; Tóth, É.; Bolskar, R. D.; Helm, L.; Asokan, S.; Wong, M. S.; Wilson, L. J.; Merbach, A. E. *Journal of the American Chemical Society* **2005,** *127*, 9368-9369.
47. Laus, S.; Sitharaman, B.; Tóth, É.; Bolskar, R. D.; Helm, L.; Wilson, L. J.; Merbach, A. E. *Journal of Physical Chemistry C* **2007,** *111*, 5633-5639.
48. Lewis, J. L. *The Merck Manuals - Online Medical Library* **2009**, http://www.merckmanuals.com/professional/sec12/ch156/ch156h.html.

Chapter IV :

Characterization and relaxivities of the complex $[Gd(DTTA)(H_2O)_2]^-$ conjugated to the polysaccharide chitosan

IV.1. Introduction 115
IV.2. Experimental Section 118
IV.2.1. Ligand synthesis and characterization 118
IV.2.2. Structural characterization of the modified chitosan 121
IV.2.3. Ng{Chi[Gd(DTTA-*N*'but)$(H_2O)_2]^-$} characterization 122
IV.2.4. Bulk Magnetic Susceptibility 122
IV.2.5. ^{1}H relaxivities 122
IV.2.6. Data treatment 123
IV.3. Results and discussion 124
IV.3.1. Ligand synthesis 124
IV.3.2. Structural characterization of the chitosan chain 126
IV.3.3. ^{1}H relaxivities of $[Gd(DTTA\text{-}N'but)(H_2O)_2]^{2-}$ 128
IV.3.4. ^{1}H relaxivities of {Chi[Gd(DTTA-*N*'but)$(H_2O)_2]^-$} 130
IV.3.5. Effect of concentration on the relaxivity 132
IV.3.6. Time stability of the relaxivity 133
IV.3.7. Formation of the nanogels Ng{Chi[Gd(DTTA-*N*'but)$(H_2O)_2]^-$} 133
IV.3.8. Ng{Chi[Gd(DTTA-*N*'but)$(H_2O)_2]^-$} characterization 134
IV.3.9. ^{1}H relaxivities of Ng{Chi[Gd(DTTA-*N*'but)$(H_2O)_2]^-$} 137
IV.4. Conclusion 139
IV.5. Acknowledgements 141
IV.6. References 142

IV.1. Introduction

The chitosan (Chi) is a linear polysaccharide made up of randomly-distributed β-(1,4)-D-glucosamine and β-(1,4)-N-acetyl-D-glucosamine (Figure IV.1). This compound is found in some microorganisms, yeasts and fungi,[1-3] but is more widely available through the partial deacetylation of chitin, the most common natural polymer apart from cellulose, constituting for instance the main component of the exoskeleton of crustaceans and insects.[4]

In addition to its non-toxic, biocompatible and biodegradable properties, this bioadhesive compound demonstrates film and gel forming ability. Due to these interesting and particular characteristics, the chitosan has been the subject of many researches over the last decades, mainly used as pharmaceutical excipient.[5] Drug transport enhancement and antimicrobial properties figure also among its most relevant applications in the pharmaceutical and biomedical fields.[1,5-7]

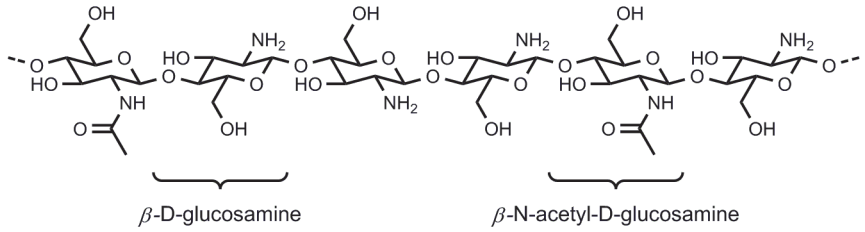

Figure IV.1 **–** Randomly-distributed glucosamine unit types in the linear polysaccharide chitosan.

Many properties of this compound depend strongly on the fraction of deacetylated units, referred as the degree of deacetylation or DD (and its one's complement, the degree of acetylation DA). For instance, the solubility of the compound is closely related to the degree of ionization of the free amines. As a result, chitosan with a DD of 0.5 is water-soluble at neutral pH, while high DD (0.85) requires a pH lower than 4.5-5 to allow solubilization.[4] However, the solubility depends also on the ionic concentration, the pKa of the acid used for the protonation or the distribution of acetyl groups along the chain.[4] The number of positive charges on the free amines, and therefore the DD, affects also the electrostatic interactions of the chitosan with negatively charged materials, such as cell surface or mucus.[1]

The possibilities offered by coupling the chitosan to a chelating unit have been noticed a few years ago, for metal adsorption[8,9] or neutron-capture therapy (NCT)[10-12] for instance. More recently, the chitosan has been investigated as a support for gadolinium complexes to design potential MRI T_1 contrast agent (CA). The coupling of the Gd^{3+} chelate complex on the polyglucosamine chain has been achieved either by ionic interactions[13-15] or covalently through amide bond formation between the primary deacetylated amine of the chitosan and one carboxylate of the chelating unit.[16-18] Some of these works presented coupling reactions with complexing (Figure IV.2 A)[16] or unprotected (Figure IV.2 B)[17] acetates of the chelating units. Both methods can however not exclude the possibility of two coupling with the same chelator. Two conjugations with the same chelating unit would induce intra- or intermolecular cross-links, destabilizing the metal complex and preventing the complete characterization of the system.

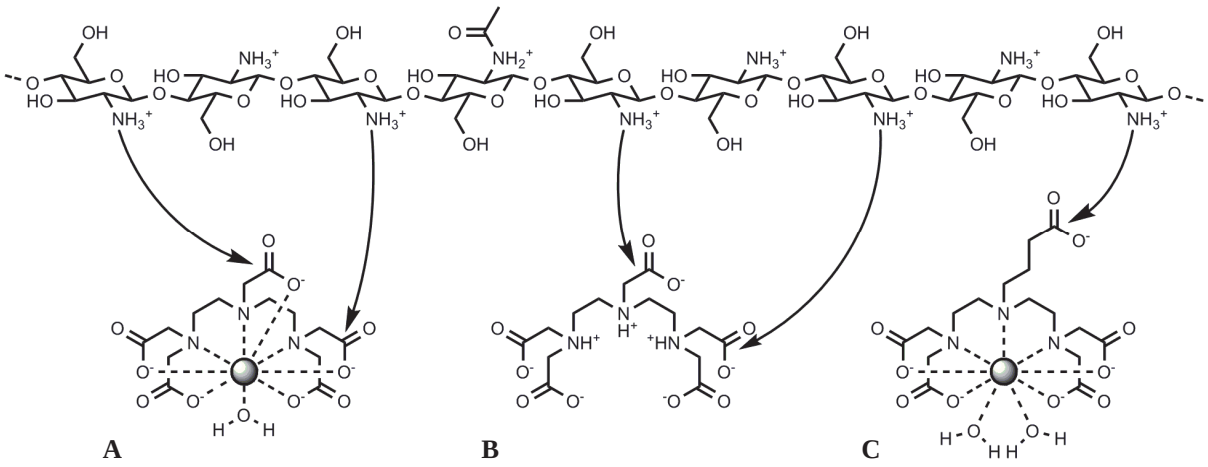

Figure IV.2 – Chitosan coupling reaction with complexed (A) or unprotected (B) acetates of the chelating unit, that can induce cross-links, and controlled coupling of the Gd-DTTA using an uncoordinated carboxylate pending arm (C).

This work reports here a new strategy for a highly controlled coupling of a Gd^{3+} complex to the free of the chitosan. This has been executed by functionalizing the central amine of the chelating agent DTTA (2,2',2'',2'''-[iminobis(ethane-2,1-diylnitrilo)]tetraacetic acid) with a non complexing carboxylate arm (Figure IV.2 C). This chapter presents the synthesis, the structural characterization and the relaxometric properties of the modified linear chitosan.

In addition to the linear polysaccharide, this chapter also presents the formation, the characterization and the relaxometric properties of nanogels (Ng), *i.e.* nano-size hydrogels, formed from the chitosan. These particles, denser and more rigid than the linear material, are constituted almost exclusively by water, surrounding a hydrophilic polymeric framework, which allows the free diffusion of water molecules within the particles. The ionotropic gelation method (Figure IV.3 A) allows the chitosan nanogels to be obtained through electrostatic interactions of the positively charged primary amine of the chitosan with the polyanionic group triphosphate, or TPP (Figure IV.1 B).[19,20] In order to stabilize the nanoparticles at physiological pH, the hydrogels were coated with the negatively charged polysaccharide alginate through ionic interactions.[21,22] This linear copolymer (Figure IV.3 C) is constituted by randomly distributed (1-4)-linked β-D-mannuronate and α-L-guluronate, abbreviated M and G respectively.

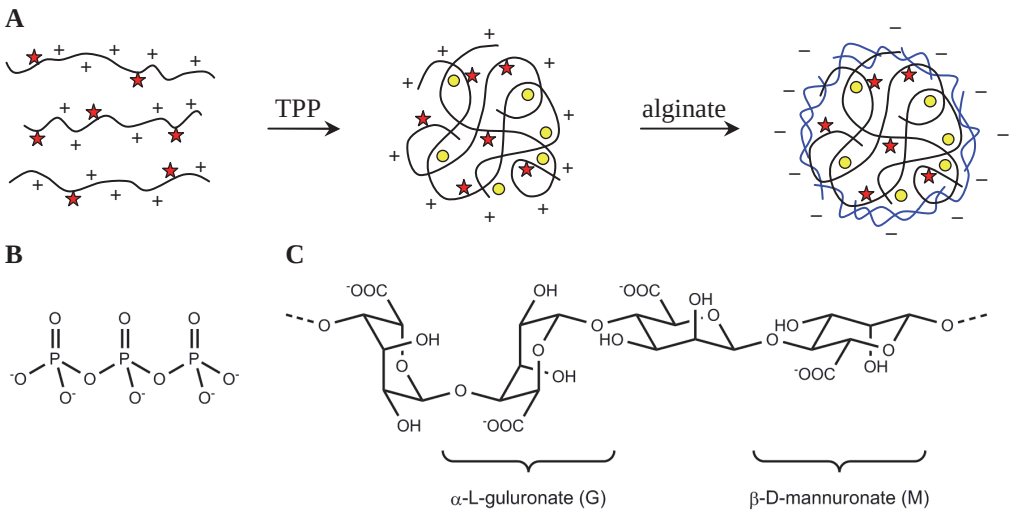

Figure IV.3 – Formation of the modified chitosan nanogels (A), with ★ the Gd^{3+} complexes, ○ the TPP and ∼ the alginate. Chemical structure of the involved compounds : triphosphate (TPP) used for the core folding (B) and the alginate for the coating (C).

IV.2. Experimental Section

IV.2.1. Ligand synthesis and characterization

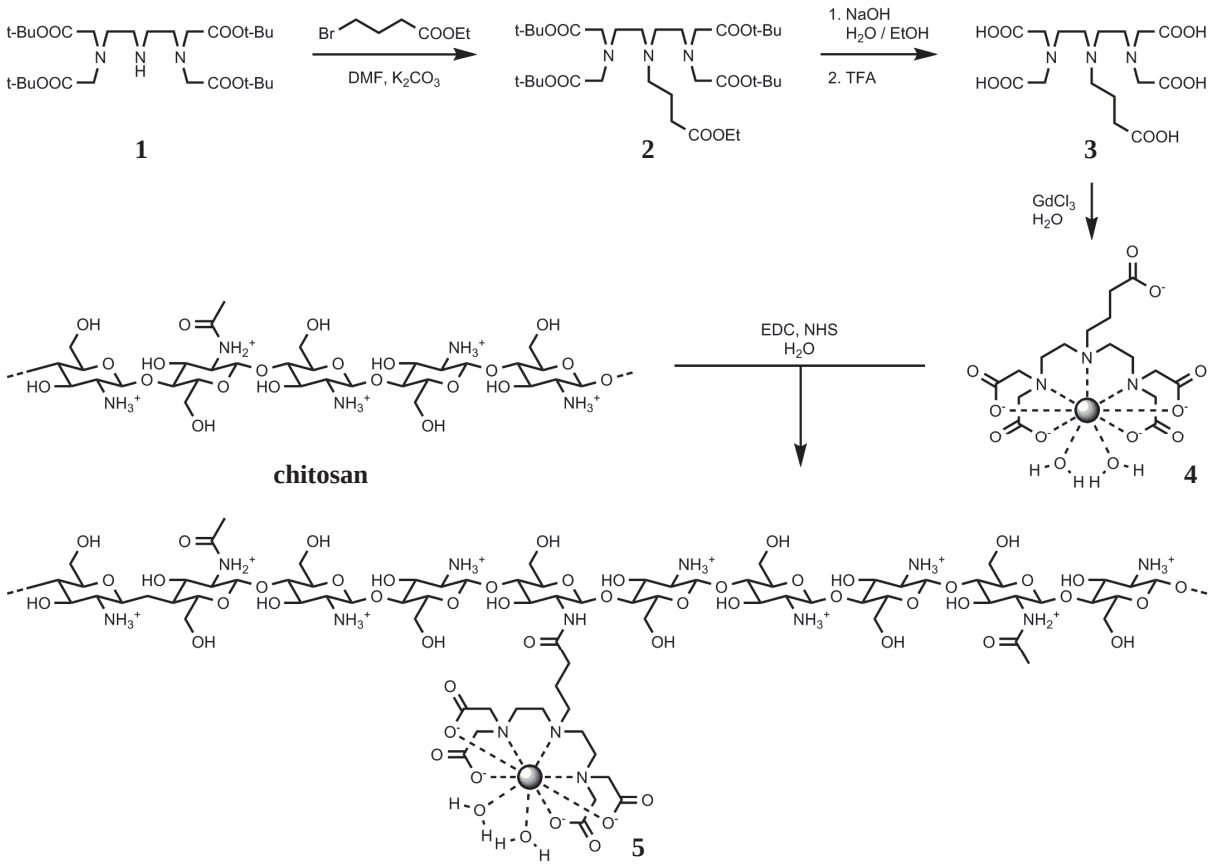

Figure IV.4 **–** Synthesis scheme of the Gd(III) complexe $\{Chi[Gd(DTTA)(H_2O)_2]^-\}$

All chemicals were purchased from high quality grade chemical sources (Sigma-Adrich, Acros) and were used as received without purification. Unless specified, H_2O is ultrapure filtered water (resistivity 18.2 MΩ/cm).

All ^{1}H and ^{13}C NMR spectra were recorded on a Bruker DRX-400 spectrometer (9.4 T). Mass Spectrometry analyses were performed on a Thermo Fischer TSQ7000 spectrometer using ESI ion source. Elemental analysis was performed at the Elemental Analysis Service at ISIC, EPFL (Dr. Euro Solari).

Synthesis of *tert*-butyl 2,2',2'',2'''-[iminobis(ethane-2,1-diylnitrilo)]tetraacetate (1)

This compound, referred as DTTA+, was synthesized according to literature.[23,24]

Synthesis of ethyl 4-(bis{2-[bis(*tert*-butyl acetate)amino]ethyl}amino) butanoate (2)

2.52 g (12.94 mmol) of ethyl 4-bromobutanoate were added dropwise under argon atmosphere to a solution of DTTA+ (**1**) (3.62 g, 6.47 mmol) in 120 mL DMF in presence of potassium carbonate (1.25 g, 9.06 mmol). The reaction mixture was stirred overnight at 70°C and evaporated to dryness. The residue was dissolved in 200 mL DCM and wash three times with 100 mL of water. The organic phase was dried over sodium sulfate and evaporated to dryness. The crude product was purified by silica gel chromatography (MeOH/DCM 7:93) (R_f = 0.10). 2.189 g (3.25 mmol, yield 50%) of pure compound **2** were obtained. ^{1}H-NMR ($CDCl_3$, 400 MHz) δ in ppm : 1.24 (t, J = 6.9 Hz, 3 H), 1.45 (s, 36 H), 1.73 (tt, J = 6.6 Hz, 2 H), 2.28 (t, J = 6.9 Hz, 2 H), 2.47 (t, J = 6.4, 2 H), 2.59 (t, J = 6.6 Hz, 4 H), 2.77 (t, J = 6.6 Hz, 4 H), 3.44 (s, 8 H), 4.11 (q, J = 6.9 Hz, 2 H). MS (ESI) m/z (%) : 674.6 (100) $[M+H]^+$.

Synthesis of 4-(bis{2-[bis(*tert*-butyl acetate)amino]ethyl}amino) butanoic acid (3)

This compound will be referred as DTTA-*N'*but. 35 mL of a 0.4 M NaOH aqueous solution were added to a solution of **2** (1.65 g, 2.45 mmol) dissolved in 50 mL EtOH. The reaction mixture was stirred 60 hrs at room temperature, and evaporated to dryness. The solid residue was dissolved in 50 mL of a 5% water solution in TFA and stirred for 3.5 hrs at room temperature. The resulting water soluble oil was dissolved in 25 mL H_2O and evaporated five times to remove the residual TFA, and purified by anionic exchange resin (BIO-RAD™ AG 50W-X4) using a 1 to 5 M HCl gradient as elution system. 756 mg (1.79 mmol, yield 65%) of pure compound **3** were obtained. ^{1}H-NMR (D_2O, 400 MHz) δ in ppm : 2.00 (tt, J undetermined, 2 H), 2.49 (t, J = 6.4 Hz, 2 H), 3.30 (t, J = 7.7 Hz, 2 H), 3.37 (t, J = 5.1 Hz, 4 H), 3.49 (t, J = 5.2 Hz, 4 H), 3.79 (s, 8 H). ^{13}C-NMR (D_2O, 54.3 MHz) δ in ppm : 17.90 (*N'*-CH_2-*C*H_2-CH_2-COOH), 29.89 (CH_2-*C*H_2-COOH), 49.74 (*N'*-*C*H_2-CH_2-N), 50.31 (*N'*-CH_2-*C*H_2-N), 52.60 (*N'*-*C*H_2-CH_2-CH_2-COOH), 55.36 (N-*C*H_2-COOH), 171.84 (N-CH_2-*C*OOH), 176.31 (CH_2-CH_2-*C*OOH). MS (ESI) m/z (%) : 422.7 (100) $[M+H]^+$, 444.7 (35) $[M+Na]^+$, 466.6 (20) $[M+2Na-H]^+$. Elemental analysis calculated (%) for $[H_8DTTA\text{-}N'but]^{3+}[Cl]^-_3 \cdot 2H_2O$ ($C_{16}H_{34}Cl_3N_3O_{12}$) : C 33.90, H 6.05, N 7.41 ; found : C 33.96, H 5.84, N 7.42.

Synthesis of [Gd(DTTA-*N*'but)(H_2O)$_2$]$^{2-}$ (4)

The solid salt $GdCl_3 \cdot xH_2O$ ($x \approx 6.7$) was dissolved in H_2O to prepare the Gd^{3+} stock solution. The exact ion concentration was measured by complexometric titration using Na_2H_2EDTA 5 mM. DTTA-*N*'but was dissolved in H_2O and its concentration in the stock solution was determined by back titration of a Gd^{3+} excess with Na_2H_2EDTA 5 mM. The titrations were performed on a Metrohm 665 Dosimat, using xylenol orange as complexometric indicator and buffered at pH 5.8 with a 5% (w/v) urotropine solution in water. The complex [Gd(DTTA-*N*'but)(H_2O)]$^{2-}$ was prepared by adding a slight deficit of Gd^{3+} (2%) to the ligand solution. The pH was brought back to 5.8 with 0.1 M NaOH and the absence of free gadolinium was checked by the xylenol orange test.

Synthesis of {Chi[Gd(DTTA-*N*'but)(H_2O)$_2$]$^-$} (5)

A 0.5% (w/v) chitosan DD ~ 0.85 was prepared by dissolving 100 mg chitosan (596 µmol of glucosamine unit) in 20 mL H_2O. The pH was stabilized at 4 by addition of HCl 1M. 4.12 mL of a 8.19 mM [Gd(DTTA-*N*'but)(H_2O)$_2$]$^{2-}$ aqueous solution (33.8 µmol) were added to the chitosan solution, followed by 29.3 mg (135.2 µmol) of sodium 1-hydroxy-2,5-dioxo-3-pyrrolidinesulfonate (*N*-hydoxysulfosuccinimide ; Sulfo-NHS). 19.4 mg (101.4 µmol) of *N*-[3-(dimethylamino) propyl]-*N'*-ethylcarbodiimide hydrochloride (EDC) were added in three times with 45 minutes between each addition, whilst stirring at room temperature. The reaction was continued for 2 hours after the last addition. The sample was purified three times by size exclusion chromatography using Sephadex™ LH20 resin in a 25 x 4.5 cm column. The absence of uncoupled Gd^{3+} complex was controlled by the stable relaxivity at 20 MHz, 25°C before and after the final size exclusion columns. See sections IV.2.2 and IV.3.2 for characterization.

Formation of the nanogels Ng{Chi[Gd(DTTA-*N*'but)(H_2O)$_2$]$^-$}

The nanogels were prepared by Catherine Schütz, group of Dr. MER Christine Wandrey, LMRP, EPFL. A 0.1% w/v {Chi[Gd(DTTA-*N*'but)(H_2O)$_2$]$^-$} solution was prepared by dissolving 5 mg of modified chitosan in 5 mL H_2O adding HCl 1M dropwise until the pH was stabilized at 2.8. The solution was left overnight at 4°C to allow complete solubilization. The pH of the chitosan solution was raised to 4.8 with NaOH 0.1 M to ensure total complexation. The solution was sterile filtered prior to nanogel formation (0.2µm filter Minisart hydrophilic cellulose acetate, Sartorius). Under sterile condition, the nanogels were prepared by a slow

dropwise addition of one volume equivalent of a 0.1% w/v sodium triphosphate (TPP) solution to the nine volume equivalents of chitosan solution under strong agitation. The pH was controlled during addition and maintained around 4.75 with HCl 0.1 M. The solution was stirred for 1h before surface coating. For the nanogel surface coating, the chitosan-TPP dispersion was diluted twice with sterile H_2O. An equal volume of the diluted nanogel dispersion was added dropwise to a 0.1% w/v sterile filtered aqueous sodium alginate (G / M ~ 0.4 : 0.6) solution under strong agitation. The pH was constantly maintained between 7.1 and 7.5 by addition of 0.02M NaOH, leading to a final pH of 7.35. The dispersion was filtered through a 1.2µm hydrophilic filter (Minisart, Sartorius) and stored at 4°C. The sample was concentrated ten times under a nitrogen flux before undergoing relaxivity measurements.[21]

IV.2.2. Structural characterization of the modified chitosan

The degree of deacetylation (DD) of the starting chitosan was determined by ^{1}H-NMR by integrating the acetyl peak (3 H) over the methylene region (6 H). The H1, very close to the HOD peak is not included in the integral region.[25,26]

The carbon mass fractions were determined by elemental analysis performed at the Elemental Analysis Service at ISIC, EPFL (Dr. Euro Solari).

The gadolinium mass fractions of linear {Chi[Gd(DTTA-*N*'but)(H_2O)$_2$]$^-$} and nanogels Ng{Chi[Gd(DTTA-*N*'but)(H_2O)$_2$]$^-$} were determined by inductively coupled plasma mass spectrometry (ICP-MS) performed on a quadrupole spectrometer Elan 6100 DRC (Perkin Elmer™, Waltham, Massachusetts, USA) at the Institut de Minéralogie et Géochimie, University de Lausanne (Dr. Alexey Ulianov). All solutions (blank, standards and samples) were prepared with a final 1.5% (w/w) HCl and 300 ppb (w/v) europium as the internal reference concentration. The measurements were performed on isotope ^{155}Gd, ^{157}Gd and ^{151}Eu. The Gd^{3+} concentration was determined with respect to two standards, whose concentrations surround the target concentration (1 ppm and 300 ppb). The exact concentration of the Eu^{3+} reference and the Gd^{3+} standards stock solutions were measured by complexometric titration (see synthesis of **4**).

IV.2.3. Ng{Chi[Gd(DTTA-N'but)(H_2O)$_2$]} characterization

The nanogels were characterized by Catherine Schütz, group of Dr. MER Christine Wandrey, LMRP, EPFL The size distribution was measured by dynamic light scattering (DLS) using a Malvern ZetaSizer (ZEN3600 Nano-ZS, Malvern Instruments, Worcestershire, UK). The surface charge of the nanogel formulations was analyzed by measuring the electrophoretic mobility and expressed as zeta potential. Both measurements were performed simultaneously in a DTS 1060 cell. With regard to the day of the production, the size distribution of the nanongels was measured at days 0, 5, 9 and 29 to control the particles stability.

For transmission electron microscopy (TEM), a drop (10 μL) of nanogel suspension was deposed on a 200-mesh carbon/formvar coated copper grid (Electron Microscopy Sciences, Hatfield, PA, USA) and air-dried. Sample was stained with a 2% w/v phosphotunstic acid solution by deposing one drop (10 μL) of solution on the grid, waiting 30-40 s and blotting the excess liquid off. Imaging was performed on a CM-10 (Philips/FEI).

IV.2.4. Bulk Magnetic Susceptibility

Unless specified, the Gd^{3+} concentrations used to calculate the relaxivities were measured by bulk magnetic susceptibility (BMS)[27] on a Bruker DRX-400 (9.4 T, 400 MHz) spectrometer. This was performed by measuring the shift of the *tert*-butanol protons in the paramagnetic environment compared to the diamagnetic reference contained in a coaxial NMR tube.

IV.2.5. ^{1}H relaxivities

T_1 were determined by the inversion-recovery method[28] using the following equipment : Fast Field Cycling (FFC) NMR relaxometer[29] $2.35 \cdot 10^{-4}$ to 0.47 T (^{1}H Larmor frequencies : 0.01 to 20 MHz) equipped with a VTC90 temperature control unit (Stelar Spinmaster, Mede, Italy), Bruker Minispec mq20 0.47 T (20 MHz), mq40 0.70 T (30 MHz), mq40 0.94 T (40 MHz) and mq60 1.41 T (60 MHz), Bruker Avance-200 console connected to a 2.35 T (100 MHz) and a 4.7 T (200 MHz) cryomagnets, Bruker Avance-II 9.4 T (400 MHz). The spectrometers were equipped with Bruker BVT3000 temperature control units and Bruker BCU05 cooling units. All temperatures were measured by substitution techniques.[30] The relaxation rates $1/T_1$ were corrected by diamagnetic contributions of 0.366 s^{-1} and 0.326 s^{-1} for 25°C and 37°C respectively.

The ^1H NMRD profiles of $[Gd(DTTA\text{-}Me)(H_2O)_2]^-$ (2.55 mM and 3.50 mM), $[Gd(DTTA\text{-}N'but)(H_2O)_2]^{2-}$ (3.30 mM and 2.97 mM), {Chi[Gd(DTTA-*N*'but)$(H_2O)_2]^-$} (0.972 mM and 0.649 mM) were measured at 25.0°C and 37.0°C. The NMRD profile of Ng{Chi[Gd(DTTA-*N*'but)$(H_2O)_2]^-$} (0.127 mM) has been measured at 25.0°C. Samples in 7.5 mm tubes were used on Bruker mq40's and mq60 while samples sealed in glass spheres adapted for 10 mm NMR tubes were used for all other instruments.

The variable-concentration {Chi[Gd(DTTA-*N*'but)$(H_2O)_2]^-$} relaxivities were measured at 20 MHz, 25°C. The time evolution of {Chi[Gd(DTTA-*N*'but)$(H_2O)_2]^-$} relaxivity was performed by measuring T_1 at 20 MHz, 25°C, after 1, 2, 3, 4, 7, 14 and 31 days. The solution was kept at 4°C between each measurement.

IV.2.6. Data treatment

The fitting of the ^1H NMRD profiles using the Solomon-Bloembergen-Morgan theory (SBM)[31-34] for $[Gd(DTTA\text{-}Me)(H_2O)_2]^-$ and $[Gd(DTTA\text{-}N'but)(H_2O)_2]^{2-}$, and the SBM theory together with the Lipari-Szabo (LS) free-model approach for the internal rotation[35,36] for {Chi[Gd(DTTA-*N*'but)$(H_2O)_2]^-$} and {Chi[Gd(DTTA-*N*'but)$(H_2O)_2]^-$} nanogels were performed on Visualiseur/Optimiseur[37,38] running on a MATLAB© 7.3.0 (R2006b) platform.

The fitting of the ^1H NMRD profiles using the "modified Florence approach"[39-41] were performed with a version of the "modified Florence program"[42] including Lipari-Szabo treatment of the internal rotation adapted to run on a MATLAB© 7.3.0 (R2006b) platform.

IV.3. Results and discussion

IV.3.1. Ligand synthesis

The coupling of two acetates of a single chelator to chitosan primary amines would prevent these groups to conjugate the metal and consequently have severe consequences on the stability of the complex, which is not suitable for a potential CA. As a result, the undetermined hydration number, water exchange rate, affected by the geometry of the complex, and size of the molecule in the case of an intermolecular cross-link, would moreover not allow the characterization of the system. The non-complexation of the fifth arm is therefore essential for this coupling strategy with the chitosan.

The first attempt to couple the chelating unit DTTA to the chitosan was performed through the partially protected derivative of DTTA-*N*'prop **6**.[43,44] This compound, presenting protected acids except the only *N*'-propionic acid, was obtained through the coupling of DTTA+ (**1**) with 3-bromopropanoic acid (Figure IV.5). The deprotection of the acetate groups however turned out to be unfeasible, as the use of TFA led to an insoluble product while highly concentrated HCl can damage and depolymerize the polysaccharide chain.[45]

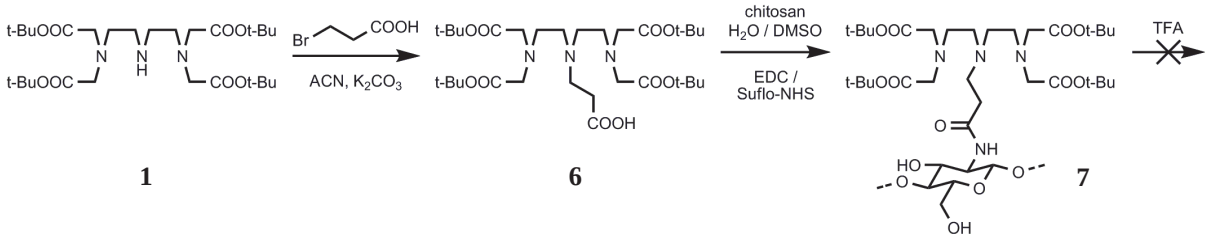

Figure IV.5 – Synthesis of chitosan- *N*'prop-DTTA+.

The second strategy to couple of DTTA on the chitosan is therefore to employ a complexed form of DTTA, using the metal centre as the "protecting group" of the acetates to avoid inter- and intramolecular cross-links. This can not be achieved with the complexe [Gd(DTTA-*N*'prop)(H_2O)]$^{2-}$ (chelator presented in Figure IV.6 A), whose all five carboxylates complex the metal centre.[43] Alternatively, based on the chelating agent H_6TTAHA[46] (Figure IV.6 B) whose six-membered pending arm was proved not to complex Gd^{3+} by X-ray crystal structure,[47] the chelator H_5DTTA-*N*'but was synthesized (Figure IV.6 C). This synthesis

could not be achieved directly with the bromobutyric acid, which undergoes a cyclization leading to the formation of the inert lactone. It was therefore accomplished with an ester derivative (the ethyl 4-bromobutanoate (Figure IV.4) was used for a matter of commercial availability). The compound had to undergo two different deprotection reactions. NaOH removes the ethyl group, but it not very efficient on *tert*-butyl because of the accessibility, while TFA is ideal for *tert*-butyl, whose tertiary carbon stabilizes the formation of a carbocation.

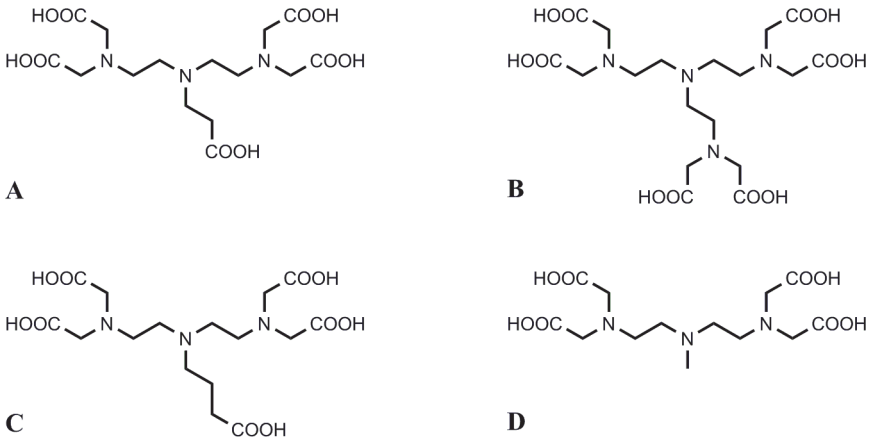

Figure IV.6 **–** The chelating units H_6DTTA-*N*'prop (A), H_6TTAHA (B), H_5DTTA-*N*'but (C) and H_4DTTA-Me (D).

The next step, consisting in coupling the complex with chitosan, had to be performed in water to allow the solubilization of the chitosan. Amongst the few coupling agents allowing an aqueous environment, the couple EDC/Sulfo-NHS (Figure IV.7) was the most promising.[48,49]

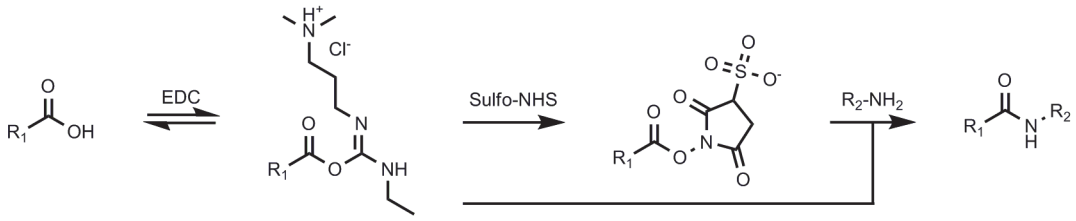

Figure IV.7 **–** Mechanism of the couple EDC/Sulfo-NHS as coupling agent in water.[50]

The coupling reaction was set up in order to modify statistically one in fifteen deacetylated units. From the perspective of forming nanogels by using the free amines, this was important

to keep the largest part of the free amines unconjugated. The number of moles of primary amines was determined by the mean molar mass of a glucosamine unit (161.16 g/mol and 203.19 g/mol for the deacetylated and the acetylated unit respectively). One equivalent of Gd^{3+} complex, four equivalents of Sulfo-NHS and three times one equivalent of EDC were used. The reagent excesses were discarded with successive Sephadex size exclusion column purification. The constant relaxivity before and after the last purification column allowed to control the absence of the unconjugated $[Gd(DTTA\text{-}N'but)(H_2O)_2]^-$ complex.

IV.3.2. Structural characterization of the chitosan chain

The initial fraction of deacetylated units, called the degree of deacetylation or DD, was calculated by integration of the acetyl peak in the ^1H NMR spectrum compared to six methylene protons (the H1, close to HOD, is difficult to isolate and therefore not taken into account). The initial degree of acetylation DA was determined at 0.156. The initial DD is therefore 0.844.

The fraction of units modified by addition of Gd^{3+} chelates with respect to all units, written DM for degree of modification, was determined with the gadolinium and carbon mass fractions, assuming that all carbons came from the modified chitosan. This ratio had to be used in order to take the effective mass, including counterions and inorganic salts, into account. The mass ratio of gadolinium was determined by ICP-MS, measuring its concentration with respect to the internal reference Eu^{3+}. The ratio of the concentrations is proportional to the ratio of the measured intensities (in counts per second) corrected by the ratio of the intensities in the blank (equation IV.1). The slope *a*, or proportionality constant, was determined by fitting the experimental values of two Gd^{3+} standards above and below the target concentration, plus the origin (0;0). The Gd^{3+} concentration is averaged from the experimental results for the two isotopes ^{155}Gd and ^{157}Gd.

$$\frac{\left[Gd^{3+}\right]}{\left[Eu^{3+}\right]} = a\left(\frac{I_{Gd}}{I_{Eu}} - \frac{I_{Gd}^{blank}}{I_{Eu}^{blank}}\right) \qquad \text{(IV.1)}$$

The mean elemental composition of the glucosamine units is dependent on the DM. The mass fractions of carbon w_C and gadolinium w_{Gd} can be expressed by equations IV.2 and IV.3, respectively.

$$w_C = \frac{(DA \cdot n_C^A + DM \cdot n_C^M + DD \cdot n_C^D) \cdot M_C}{DA \cdot M^A + DM \cdot M^M + DD \cdot M^D} \quad \text{(IV.2)}$$

$$w_{Gd} = \frac{DM \cdot M_{Gd}}{DA \cdot M^A + DM \cdot M^M + DD \cdot M^D} \quad \text{(IV.3)}$$

Where n_C^A, n_C^M and n_C^D express the number of carbon atoms in acetylated, modified and deacetylated unit respectively, M_C and M_{Gd} the atomic mass of carbon and gadolinium and M^A, M^M and M^D the molecular mass of acetylated, modified and deacetylated glucosamine respectively.

The conjugation is performed on deacetylated amines, the DM affects therefore the DD, which can be written DD = 1 – DA – DM. The molar mass ratio w_{Gd} / w_C is therefore given by equation IV.4, which is developed and rearranged to give equation IV.5.

$$\frac{w_{Gd}}{w_C} = \frac{DM \cdot M_{Gd}}{(DA \cdot n_C^A + DM \cdot n_C^M + (1 - DA - DM) \cdot n_C^D) \cdot M_C} \quad \text{(IV.4)}$$

$$DM = \frac{w_{Gd} \cdot M_C \left(DA\left(n_C^A - n_C^D\right) + n_C^D\right)}{w_C \cdot M_{Gd} + w_{Gd} \cdot M_C (n_C^D - n_C^M)} \quad \text{(IV.5)}$$

The carbon mass ratio w_C measured by elemental analysis is equal to 23.4%, the gadolinium mass ration determined at 1.53 % by ICP-MS, and the number of number of carbon atoms in acetylated, modified and deacetylated unit is 8, 22 and 6 respectively. From this calculation, the fraction of modified units in the modified chitosan, whose final composition is presented in Table IV.1, is determined at 3.4%. With respect to the deacetylated units, this degree of modification corresponds to 4.1%. The reaction was set up in order to conjugate statistically one over fifteen deacetylated units, *i.e.* 6.7%. This ratio allows the determination of the reaction yield, which is 60%.

	DA	DD	DM
Glucosamide unit fraction	0.156	0.810	0.034

Table IV.1 – Ratio of the different unit type in the final composition of the modified chitosan, expressed in degrees of acetylation (DA), deacetylation (DD) and modification (DM).

IV.3.3. ^1H relaxivities of $[Gd(DTTA\text{-}N'but)(H_2O)_2]^{2-}$

The relaxivities of $Gd(DTTA\text{-}N'but)(H_2O)_2]^{2-}$ were measured to ensure the non-complexation of the *N'*-butanoate. This element is essential in order to couple the complex covalently using the free carboxylic acid, while the metal centre acts as a protecting group on the four acetates to prevent any reaction of these groups, and therefore cross-links. The evidence of two water molecules in the inner sphere of the complex, proved by relaxivity, would therefore certify the non-coordination of the pending arm and its accessibility for the coupling reaction. Let's mention that even a fluxonial butanoate group, characterized by an equilibrium between the coordinating and the non-coordinating forms, would allow the complete conjugation, as the coupling shifts the equilibrium towards the uncomplexing form.

The ^1H NMRD profiles of $[Gd(DTTA\text{-}N'but)(H_2O)_2]^{2-}$ and $[Gd(DTTA\text{-}Me)(H_2O)_2]^{-}$ are measured at 25°C and 37°C (Figure IV.8). The complex $[Gd(DTTA\text{-}Me)(H_2O)_2]^{-}$ has two water molecules in its inner sphere (chelator presented in Figure IV.6).[51] Considering the few differences between the two complex structures, it becomes clear that $[Gd(DTTA\text{-}N'but)(H_2O)_2]^{2-}$ can not have a smaller hydration number, relaxivity being directly proportional to it. The modest relaxivities enhancement observed is most probably due to the more voluminous *N'*-substituent of the $[Gd(DTTA\text{-}N'but)(H_2O)_2]^{2-}$ complex.

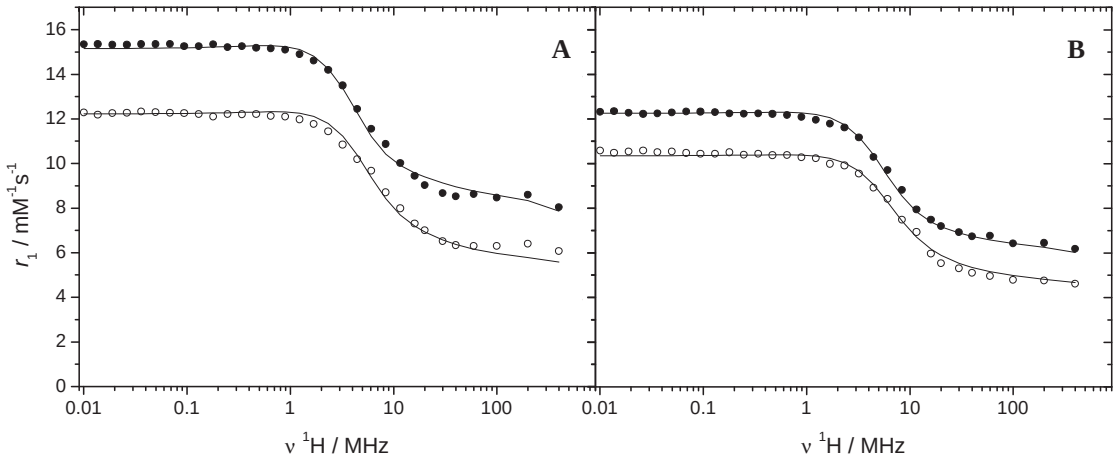

Figure IV.8 – ^1H NMRD profiles (A) $[Gd(DTTA\text{-}N'but)(H_2O)_2]^{2-}$ at 25°C (●) and 37°C (○) ; (B) $[Gd(DTTA\text{-}Me)(H_2O)_2]^{-}$ at 25°C (●) and 37°C (○). Lines obtained by SBM fit with parameters presented in Table IV.2.

The NMRD profiles are fitted with the Solomon-Bloembergen-Morgan theory to corroborate this assumption. The best fitting parameters for both fits are presented in Table IV.2. As expected, the rotational correlation time τ_R^{298} of $[Gd(DTTA\text{-}N'but)(H_2O)_2]^{2-}$ is slightly higher. The correlation time for the transient zero-field-splitting fluctuation τ_v^{298} and the mean square zero-field-splitting energy Δ^2 change significantly for the two fits. It should however be kept in mind that only the product of these two terms is considered in the electronic relaxation treatment (equation I.59). Though it is not constant, this product is consistent ($\Delta^2 \tau_v^{298} = 7.48 \cdot 10^8$ and $8.6 \cdot 10^8$ for $[Gd(DTTA\text{-}N'but)(H_2O)_2]^{2-}$ and $[Gd(DTTA\text{-}Me)(H_2O)_2]^-$, respectively).

In the absence of ^{17}O NMR data, the activation enthalpy $\Delta H^{\ddagger}$ and the water exchange rate k_{ex}^{298} cannot be reasonably fitted. Fitted values for the water exchange rate constant of the well described DTTA system $[Gd_2(pX(DTTA)_2)(H_2O)_4]^{2-}$ were therefore used to fix these parameters.[52]

Parameters / Complex	$[Gd(DTTA\text{-}N'but)(H_2O)_2]^{2-}$	$[Gd(DTTA\text{-}Me)(H_2O)_2]^-$
$\Delta H^{\ddagger}$ / kJ mol^{-1}	<u>45.4</u>	<u>45.4</u>
k_{ex}^{298} / 10^6 s^{-1}	<u>9</u>	<u>9</u>
E_R / kJ mol-1	26.0 ± 0.8	16.2 ± 0.6
τ_R^{298} / ps	136 ± 2	91 ± 1
E_v / kJ mol-1	<u>1</u>	<u>1</u>
τ_v^{298} / ps	34 ± 2	20 ± 1
D_{GdH}^{298} / 10^{-10} m^2 s^{-1}	<u>25</u>	<u>25</u>
E_{DGdH} / kJ mol^{-1}	<u>22</u>	<u>22</u>
Δ^2 / 10^{20} s^{-1}	0.22 ± 0.01	0.43 ± 0.03
q_{WAT}	<u>2</u>	<u>2</u>
$r_{GdH\ 1^{st}}$ / Å	<u>3.1</u>	<u>3.1</u>
$r_{GdH\ 2^{nd}}$ / Å	<u>3.5</u>	<u>3.5</u>

Table IV.2 – SBM fitted parameters of the NMRD profiles of $[Gd(DTTA\text{-}N'but)(H_2O)_2]^{2-}$ and $[Gd(DTTA\text{-}Me)(H_2O)_2]^-$. Fixed values underlined.

IV.3.4. ^{1}H relaxivities of {Chi[Gd(DTTA-N'but)(H$_2$O)$_2$]$^-$}

The NMRD profile of the linear chitosan compound were measured at 25°C and 37°C to characterize the ^{1}H relaxivity of this potential contrast agent (Figure IV.4). The relaxivities at low magnetic field are more than twice as high as that of the uncoupled complex. The profiles present a relaxivity hump between 10 and 200 MHz, characteristic for slowly rotating molecules.

The profiles were fitted first with the SBM-LS theory. The LS approach for internal rotation has been introduced, in comparison to the previous fittings, because the modified chitosan is a linear and most probably very flexible chain. The degree of freedom for the internal rotation is therefore expected to be high, characterized by a low LS factor S^2. Once again, the absence of ^{17}O NMR data has constrained us to fix the activation enthalpy $\Delta H^{\ddagger}$ and the water exchange rate constant k_{ex}^{298} using the fitted values of a well characterized DTTA system.

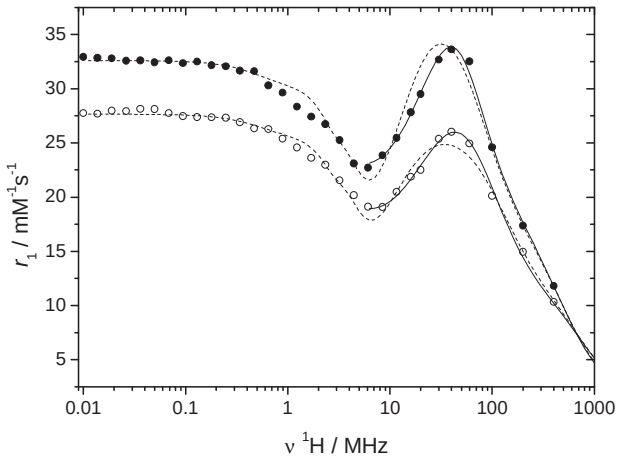

Figure IV.9 – NMRD profile of {Chi[Gd(DTTA-*N*'but)(H$_2$O)$_2$]$^-$} at 25°C (●) and 37°C (○) fitted with SBM-LS theory (straight line) and the Florence approach (dashed line) using parameters presented in Table IV.3.

Because of its very simple description of the electron spin relaxation,[40] the SBM theory fails at low magnetic field, particularly for slowly tumbling molecules.[53] A reasonable fit on the whole frequency range was consequently not achievable. For this reason, the fitting has been performed only above 6 MHz. The fit of this region, using the SBM-LS parameters presented in Table IV.3, is remarkably good. As expected, S^2 is particularly low, indicating a great freedom for the internal rotation.

The profile was subsequently fitted with the "modified Florence approach",[39-41] which was proved to be appropriate to fit slowly rotating molecules (Chapter I.4.11). Here again, the activation energy E_a and water exchange rate k_{ex}^{298} were fixed, using literature values.[52] The activation energy was calculated with the equation (I.65), obtained by comparison of the Arrhenius and the Eyring equations. The transient ZFS amplitude Δ and static ZFS amplitude D, given in cm^{-1}, have been converted into s^{-1} in order to use the same units than the SBM-LS fitted parameters (equation III.3). The Lipari-Szabo factor S^2 was fixed, using the values obtained with SBM-LS model.

Parameters / Fitting Method	SBM-LS	Florence
$\Delta H^{\ddagger}$ / kJ mol^{-1}	<u>45.4</u>	-
E_a / kJ mol^{-1}	-	<u>47.9</u>
k_{ex}^{298} $(1/\tau_M)$ / 10^6 s^{-1}	<u>9</u>	<u>9</u>
E_R / kJ mol^{-1}	28.3 ± 4.2	34.5
τ_R^{298} / ps	2700 ± 320	2170
E_l / kJ mol^{-1}	31 ± 3	25
τ_l^{298} / ps	367 ± 16	351
E_v / kJ mol^{-1}	<u>1</u>	<u>1</u>
τ_v^{298} / ps	11.0 ± 0.9	81.0
D_{GdH}^{298} / 10^{-10} m^2 s^{-1}	<u>25</u>	<u>25</u>
E_{DGdH} / kJ mol^{-1}	<u>22</u>	<u>22</u>
Δ / 10^{10} s^{-1}	0.34 ± 0.02	0.52
D / 10^{10} s^{-1}	-	0.87
S^2	0.21 ± 0.02	<u>0.21</u>
q	<u>2</u>	<u>2</u>
$r_{GdH\ 1^{st}}$ / Å	<u>3.1</u>	<u>3.1</u>
$r_{GdH\ 2^{nd}}$ / Å	<u>3.5</u>	<u>3.5</u>

Table IV.3 – Best fitting parameters of the NMRD profiles of the modified chitosan {Chi[Gd(DTTA-*N*'but)$(H_2O)_2]^-$} using the SBM-LS theory and the Florence approach. Fixed values underlined.

The two fitting methods lead to astonishingly coherent values for the global and local rotational correlation times τ_R^{298} and τ_l^{298} respectively, which suggests a particularly good characterization of the system.

IV.3.5. Effect of concentration on the relaxivity

The chitosan solution becomes very viscous when its concentration is higher than 0.1 % (w/v) (1 mg/mL). In order to determine the effect of the solution viscosity to allow working at higher concentrations, the relaxation times were measured at variable concentrations within the working range (Figure IV.10). The relationship between Gd^{3+} and chitosan concentrations is set with the ratio of modified unit DM and the mean molar mass of a glucosamine unit (M_{chi} = 187.01 g / mol), determined with the experimental chitosan composition (equation IV.6).

$$\%\ (w/v) = \frac{10^2}{10^3}\frac{m_{Chi}}{V} = 0.1\ \frac{M_{chi}n_{chi}}{V} = 0.1\ \frac{M_{chi}}{DM}\frac{n_{Gd}}{V} = 0.1\ \frac{M_{chi}}{DM}\left[Gd^{III}\right] \qquad \text{(IV.6)}$$

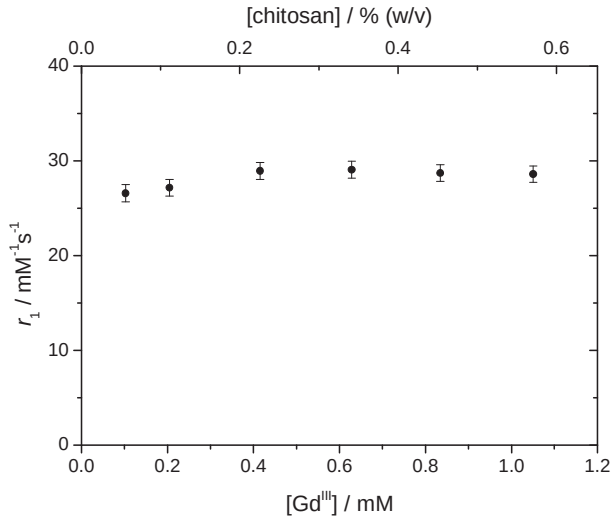

Figure IV.10 – Influence of the viscosity, due to the chitosan concentration, on the relaxivity of {Chi[Gd(DTTA-*N*'but)$(H_2O)_2]^-$} ; 20 MHz, 25°C.

The Figure IV.10 shows that the high viscosity of the concentrated chitosan solution (more than 0.2%) has no significant influence on the relaxivity within the working concentration range. Calculations of the propagation of uncertainty has been performed by considering a relative error of 3% on both the observed and the diamagnetic reference relaxation times and

by assuming the Gd^{3+} concentration as being exact. The equation III.2 has been used to determine the relative error on the relaxivity r_1.

IV.3.6. Time stability of the relaxivity

As a carbohydrate, the chitosan solution is a perfect media for bacterial growth. The stability of the relaxivity was controlled during one month to ensure metabolization or internalization of the Gd^{3+} complex in invisible microorganisms could not induce undesirable effect on the measurements (Figure IV.11). The relaxivity of the clear solution turned out to be very stable in a time period of one month when the solution was kept at 4°C. When the white cottony bacterial colony is visible, the solution has to be discarded.

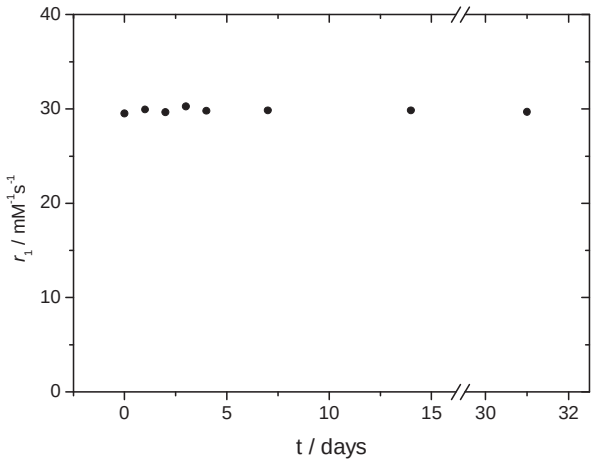

Figure IV.11 – Evolution of the relaxivity of {Chi[Gd(DTTA-*N*'but)$(H_2O)_2]^-$} with time ; 20 MHz, 25°C.

*IV.3.7. Formation of the nanogels Ng{Chi[Gd(DTTA-*N*'but)$(H_2O)_2]^-$}*

The formation of nanogels with the modified chitosan has potentially very interesting contrast agent properties. Contrary to other nanoparticles implying gadolinium complexes,[54,55] constituted by a rigid core with chelate complexes on the surface, this nanogel is formed by a folded linear chain, with randomly distributed Gd^{3+} complexes. This leads to a flexible and porous material, constituted mainly by water, which can freely diffuse within the particle. A potential CA formed by such a hydrogel would therefore present the benefits of nanoparticle based CA, *i.e.* the size and the Gd^{3+} complex density, with a biocompatible and biodegradable core.

The principle of the ionotropic, or ionic, gelation (Figure IV.3 A) forming such structures is to use the anion triphosphate (TPP) to form linkage between the positively charged primary amines by electrostatic interaction, inducing a dynamic intra- and intermolecular folding. The nanogels are subsequently electrostatically coated with sodium alginate, to stabilize the particles at physiological pH and to obtain negatively charged surfaces.[21] The method has been chosen amongst the several methods allowing the preparation of nanoparticles from the chitosan for its simplicity and its mild and aqueous conditions.[56] The formation of the nanogels was not trivial and hardly reproducible, because of the easy precipitation of the material in presence of TPP and difficulty of complete solubilisation of the modified chitosan. It had however been possible to form the nanogels, which was confirmed by dynamic light scattering (DLS), and transmission electron microscopy (TEM), two methods commonly used to characterize the physicochemical properties of nanoparticles, including their size, morphology, surface charge and stability.

IV.3.8. Ng{Chi[Gd(DTTA-N'but)(H_2O)$_2$]} characterization

Dynamic Light Scattering

The DLS measures time dependent fluctuations in scattering intensity produced by particles in Brownian motion.[57] The velocity of the Brownian motion of particles, defined as the translational diffusion coefficient *D*, is related to their size by the Stokes-Einstein relation (equation IV.7), where k_B is the Boltzmann constant, *T* the temperature and η the viscosity coefficient of the solvent. The reported diameter corresponds to that of a sphere having the same diffusion coefficient, implying the necessary assumption of the sphericity of the nanogels. Moreover, this diameter does not correspond to the "hard core" of the particles, but encompasses the solvent layer diffusing with the particle. This diameter is known as the hydrodynamic diameter d_H and the boundary demarcating the hydrodynamic entity from the bulk is called the slipping plane.

$$d_H = \frac{k_B T}{3\pi\eta D} \qquad \text{(IV.7)}$$

The most common parameters for nanoparticle size DLS characterization are the Z-average and the polydispersity index PdI (Table IV.4). The Z-average arises from a single exponential fitting of the correlation function and corresponds to the intensity average hydrodynamic size. The size distribution is characterized by the PdI, related to the standard deviation of the single

exponential fit. The complete size distribution (Figure IV.12), obtained by fitting the correlation function with multi-exponential algorithms, is another way of presenting the result of particle size measurements.

Parameters	modified chi-Ng	standard chi-Ng (average on 6 batches)	
		in H_2O	in PBS
Z-average / nm	374 ± 4	535 ± 74	403 ± 36
PdI	0.20 ± 0.02	0.465 ± 0.050	0.252 ± 0.018
Zeta potential / mV	-56.8 ± 1.0	-63.3 ± 0.7	-

Table IV.4 **–** Z-average, PdI and zeta potential of Ng{Chi[Gd(DTTA-*N*'but)$(H_2O)_2]^-$} at day 0 compared to unmodified chitosan nanogels in water and in PBS.

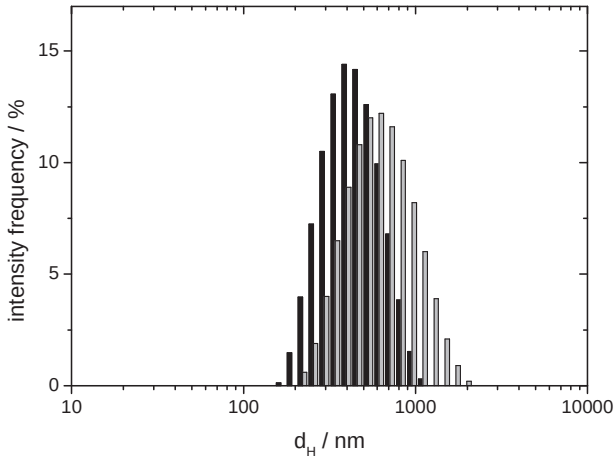

Figure IV.12 **–** Size distribution of the modified nanogels Ng{Chi[Gd(DTTA-*N*'but)$(H_2O)_2]^-$} (black) and an example of unmodified chitosan nanogels (grey) determined by Dynamic Light Scattering.

The temporal stability of the formed nanogels was confirmed by the tallying results of the DLS experiments performed on the day of the particles production and after 5, 9 and 29 days.

The colloidal stability of the particles was demonstrated with the same instrumentation by measuring the zeta potential. The latter is a function of the surface charge density and corresponds to the electrostatic potential at the slipping plane, *i.e.* the boundary inside which ions and nanoparticles form a stable entity. This parameter is determined from the mobility of the particles and the ions within the slipping plane when performing an electrophoretic light

scattering (ELS) experiment. During this experiment, an electric field is applied through the dispersion, which induces a migration of the entities with velocities proportional to their zeta potential. This potential can be considered as the force preventing the particles aggregating or flocculating, and gives therefore indications on their colloidal stability. Entities with zeta potential higher than ± 30 mV are generally considered as stable.[58,59]

When compared to unmodified chitosan nanogels, one can notice that the Ng{Chi[Gd(DTTA-*N'*but)$(H_2O)_2]^-$} are significantly smaller (ΔZ-average ≈ 160 nm, Table IV.4). The inaccessible substituted amines and the resulting steric hindrance, preventing more ionic interactions, might explain this difference. The PdI is also smaller than the unmodified nanogels, indicating a narrower distribution, which could arise from the absence of bigger particles. The Z-average and the PdI of the formed Ng are comparable to that of unmodified Ng in a high ionic force medium, such as PBS (Table IV.4).

Transmission Electron Microscopy

The TEM is another widely used technique to observe the particles size and their morphology. It should however be kept in mind that the sample has to be dried, which might alter the size and the morphology of the particles, particularly for the water-soaked hydrogels. Moreover, the reconcentration of the dispersion induced by the droplet evaporation can generate bigger aggregates. Evidence of the formation of modified chitosan nanogels is nevertheless visible (Figure IV.13). The observed light grey streaks arise probably from salts residues (NaCl) and alginate excess, inherent to this dynamic coating method.

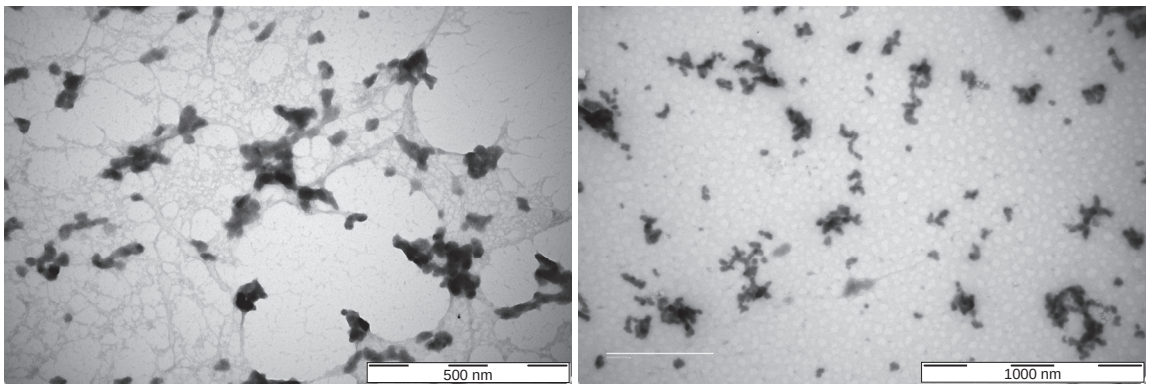

Figure IV.13 – Transmission Electron Microscopy of the formed nanogels.

IV.3.9. ^1H relaxivities of Ng{Chi[Gd(DTTA-N'but)$(H_2O)_2]^-$}

The relaxivity of the nanogel was characterized by the measuring of its $1/T_1$ NMRD profile (Figure IV.14). Despite the reconcentration, the final Gd^{3+} concentration was rather low (~ 0.13 mM) and had to be determined by ICP-MS. The long relaxation times (~ 500 ms) induced by so low concentrations imply a substantial uncertainty on the relaxivities, particularly on the FFC relaxometer, which had some difficulties measuring coherent relaxation times.

It is relevant to notice that the relaxivities are lower than those of the linear chitosan chains. Moreover, the small hump from 10 to 200 MHz suggests that the formed particles are smaller than the starting linear chitosan, while the opposite was expected because a nanogel is formed by several chitosan strains. The experimental data were fitted the same way than as in section IV.3.4, *i.e.* using the SBM-LS approach from mid-field to high-field and the modified Florence approach to fit the whole profile. The fitted parameters are presented in Table IV.5.

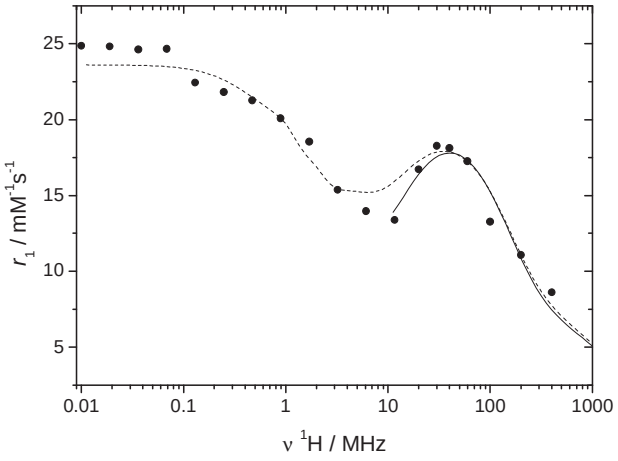

Figure IV.14 – NMRD profile and SBM-LS (straight) and Florence approach (dash) fittings of the Ng{Chi[Gd(DTTA-*N*'but)$(H_2O)_2]^-$} at 25°C.

While the nanogels formed were expected to be bigger than the linear chitosan chain, the two methods led to surprisingly low rotational correlation times τ_R^{298} and τ_l^{298}. The fixation of certain fitting parameters might induce such incongruous values. First, the number of water molecules in the inner sphere has a proportional effect on the relaxivities. A partial Gd^{3+} complexation by the triphosphate oxygen would induce a q lower than 2, and would have repercussions on the fitted parameters ($\tau_R^{298} \approx 2000$ ps when q is fixed to 1). Secondly, the

water exchange rate k_{ex}^{298} has been fixed to a rapid exchange value, taken from a well characterized system.[52] A slower exchange, caused by a limited diffusion of the water molecules inside the nanogels for instance, would considerably influence the fitted parameters ($\tau_R^{298} \approx 2700$ ps when k_{ex}^{298} is fixed to $1 \cdot 10^6$ s^{-1}). Finally, the LS factor S^2, expected to be higher in the case of the more rigid nanogels, reaches the unreasonable value of 0.1 when fitted, indicating a higher degree of freedom for internal rotation. It was therefore fixed to the value fitted for the linear chitosan, resulting in a drop of the global rotation correlation time ($\tau_R^{298} \approx 2600$ ps when S^2 is fitted to 0.1).

Parameters / Fitting Method	SBM-LS	Florence
k_{ex}^{298} $(1/\tau_M)$ / 10^6 s^{-1}	<u>9</u>	<u>9</u>
τ_R^{298} / ps	1080 ± 150	1050
τ_l^{298} / ps	98 ± 21	107
τ_v^{298} / ps	87 ± 25000	25
D_{GdH}^{298} / 10^{-10} m^2 s^{-1}	<u>25</u>	<u>25</u>
E_{DGdH} / kJ mol^{-1}	<u>22</u>	<u>22</u>
Δ / 10^{10} s^{-1}	0.7 ± 200	0.33
D / s^{-1}	-	0.39
S^2	<u>0.21</u>	<u>0.21</u>
q	<u>2</u>	<u>2</u>
$r_{GdH\ 1^{st}}$ / Å	<u>3.1</u>	<u>3.1</u>
$r_{GdH\ 2^{nd}}$ / Å	<u>3.5</u>	<u>3.5</u>

Table IV.5 – Best fitting parameters of the NMRD profiles of {Chi[Gd(DTTA-*N*'but)$(H_2O)_2]^-$} nanogels using the SBM-LS theory and the Florence approach. Fixed values underlined.

^{17}O NMR measurement would be an indispensable tool to investigate further this system by determining the water exchange rate and the number of water molecules in the inner sphere. These experiments require however a solution about 100 more concentrated, and therefore much larger amount of modified chitosan nanogels. Moreover, highly concentrated solutions would probably induce undesirable effects such as precipitation, aggregation of the nanogels or really important viscosity.

IV.4. Conclusion

This work described the synthesis, the structural characterization and the relaxivity measurements of potential contrast agents based on the polysaccharide chitosan. The idea developed to create such a compound was to bind covalently a Gd^{3+} chelate complex to the deacetylated amine of the chitosan. Experimental limitations have constrained us to use an alternative method for the conjugation of the CA on the polymer, by complexing the chelator first and then grafting the complex. This has been performed though an uncomplexing arm of a modified DTTA chelating agent. The non-complexation and availability of this arm was proved by comparing the $1/T_1$ NMRD profiles of the synthesized complex to that of the well known system [Gd(DTTA-Me)(H_2O)$_2$]$^-$.

The coupling of the uncomplexing butanoate arm with the primary amine of the chitosan has been performed successfully using the coupling agents EDC / Sulfo-NHS in water. The structural characterization of the modified chitosan has been performed by ^{1}H NMR to determine the degree of acetylation DA and by elemental analysis and ICP-MS to determine the degree of modification DM. The final chitosan linear chain was composed by 81% of deacetylated, 15.6% of acetylated and 3.4% of modified units. The NMRD profile of the linear modified chain {Chi[Gd(DTTA-*N*'but)(H_2O)$_2$]$^-$}, characterizing its relaxivity, have been measured and fitted with the Solomon-Bloembergen-Morgan theory with the Lipari-Szabo model for internal rotation (SBM-LS) and with the modified Florence approach.

In the absence of relaxometric characterization for comparable chitosan conjugates, the relaxivity of the modified linear chitosan are compared with other linear systems. The relaxivity of {Chi[Gd(DTTA-*N*'but)(H_2O)$_2$]$^-$} turned out to be comparable to other linear polymers (Table IV.6). The relaxivities of less flexible and more compact highly branched macromolecular contrast agents, such as the dendritic PAMAM-G4-[Gd(DOTA *p*Bn)(H_2O)]$^-$, are however about twice as high.[60]

To make this material more rigid and more compact, nanogels have been formed from the modified linear chitosan. This was done by means of the anion triphosphate, which induced a folding through ionic interaction with the positively charged amines of the chitosan. The

formed particles were subsequently coated, always via ionic interactions, with the negatively charged polysaccharide alginate. The nanogels were characterized with DLS and TEM, determining their hydrodynamic size and size distribution. Finally the NMRD profiles of the hydrogels measured and fitted with the SBM-LS and the Florence approaches. This system presented unfortunately disappointing relaxivities. Some fixed parameters used for the fits, such as the water exchange rate k_{ex}^{298} and the number of water molecules in the inner sphere of the complex *q*, might have been erroneous. Moreover, the fitted parameters, including the LS factor S^2 and the global and local rotational correlation times τ_R^{298} and τ_l^{298}, presented some unreasonable values. The impossibility of performing ^{17}O NMR measurements on this system did unfortunately not allow further investigations on this interesting and promising compound.

Linear compound	r_1 $mM^{-1}s^{-1}$	q	ν ^1H MHz	T °C	Ref
{Chi[Gd(DTTA-*N*'but)$(H_2O)_2$]$^-$}	33.6	2	40	25	
[Gd(EGTA-BA)(H_2O)-$(CH_2)_{12}]_n^{n+}$	15.5	1	40	20	61
P(Gd-DTPA-PETO-EG-PM)	15.2	1	80	25	62
Gd(DTPA-CHD)	8.8	1	40	37	63
Gd(DTPA-BA)-PEG	5.5	1	40	25	64

Table IV.6 **–** Comparative table for the relaxivities of linear polymeric compounds designed as potential CA.

IV.5. Acknowledgements

I warmly thank the following persons for their precious contributions to this work :

Dr. MER Christine Wandrey and Catherine Schütz, from the Laboratory for Regenerative Medicine & Pharmacobiology at EPFL for having initiated this collaboration.

Catherine Schütz for her excellent work on the nanogels, including the formation, the DLS and TEM measurements, and for the numerous discussions and pieces of advice regarding this project.

Kim Von Allmen for his help on sephadex purifications and the various assists.

Dr. Alexei Ulianov from Institute of Mineralogy and Geochemistry at Université de Lausanne for the ICP-MS measurements.

Dr. Emmanuel Deiters for his advice on the organic synthesis of the ligand.

IV.6. References

1. Illum, L.; Jabbal-Gill, I.; Hinchcliffe, M.; Fisher, A. N.; Davis, S. S. *Advanced Drug Delivery Reviews* **2001,** *51*, 81-96.
2. Hudson, S. M.; Smith, C. In *Biopolymers from Renewable Resources;* Kaplan, D. L. Ed.; Springer: New York, 1998; pp. 96-118.
3. Arcidiacono, S.; Kaplan, D. L. *Biotechnology and Bioengineering* **1992,** *39*, 281-286.
4. Rinaudo, M. *Progress in Polymer Science* **2006,** *31*, 603-632.
5. Illum, L. *Pharmaceutical Research* **1998,** *15*, 1326-1331.
6. Illum, L.; Farraj, N. F.; Davis, S. S. *Pharmaceutical Research* **1994,** *11*, 1186-1189.
7. Lim, S. H.; Hudson, S. M. *Journal of Macromolecular Science-Polymer Reviews* **2003,** *C43*, 223-269.
8. Inoue, K.; Ohto, K.; Yoshizuka, K.; Yamaguchi, T.; Tanaka, T. *Bulletin of the Chemical Society of Japan* **1997,** *70*, 2443-2447.
9. Inoue, K.; Yoshizuka, K.; Ohto, K. *Analytica Chimica Acta* **1999,** *388*, 209-218.
10. Tokumitsu, H.; Ichikawa, H.; Fukumori, Y.; Block, L. H. *Chemical & Pharmaceutical Bulletin* **1999,** *47*, 838-842.
11. Shikata, F.; Tokumitsu, H.; Ichikawa, H.; Fukumori, Y. *European Journal of Pharmaceutics and Biopharmaceutics* **2002,** *53*, 57-63.
12. Saha, T. K.; Ichikawa, H.; Fukumori, Y. *Carbohydrate Research* **2006,** *341*, 2835-2841.
13. Aime, S.; Gianolio, E.; Uggeri, F.; Tagliapietra, S.; Barge, A.; Cravotto, G. *Journal of Inorganic Biochemistry* **2006,** *100*, 931-938.
14. Fujimoto, T.; Ichikawa, H.; Akisue, T.; Fujita, I.; Kishimoto, K.; Hara, H.; Imabori, M.; Kawamitsu, H.; Sharma, P.; Brown, S. C.; Moudgil, B. M.; Fujii, M.; Yamamoto, T.; Kurosaka, M.; Fukumori, Y. *Applied Radiation and Isotopes* **2009,** *67*, S355-S358.
15. Tan, W. B.; Zhang, Y. *Journal of Nanoscience and Nanotechnology* **2007,** *7*, 2389-2393.
16. Huang, M.; Huang, Z. X. L.; Bilgen, M.; Berkland, C. *Nanomedicine-Nanotechnology Biology and Medicine* **2008,** *4*, 30-40.
17. Darras, V.; Nelea, M.; Winnik, F. M.; Buschmann, M. D. *Carbohydrate Polymers* **2010,** *80*, 1137-1146.

18. Nam, T.; Park, S.; Lee, S. Y.; Park, K.; Choi, K.; Song, I. C.; Han, M. H.; Leary, J. J.; Yuk, S. A.; Kwon, I. C.; Kim, K.; Jeong, S. Y. *Bioconjugate Chemistry* **2010,** *21*, 578-582.
19. Bodmeier, R.; Chen, H. G.; Paeratakul, O. *Pharmaceutical Research* **1989,** *6*, 413-417.
20. Pan, Y.; Li, Y. J.; Zhao, H. Y.; Zheng, J. M.; Xu, H.; Wei, G.; Hao, J. S.; Cui, F. D. *International Journal of Pharmaceutics* **2002,** *249*, 139-147.
21. Schutz, C. A.; Schmitt, F.; Juillerat-Jeanneret, L.; Wandrey, C. *Chimia* **2009,** *63*, 220-222.
22. Borges, O.; Borchard, G.; Verhoef, J. C.; de Sousa, A.; Junginger, H. E. *International Journal of Pharmaceutics* **2005,** *299*, 155-166.
23. Platzek, J.; Niedballa, U.; Radüchel, B. **1996,** *DE 19508058*, 13.
24. Livramento, J. B.; Helm, L.; Sour, A.; O'Neil, C.; Merbach, A. E.; Tóth, É. *Dalton Transactions* **2008**, 1195-1202.
25. Hirai, A.; Odani, H.; Nakajima, A. *Polymer Bulletin* **1991,** *26*, 87-94.
26. Vårum, K. M.; Anthonsen, M. W.; Grasdalen, H.; Smidsrød, O. *Carbohydrate Research* **1991,** *211*, 17-23.
27. Corsi, D. M.; Platas-Iglesias, C.; Bekkum, H. v.; Peters, J. A. *Magnetic Resonance in Chemistry* **2001,** *39*, 723-726.
28. Vold, R. L.; Waugh, J. S.; Klein, M. P.; Phelps, D. E. *Journal of Chemical Physics* **1968,** *48*, 3831-&.
29. Ferrante, G.; Sykora, S. In *Advances in Inorganic Chemistry;* van Eldik, R.; Bertini, I. Eds.: San Diego, 2005; pp. 405-470.
30. Ammann, C.; Meier, P.; Merbach, A. E. *Journal of Magnetic Resonance* **1982,** *46*, 319-321.
31. Solomon, I. *Physical Review* **1955,** *99*, 559-565.
32. Solomon, I.; Bloembergen, N. *Journal of Chemical Physics* **1956,** *25*, 261-266.
33. Bloembergen, N. *Journal of Chemical Physics* **1957,** *27*, 572-573.
34. Bloembergen, N.; Morgan, L. O. *The Journal of Chemical Physics* **1961,** *34*, 842-850.
35. Lipari, G.; Szabo, A. *Journal of the American Chemical Society* **1982,** *104*, 4546-4559.
36. Lipari, G.; Szabo, A. *Journal of the American Chemical Society* **1982,** *104*, 4559-4570.
37. Yerly, F. *VISUALISEUR 2.3.6* **2004,** *EPFL*.
38. Yerly, F. *OPTIMISEUR 3.0.0* **2002,** *EPFL*.
39. Bertini, I.; Kowalewski, J.; Luchinat, C.; Nilsson, T.; Parigi, G. *Journal of Chemical Physics* **1999,** *111*, 5795-5807.

40. Kruk, D.; Nilsson, T.; Kowalewski, J. *Physical Chemistry Chemical Physics* **2001,** *3*, 4907-4917.
41. Kowalewski, J.; Kruk, D.; Parigi, G. In *Advances in Inorganic Chemistry*; Academic Press, 2005; pp. 41-104.
42. Bertini, I.; Galas, O.; Luchinat, C.; Parigi, G. *Journal of Magnetic Resonance Series A* **1995,** *113*, 151-158.
43. Laus, S.; Ruloff, R.; Toth, E.; Merbach, A. E. *Chemistry-a European Journal* **2003,** *9*, 3555-3566.
44. Kubícek, V.; Tóth, É.; Rudi van Eldik and Colin, D. H. In *Advances in Inorganic Chemistry*; Academic Press, 2009; pp. 63-129.
45. Kato, Y.; Onishi, H.; Machida, Y. *Carbohydrate Research* **2002,** *337*, 561-562.
46. Ruloff, R.; Arnold, K.; Beyer, L.; Grunder, W.; Wagner, M.; Hoyer, E. *Zeitschrift Fur Anorganische Und Allgemeine Chemie* **1995,** *621*, 807-811.
47. Ruloff, R.; Muller, R. N.; Pubanz, D.; Merbach, A. E. *Inorganica Chimica Acta* **1998,** *276*, 15-23.
48. Sheehan, J. C.; Hlavka, J. J. *Journal of the American Chemical Society* **1957,** *79*, 4528-4529.
49. Staros, J. V.; Wright, R. W.; Swingle, D. M. *Analytical Biochemistry* **1986,** *156*, 220-222.
50. *http://www.piercenet.com/products/browse.cfm?fldID=02030312*.
51. Moriggi, L.; Cannizzo, C.; Prestinari, C.; Berriere, F.; Helm, L. *Inorganic Chemistry* **2008,** *47*, 8357-8366.
52. Costa, J.; Toth, E.; Helm, L.; Merbach, A. E. *Inorganic Chemistry* **2005,** *44*, 4747-4755.
53. Helm, L. *Progress in Nuclear Magnetic Resonance Spectroscopy* **2006,** *49*, 45-64.
54. Moriggi, L.; Cannizzo, C.; Dumas, E.; Mayer, C. R.; Ulianov, A.; Helm, L. *Journal of the American Chemical Society* **2009,** *131*, 10828-10829.
55. Oyewumi, M. O.; Yokel, R. A.; Jay, M.; Coakley, T.; Mumper, R. J. *Journal of Controlled Release* **2004,** *95*, 613-626.
56. Nagpal, K.; Singh, S. K.; Mishra, D. N. *Chemical & Pharmaceutical Bulletin* **2010,** *58*, 1423-1430.
57. Dhawan, A.; Sharma, V. *Analytical and Bioanalytical Chemistry***,** *398*, 589-605.
58. *www.malvern.com*, Malvern Instuments : Technical support Library.
59. *http://www.nbtc.cornell.edu/facilities/downloads/Zeta potential - An introduction in 30 minutes.pdf*, Malvern Instruments : Zeta Potential An Introduction in 30 Minutes

60. Jászberényi, Z.; Moriggi, L.; Schmidt, P.; Weidensteiner, C.; Kneuer, R.; Merbach, A. E.; Helm, L.; Tóth, E. *Journal of Biological Inorganic Chemistry* **2007,** *12*, 406-420.
61. Dunand, F. A.; Tóth, É.; Hollister, R.; Merbach, A. E. *Journal of Biological Inorganic Chemistry* **2001,** *6*, 247-255.
62. Yan, G. P.; Zhuo, R. X.; Xu, M. Y.; Zhang, X.; Li, L. Y.; Liu, M. L.; Ye, C. H. *Polymer International* **2002,** *51*, 892-898.
63. Duarte, M. G.; Gil, M. H.; Peters, J. A.; Colet, J. M.; Vander Elst, L.; Muller, R. N.; Geraldes, C. F. G. C. *Bioconjugate Chemistry* **2001,** *12*, 170-177.
64. Tóth, E.; van Uffelen, I.; Helm, L.; Merbach, A. E.; Ladd, D.; Briley-Sæbø, K.; Kellar, K. E. *Magnetic Resonance in Chemistry* **1998,** *36*, S125-S134.

Chapter V :

Monomeric and dimeric bombesin Gd-DOTA complexes : potential MRI contrast agents for tumor targeting

V.1. Introduction 149
V.2. Experimental Section 151
V.2.1 Synthesis and characterization 151
V.2.2 Sample preparation 156
V.2.3 ^{1}H relaxivities 156
V.2.4 Data treatment 157
V.3. Results and discussion 158
V.3.1 Ligands and conjugates synthesis 158
V.3.2 ^{1}H relaxivities of the four Gd-DOTA-bombesin conjugates 158
V.4. Conclusion 163
V.5. Acknowledgements 164
V.6. References 165

V.1. Introduction

The overexpression of various peptide receptors on the surface of many malignant tumor cells has been investigated intensively over the last decades as a target for MRI and radionuclide therapy.[1-3] Somatostatin, which has been successfully exploited for imaging and therapy, but also cholecystokinin, neurotensin and bombesin receptors showed the most interesting and promising potential.[4-9] The bombesin receptors, and more precisely the subtype gastrin-releasing peptide (GRP) receptors, present a particular interest, as they are overexpressed by many prevalent malignant tumor cells, such as prostate, breast or lung cancer.[10-12] The development of MRI contrast agents (CAs) coupled to the neurotransmitter bombesin (BN) analogues represents therefore a promising route to target GRP receptor-expressing tumors as a MRI diagnostic tool (Figure V.1).

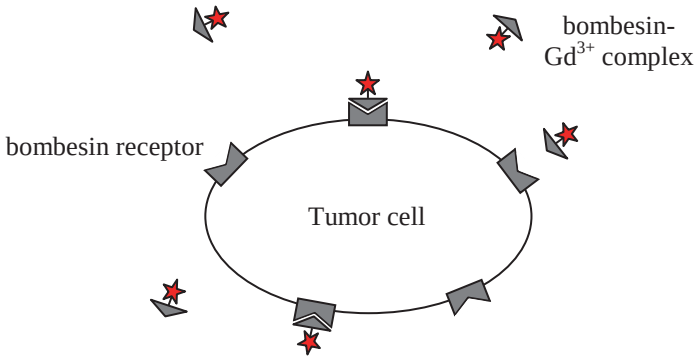

Figure V.1 – Strategy to target BN receptor overexpressing tumor cell with a MRI CA (★) through the interaction bombesin-bombesin receptor.

A strong and specific interaction between the peptide vector and its receptor is an essential factor for an effective targeting and imaging of the targeted cell. The optimization of the affinity and the specificity of this interaction through the development of different peptides analogues is therefore an important contribution to this targeting strategy. Moreover, the use of multivalent peptide compounds has been proved to increase markedly the binding affinity between of the labeled peptide and its receptor.[13,14]

Within this framework, four compounds presenting bombesin peptide coupled to the chelating unit DOTA and developed as potential targeted CAs have been synthesized by Dr. Abiraj Keelara.[4] These potential CAs were prepared as mono-peptide and bis-peptide conjugates, involving two different bombesin analogues, the Ahx-Bombesin(4-14) and the Lys^3-Bombesin (Figure V.2). The tumor cell uptake and the cellular retention of these four compounds have been measured and compared.[4]

This chapter presents the synthesis, the relaxometric measurements and the theoretical fit characterization of the two mono-bombesin Gd^{3+} complexes {Lys^3-BN[Gd(DOTA)(H_2O)]} and {Ahx-BN(4-14)[Gd(DOTA)(H_2O)]} and their dimeric analogues {Ahx-BN(4-14)$_2$[Gd(DOTA)(H_2O)]} and {(Lys^3-BN)$_2$[Gd(DOTA)(H_2O)]}.

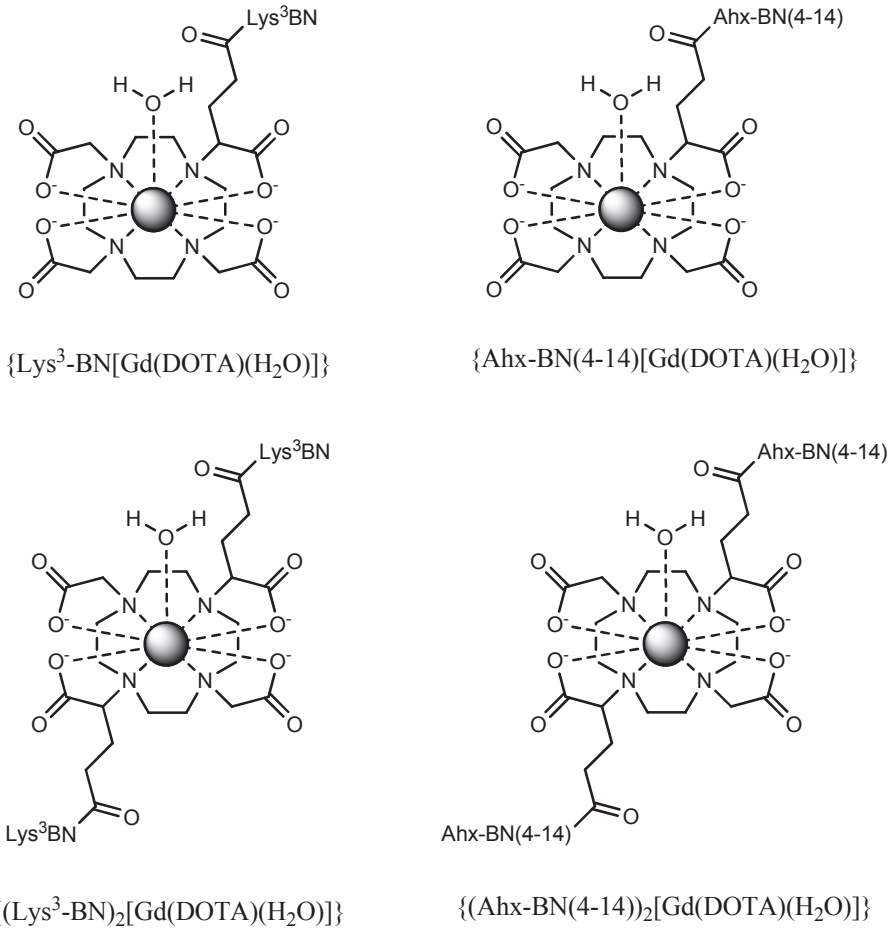

{Lys^3-BN[Gd(DOTA)(H_2O)]}

{Ahx-BN(4-14)[Gd(DOTA)(H_2O)]}

{(Lys^3-BN)$_2$[Gd(DOTA)(H_2O)]}

{(Ahx-BN(4-14))$_2$[Gd(DOTA)(H_2O)]}

Figure V.2 – The four studied Gd-DOTA complexes composed by the two mono-peptide conjugates and their dimeric analogues.

V.2. Experimental Section

V.2.1 Synthesis and characterization

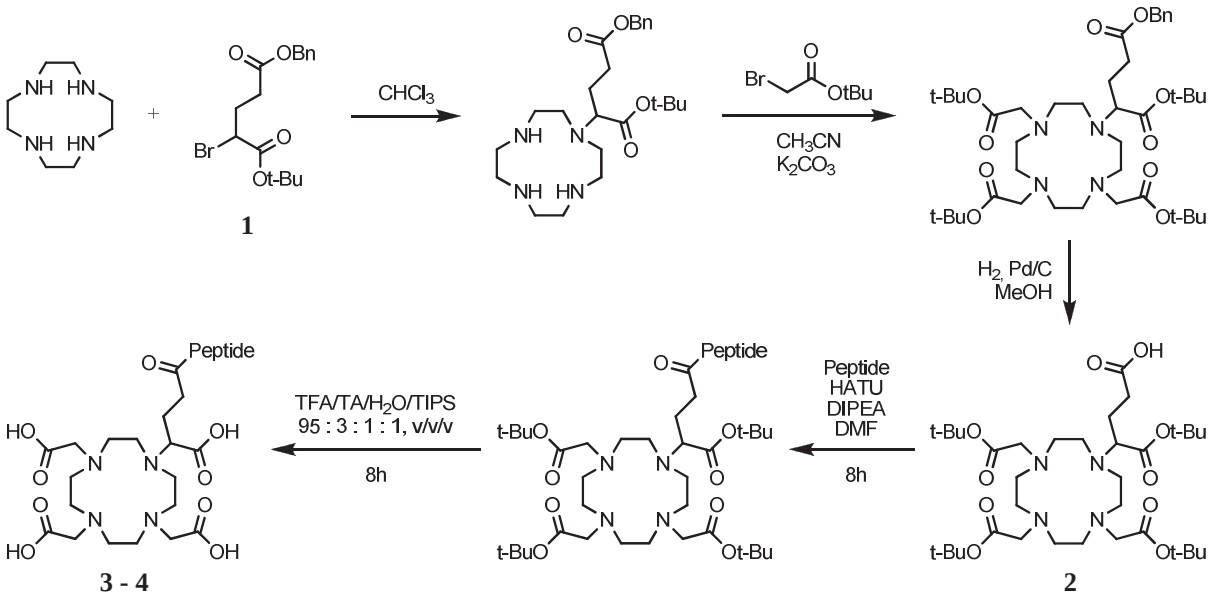

Figure V.3 **–** General synthesis scheme for the mono-peptide compounds.[4,15]

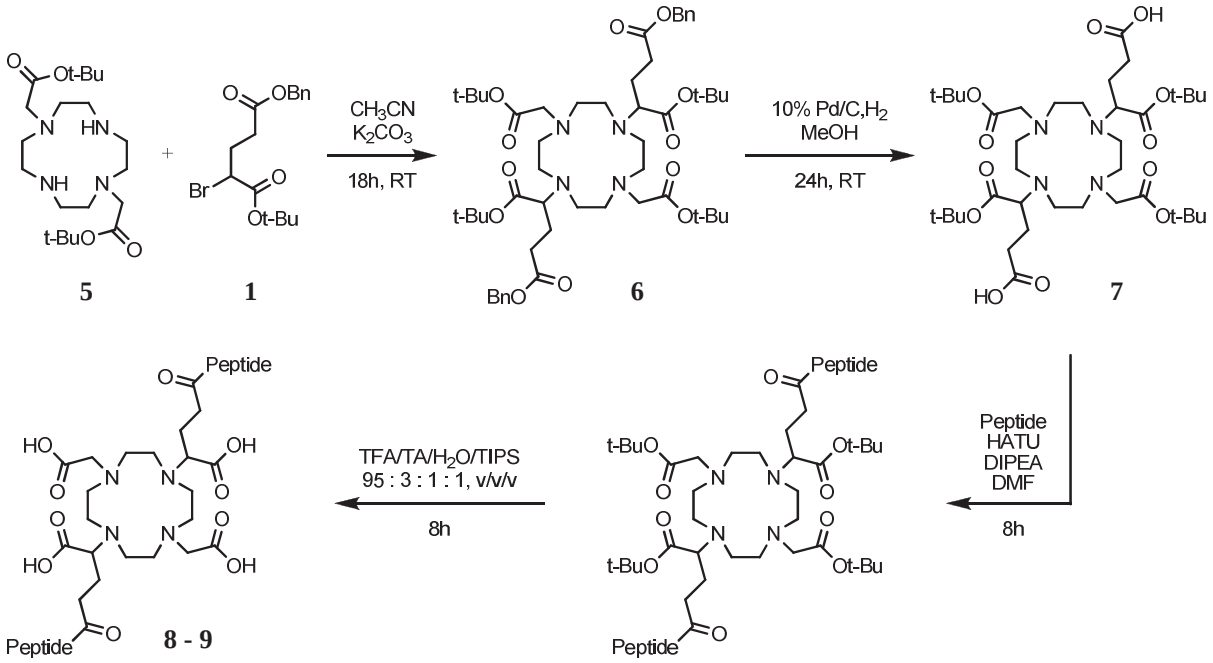

Figure V.4 **–** General synthesis scheme for bis-peptide compounds.[4]

Monomeric and dimeric peptide compounds have been synthesized with two bombesin analogues : the Ahx-Bombesin(4-14) and the Lys^3-Bombesin (Figure V.5).

Lys^3-Bombesin =

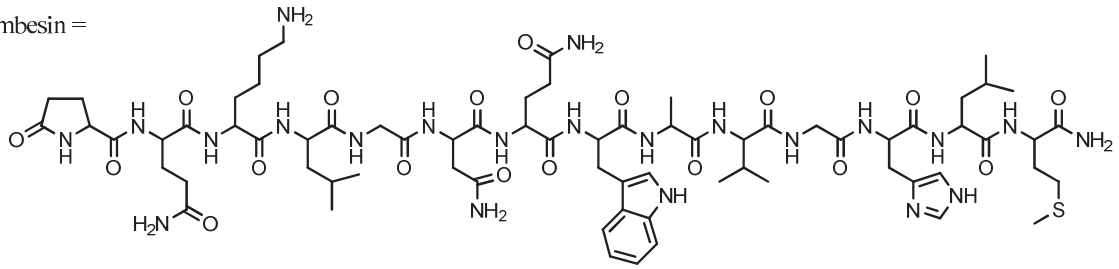

Ahx-Bombesin(4-14) =

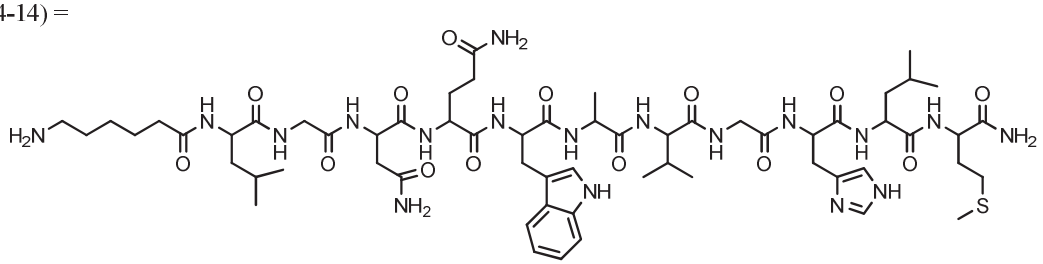

Figure V.5 – The bombesin analogues Lys^3-Bombesin and Ahx-Bombesin(4-14).

All the synthesis have been performed by Dr. Abiraj Keelara in the laboratory of Prof. Helmut R. Maecke, Division of Radiological Chemistry, University Hospital Basel, Switzerland.

Materials and Methods

All chemicals were obtained from commercial sources and used without further purification. Rink amide 4-methylbenzhydrylalanine (MBHA) resin (0.34 mmole/g; 100-200 mesh) and all the Fmoc-protected amino acids are commercially available from NovaBiochem (Laeufelfingen, Switzerland). 1,4,7,10-Tetraazacyclododecane and 1,4,7,10-Tetraazacyclododecane-1,7-bis(t-butyl acetate) (**5**) was purchased from Macrocyclics, Dallas, Texas, USA. Electrospray ionisation (ESI) mass spectroscopy was carried out with a Finnigan SSQ7000 (Bremen, Germany) and MALDI-MS measurements on a Voyager sSTR equipped with an Nd:YAG laser (Applied Biosystems, Framingham, USA). Analytical high-performance liquid chromatography (HPLC) was performed on a Hewlett Packard 1050 HPLC system with a multiwavelength detector and a flow-through Berthold LB 506 Cl γ-detector using a Macherey-Nagel Nucleosil 120 C18 column. Preparative HPLC was performed on a Metrohm HPLC system LC-CaDI 22–14 with a Macherey-Nagel VP 250/21 Nucleosil 100–5 C18 column. Both analytical and preparative columns were eluted with a

gradient system of mixtures of H_2O with 0.1% TFA (solvent A) and acetonitrile (solvent B). The NMR spectra were recorded on a Bruker DRX 500 spectrometer using a triple inverse probe. ^1H shifts were referenced to DMSO-d6 at 2.49 ppm. The 1D-^1H, ^1H-^1H-COSY, 1D-^{13}C and ^1H-^{13}C-COSY (HSQC) experiments were conducted.

Peptide Synthesis

The SPPS was performed on a semiautomatic peptide synthesizer (RinkCombichem, Bubendorf, Switzerland) employing standard Fmoc strategy.[16] The required peptides were assembled on Rink amide MBHA resin. The Trt was used as protecting group for Gln, Asn and His, ivDde for Lys and Boc for Trp. The coupling reactions were achieved with 3 fold excess of Fmoc-amino acids, using DIC/HOBt as activating agents in NMP. After a coupling time of 2 h, the completeness of the reaction was monitored by standard ninhydrin test. Fmoc removal was achieved with 20% piperidine in DMF in three successive 10 min treatments. After assembling the desired amino acids, cleavage from the resin and simultaneous sidechain deprotection of the peptides was accomplished by incubating for 3.5 h in a cleavage cocktail comprising TFA / thioanisole / H_2O / triisopropylsilane 95 : 3 : 1 : 1. The resin was then filtered and washed with the above mixture, evaporation of the filtrate followed by trituration with diethyl ether yielded the crude peptide. The yields of the crude peptides ranged from 70-80% and were further purified by semi-preparative HPLC.

Synthesis of (*R*/*S*) α-bromoglutaric acid 1-*tert*-butyl ester 5-benzyl ester (1)

This compound was synthesized starting from the commercially available L-glutamic acid 5-benzyl ester in two steps as described before.[15]

Synthesis of 1,4,7,10- tetraazacyclododecane-1,4,7-tris(*tert*-butyl acetate)-10- (glutaric acid 1-*tert*-butyl ester) (2)

This prochelator was synthesized from 1,4,7,10-tetraazacyclododecane in three steps using the reported procedure.[15]

General procedure for monovalent conjugation (3 and 4)

After assembling the desired amino acids on the resin, the final Fmoc group was removed. The prochelator **2** (3 equivalents) was coupled to the *N*-terminal of the peptides using HATU (3.3 equivalents) and DIPEA (7 equivalents) for 4h. The monovalent peptide-chelator conjugates were then cleaved from the resin as described above. The conjugates were further

subjected to deprotection for 3h using the same cleavage cocktail, triturated with diethyl ether, filtered and dried. This deprotection and trituration steps were repeated until the complete removal of t-Bu was observed (by analytical HPLC). The monovalent peptide-chelator conjugates were further purified by semi-preparative HPLC (0 min, 80% A, 20 min 40% A) and characterized by ESI-MS.

	Molecular Formula	M	Yield[a] (%)	R_t (min)	MS-ESI: *m/z* (%)
Lys^3-BN-DOTA (**4**)	$C_{90}H_{140}N_{26}O_{27}S$	2050.30	38	20.85	2089.4 $[M+K]^+$ (22) 1044.9 $[M+K]^{++}$ (100)
Ahx-Bn(4-14)-DOTA (**5**)	$C_{80}H_{126}N_{22}O_{23}S$	1796.06	44	22.14	1835.1 $[M+K]^+$ (100) 918.0 $[M+K]^{++}$ (74)

Table V.1 **–** Analytical data for the monovalent peptide conjugates Lys^3-bombesin-DOTA (**4**) and Ahx-bombesin(4-14)-DOTA (**5**). [a]Yields were based on the first Fmoc cleavage. [b]Analytical HPLC (0 min, 95% A; 30 min 55% A).

Synthesis of 1,4,7,10-tetraazacyclododecane-1,7-bis(tert-butyl acetate)-4,10-bis(glutaric acid 1-tert-butyl ester-5-benzyl ester) (6)

To a stirred solution of **5** (0.8 g, 2 mmol) in dry acetonitrile (10 mL) was added K_2CO_2 (1.146 g, 8 mmol) followed by the drop wise addition of racemic **1** (1.43 g, 4 mmol). After stirring for 18 h at room temperature, the mixture was filtered over Celite and concentrated under reduced pressure. Flash chromatography on silica gel 60 (CH_2Cl_2 / EtOH 9 : 1 followed by EtOH / NH_3 95 : 5) yielded **6** (1.21 g, 63%) as a pale yellow oil. R_f: 0.54 (CH_2Cl_2 / EtOH 9:1); MS-ESI: *m/z* (%): 953.7 $[M+H]^+$ (11), 975.6 $[M+Na]^+$ (100) ; ^1H NMR (d^6-DMSO) : δ (ppm) = 7.35 (m, 10H, Ar-*H*), 5.1 (m, 4H, C*H*$_2$-Ar), 3.45 (m, 4H, -N-C*H*$_2$-$CO_2C(CH_3)_3$), 3.4 (m, 2H, -N-C*H*(R)-CH_2-CH_2-COOBn), 3.2-2.0 (m, 16H, -N-C*H*$_2$-C*H*$_2$-N-), 2.41 (m, 4H, -N-CH(R)-CH_2-C*H*$_2$-COOBn), 1.9 (m, 4H, -N-CH(R)-C*H*$_2$-CH_2-COOBn), 1.46 (m, 36H, -C(C*H*$_3$)$_3$); ^{13}C NMR (d^6-DMSO) : δ (ppm) = 172.8 (2C, -N-CH(R)-CH_2-CH_2-*C*OOBn), 172.2 (4C, -N-CH_2-*C*$O_2C(CH_3)_3$), 136.1 (2C, -CH_2-*C*(Ar)), 128.4, 128.1, 128.0 & 127.9 (10C, -*C*(Ar)), 81.4 & 81.6 (4C, -*C*$(CH_3)_3$), 64.5 (2C, -*C*H_2-Ar), 63.2 (2C, -N-*C*H(R)-$CO_2C(CH_3)_3$), 56.5 (2C, -N-*C*H_2-$CO_2C(CH_2)_2$), 50-44 (8C, -N-*C*H_2-*C*H_2-N-), 32.0 (2C, -N-CH(R)-CH_2-*C*H_2-COOBn), 27.4, 27.5, 27.6 & 27.8 (12C, -C(*C*$H_3)_3$), 23.5 (2C, -N-CH(R)-*C*H_2-CH_2-COOBn).

Synthesis of 1,4,7,10-tetraazacyclododecane-1,7-bis(tert-butyl acetate)-4,10-bis(glutaric acid 1-tertbutyl ester) (7)

To a solution of **6** (1 g, 1.05 mmol) in methanol (100 mL) was added 100 mg of 10% Pd/C suspended in 5 mL of H_2O and H_2 was bubbled through the solution under normal pressure. After completion of hydrogenation (as monitored by TLC), the catalyst was removed by filtration through Celite. The solvent was evaporated under reduced pressure and the residue obtained was triturated with diethyl ether. The solid crude product thus obtained was subjected to flash chromatography on silica gel 60 (EtOH / NH_3 98 : 2 to 95 : 5) to yield **7** (695 mg, 86%) as a white solid. R_f: 0.38 (EtOH / NH_3 95 : 5) ; mp 206-208°C; MS-ESI: *m/z* (%) : 773.5 $[M+H]^+$ (18), 795.6 $[M+Na]^+$ (100); ^{1}H NMR (d^6-DMSO): δ (ppm) = 3.42 (m, 2H, -NC*H*(R)-CH_2-CH_2-COOH), 2.74 & 3.46 (m, 4H, -N-C*H*$_2$-$CO_2C(CH_3)_3$), 2.5 (m, 4H, -N-CH(R)-CH_2-C*H*$_2$-COOH), 2.14 & 2.64 and 2.0 & 3.1 (m, 8H, -N-C*H*$_2$-CH_2-N-), 2.1 & 2.5 and 2.35 & 3.0 (m, 8H, -N-CH_2-C*H*$_2$-N-), 1.63 & 1.9 (m, 4H, -N-CH(R)-C*H*$_2$-CH_2-COOH), 1.45 (m, 36H, -C(C*H*$_3$)$_3$); ^{13}C NMR (d^6-DMSO): δ (ppm) = 174.9 & 174.7 (2C, -N-CH(R)-CH_2-CH_2-*C*OOH), 173.1 (4C, -N-CH_2-*C*O_2C$(CH_3)_3$), 81.8 (2C, -N-CH(R)-CO_2*C*$(CH_3)_3$), 79.6 (2C, -N-CH_2-CO_2*C*$(CH_3)_3$), 59.8 (2C, -N-*C*H(R)-$CO_2C(CH_3)_3$), 56.2 (2C, -N-*C*H_2-$CO_2C(CH_3)_3$), 52.9 & 44.0 (4C, -N-CH_2-*C*H_2-N-), 48.5 & 47.2 (4C, -N-*C*H_2-CH_2-N-), 32.6 (2C, -N-CH(R)-CH_2-*C*H_2-COOH), 28.2, 27.8 & 27.7 (12C, -C(*C*H_3)$_3$), 19.4 (2C, -N-CH(R)-*C*H_2-CH_2-COOH).

General procedure for divalent conjugation (8 and 9)

To a solution of prochelator **7** (10 mg, 13 μmol) in dry DMF (2 mL) was added purified peptide (28.6 μmol, 2.2 equivalents) and HATU (11 mg, 28.6 μmol) and adjusted the pH to 8 using DIPEA. The mixture was stirred at room temperature overnight and DMF was evaporated under reduced pressure. The residue was triturated with diethyl ether, dried and subjected to t-Bu deprotection as described above. The divalent peptide-chelator conjugates were purified by semipreparative HPLC (0 min, 80% A, 30 min 40% A) and characterized by ESI-MS.

	Molecular Formula	M	Yield[a] (%)	R_t[b] (min)	MS-ESI: *m/z* (%)
$(Lys^3\text{-BN})_2$-DOTA (**8**)	$C_{164}H_{252}N_{48}O_{46}S_2$	3696.18	48	21.99	1867.1 $[M+K]^{++}$ (18) 1245.2 $[M+K]^{+++}$ (100)
$(Ahx\text{-Bn(4-14)})_2$-DOTA (**9**)	$C_{144}H_{224}N_{40}O_{38}S_2$	3188.08	55	22.88	1613.33 $[M+K]^{++}$ (35) 1076.12$[M+K]^{+++}$ (100)

Table V.2 – Analytical data for the divalent peptide conjugates $(Lys^3\text{-bombesin})_2$-DOTA (**8**) and $(Ahx\text{-bombesin(4-14)})_2$-DOTA (**9**). [a]Yields refer to the final divalent conjugation and deprotection steps. [b]Analytical HPLC (0 min, 95% A; 30 min 55% A).

V.2.2 Sample preparation

A mixture of peptide-chelator conjugate (5 μmol) in 4 mL of sodium acetate buffer (0.4M, pH 5) was incubated with 10 μmol $Gd(OAc)_3{\cdot}6H_2O$ at 95°C for 25 min, cooled to room temperature, and purified over a SepPak C_{18} cartridge preconditioned with 10 mL of methanol and 10 mL of water. The cartridge was eluted with 30 mL of sodium acetate buffer followed by 20 mL of methanol. The absence of free Gd(III) ions in methanol solution was verified by using xylenol orange indicator. The methanol was evaporated to afford the corresponding Gd(III) complexes (purity > 96% on HPLC), which were further characterized by MALDI-MS. The well resolved MALDI-MS spectra of gadolinium conjugated peptides showed broad isotopic distribution. The broad isotope pattern is due to the fact that gadolinium has five main isotopes (14.80% of ^{155}Gd, 20.47% of ^{156}Gd, 15.65% of ^{157}Gd, 24.84% of ^{158}Gd, 21.86% of ^{160}Gd) with similar abundance plus two isotopes of minor abundance.[17]

The exact final Gd^{3+} concentration was measured by bulk magnetic susceptibility (BMS)[18] at 23.3°C on a Bruker DRX-400 (9.4 T, 400 MHz) spectrometer. This was performed by measuring the shift of the tert-butanol alkyl protons in the paramagnetic environment compared to the diamagnetic reference contained in a coaxial NMR tube.

V.2.3 ^{1}H relaxivities

T_1 were determined by the inversion-recovery method[19] using the following equipment : Stelar Spinmaster Fast Field Cycling (FFC) NMR relaxometer[20] ($2.35 \cdot 10^{-4}$ to 0.47 T; ^{1}H Larmor frequencies : 0.01 to 20 MHz) equipped with a VTC90 temperature control unit,

Bruker Minispec mq20 0.47 T (20 MHz), mq40 0.70 T (30 MHz), mq40 0.94 T (40 MHz) and mq60 1.41 T (60 MHz), Bruker Avance-200 console connected to a 2.35 T (100 MHz) and a 4.7 T (200 MHz) cryomagnets, Bruker Avance-II 9.4 T (400 MHz). The spectrometers were equipped with Bruker BVT3000 temperature control units and Bruker BCU05 cooling units. All temperatures were measured by substitution techniques.[21] The relaxation rates $1/T_1$ were corrected by diamagnetic contributions of 0.366 s^{-1} and 0.326 s^{-1} for 25°C and 37°C respectively.

The $1/T_1$ NMRD profiles of the four complexes were measured at 25.0°C and 37.0°C with Gd^{3+} concentrations of 0.752 mM for {Lys^3-BN[Gd(DOTA)(H_2O)]} (**4**), 1.625 mM for {Ahx-BN(4-14)[Gd(DOTA)(H_2O)]} (**5**), 0.478 mM for {(Lys^3-BN)$_2$[Gd(DOTA)(H_2O)]} (**8**) and 1.618 mM for {(Ahx-BN(4-14))$_2$[Gd(DOTA)(H_2O)]} (**9**). Samples in 7.5 mm tubes were used on Bruker mq40s and mq60 while samples sealed in glass spheres adapted for 10 mm NMR tubes were used for all other instruments.

V.2.4 Data treatment

The fitting of the ^{1}H NMRD profiles using the Solomon-Bloembergen-Morgan theory (SBM)[22-25] together with the Lipari-Szabo (LS) free-model approach for the internal rotation[26,27] were performed on Visualiseur/Optimiseur[28,29] running on a MATLAB© 7.3.0 (R2006b) platform. The fitting of the ^{1}H NMRD profiles using the "modified Florence approach"[30-32] were performed with a version of the "modified Florence program"[33] including Lipari-Szabo treatment of the internal rotation adapted to run on a MATLAB© 7.3.0 (R2006b) platform.

V.3. Results and discussion

V.3.1 Ligands and conjugates synthesis

The synthesis of prochelator **7** containing two free carboxylic acid groups for the divalent vectorization of targeting peptides started from commercially available DO2A-*tert*-butyl ester **5** (Figure V.4). *N*-alkylation of **5** with 2 equivalents of (*R/S*)-α-bromoglutaric acid 1-*tert*-butyl ester 5-benzyl ester **1**[15] yielded 6 in 63%. Subsequent hydrogenation of **6** over 10% Pd/C catalyst followed by chromatographic purification yielded the prochelator **7** in 86%, which was further characterized by using ESI-MS and NMR (1D-^{1}H, ^{1}H-^{1}H-COSY, 1D-^{13}C and ^{1}H-^{13}C-HSQC experiments). The new prochelator **7** exists in different isomeric forms (*RR, SS, RS & SR*) as it was synthesized by using racemic **1**.[34] The prochelator **2** containing one free carboxylic acid group was synthesized following the procedure described earlier.[15]

The application of prochelator **7** for the divalent vectorization with peptide ligands has been demonstrated by synthesizing divalent bombesin analogues (Figure V.4). Analysis of HPLC fractions by MALDI-MS revealed the presence of considerable quantities of undesired modified divalent peptide conjugates produced by the HATU mediated nitrile formation via dehydration of the carboxamide side chain of asparagine and glutamine.[35]

V.3.2 ^{1}H relaxivities of the four Gd-DOTA-bombesin conjugates

The $1/T_1$ NMRD profiles of the four Gd-DOTA-BN complexes were measured at 25°C and 37°C to characterize the ^{1}H relaxivity properties of these potential MRI CAs. It should however be kept in mind that the relaxivities would drastically change when these compounds are bound to the targeted cells thanks to the bombesin-bombesin receptor interaction. This *in vivo* system would mainly affect two determining parameters : the rotational correlation time, related to the size of the entity, that would considerably increase and internal flexibility, which would be restricted.

The NMRD profiles of the mono-peptide compounds {Lys^{3}-BN[Gd(DOTA)(H_2O)]} and {Ahx-BN(4-14)[Gd(DOTA)(H_2O)]} are presented in Figure V.6. The relaxivity difference of the two compounds is most probably due to the more voluminous Lys^{3}-BN compound, which

has three extra amino-acids (Figure V.5), and hence resulting in longer rotational correlation time.

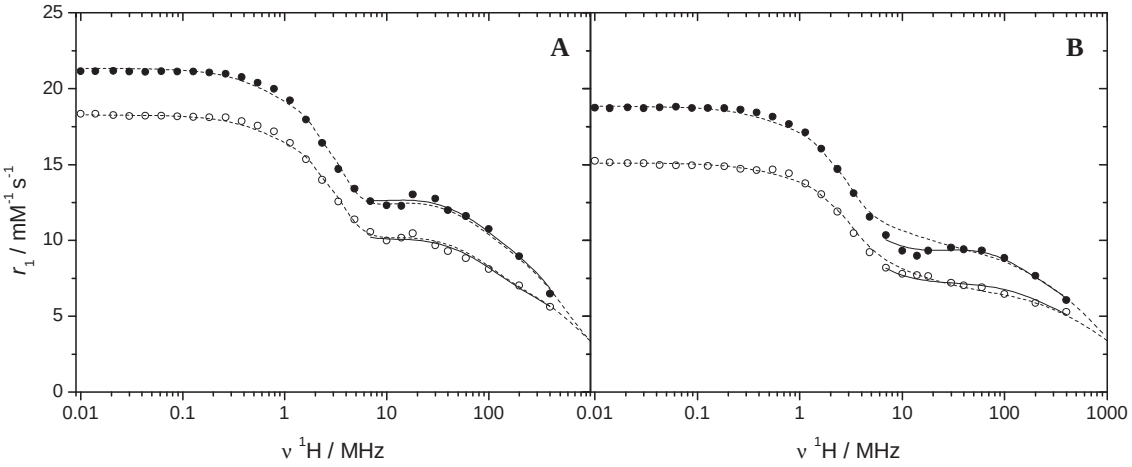

Figure V.6 – NMRD profiles of the mono-peptide compounds {Lys^3-BN[Gd(DOTA)(H_2O)]} (A) and {Ahx-BN(4-14)[Gd (DOTA)(H_2O)]} (B) at 25°C (●) and 37°C (○), fitted with the SBM-LS theory (straight line) and the Florence approach (dashed line).

The Figure V.7 presents the NMRD profiles of the two bis-bombesin compounds {(Lys^3-BN)$_2$[Gd(DOTA)(H_2O)]} and {(Ahx-BN(4-14))$_2$[Gd(DOTA)(H_2O)]}. The Lys^3-BN complex holds this time six extra amino acids, resulting in a more marked relaxivity difference.

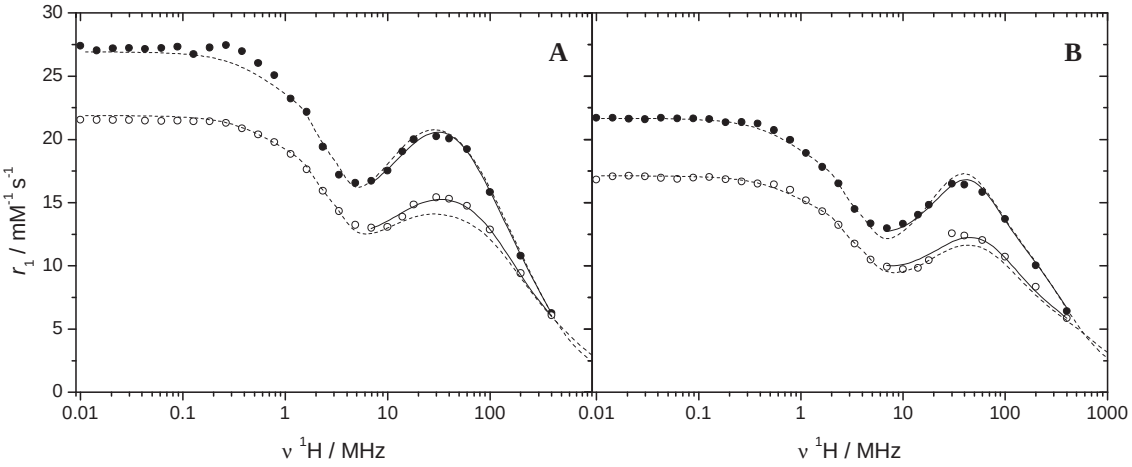

Figure V.7 – NMRD profiles of the bis-peptide compounds {(Lys^3-BN)$_2$[Gd(DOTA)(H_2O)]} (A) and {(Ahx-BN(4-14))$_2$ [Gd (DOTA)(H_2O)]} at 25°C (●) and 37°C (○), fitted with the SBM-LS theory (straight line) and the Florence approach (dashed line).

Because the size of the compounds is substantial, implying a slow molecular tumbling, the simple electronic relaxation described by the SBM theory is not valid,[36] resulting in a bad theoretical fit in the low field region, where the relaxivity is governed by the electron spin relaxation. The experimental data of the four complexes have therefore been fitted with the SBM-LS theory at high frequencies (≥ 7 MHz). The whole profiles have subsequently been fitted with the Florence approach,[30,31] suitable for slowly rotating molecules. In the absence of ^{17}O NMR data, the activation enthalpy $\Delta H^{\ddagger}$ and the water exchange rate k_{ex}^{298} cannot be reasonably fitted. Fitted values for the water exchange rate constant of $[Gd(DOTA)(H_2O)]^-$ were therefore used to fix these parameters (the activation energy was calculated from the equation I.65).[37] The Lipari-Szabo parameters S^2 obtained from the SBM-LS fit have been used for the Florence fit. The best fitting parameters of the mono- and bis-bombesin conjugates are presented in Table V.3 and Table V.4 respectively. To allow direct comparison, the transient ZFS amplitude Δ and static ZFS amplitude D obtained with the Florence fit, given in cm^{-1}, have been converted into s^{-2} (equation III.3).

	{Lys^3-BN[Gd(DOTA)(H$_2$O)]}		{Ahx-BN(4-14)[Gd(DOTA)(H$_2$O)]}	
	SBM-LS	Florence	SBM-LS	Florence
$\Delta H^{\ddagger}$ / kJ mol^{-1}	49.8	-	49.8	-
E_a / kJ mol^{-1}	-	52.3	-	52.3
k_{ex}^{298} $(1/\tau_M)$ / 10^6 s^{-1}	4.1	4.1	4.1	4.1
E_R / kJ mol^{-1}	9.5 ± 11.0	8.7	30.4 ± 17.0	32.1
τ_R^{298} / ps	1670 ± 560	1670	1140 ± 670	903
E_l / kJ mol^{-1}	32.4 ± 6.2	29.0	21.2 ± 8.5	22.8
τ_l^{298} / ps	338 ± 23	330	240 ± 19	253
E_v / kJ mol^{-1}	1	1	1	1
τ_v^{298} / ps	21.0 ± 17.2	25.6	7.2 ± 3.3	47.6
D_{GdH}^{298} / 10^{-10} m^2 s^{-1}	25	25	25	25
E_{DGdH} / kJ mol^{-1}	20	20	20	20
Δ^2 / 10^{20} s^{-2}	0.032 ± 0.006	0.044	0.10 ± 0.04	0.029
D^2 / 10^{20} s^{-2}	-	0.417	-	0.185
S^2	0.08 ± 0.03	0.08	0.09 ± 0.06	0.09
q	1	1	1	1
$r_{GdH\ 1^{st}}$ / Å	3.1	3.1	3.1	3.1
$r_{GdH\ 2^{nd}}$ / Å	3.6	3.6	3.6	3.6

Table V.3 – Best fitted parameters of the monovalent peptide compounds {Lys^3-BN[Gd(DOTA)(H$_2$O)]} and {Ahx-BN(4-14)[Gd(DOTA)(H$_2$O)]} obtained with the SBM-LS theory and the Florence approach. Fixed values underlined.

Let's point out that the use of the Florence approach is questionable for mid-size molecules, particularly for the smaller {Ahx-BN(4-14)[Gd(DOTA)(H$_2$O)]}, which is not fitted perfectly with this method (Figure V.6 B). The very small LS factors $S^2 < 0.1$ denotes a high freedom for fast internal rotation and indicates that the bombesin analogue Lys^3-BN is not more rigid than Ahx-BN. The global and local rotational correlation times are however actually shorter for the Ahx-BN(4-14) conjugate.

	{(Lys^3-BN)$_2$[Gd(DOTA)(H$_2$O)]}		{(Ahx-BN(4-14))$_2$[Gd(DOTA)(H$_2$O)]}	
	SBM-LS	Florence	SBM-LS	Florence
$\Delta H^{\ddagger}$ / kJ mol^{-1}	49.8	-	49.8	-
E_a / kJ mol^{-1}	-	52.3	-	52.3
k_{ex}^{298} $(1/\tau_M)$ / 10^6 s^{-1}	4.1	4.1	4.1	4.1
E_R / kJ mol^{-1}	32.6 ± 3.7	38.2	39.2 ± 11.6	48.1
τ_R^{298} / ps	1835 ± 238	1725	2704 ± 909	2821
E_l / kJ mol^{-1}	50.9 ± 6.2	61.7	44.2 ± 6.1	52.2
τ_l^{298} / ps	656 ± 60	722	487 ± 38	506
E_v / kJ mol^{-1}	1	1	1	1
τ_v^{298} / ps	17.5 ± 2.8	24.3	10.8 ± 2.1	14.1
D_{GdH}^{298} / 10^{-10} m^2 s^{-1}	25	25	25	25
E_{DGdH} / kJ mol^{-1}	20	20	20	20
Δ^2 / 10^{20} s^{-2}	0.062 ± 0.003	0.061	0.13 ± 0.02	0.14
D^2 / 10^{20} s^{-2}	-	0.375	-	0.654
S^2	0.32 ± 0.06	0.32	0.18 ± 0.04	0.18
q	1	1	1	1
$r_{GdH\ 1^{st}}$ / Å	3.1	3.1	3.1	3.1
$r_{GdH\ 2^{nd}}$ / Å	3.6	3.6	3.6	3.6

Table V.4 – Best fitted parameters of the bis-peptide compounds {(Lys^3-BN)$_2$[Gd(DOTA)(H$_2$O)]} and {(Ahx-BN(4-14))$_2$ [Gd(DOTA)(H$_2$O)]} obtained with the SBM-LS theory and the Florence approach. Fixed values underlined.

The global rotational correlation time is in the case of the bis-bombesin complexes surprisingly longer for the (Ahx-BN)$_2$ conjugate. The local rotational correlation time is nevertheless still longer for the Lys^3-BN constant. The S^2 factors are two to three times higher for both bis-BN compounds. The lack of coherence of several fitting parameters, particularly the ones involved in the electronic treatment, arises most probably from the high correlation between the parameters in both fitting methods, which compensate during the fittings. The rotational activation energies E_R are also unreasonable (too low for {Lys^3-BN[Gd(DOTA)(H$_2$O)]} and too high for the three other compounds). This phenomenon will however not be investigated in this coarse analysis.

V.4. Conclusion

With a view to develop targeted MRI contrast agents using the overexpression of peptide receptor by malignant tumor cell, the peptide neurotransmitter bombesin has been conjugated to the chelating unit DOTA. Two bombesin analogues, the Lys^3-BN and the Ahx-BN, have been employed to synthesize mono- and bis-peptide compounds. After complexation with gadolinium, the $1/T_1$ NMRD profiles of the four compounds have been measured at 25°C and 37°C and fitted with two different methods.

Because the size of these BN-conjugated Gd^{3+} complexes is significant, the electron spin relaxation described by the SBM theory do not allow good relaxivity fitting at low magnetic field, where the electronic relaxation predominate the nuclear relaxation. The relaxometry data have therefore been treated with the SBM-LS for resonance frequencies $\nu > 7$ MHz and with the Florence approach, using the Lipari-Szabo factor S^2 obtained from the SBM-LS fit. The Florence approach turned out to be imperfect to treat mid-size molecules, and particularly the smallest compound {Ahx-BN(4-14)[Gd(DOTA)(H_2O)]}.

The most relevant information obtained from the NMRD profiles is the higher relaxivity for both Lys^3-BN conjugates. This relaxivity enhancement is accredited to the bigger size of this peptide analogue, which comprises three amino acids more than the Ahx-BN(4-14). This was confirmed by the fitted rotational correlation times. The very low and similar S^2 factors obtained from the fit of the mono-bombesin conjugates indicated respectively a high degree of freedom for the internal rotation and a similar rigidity of both compounds. Unsurprisingly, these parameters increased significantly for their dimeric analogues. The strong correlation between the fitted parameters led unfortunately to some incoherent values, particularly for the electronic relaxation and the rotational activation energies.

One should however keep in mind that the relaxometry of the four systems would change radically when the compounds are bound to a cell thanks to the peptide-peptide receptor interaction. The rotational correlation times and the internal rotation would be the most affected parameters in such systems.

V.5. Acknowledgements

I warmly thank the following persons for their essential contributions to this work :

Prof. Helmut R. Maecke and Dr. Abiraj Keelara, from the Division of Radiological Chemistry, University Hospital Basel, for having initiated this collaboration.

Dr. Abiraj Keelara for the peptide, ligand and complex synthesis and all the things he taught me about this synthesis and this subject.

V.6. References

1. Reubi, J. C. Endocrine *Reviews* **2003,** *24*, 389-427.
2. Reubi, J. C.; Macke, H. R.; Krenning, E. P. *Journal of Nuclear Medicine* **2005,** *46*, 67S-75S.
3. Reubi, J. C.; Maecke, H. R. *Journal of Nuclear Medicine* **2008,** *49*, 1735-1738.
4. Abiraj, K.; Jaccard, H.; Kretzschmar, M.; Helm, L.; Maecke, H. R. *Chemical Communications* **2008**, 3248-3250.
5. Kwekkeboom, D. J.; Teunissen, J. J.; Bakker, W. H.; Kooij, P. P.; de Herder, W. W.; Feelders, R. A.; van Eijck, C. H.; Esser, J. P.; Kam, B. L.; Krenning, E. P. *Journal of Clinical Oncology* **2005,** *23*, 2754-2762.
6. Waldherr, C.; Pless, M.; Maecke, H. R.; Haldemann, A.; Mueller-Brand, J. *Annals of Oncology* **2001,** *12*, 941-945.
7. Weiner, R. E.; Thakur, M. L. *Biodrugs* **2005,** *19*, 145-163.
8. Smith, C. J.; Volkert, W. A.; Hoffman, T. J. *Nuclear Medicine and Biology* **2005,** *32*, 733-740.
9. Behe, M.; Behr, T. M. *Biopolymers* **2002,** *66*, 399-418.
10. Zhang, H.; Schuhmacher, J.; Waser, B.; Wild, D.; Eisenhut, M.; Reubi, J.; Maecke, H. *European Journal of Nuclear Medicine and Molecular Imaging* **2007,** *34*, 1198-1208.
11. Nock, B. A.; Nikolopoulou, A.; Galanis, A.; Cordopatis, P.; Waser, B.; Reubi, J. C.; Maina, T. *Journal of Medicinal Chemistry* **2005,** *48*, 100-110.
12. Zhang, H. W.; Chen, J. H.; Waldherr, C.; Hinni, K.; Waser, B.; Reubi, J. C.; Maecke, H. R. *Cancer Research* **2004,** *64*, 6707-6715.
13. Kiessling, L. L.; Gestwicki, J. E.; Strong, L. E. *Angewandte Chemie-International Edition* **2006,** *45*, 2348-2368.
14. Rao, J. H.; Lahiri, J.; Isaacs, L.; Weis, R. M.; Whitesides, G. M. *Science* **1998,** *280*, 708-711.
15. Eisenwiener, K.-P.; Powell, P.; Mäcke, H. R. *Bioorganic & Medicinal Chemistry Letters* **2000,** *10*, 2133-2135.
16. Atherton, E.; Sheppard, R. C. *Peptides (N. Y.)* **1987,** *9*, 1-38.
17. Kruger, R.; Braun, K.; Pipkorn, R.; Lehmann, W. D. *Journal of Analytical Atomic Spectrometry* **2004,** *19*, 852-857.

18. Corsi, D. M.; Platas-Iglesias, C.; Bekkum, H. v.; Peters, J. A. *Magnetic Resonance in Chemistry* **2001,** *39*, 723-726.
19. Vold, R. L.; Waugh, J. S.; Klein, M. P.; Phelps, D. E. *Journal of Chemical Physics* **1968,** *48*, 3831-&.
20. Ferrante, G.; Sykora, S. In *Advances in Inorganic Chemistry;* van Eldik, R.; Bertini, I. Eds.: San Diego, 2005; pp. 405-470.
21. Ammann, C.; Meier, P.; Merbach, A. E. *Journal of Magnetic Resonance* **1982,** *46*, 319-321.
22. Solomon, I. *Physical Review* **1955,** *99*, 559-565.
23. Solomon, I.; Bloembergen, N. *Journal of Chemical Physics* **1956,** *25*, 261-266.
24. Bloembergen, N. *Journal of Chemical Physics* **1957,** *27*, 572-573.
25. Bloembergen, N.; Morgan, L. O. *The Journal of Chemical Physics* **1961,** *34*, 842-850.
26. Lipari, G.; Szabo, A. *Journal of the American Chemical Society* **1982,** *104*, 4546-4559.
27. Lipari, G.; Szabo, A. *Journal of the American Chemical Society* **1982,** *104*, 4559-4570.
28. Yerly, F. VISUALISEUR *2.3.6* **2004,** *EPFL*.
29. Yerly, F. OPTIMISEUR *3.0.0* **2002,** *EPFL*.
30. Bertini, I.; Kowalewski, J.; Luchinat, C.; Nilsson, T.; Parigi, G. *Journal of Chemical Physics* **1999,** *111*, 5795-5807.
31. Kruk, D.; Nilsson, T.; Kowalewski, J. *Physical Chemistry Chemical Physics* **2001,** *3*, 4907-4917.
32. Kowalewski, J.; Kruk, D.; Parigi, G. In *Advances in Inorganic Chemistry*; Academic Press, 2005; pp. 41-104.
33. Bertini, I.; Galas, O.; Luchinat, C.; Parigi, G. *Journal of Magnetic Resonance Series A* **1995,** *113*, 151-158.
34. Woods, M.; Aime, S.; Botta, M.; Howard, J. A. K.; Moloney, J. M.; Navet, M.; Parker, D.; Port, M.; Rousseaux, O. *Journal of the American Chemical Society* **2000,** *122*, 9781-9792.
35. Katsoyannis, P. G.; Gish, D. T.; Hess, G. P.; Vigneaud, V. D. *Journal of the American Chemical Society* **1958,** *80*, 2558-2562.
36. Helm, L. Progress in Nuclear Magnetic Resonance Spectroscopy **2006,** 49, 45-64.
37. Powell, D. H.; Ni Dhubhghaill, O. M.; Pubanz, D.; Helm, L.; Lebedev, Y. S.; Schlaepfer, W.; Merbach, A. E. *Journal of the American Chemical Society* **1996,** *118*, 9333-9346.

Chapter VI :

General conclusions

VI.1. Conclusions and perspectives 169
VI.2. General acknowledgements 173
VI.3. References 175

VI.1. Conclusions and perspectives

From its invention in the early 70's,[1-3] the magnetic resonance imaging has increasingly become an incontrovertible method for medical diagnostic, thanks to its capability to differentiate different soft tissues of living bodies. The possibilities that offer this powerful tool, based on nuclear magnetic resonance pulsed field gradients, are almost infinite through the development of new NMR pulse sequences. Nowadays, the measurements of the water proton relaxation times T_1 and T_2 represent the great majority of MRI experiments. This imaging technique, like NMR, has however an important drawback : its low sensitivity, involving long examination times. This tedious time can be reduced through the use of MRI contrast agents, which decrease the relaxation times of water protons. Stable chelate complexes with the paramagnetic metal Gd^{3+}, that reduce the longitudinal relaxation time though the interaction with the water proton are currently the most employed T_1 contrast agents.

As the relaxation rate enhancement depends on the concentration of the paramagnetic species, the notion of relaxivity, defined as the paramagnetic contribution to the relaxation rate divided by the concentration of the paramagnetic ion, has been introduced to define the efficiency of a contrast agent.[4] This relaxivity is field-dependent and depends mainly on four parameters : the hydration number *q, i.e.* the number of water molecules in the inner sphere of the paramagnetic ion complex, the exchange rate of these water molecules k_{ex}, the rotational correlation time of the molecule τ_R, related to its size, and the electron spin longitudinal transverse relaxation rates $1/T_{1e}$ and $1/T_{2e}$.[5,6]

The development of T_1 CAs can be achieved by many different ways, depending on the desired effect. For instance, the optimization of the relaxivity at 64 MHz (1.5 T) requires big and rigid molecules while mid-size and supple entities would allow to increase relaxivity at 127 MHz (3 T) (Figure III.1).[7] The unceasing evolution in the magnet technology constrains the development of high field contrast agents. Moreover, the progress in this field has to be achieved through responsive contrast agents, whose relaxivity allow the determination of some variable in their immediate environment, such as pH, temperature or metal ion

concentration, or through the development of targeted CA, that determines the geographic position of the target, such as tumors.[8]

This work presented the synthesis, characterization and relaxometric properties of four new types of compounds developed as potential T_1 CAs.

Chapter II presented the mid-size trimeric Gd^{3+} complex {Mes[Gd(DO3A)$(H_2O)_2$}, developed as a high field CAs.[9] The standard complexation method did allow the complexation of only two metal ions per molecule. This difficulty could arise from the important pH drop during the first complexations, which induces the protonation of the uncomplexing acetates and prevents the introduction of the third Gd^{3+}. After restoring the pH to 5.8, the acetates are supposed to complex immediately the neighboring Gd^{3+} ions. This adjacent complexation leads to only one water molecule in the inner sphere of the two Gd^{3+}. This was confirmed by relaxometry and ^{17}O NMR measurements. A new complexation strategy, occurring at higher pH, has therefore been developed to sidestep this difficulty. Gadolinium, that forms insoluble hydroxides at pH higher than 6.2 could not be used directly. The alternative method was therefore achieved though pre-complexation with Mn^{2+} at pH 9 and transmetallation with Gd^{3+} at pH 5.8. The complete complexation achieved with this method has been proved by elemental analysis and ICP-MS, and confirmed by NMRD profiles and ^{17}O NMRD measurements. The hydration number of the Gd^{3+} in this fully complexed compound is two, as expected. The new complexation method turned out to be very efficient and can be helpful for the complexation of mid-size CAs.

Chapter III dealt with another trimeric mid-size complex, {Ph_4[Gd(DTTA)$(H_2O)_2$]$^-_3$}. This compound has however not been developed as a high-field CAs, but has been designed to form big entities through aggregation, most probably by π-stacking interaction of the aromatic core. The dynamic aggregations have been observed through exceptionally high relaxivity for such a mid-size molecule and the concentration dependence of this relaxivities. Thanks to the parameters obtained by a simultaneous fit of NMRD and ^{17}O NMR data, the NMRD profiles of the compound at other concentrations have been fitted almost perfectly by varying only the global rotational correlation and the Lipari-Szabo factor S^2 using two fit methods, the SB-LS-RFB and the modified Florence approaches. From the obtained rotational correlation times, an approximation using the equation of Stokes-Einstein-Debye allowed us to determine that the monomer was predominantly present in diluted solutions and that aggregates were formed by

two or three molecules in more concentrated solutions. The small number of compounds in the aggregates, relatively to that of Costa *et al.* where the number of molecules in the aggregates was estimated to about ten, probably arises from steric hindrance of the chelate complexes, which prevents interactions of the central core. Its mono- or di-substituted analogues would probably leave enough space for chelate complexes and would perhaps lead to bigger aggregates and therefore higher relaxivities between 10 and 200 MHz.

Chapter IV presented a strategy to couple covalently Gd^{3+} chelate complexes to the chitosan, a polysaccharide linear polymer with remarkable biological and biomedical properties. This was achieved through the amide bond formation between the deacetylated free amine of the chitosan with the pending butyrate arm of the compound $[Gd(DTTA\text{-}N'but)(H_2O)_2]^{2-}$. The structural characterization, in terms of degree of acetylation, deacetylation and modification, was determined by elemental analysis and ICP-MS. This material was subsequently used to form hydrogel nanoparticles, or nanogels, *via* a folding induced by the interaction of the anion triphosphate TPP with the protonated chitosan amines. The nanogels, coated with the negatively charged polysaccharide alginate to stabilize the material at physiological pH, were characterized by DLS and TEM. Though the linear polymer presented interesting relaxivities, the relaxivities of the nanogel considerably drops. This might be due to the partial complexation of the Gd^{3+} by the pentaanion TPP, reducing the average hydration number of the complexes. The low quantity of available material, the high viscosity of concentrated solutions and the stability of the nanogel did unfortunately not allow to further investigate this system, typically by ^{17}O NMR measurements.

Chapter V presented potential targeted CAs composed by Gd^{3+} conjugated with the peptide neurotransmitter bombesin, whose receptors are overexpressed by a number of malignant tumor cells.[10] To optimize the affinity of the compound with the targeted cells *via* bombesin-bombesin receptor interaction, two bombesin analogues, the Lys^3-BN and the Ahx-BN(4-14) were used to prepare the monovalent and the divalent peptide conjugates. These compounds, and particularly the divalent peptide conjugates, presented interesting relaxivities for a DOTA system with a hydration number of 1. One should however realize that such CAs are expected to be bound to the cell when measured, which would drastically influence the rotational correlation time and the internal rotation and therefore affect radically the relaxivity. The next step to optimize this family of potential targeted CAs composed by a Gd^{3+} complex bound to the bombesin would be achieved by increasing the number of chelate complexes. Though the

relaxivity would not, or nearly not, be affected, the relaxivity density would be enhanced, increasing the efficiency of the CA. Attempts to intercalate a dendron between the peptide and the chelating units have up to now not been successful, but seem to be a promising route to enhance the number of Gd^{3+} chelate complexes.

To conclude, we can affirm that the field of MRI contrast agents has still numerous promising directions for its development, in which some major challenges remain, such as responsive, targeted or bimodal CAs. The fitting methods and the ^{17}O NMR measurement can provide a number of essential information on the developed systems. The understanding of the meaning of the fitted parameters is therefore essential to tune and optimize the properties of newly developed potential CAs.

VI.2. General acknowledgements

First of all, I would like to deeply thank Prof. Lothar Helm, my thesis director, for having welcoming me in his group as a PhD student and having given me the opportunity to take part in his research. His impressive knowledge in the fields of NMR in general and relaxation in particular was a constant inspiration, and his availability and his sense of humor made this period not only exciting but also very enjoyable.

I am extremely grateful to my thesis jury, Prof. Gábor Laurenczy, president, Dr. Éva Jakab Tóth, Prof. Carlos Geraldes and Prof. Kay Severin, examiners, for having accepted to invest precious time to review and consider this work.

I send all my thanks to Dr. Loïck Moriggi and Dr. Caroline Cannizzo, who taught me so much on my arrival in the laboratory, and Dr. MER Anne-Sophie Chauvin, who generously helped and advised me so many times.

Pascal Miéville, for his excellent work during his master project, Catherine Schütz for the collaboration on the chitosan project, Dr. Abiraj Keelara for the collaboration on the bombesin conjugates, Kim Von Allmen for the many assists, Dr. Alexey Ulianov, for the ICP-MS measurements, Dr. MER Sandrine Gerber and Dr. Emmanuel Deiters, for their advice in organic synthesis, and Prof. Hon. André E. Merbach for the discussions on analytical chemistry, are warmly thanked.

I am deeply grateful to Dr. MER Anne-Sophie Chauvin, Pascal Miéville, Dr. Alain Borel and Catherine Schütz for the time they devoted to the review of this work.

Maria Szuman, Anne Lene Odegaard and Madeleine Steffen, for administrative matters, Giovanni Petrucci, Gladys Pache and Annelise Carrupt, in the chemical store, Martial Rey, in the NMR service, Dr. Laure Menin, Francisco Sepulveda and Daniel Baumann, in the MS service, Dr. Luc Patiny and Donald Zbinden, in the cheminformatics service, Patrick Favre, in the computer workshop, Dr. Euro Solari in the elemental analysis service, Dr. Alain Borel, in Scientific Information and Libraries, Gil Corbaz, Vladan Jankovic, Christophe Clément and

the team of the mechanical workshop, Dr. Christophe Roussel and Stéphane Thonney are greatly acknowledged for the frequent helping hands.

I thank also the actual and former coworkers in the lab, Bibimaryam Mousavi, Dr. Gabriella Bodizs, Céline Xayaphoummine and Dr. Oleg Yazyev, as well as Prof. Gábor Laurenczy, Dr. MER Anne-Sophie Chauvin, Dr. Christophe Roussel, Hami Öz, Doris Meylan and Stéphane Thonney, with whom I worked in the framework of teaching and assistantship.

I send a special thank you to Dr. Joël Teuscher, Dr. Loïck Moriggi, Dr. Jérémy Bérard, Bibimaryam Mousavi, Dr. Luc Patiny, Dr. Alain Borel, Catherine Schütz and the groups of Prof. Moser and Prof. Graetzel for all the discussions and all the good times we had during the past years.

Finally, I would like to thank my parents, Danièle and Bertrand, my brother Renaud and all my friends for their permanent support and continual encouragements.

VI.3. References

1. Damadian, R. *Science* **1971,** 171, 1151-1153.
2. Lauterbur, P. C. *Nature* **1973,** *242*, 190-191.
3. Mansfield, P.; Grannell, P. K. *Journal of Physics C: Solid State Physics* **1973,** *6*.
4. Mansson, S.; Bjornerud, A. In *The Chemistry of Contrast Agents in Medical Magnetic Resonance Imaging;* Merbach, A. E.; Tóth, É. Eds.; John Wiley & Sons, Ltd: Chichester, 2001; pp. 1-43.
5. Tóth, É.; Helm, L.; Merbach, A. E. In *The Chemistry of Contrast Agents in Medical Magnetic Resonance Imaging;* Merbach, A. E.; Tóth, É. Eds.; John Wiley & Sons, Ltd: Chichester, 2001; pp. 45-119.
6. Caravan, P. *Chemical Society Reviews* **2006,** *35*, 512-523.
7. Helm, L. *Future Medicinal Chemistry* **2010,** *2*, 385-396.
8. Jacques, V.; Desreux, J. In *Contrast Agents I;* Krause, W. Ed.; Springer Berlin / Heidelberg, 2002; pp. 123-164.
9. Miéville, P.; Jaccard, H.; Reviriego, F.; Tripier, R.; Helm, L. *Dalton Transactions* **2011,** *40*, 4260-4267.
10. Abiraj, K.; Jaccard, H.; Kretzschmar, M.; Helm, L.; Maecke, H. R. *Chemical Communications* **2008**, 3248-3250.

Chapter VII :

Appendix

VII.1. General Appendix 179
VII.1.1 Symbols 179
VII.1.2 Abbreviations 181
VII.1.3 Constants and numbers 182
VII.2. Appendix to Chapter II 183
VII.2.1. Transmetallation 183
VII.2.2. Normalized peak areas as a function of pH 184
VII.2.3. ^{17}O NMR data of $\{Mes(H_2DO3A)[Gd(DO3A)(H_2O)]_2\}^-$ 184
VII.2.4. ^{17}O NMR data of $\{Mes[Gd(DO3A)(H_2O)_2]_3\}$ 185
VII.2.5. ^{1}H NMRD data of bis-Gd and tris-Gd complexes 186
VII.3. Appendix to Chapter III 187
VII.3.1 Relaxivity of $\{Ph_4[Gd(DTTA)(H_2O)_2]^-_3\}$ as a function of $[Gd^{3+}]$ 187
VII.3.2 ^{1}H NMRD data of $\{Ph_4[Gd(DTTA)(H_2O)_2]^-_3\}$ 188
VII.3.3 ^{17}O NMR data of $\{Ph_4[Gd(DTTA)(H_2O)_2]^-_3\}$ 189
VII.3.4 Relaxivities of $\{Ph_4[Gd(DTTA)(H_2O)_2]^-_3\}$ as a function of pH 189
VII.3.5 Relaxivities time evolution of $\{Ph_4[Gd(DTTA)(H_2O)_2]^-_3\}$ vs. $[PO_4^{3-}]$ 190
VII.3.6 Relaxivities time evolution of $\{Ph_4[Gd(DTTA)(H_2O)_2]^-_3\}$ in human serum 190
VII.4. Appendix to Chapter IV 191
VII.4.1. ICP-MS instrumentation parameters and performance report 191
VII.4.2. ICP-MS experimental data 192
VII.4.3. ^{1}H NMRD data of $[Gd(DTTA\text{-}N\text{'but})(H_2O)_2]^{2-}$ and $[Gd(DTTA\text{-}Me)(H_2O)_2]^-$ 193
VII.4.4. ^{1}H NMRD data of $\{Chi[Gd(DTTA\text{-}N\text{'but})(H_2O)_2]^-\}$ and Ng$\{Chi[Gd(DTTA\text{-}N\text{'but})(H_2O)_2]^-\}$ 194
VII.4.5. Relaxivities of $\{Chi[Gd(DTTA\text{-}N\text{'but})(H_2O)_2]^{2-}\}$ as a function of $[Gd^{3+}]$ 195
VII.4.6. Relaxivities time evolution of $\{Chi[Gd(DTTA\text{-}N\text{'but})(H_2O)_2]^{2-}\}$ 195
VII.4.7. ZetaSizer Nano-ZS parameters of the Standard Operating Procedures (SOP) 195
VII.4.8. DLS size distribution of Ng$\{Chi[Gd(DTTA\text{-}N\text{'but})(H_2O)_2]^-\}$ 196
VII.5. Appendix to Chapter V 197
VII.5.1. ^{1}H NMRD data of monovalent peptide conjugates 197
VII.5.2. ^{1}H NMRD data of divalent peptide conjugates 198

VII.1. General Appendix

VII.1.1 Symbols

β_1	flip angle induced by the applied radiofrequency field
χ_v	volume magnetic susceptibility
χ_M	molar magnetic susceptibility
$\chi(1+\eta^2/3)^{1/2}$	nuclear quadrupole coupling constant
Δ	magnitude of the transient ZFS interaction (= a_{2T})
$\Delta H^{\ddagger}$	activation enthalpy
$\Delta S^{\ddagger}$	activation entropy
$\Delta\sigma$	chemical shift anisotropy
$\Delta V(\boldsymbol{r})$	voxel of dimensions $\boldsymbol{r}$
$\Delta\omega_M$	chemical shift difference in paramagnetic environment (rad s^{-1})
$\Delta\omega_{OS}$	chemical shift difference due to outer-sphere contribution (rad s^{-1})
$\Delta\omega_r$	reduced chemical shift difference (rad s^{-1})
δ	chemical shift
γ_I	gyromagnetic ratio of the particle I (generally the nucleus)
γ_S	gyromagnetic ratio of the particle I (generally the electron)
η	asymmetry parameter of the electric field gradient
η	viscosity coefficient
$\boldsymbol{\mu}$	magnetic moment
ν	frequency (s^{-1})
ν_0	nuclear Larmor frequency (s^{-1})
ρ	spin density
τ	variable delay
τ_c	correlation time
τ_{di}	dipolar correlation time
τ_g	global rotational correlation time
τ_l	local rotational correlation time
τ_M	mean residence time in paramagnetic environment M
τ_R	rotational correlation time
τ_R^{298}	rotational correlation time at 25°C
τ_R^{HW}	rotational correlation time of the water proton
τ_R^{OW}	rotational correlation time of the water oxygen
τ_{S0}	electronic relaxation time at zero-field
τ_{sci}	scalar correlation time
τ_v	correlation time for transient ZFS
Ω	angular frequency of the applied radiofrequency pulse
ω	angular frequency (rad s^{-1})
ω_0	resonance angular frequency, angular Larmor frequency
$A/\hbar$	scalar coupling constant (rad s^{-1})
a_{2T}	second order transient ZFS parameter (= Δ)
a_k	static ZFS parameter of order k = 2, 4, 6 ($a_2 = D$)
$\boldsymbol{B}$	magnetic field
$\boldsymbol{B}_0$	static magnetic field
B_0	magnitude of the magnetic field $\boldsymbol{B}_0$
$\boldsymbol{B}_1$	applied radiofrequency magnetic field
$\boldsymbol{B}_{eff}$	effective (experienced) magnetic field
C_{SR}	spin-rotation constant
C_{DD}	dipolar coupling constant
C_{OS}	outer-sphere empirical constant

D	axial ZFS parameter (second order parameter for the static ZFS) (= a_2) (cm^{-1})
D	translational diffusion coefficient
d	density
d_{12}	closest distance of approach of particles 1 and 2
D_{GdH}^{298}	relative translational diffusion coefficient for diffusion of Gd and water proton at 25°C
d_H	hydrodynamic diameter
E	energy
E_a	activation energy
E_{DGdH}	translational diffusion activation energy for mutual diffusion of Gd and water proton
E_l	internal rotation activation energy
E_m	energy of the nuclear spin state m
eq_{zz}	electric field gradient along the z-axis
E_R	rotational activation energy
E_v	transient zero-field splitting activation energy
$\boldsymbol{F}$	torque
$\boldsymbol{G}$	field gradient
g	Landé g-factor
$G(\tau)$	correlation function
g_e	Landé g-factor for free electron
$\boldsymbol{I}$	spin angular momentum
I	nuclear spin quantum number
I_r	molecular inertia moment
$J(\omega,\tau)$	spectral density function
k_{ex}^{298}	exchange rate constant at 25°C
M	molar mass
$\boldsymbol{M}$	magnetization
m	magnetic quantum number
M_0	equilibrium magnetization along the z-axis
M_{xy}	magnetization component in the xy-plane
M_z	magnetization component along the z-axis
N_0	total number of spins
N_m	nuclear spin population in the spin state m
P_m	mole fraction of water bound to a metal ion
Q	nuclear quadropole moment
q	hydration number (number of water molecules in the inner sphere of a complex)
r	radius
R_1	longitudinal relaxation rate = $1/T_1$
r_1	relaxivity
R_2	transverse relaxation rate = $1/T_2$
r_{IS}	interspin distance between the spins I and S
r_{GdH}	water proton-gadolinium distance in the inner sphere of the complex (= $r_{GdH\ 1st}$)
$r_{GdH\ 2nd}$	water proton-gadolinium closest distance of the bulk water (= d_{GdH})
r_{GdO}	water oxygen-gadolinium distance in the inner sphere of the complex
S	spin of the particle S
S^2	Lipari-Szabo parameter
T	temperature
t	time
T_1	longitudinal nuclear relaxation time
T_2	transverse nuclear relaxation time
T_i^C (i = 1, 2)	nuclear relaxation times due to Curie relaxation
T_i^{CSA} (i = 1, 2)	nuclear relaxation times due to chemical shift anisotropy relaxation
T_i^d (i = 1, 2)	diamagnetic nuclear relaxation times
T_i^{DD} (i = 1, 2)	nuclear relaxation times due to dipolar relaxation
T_{ie} (i = 1, 2)	electron spin relaxation times
T_{iM} (i = 1, 2)	nuclear relaxation times in paramagnetic environment M (without chemical exchange)
T_i^{obs} (i = 1, 2)	observed nuclear relaxation times
T_i^p (i = 1, 2)	paramagnetic nuclear relaxation times
T_i^Q (i = 1, 2)	nuclear relaxation time due to quadropolar relaxation
T_i^{ref} (i = 1, 2)	nuclear relaxation time of the reference
T_{ir} (i = 1, 2)	reduced nuclear relaxation time

T_i^{SC} (i = 1, 2)	nuclear relaxation times due to scalar relaxation
T_i^{SR} (i = 1, 2)	nuclear relaxation times due to spin-rotation relaxation
w_X	mass fraction of the element X
+	*tert*-butyl

VII.1.2 Abbreviations

Ar	aromatic
AUC	analytical ultracentrifugation
br s	broad signal
bisoxa(DO3A)$_2^{6-}$	bis(1,4-(1-(carboxymethyl)-1,4,7,10-tetraaza-4,7,10-tris(carboxymethyl)-1-cyclododecyl))-1,10-diaza-3,6-dioxadecane
BMS	bulk magnetic susceptibility
BN	bombesin
Bn	benzyl
BPO	benzyl peroxide
CA	contrast agent
Cbz	carbobenzyle
CCW	counterclockwise
Chi	chitosan
CPMG	Carr-Purcell-Meiboom-Gill
CSA	chemical shift anisotropy
CW	clockwise
DA	degree of acetylation
DCM	dichloromethane
DD	degree of deacetylation
DD	dipole-dipole (or dipolar) interaction
DIPEA	diisopropylethylamine
DLS	dynamic light scattering
DM	degree of modification
DMF	dimethylformamide
DMSO	dimethylsulfoxide
DO3A^{3-}	1,4,7,10-tetraazacyclododecane-*N*,*N*',*N*''-triacetate
DOSY	diffusion ordered spectroscopy
DOTA^{4-}	1,4,7,10-tetraazacyclododecane-*N*,*N*',*N*'',*N*'''-tetraacetate
DTPA^{5-}	diethylenetriamine-*N*,*N*,*N*',*N*'',*N*''-pentaacetate
DTTA^{4-}	diethylenetriamine-*N*,*N*,*N*'',*N*''-tetraacetate
DTTA-*N*'but^{5-}	diethylenetriamine-*N*,*N*,*N*'',*N*''-tetraacetate-*N*'-propionic acetate
DTTA-*N*'prop^{5-}	diethylenetriamine-*N*,*N*,*N*'',*N*''-tetraacetate-*N*'-butyric acetate
DTPA-BA^{3-}	diethylenetriamine-*N*,*N*''-bis amide-*N*',*N*',*N*''-triacetate
DTPA-CHD^{3-}	diethylenetriamine-*N*,*N*''-cyclohexanediamide -*N*',*N*',*N*''-triacetate
DTPA-BMA^{3-}	1,7-bis[(*N*-methylcarbonyl)methyl]-1,4,7-triazaheptane-1,4,7-triacetate
EDC	*N*-[3-(dimethylamino) propyl]-*N*'-ethylcarbodiimide hydrochloride
EDTA^{4-}	1,2-ethylenediamine-*N*,*N*,*N*',*N*'-tetraacetate
ELS	electrophoretic light scattering
eq	equivalent
EPR	electron paramagnetic relaxation
ESI	electron spray ionisation
Et	ethyl
EtOH	ethanol
FAB-MS	fast atom bombardment mass spectroscopy
FFC	fast field cylce
FID	free induction decay
Fmoc	fluorenylmethyloxycarbonyl
G	(1-4)-linked α-L-guluronate
GBCA	gadolinium-based contrast agent
hrs	hours
HP-DO3A	10-(2-hydroxypropyl)-1,4,7,10-tetraazacyclododecane-*N*,*N*',*N*'',*N*'''-triacetic acid
HPLC	high pressure liquid chromatography

ICP-MS	induced coupled plasma mass spectroscopy
IR	inversion recovery pulse sequence
IS	inner-sphere
LS	Lipari-Szabo
M	(1-4)-linked β-D-mannuronate
MALDI	matrix-assisted laser desorption
Me	methyl
MeOH	methanol
Mes	mesithylene
min	minutes
MRI	magnetic resonance imaging
MS	mass spectrometry
*m*X(DO3A)$_2^{6-}$	1,3-bis{[4,7,10-tris(carboxymethyl)-1,4,7,10-tetraazacyclododecane-1-yl]methyl}benzene
NBS	*N*-bromosuccinimide
NCF	neutron-capture therapy
NFS	nephrogenic systemic fibrosis
Ng	nanogel
NMR	nuclear magnetic resonance
NMRD	nuclear magnetic relaxation dispersion
OS	outer-sphere
PAMAM	poly(amido amine)
PBS	Phosphate Buffered Saline
PdI	polydispersity index
PEG	polyethylene glycol
PRE	paramagnetic relaxation enhancement
*p*X(DO3A)$_2^{6-}$	1,4-bis{[4,7,10-tris(carboxymethyl)-1,4,7,10-tetraazacyclododecane-1-yl]methyl}-benzene
RF	radiofrequency
RFB	Rast-Fries-Belorizky
SBM	Solomon-Bloembergen-Morgan
SC	scalar (or Fermi contract) interaction
SED	Stokes-Einstein-Debye
SOMO	singly occupied molecular orbital
SOP	Standard Operating Procedures
SPIO	nanoparticular superparamagnetic ion oxides
SPPS	solid phase peptide synthesis
Sulfo-NHS	N-hydoxysulfosuccinimide
t-Bu	*tert*-butyl
TEM	transmission electron microscopy
TOF	time of flight
TEA	triethylamine
TFA	trifluoroacetic acid
TPP	triphosphate
TTAHA^{6-}	*N*-tris(2-aminoethyl)amine-*N'*,*N'*,*N''*,*N''*,*N'''*,*N'''*-hexaacetate
UV-Vis	ultraviolet-visible
vbr s	very broad signal
ZFS	zero-field-splitting

VII.1.3 Constants and numbers

γ_e	gyromagnetic ratio of the electron	$-1.7609 \cdot 10^{11}$	rad T^{-1} s^{-1}
γ_H	gyromagnetic ratio of the proton	$2.6751 \cdot 10^{8}$	rad T^{-1} s^{-1}
μ_0	vacuum permeability	$4\pi \cdot 10^{-7}$	N A^{-2}
μ_B	Bohr magneton	$9.274 \cdot 10^{-24}$	J T^{-1}
e	Euler's number	2.71828	
h	Planck constant	$6.6261 \cdot 10^{-34}$	J s
$\hbar$	Reduced Planck constant (= h / 2π)	$1.054 \cdot 10^{-34}$	J s
k_B	Boltzmann constant	$1.3807 \cdot 10^{-34}$	J K^{-1}
N_A	Avogadro constant	$6.022 \cdot 10^{-23}$	mol^{-1}
R	gas constant	8.3145	J K^{-1} mol^{-1}

VII.2. Appendix to Chapter II

VII.2.1. Transmetallation

t / min	T_1^{obs} / ms	t / min	T_1^{obs} / ms	t / min	T_1^{obs} / ms
0	566.08	216	470.97	526	465.46
5	537.08	226	471.07	536	465.66
8	530.57	236	470.47	546	465.07
10	527.00	246	469.56	556	465.17
12	522.84	256	469.46	566	465.36
14	519.74	266	468.85	576	465.07
17	516.79	276	468.55	586	465.26
23	512.92	286	468.65	596	464.97
27	506.27	296	468.45	606	464.77
33	500.83	306	468.25	616	464.87
38	496.40	316	467.85	626	465.46
40	495.16	326	467.85	636	464.97
46	492.71	336	467.75	646	464.47
47	491.60	346	467.35	656	465.17
53	488.42	356	467.35	666	464.87
56	487.77	366	467.15	676	464.77
66	487.77	376	466.95	686	464.77
76	484.10	386	467.25	696	464.67
86	481.65	396	467.05	706	464.97
96	479.64	406	466.95	716	465.07
106	478.39	416	466.65	726	464.67
116	476.72	426	466.26	736	464.67
126	475.48	436	466.55	746	464.47
136	474.75	446	466.75	756	464.47
146	473.52	456	465.96	766	464.87
156	474.44	466	465.96	776	464.08
166	473.52	476	465.66	786	464.38
176	473.01	486	466.26	796	464.57
186	472.29	496	465.56	806	464.47
196	471.48	506	465.66		
206	471.28	516	465.46		

Table VII.1 **–** Relaxation times T_1 at 25°C, 30 MHz of the system Gd^{3+} / {Mes[Gd(DO3A)$(H_2O)_2$]$_3$} during transmetallation

VII.2.2. Normalized peak areas as a function of pH

pH	normalized peak area @ 7.09 ppm	normalized peak area @ 7.52 ppm
1.15	0	1
2.95	0.17	0.83
5.60	0.72	0.28
9.18	0.85	0.15
13.29	0.97	0.03

Table VII.2 – Normalized aromatic peak areas of isomers A and B of the bis-Gd complex $\{Mes(H_2DO3A)[Gd(DO3A)(H_2O)]_2\}^-$ as a function of pH.

VII.2.3. ^{17}O NMR data of $\{Mes(H_2DO3A)[Gd(DO3A)(H_2O)]_2\}^-$

T / °C	1000/T / K^{-1}	ln ($1/T_{1r}$)	ln ($1/T_{2r}$)	$\Delta\omega_r$ / 10^6 rad s^{-1}
89.6	2.76	9.226	12.48	-0.5686
76.4	2.86	9.461	12.83	-0.5686
66.9	2.94	9.559	12.68	-0.6053
58.4	3.02	9.754	12.79	-0.6039
55.7	3.04	9.813	12.93	-0.6583
44.4	3.15	10.04	13.19	-0.6583
38.6	3.21	10.18	13.66	-0.6726
29.4	3.31	10.33	14.24	-0.6398
17.5	3.44	10.67	14.70	-0.5653
2.0	3.63	11.07	14.87	-0.3912

Table VII.3 – Variable temperature reduced relaxation rates ($1/T_{ir}$, i = 1, 2) and chemical shifts $\Delta\omega_r$ of the water ^{17}O of the bis-Gd complex $\{Mes(H_2DO3A)[Gd(DO3A)(H_2O)]_2\}^-$ ($[Gd^{3+}]$ = 20.15 mM).

VII.2.4. ^{17}O NMR data of {Mes[Gd(DO3A)(H$_2$O)$_2$]$_3$}

T / °C	1000/T / K^{-1}	ln (1/T_{1r})	ln (1/T_{2r})	$\Delta\omega_r$ / 10^6 rad s^{-1}
89.6	2.76	8.893	12.24	-0.4682
76.4	2.86	9.155	12.60	-0.5540
66.9	2.94	9.380	13.00	-0.5532
58.4	3.02	9.657	13.16	-0.6044
55.7	3.04	9.751	13.21	-0.5946
44.4	3.15	9.949	13.51	-0.5946
38.6	3.21	10.21	13.52	-0.6622
29.4	3.31	10.41	13.93	-0.6421
17.5	3.44	10.64	14.39	-0.5790
2.0	3.63	11.14	14.76	-0.4597

Table VII.4 – Variable temperature reduced relaxation rates (1/T_{ir}, i = 1, 2) and chemical shifts $\Delta\omega_r$ of the water ^{17}O of the tris-Gd complex {Mes[Gd(DO3A)(H$_2$O)$_2$]$_3$} ([Gd^{3+}] = 20.61 mM).

VII.2.5. ^{1}H NMRD data of bis-Gd and tris-Gd complexes

ν (^{1}H) / MHz	r_1 / mM^{-1} s^{-1}			
	Bis-Gd {Mes(H_2DO3A)[Gd(DO3A)(H_2O)]$_2$}$^{-}$		Tris-Gd {Mes[Gd(DO3A)(H_2O)$_2$]$_3$}	
	25.0°C	37.0°C	25.0°C	37.0°C
0.0100	7.70	6.78	16.04	13.80
0.0144	7.71	6.78	16.06	13.72
0.0208	7.73	6.78	16.09	13.72
0.0298	7.70	6.78	16.07	13.77
0.0428	7.71	6.78	16.06	13.72
0.0616	7.73	6.79	16.01	13.80
0.0887	7.72	6.79	16.01	13.85
0.127	7.82	6.80	16.03	13.81
0.183	7.84	6.81	16.04	13.89
0.264	7.92	6.83	16.10	13.89
0.379	7.92	6.85	16.12	13.91
0.546	7.94	6.88	16.07	13.96
0.785	7.90	6.91	16.05	13.70
1.13	7.80	6.94	15.63	13.97
1.62	7.83	6.95	15.60	13.91
2.34	7.80	6.90	15.28	13.80
3.36	7.87	6.74	14.71	13.49
4.83	7.83	6.44	14.10	13.13
6.95	7.47	6.13	13.63	11.94
10	7.00	5.99	13.19	11.15
12	6.93	5.99	13.04	10.48
14	7.05	6.01	13.09	10.37
16	7.23	6.03	13.16	10.37
18	7.31	6.05	13.82	10.32
20	7.45	6.07	13.65	10.23
30	7.73	6.09	14.08	10.68
40	7.97	6.06	14.21	10.63
60	7.73	5.98	14.33	10.52
100	7.52	5.85	13.87	10.23
200	6.69	5.63	13.42	9.80
400	5.91	5.17	11.14	8.96

Table VII.5 **–** Water proton relaxivities r_1 at 25°C and 37°C of the bis-Gd complex ([Gd^{3+}] = 5.53 mM) and the tris-Gd complex ([Gd^{3+}] = 12.79 mM) as a function of the proton Larmor frequency.

VII.3. Appendix to Chapter III

VII.3.1 Relaxivity of {$Ph_4[Gd(DTTA)(H_2O)_2]^-_3$} as a function of [$Gd^{3+}$]

$[Gd^{3+}]$ / mM	T_1 / s	r_1 / mM^{-1} s^{-1}
1.515	0.01535	42.76
1.264	0.01870	42.02
0.999	0.02480	39.98
0.746	0.03430	38.61
0.508	0.05348	36.11
0.295	0.09880	33.03
0.146	0.2109	29.98
0.0740	0.4057	28.38
0.0486	0.5855	27.62
0.0237	0.9790	27.62
0.00938	1.649	25.63
18.92	48.14	48.14
18.18	50.56	50.56
9.906	48.19	48.19
4.235	44.98	44.98
1.838	43.06	43.06
0.947	41.71	41.71
0.471	36.81	36.81
0.226	32.14	32.14
0.103	27.05	27.05
0.0478	26.35	26.35
0.0227	24.89	24.89
0.0103	25.63	25.63

Table VII.6 **–** Water proton relaxation times T_1 and relaxivities r_1 at 25°C, 30MHz of two $\{Ph_4[Gd(DTTA)(H_2O)_2]^-_3\}$ systems resulting from different synthesis batches as a function of the Gd^{3+} concentration.

VII.3.2 ^{1}H NMRD data of {$Ph_4[Gd(DTTA)(H_2O)_2]^-_3$}

	r_1 / mM^{-1} s^{-1}				
$[Gd^{3+}]$ / mM	18.18		1.838		0.101
ν (^{1}H) / MHz	25.0°C	37.0°C	25.0°C	37.0°C	25.0°C
0.0100			37.78	32.37	28.39
0.0137			37.44	32.31	28.92
0.0190			37.61	32.12	29.03
0.0262			37.22	32.26	28.99
0.0360			37.16	32.12	28.97
0.0497			37.36	32.36	29.29
0.0686			37.22	32.32	28.98
0.0943			37.22	32.20	28.76
0.130			37.27	31.76	28.78
0.180			36.91	31.99	28.91
0.247			36.62	31.82	28.76
0.341			36.73	31.31	28.39
0.469			35.86	31.17	28.60
0.647			34.95	30.58	27.91
0.892			34.14	29.32	26.98
1.23			32.88	28.55	25.40
1.69			31.35	27.13	24.92
2.33			29.60	25.60	23.95
3.22			27.91	24.32	22.61
4.43			26.59	22.68	20.94
6.11			26.14	22.01	19.97
8.42			28.45	23.18	20.05
11.6			32.11	25.40	21.28
16			35.72	27.71	22.38
20	46.67	38.28	38.52	29.68	22.84
30	50.55	41.64	42.47	32.32	24.67
40	53.15	44.16	43.49	33.26	25.27
60	47.75	40.80	42.16	32.32	25.27
100	34.61	32.72	31.69	27.27	23.76
200	15.01	17.43	16.74	16.72	17.63
400	7.51	7.86	7.94	8.40	9.97
800	4.17	4.00	4.17	4.19	4.70

Table VII.7 – Water proton relaxivities r_1 at 25°C and 37°C of {$Ph_4[Gd(DTTA)(H_2O)_2]^-_3$} at different concentrations as a function of the proton Larmor frequency.

VII.3.3 ^{17}O NMR data of $\{Ph_4[Gd(DTTA)(H_2O)_2]^-_3\}$

T / °C	1000/T / K^{-1}	ln ($1/T_{1r}$)	ln ($1/T_{2r}$)	$\Delta\omega_r$ / 10^6 rad s^{-1}
25.2	3.35	11.66	14.00	-0.763
44.2	3.15	11.30	13.66	-0.783
61.8	2.99	10.89	13.15	-0.678
89.9	2.75	10.50	12.28	-0.582
79.6	2.83	10.48	12.59	-0.674
70.4	2.91	10.72	12.88	-0.668
52	3.08	11.14	13.45	-0.790
35.3	3.24	11.39	13.83	-0.805
14	3.48	11.85	14.17	-0.687
2	3.63	11.88	14.10	-0.423
-2	3.69	11.83	14.08	-0.369

Table VII.8 – Variable temperature reduced relaxation rates ($1/T_{ir}$, i = 1, 2) and chemical shifts $\Delta\omega_r$ of the water ^{17}O of $\{Ph_4[Gd(DTTA)(H_2O)_2]^-_3\}$ ($[Gd^{3+}]$ = 15.37 mM).

VII.3.4 Relaxivities of $\{Ph_4[Gd(DTTA)(H_2O)_2]^-_3\}$ as a function of pH

pH	$[Gd^{3+}]$ / mM	T_1 / ms	r_1 / mM^{-1} s^{-1}
7.07	0.756	31.53	41.45
5.7	0.767	31.64	40.73
4.71	0.792	31.06	40.19
4.47	0.763	32.10	40.35
4.16	0.763	31.96	40.50
4.07	0.761	31.20	41.62

Table VII.9 – Water proton relaxivities r_1 of $\{Ph_4[Gd(DTTA)(H_2O)_2]^-_3\}$ ~ 0.8 mM at 25°C, 20 MHz as a function of pH

VII.3.5 Relaxivities time evolution of {$Ph_4[Gd(DTTA)(H_2O)_2]^-_3$} vs. [$PO_4^{3-}$]

	r_1 / mM^{-1} s^{-1}						
$[PO_4^{3-}]$ / mM / t / h	0.17	24	48	72	96	120	144
0	54.94	54.74	54.74	54.40	54.09	54.36	54.77
11.5	55.26	52.72	51.67	51.10	50.46	50.84	51.13
21.2	54.96	51.61	49.26	48.24	47.49	47.29	47.21
50.9	53.74	47.01	39.02	35.75	33.62	31.42	30.24
115.6	49.77	33.29	13.34	8.42	5.27	3.72	2.99
221.7	42.84	16.58	2.50	1.80	1.31	1.13	1.06
506.8	32.42	4.56	1.36	1.24	1.19	1.02	1.00

Table VII.10 – Time evolution of the water proton relaxivities r_1 at 25°C, 30 MHz of {$Ph_4[Gd(DTTA)(H_2O)_2]^-_3$} ($[Gd^{3+}]$ = 2.25 mM) as a function of the phosphate concentration.

VII.3.6 Relaxivities time evolution of {$Ph_4[Gd(DTTA)(H_2O)_2]^-_3$} in human serum

t / h	r_1 / mM^{-1} s^{-1}
0.17	60.51
24	59.03
48	58.01
72	57.55
96	57.18
120	56.69
144	56.18
168	56.77

Table VII.11 – Time evolution of the water proton relaxivities r_1 at 25°C, 30 MHz of {$Ph_4[Gd(DTTA)(H_2O)_2]^-_3$} ($[Gd^{3+}]$ = 2.25 mM) in 32% w/w human serum.

VII.4. Appendix to Chapter IV

VII.4.1. ICP-MS instrumentation parameters and performance report

Daily Performance Report

Sample ID: au30prf
Sample Date/Time: Monday, August 30, 2010 15:15:49
Sample Description:
Method File: c:\elandata\Method\Daily Performance LMode Alex.mth
Dataset File: c:\elandata\Dataset\Def\au30prf.430
Tuning File: c:\elandata\Tuning\default.tun
Optimization File: c:\elandata\Optimize\default.dac
Dual Detector Mode: Dual
Acq. Dead Time(ns): 45
Current Dead Time (ns): 45

Summary

	Analyte	Mass	Meas. Intens. Mean	Net Intens. Mean	Net Intens. SD	Net Intens. RSD
	Mg	24.0	5142.4	5142.398	469.731	9.1
	In	114.9	27642.8	27642.763	747.153	2.7
	U	238.1	28442.0	28441.997	1063.223	3.7
ε>	Ce	139.9	35353.0	35353.032	1485.663	4.2
ε	CeO	155.9	528.8	0.015	0.000	3.0
ε>	Ba	137.9	28570.3	28570.286	953.308	3.3
ε	Ba++	69.0	830.2	0.029	0.001	4.8
	220	220.0	1.2	1.200	0.837	69.7
	8.5	8.5	1.0	1.000	1.225	122.5

Current Optimization File Data

Current Value	Description
0.88	Nebulizer Gas Flow [NEB]
1.20	Auxiliary Gas Flow
15.00	Plasma Gas Flow
5.50	Lens Voltage
1200.00	ICP RF Power
-1760.00	Analog Stage Voltage
1175.00	Pulse Stage Voltage
-5.50	Quadrupole Rod Offset Std [QRO]
0.50	Cell Rod Offset Std [CRO]
60.00	Discriminator Threshold
-22.50	Cell Path Voltage Std [CPV]
0.00	RPa
0.25	RPq
0.90	DRC Mode NEB
-5.00	DRC Mode QRO
0.00	DRC Mode CRO
-23.00	DRC Mode CPV
0.00	Cell Gas A

Current Autolens Data

Analyte	Mass	Num of Pts	DAC Value	Maximum Intensity
Mg	24	71	5.3	5831.5
Mn	55	71	6.3	23935.8
In	115	71	6.4	27293.5
Pb	208	71	9.6	13748.5
U	238	71	9.9	30331.3

Sample ID: au30prf
Report Date/Time: Monday, August 30, 2010 15:16:33

VII.4.2. ICP-MS experimental data

	isotope	concentr. ppm	$\frac{[Gd^{3+}]}{[Eu^{3+}]}$	I cps	$\frac{I_{Gd}}{I_{Eu}}$	$\frac{I_{Gd}^{blank}}{I_{Eu}^{blank}}$
Blank	^{151}Eu	0.2974		13852135.4		
	^{155}Gd	0		481.6	0.00003477	
	^{157}Gd			472	0.00003407	
Standard 1	^{151}Eu	0.3011		14831723		
	^{155}Gd	0.9763	3.242	13173741	0.88821	0.88818
	^{157}Gd			15266177	1.02929	1.02926
Standard 2	^{151}Eu	0.2907		14720575		
	^{155}Gd	0.2885	0.9924	4123073	0.28009	0.28005
	^{157}Gd			4786912	0.32519	0.32515
Sample	^{151}Eu	0.2904		15780928		
	^{155}Gd	**0.64428**	**0.2188**	9616625	0.60938	0.60935
	^{157}Gd	**0.64400**	**0.2178**	11141001	0.70598	0.70595

Table VII.12 – Experimental values of ICP-MS intensities, in counts per seconds, for the isotopes ^{151}Eu, ^{155}Gd and ^{157}Gd at precise concentrations to determine $[Gd^{3+}]$ for 10.54 mg of sample in 5.00533 g of solution. Bold values obtained from linear fit of experimental points (Figure VII.1)

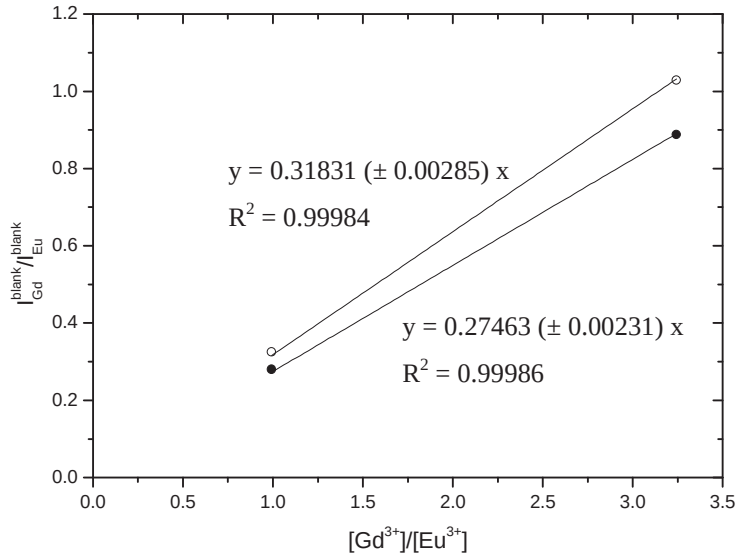

Figure VII.1 – Linear fits, allowing the determination of the Gd^{3+} concentration, for corrected ^{155}Gd (●) and ^{157}Gd (○) intensities with respect to the internal reference ^{151}Eu.

VII.4.3. ^{1}H NMRD data of $[Gd(DTTA\text{-}N'but)(H_2O)_2]^{2-}$ and $[Gd(DTTA\text{-}Me)(H_2O)_2]^{-}$

ν (^{1}H) / MHz	r_1 / mM^{-1} s^{-1}			
	$[Gd(DTTA\text{-}N'but)(H_2O)_2]^{2-}$		$[Gd(DTTA\text{-}Me)(H_2O)_2]^{-}$	
	25.0°C	37.0°C	25.0°C	37.0°C
0.0100	15.34	12.29	12.31	10.58
0.0137	15.34	12.19	12.34	10.49
0.0190	15.32	12.25	12.28	10.54
0.0262	15.32	12.28	12.22	10.58
0.0360	15.35	12.32	12.25	10.51
0.0497	15.35	12.31	12.29	10.53
0.0686	15.36	12.28	12.34	10.48
0.0943	15.25	12.25	12.33	10.44
0.130	15.26	12.22	12.30	10.45
0.180	15.34	12.10	12.25	10.51
0.247	15.21	12.21	12.23	10.39
0.341	15.25	12.21	12.24	10.45
0.469	15.18	12.22	12.22	10.38
0.647	15.16	12.13	12.17	10.38
0.892	15.10	12.10	12.09	10.28
1.23	14.89	11.98	11.96	10.24
1.69	14.62	11.77	11.79	9.98
2.33	14.20	11.44	11.62	9.92
3.22	13.50	10.85	11.17	9.55
4.43	12.45	10.18	10.30	8.92
6.11	11.55	9.67	9.71	8.41
8.42	10.87	8.70	8.82	7.48
11.6	10.02	7.99	7.95	6.94
16	9.44	7.30	7.48	5.97
20	9.02	7.01	7.21	5.54
30	8.67	6.52	6.92	5.30
40	8.52	6.34	6.74	5.10
60	8.62	6.30	6.77	4.96
100	8.47	6.30	6.43	4.80
200	8.60	6.40	6.45	4.77
400	8.04	6.08	6.18	4.61

Table VII.13 – Water proton relaxivities r_1 at 25°C and 37°C of $[Gd(DTTA\text{-}N'but)(H_2O)_2]^{2-}$ ($[Gd^{3+}]$ = 2.55/3.50 mM) and $[Gd(DTTA\text{-}Me)(H_2O)_2]^{-}$ ($[Gd^{3+}]$ = 3.30/2.97 mM) as a function of the proton Larmor frequency.

VII.4.4. ^1H NMRD data of {Chi[Gd(DTTA-N'but)$(H_2O)_2]^-$} and Ng{Chi[Gd(DTTA-N'but)$(H_2O)_2]^-$}

ν (^{1}H) / MHz	r_1 / mM^{-1} s^{-1}		
	{Chi[Gd(DTTA-*N*'but)$(H_2O)_2]^{2-}$}		Ng{Chi[Gd(DTTA-*N*'but)$(H_2O)_2]^{2-}$}
	25.0°C	37.0°C	25.0°C
0.0100	32.93	27.76	24.86
0.0137	32.85	27.70	
0.0190	32.81	27.99	24.83
0.0262	32.58	27.94	
0.0360	32.61	28.13	24.62
0.0497	32.44	28.12	
0.0686	32.63	27.76	24.66
0.0943	32.35	27.47	
0.130	32.51	27.38	22.44
0.180	32.17	27.37	
0.247	32.08	27.32	21.81
0.341	31.66	26.90	
0.469	31.61	26.33	21.26
0.647	30.32	26.29	
0.892	29.64	25.41	20.08
1.23	28.34	24.57	
1.69	27.42	23.62	18.54
2.33	26.73	22.98	
3.22	25.26	21.54	15.37
4.43	23.11	20.18	
6.11	22.71	19.11	13.97
8.42	23.86	19.09	
11.6	25.46	20.49	13.38
16	27.83	21.87	
20	29.52	22.51	16.72
30	32.69	25.38	18.27
40	33.64	26.03	18.12
60	32.52	24.94	17.25
100	24.59	20.11	13.27
200	17.38	14.96	11.07
400	11.81	10.33	8.61

Table VII.14 – Water proton relaxivities r_1 of {Chi[Gd(DTTA-*N*'but)$(H_2O)_2]^-$} ([Gd^{3+}] = 0.97/0.65 mM) and Ng{Chi[Gd(DTTA-*N*'but)$(H_2O)_2]^-$} ([Gd^{3+}] = 0.13 mM) as a function of the proton Larmor frequency.

VII.4.5. Relaxivities of {Chi[Gd(DTTA-N'but)(H_2O)$_2$]$^{2-}$} as a function of [Gd^{3+}]

[Gd^{3+}] / mM	[Chi] / %(w/w)	r_1 / mM^{-1} s^{-1}
1.05	0.57	28.60
0.835	0.45	28.72
0.629	0.34	29.07
0.415	0.23	28.94
0.205	0.11	27.15
0.103	0.056	26.58

Table VII.15 – Water proton relaxivities r_1 at 25°C, 20 MHz as a function of the Gd^{3+} and chitosan concentration.

VII.4.6. Relaxivities time evolution of {Chi[Gd(DTTA-N'but)(H_2O)$_2$]$^{2-}$}

time / day	r_1 / mM^{-1} s^{-1}
0	29.52
1	29.92
2	29.64
3	30.27
4	29.80
7	29.84
14	29.83
31	29.66

Table VII.16 – Water proton relaxivities r_1 at 25°C, 20 MHz as a function of time.

VII.4.7. ZetaSizer Nano-ZS parameters of the Standard Operating Procedures (SOP)

Parameters	
Equilibrium time / s	180
Temperature / °C	25
Refractive index	1.59
Absorption	0.0 / 0.3 *(samples in DMEM)*
Dispersant	Water
Number of measures	3
Runs	Automatic
Angle	173° - Backscatter (size)
Model	Smoluchowski (zeta)

Table VII.17 – Parameters of the SOP for the analysis of nanogel size distribution and zeta potential in the ZetaSizer Nano-ZS.

VII.4.8. DLS size distribution of Ng{Chi[Gd(DTTA-N'but)(H$_2$O)$_2$]$^-$}

size d_H / nm	intensity / %		size d_H / nm	intensity / %	
	modified Ng	standard Ng		modified Ng	standard Ng
0.7195	0	0	91.28	0	0
0.8332	0	0	105.7	0	0
0.9649	0	0	122.4	0	0
1.117	0	0	141.8	0	0
1.294	0	0	164.2	0.133	0
1.499	0	0	190.1	1.467	0
1.736	0	0	220.2	3.967	0.6
2.01	0	0	255	7.233	1.9
2.328	0	0	295.3	10.5	4
2.696	0	0	342	13.067	6.5
3.122	0	0	396.1	14.4	8.9
3.615	0	0	458.7	14.167	10.8
4.187	0	0	531.2	12.6	12
4.849	0	0	615.1	9.933	12.2
5.615	0	0	712.4	6.8	11.6
6.503	0	0	825	3.833	10.1
7.531	0	0	955.4	1.533	8.2
8.721	0	0	1106	0.3	6
10.1	0	0	1281	0	3.9
11.7	0	0	1484	0	2.1
13.54	0	0	1718	0	0.9
15.69	0	0	1990	0	0.2
18.17	0	0	2305	0	0
21.04	0	0	2669	0	0
24.36	0	0	3091	0	0
28.21	0	0	3580	0	0
32.67	0	0	4145	0	0
37.84	0	0	4801	0	0
43.82	0	0	5560	0	0
50.75	0	0	6439	0	0
58.77	0	0	7456	0	0
68.06	0	0	8635	0	0
78.82	0	0	10000	0	0

Table VII.18 – Intensity frequencies of Ng{Chi[Gd(DTTA-*N*'but)(H$_2$O)$_2$]$^-$} (modified Ng) and unmodified nanogels as a function of the hydrodynamic diameter.

VII.5. Appendix to Chapter V

VII.5.1. ^{1}H NMRD data of monovalent peptide conjugates

ν (^{1}H) / MHz	r_1 / mM^{-1} s^{-1}			
	{Lys^{3}-BN[Gd(DOTA)(H_2O)]}		{Ahx-BN(4-14)[Gd(DOTA)(H_2O)]}	
	25.0°C	37.0°C	25.0°C	37.0°C
0.0100	21.15	18.35	18.74	15.24
0.0144	21.16	18.34	18.71	15.14
0.0208	21.16	18.26	18.75	15.10
0.0298	21.13	18.20	18.72	15.08
0.0428	21.11	18.21	18.77	14.97
0.0616	21.14	18.21	18.79	14.95
0.0887	21.12	18.17	18.72	14.95
0.127	21.13	18.14	18.72	14.91
0.183	21.06	18.11	18.71	14.88
0.264	20.98	18.11	18.60	14.72
0.379	20.76	17.86	18.44	14.64
0.546	20.39	17.56	18.15	14.67
0.784	19.99	17.17	17.68	14.41
1.13	19.23	16.43	17.11	13.76
1.62	17.97	15.35	16.05	13.03
2.34	16.41	13.99	14.71	11.90
3.36	14.71	12.55	13.11	10.48
4.83	13.41	11.39	11.55	9.21
6.95	12.58	10.57	10.34	8.20
10	12.23	9.99	9.23	7.79
14	12.27	10.16	8.98	7.70
18	13.03	10.46	9.31	7.65
30	12.76	9.66	9.53	7.20
40	11.98	9.29	9.41	7.04
60	11.60	8.82	9.33	6.91
100	10.76	8.10	8.83	6.46
200	8.96	7.02	7.67	5.87
400	6.48	5.62	6.05	5.28

Table VII.19 – Water proton relaxivities r_1 of {Lys^{3}-BN[Gd(DOTA)(H_2O)]} ([Gd^{3+}] = 0.75 mM) and {Ahx-BN(4-14)[Gd(DOTA)(H_2O)]} ([Gd^{3+}] = 1.63 mM) as a function of the proton Larmor frequency.

VII.5.2. ^{1}H NMRD data of divalent peptide conjugates

ν (^{1}H) / MHz	r_1 / mM^{-1} s^{-1}			
	{(Lys^3-BN)$_2$[Gd(DOTA)(H$_2$O)]}		{(Ahx-BN(4-14))$_2$[Gd(DOTA)(H$_2$O)]}	
	25.0°C	37.0°C	25.0°C	37.0°C
0.0100	27.40	21.55	21.71	21.71
0.0144	27.03	21.54	21.70	21.70
0.0208	27.21	21.52	21.64	21.64
0.0298	27.22	21.52	21.59	21.59
0.0428	27.15	21.48	21.69	21.69
0.0616	27.23	21.45	21.65	21.65
0.0887	27.33	21.46	21.64	21.64
0.127	26.75	21.44	21.61	21.61
0.183	27.27	21.42	21.35	21.35
0.264	27.46	21.30	21.36	21.36
0.379	26.97	20.87	21.24	21.24
0.546	26.03	20.39	20.74	20.74
0.784	25.07	19.78	19.95	19.95
1.13	23.23	18.84	18.93	18.93
1.62	22.17	17.63	17.82	17.82
2.34	19.42	15.93	16.51	16.51
3.36	17.21	14.33	14.48	14.48
4.83	16.56	13.24	13.35	13.35
6.95	16.72	13.01	12.97	12.97
10	17.53	13.06	13.33	13.33
14	19.05	13.88	14.03	14.03
18	20.00	14.84	14.82	14.82
30	20.24	15.42	16.48	16.48
40	20.07	15.30	16.41	16.41
60	19.22	14.75	15.83	15.83
100	15.83	12.86	13.70	13.70
200	10.80	9.41	10.03	10.03
400	6.27	6.09	6.40	6.40

Table VII.20 – Water proton relaxivities r_1 of {(Lys^3-BN)$_2$[Gd(DOTA)(H$_2$O)]} ([Gd^{3+}] = 0.48 mM) and {(Ahx-BN(4-14))$_2$[Gd(DOTA)(H$_2$O)]} ([Gd^{3+}] = 1.62 mM) as a function of the proton Larmor frequency.

Hugues Jaccard
Rue de Bourg 11
1003 Lausanne
Switzerland
+41 79 371 40 10
hugues.jaccard@epfl.ch

33 years old
27.10.1977
Single
Swiss citizenship

Education

PhD in Chemistry (19.07.2011), Ecole Polytechnique Fédérale de Lausanne (EPFL), Switzerland — 2007-2011

Master of Science MSc in Molecular and Biological Chemistry, EPFL — 1998-2004

Maturité Fédérale Type C, Yverdon-les-Bains, Switzerland — 1993-1996

Professional Experience

PhD in the field of MRI contrast agents, Group of Inorganic and Bioinorganic Chemistry, Prof. Lothar Helm, EPFL. (Title : "Development and understanding of novel compounds designed as potential MRI contrast agents") — 2007-2011

- Organic synthesis of poly(amino carboxylate) chelating units
- Inorganic complexation, analytical chemistry
- NMR measurements and theoretical treatment of relaxometric properties of paramagnetic ion complexes.

Teacher of Mathematics, Physics and Sciences at Secondary School, Etablissement Secondaire Léon Michaud, Yverdon-les-Bains, Switzerland — 2006-2007

Research assistant in molecular and cellular biology in the field of protozoan parasites, Prof. Nicolas Fasel, Université de Lausanne, Switzerland — 2004-2005

Laboratory assistant, Green Coffee Laboratory, Nespresso, Orbe, Switzerland — 2004

Master project in organic chemisty and biochemistry, Prof. Kai Johnsson, Laboratory of Protein Engineering, EPFL (Title : "New Substrates for Specific Quenching of hAGT for *in vivo* experiments") — 2003-2004

Skills

Chemistry	Multli-stage organic synthesis NMR analytical methods, theoretical analysis Purification (chromatography, HPLC) and analytical techniques (NMR, potentiometry, MS, LC-MS, ICP-MS, HPLC, UV-Vis, DLS)
Biochemistry	Molecular biology / biochemistry methods (Western blot, PCR, ELISA) Sterile culture of mammalian and protozoan cells
Languages	French : mother tongue English : fluent German : good (C1 level, ZMP Goethe Institut, 2006) Italian : basic (A1 level, EPFL, 2008)
Informatics	Standard office and graphics software, Origin, Matlab, ChemDraw, Topspin, XWinNMR

Publications

P. Miéville, **H. Jaccard**, F. Reviriego, R. Tripier, L. Helm, Synthesis, complexation and NMR relaxation properties of Gd^{3+} complexes of $Mes(DO3A)_3$, *Dalton Transactions* **2011**, *40(16)*, 4260-4267.

K. Abiraj, **H. Jaccard**, M. Kretzschmar, L. Helm, H.R. Maecke, Novel DOTA-based prochelator for divalent peptide vectorization: Synthesis of dimeric bombesin analogues for multimodality tumor imaging and therapy, *Chemical Communications* **2008**, *(28)*, 3248-3250.

A. Juillerat, C. Heinis, I. Sielaff, J. Barnikow, **H. Jaccard**, B. Kunz, A. Terskikh, K. Johnsson, Engineering substrate specificity of O-6-alkylguanine-DNA alkyltransferase for specific protein labeling in living cells, *Chembiochem*, **2005**, *6(7)*, 1263-1269.

Patents

"Mutants of human O6-alkylguanine-DNA alkyltransferase with improved properties" J. Barnikov, C. Chidley, T. Gronemeyer, C. Heinis, **H. Jaccard**, K. Johnsson, A. Juillerat, A. Keppler. (EPFL Ecole Polytechnique Fédérale de Lausanne, Switz.). PCT Int. Appl. (2005), WO 2005085431.

"Specific substrates for O6- alkylguanine-DNA alkyltransferase"; **H. Jaccard**, K. Johnsson, M. Kindermann, I. C. Sielaff, (EPFL Ecole Polytechnique Fédérale de Lausanne, Switz.). WO 2005085470.

Posters Presentations

COST Action D38 Annual Meeting 2008 – Sacavém, Portugal, April 27-29th 2008, H. Jaccard, C. Cannizzo, C.R. Mayer, L. Moriggi, L. Helm "Surprisingly high relaxivities of the $[Ph_4\{Gd(DTTA)(H_2O)_2\}_3]^{3-}$ complex"

Swiss Chemical Society Fall Meeting 2008 – Zurich, Switzerland, September 11th 2008, H. Jaccard, C. Cannizzo, C.R. Mayer, L. Moriggi, L. Helm "Remarkably high T1 relaxivities of the complex $[Ph_4\{Gd(DTTA)(H_2O)_2\}_3]^{3-}$"

COST Action D38 Working Group 2 Annual Meeting 2009 – Delft, Netherlands, February 19-20th 2009, P. Miéville, H. Jaccard, R. Tripier, L. Helm "Synthesis and relaxation properties of the conformation-switching complex $[Mes\{Gd(DO3A)(H_2O)_2\}_3]$"

COST Action D38 Annual Meeting 2009 – Warsaw, Poland, April 25-27th 2009, P. Miéville, H. Jaccard, R. Tripier, L. Helm "Synthesis and relaxation properties of the conformation-switching complex $[Mes\{Gd(DO3A)(H_2O)_2\}_3]$"

Swiss Chemical Society Fall Meeting 2009 – Lausanne, Switzerland, September 4th 2009, P. Miéville, H. Jaccard, R. Tripier, L. Helm "New complexation strategy and relaxation properties of the conformation-switching complex $\{Mes[Gd(DO3A)(H_2O)_2]_3\}$"

COST Action D38 Annual Meeting 2010 – Thessaloniki, Greece, June 20-22nd 2010, H. Jaccard, L. Helm "Highly-controlled coupling of the MRI contrast agent DTTA-Gd(III) on the polysaccharide chitosan"

COST Action D38 Working Groups 2-6 Annual Meeting 2011 – Torino, Italy, March 24-26th 2011, H. Jaccard, C. Cannizzo, C.R. Mayer, L. Helm "Dynamic aggregation of the mid-size gadolinium complex $[Gd_3(Ph_4DTTA_3)(H_2O)_6]^{3-}$"